

CAPITAL UNIVERSITY OF SCIENCE AND  
TECHNOLOGY, ISLAMABAD



Effectiveness of Geometrical  
Design of Stilling Basin  
Appurtenances Downstream of  
the Barrage

by

Muhammad Waqas Zaffar

A thesis submitted in partial fulfillment for the  
degree of Doctor of Philosophy

in the

Faculty of Engineering

Department of Civil Engineering

2024

# Effectiveness of Geometrical Design of Stilling Basin Appurtenances Downstream of the Barrage

By

Muhammad Waqas Zaffar

(DCE-171001)

Dr. Assefa M. Melese, Professor

Florida International University, Miami, USA

(Foreign Evaluator 1)

Dr. Dawei Han, Professor

Bristol University, Clifton, UK

(Foreign Evaluator 2)

Dr. Ishtiaq Hassan

(Research Supervisor)

Dr. Ishtiaq Hassan

(Head, Department of Civil Engineering)

Dr. Imtiaz Ahmad Taj

(Dean, Faculty of Engineering)

DEPARTMENT OF CIVIL ENGINEERING  
CAPITAL UNIVERSITY OF SCIENCE AND TECHNOLOGY  
ISLAMABAD

2024

Copyright © 2024 by Muhammad Waqas Zaffar

All rights reserved. No part of this dissertation may be reproduced, distributed, or transmitted in any form or by any means, including photocopying, recording, or other electronic or mechanical methods, by any information storage and retrieval system without the prior written permission of the author.

*This PhD degree is dedicated to "My  
Father", as this is his aspiration and  
motivation which make me able to complete it;  
Last but not the least, I dedicate this work to  
Love of my Life "My Mother" for her  
emotional & moral support and her  
never-ending prayers.*



**CAPITAL UNIVERSITY OF SCIENCE & TECHNOLOGY  
ISLAMABAD**

Expressway, Kahuta Road, Zone-V, Islamabad  
Phone: +92-51-111-555-666 Fax: +92-51-4486705  
Email: [info@cust.edu.pk](mailto:info@cust.edu.pk) Website: <https://www.cust.edu.pk>

**CERTIFICATE OF APPROVAL**

This is to certify that the research work presented in the dissertation, entitled “**Effectiveness of Geometrical Design of Stilling Basin Appurtenances Downstream of the Barrage**” was conducted under the supervision of **Dr. Ishtiaq Hassan**. No part of this dissertation has been submitted anywhere else for any other degree. This dissertation is submitted to the **Department of Civil Engineering, Capital University of Science and Technology** in partial fulfillment of the requirements for the degree of Doctor in Philosophy in the field of **Civil Engineering**. The open defence of the dissertation was conducted on **December 27, 2023**.

**Student Name :** Muhammad Waqas Zaffar  
(DCE171001)

The Examination Committee unanimously agrees to award PhD degree in the mentioned field.

**Examination Committee :**

- (a) External Examiner 1: Dr. Hamza Farooq Gabriel  
Professor  
NICE, SCEE, NUST, Islamabad
- (b) External Examiner 2: Dr. Naeem Ejaz  
Professor  
UET, Taxila
- (c) Internal Examiner : Dr. Muazzam Ghous Sohail  
Associate Professor  
CUST, Islamabad

**Supervisor Name :** Dr. Ishtiaq Hassan  
Professor  
CUST, Islamabad

**Name of HoD :** Dr. Ishtiaq Hassan  
Professor  
CUST, Islamabad

**Name of Dean :** Dr. Imtiaz Ahmed Taj  
Professor  
CUST, Islamabad

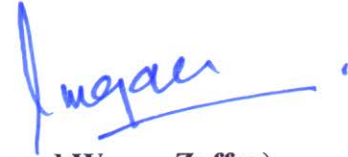
## AUTHOR'S DECLARATION

I, **Muhammad Waqas Zaffar** (Registration No. **DCE17001**), hereby state that my dissertation titled, "**Effectiveness of Geometrical Design of Stilling Basin Appurtenances Downstream of the Barrage**" is my own work and has not been submitted previously by me for taking any degree from Capital University of Science and Technology, Islamabad or anywhere else in the country/ world.

At any time, if my statement is found to be incorrect even after my graduation, the University has the right to withdraw my PhD Degree.

27/12/2023

Dated: December, 2023



(Muhammad Waqas Zaffar)

Registration No : DCE171001

## PLAGIARISM UNDERTAKING

I solemnly declare that research work presented in the dissertation titled “**Effectiveness of Geometrical Design of Stilling Basin Appurtenances Downstream of the Barrage**” is solely my research work with no significant contribution from any other person. Small contribution/ help wherever taken has been duly acknowledged and that complete dissertation has been written by me.

I understand the zero-tolerance policy of the HEC and Capital University of Science and Technology towards plagiarism. Therefore, I as an author of the above titled dissertation declare that no portion of my dissertation has been plagiarized and any material used as reference is properly referred/ cited.

I undertake that if I am found guilty of any formal plagiarism in the above titled dissertation even after award of PhD Degree, the University reserves the right to withdraw/ revoke my PhD degree and that HEC and the University have the right to publish my name on the HEC/ University Website on which names of students are placed who submitted plagiarized dissertation.

27/12/2023

Dated: December, 2023

  
(Muhammad Waqas Zaffar)

Registration No : DCE171001

## *List of Publications*

It is certified that following publications have been made out of the research work that has been carried out for this dissertation:-

1. **M. W. Zaffar**, and I. Hassan, , “Hydraulic investigation of stilling basins of the barrage before and after remodelling using FLOW-3D,” *Water Supply*, vol. 23, no. 2, pp. 796–820, Feb. 2023, doi: 10.2166/ws.2023.032.
2. **M. W. Zaffar**, and I. Hassan, “Numerical investigation of hydraulic jump for different stilling basins using FLOW-3D,” *AQUA - Water Infrastructure, Ecosyst. Soc.* vol. 72, no. 7, pp.1320–1343. jws2023290, July. 2023, doi: 10.2166/aqua.2023.290.
3. **M. W. Zaffar**, I. Hassan, U. Latif, S. Jahan, and Z. Ullah, “Numerical Investigation of Scour Downstream of Diversion Barrage for Different Stilling Basins at Flood Discharge,” *Sustainability*, vol. 15, no. 14, pp. 11032, Jul. 2023, doi: 10.3390/su151411032.
4. **M.W. Zaffar**, I. Hassan, Z. Ali, K. Sarwar, M. Hassan, M. T. Mustafa, F. A. Waris; Numerical investigation of hydraulic jumps with USBR and wedge-shaped baffle block basins for lower tailwater. *AQUA - Water Infrastructure, Ecosyst. Soc.* 2023; jws2023261. doi: <https://doi.org/10.2166/aqua.2023.261>
5. **Zaffar MW**, Haasan I, Ghumman AR. Numerical Investigation of Critical Hydraulic Parameters Using FLOW-3D: A Case Study of Taunsa Barrage, Pakistan. *Fluid.* 2023 Nov 28;8(12):310.
6. **Zaffar MW**, Haasan I, Ghumman AR. Performance Evaluation of Different Stilling Basins Downstream of Barrage Using FLOW-3D Scour Models. *Hydrology.* 2023 Nov 27;10(12):223

**(Muhammad Waqas Zaffar)**

Registration No: DCE-171001



## *Acknowledgement*

In the name of **ALLAH**, the most beneficent and the most merciful. All the praises to HIM, and without HIS help and support, it would not possible for me to complete my PhD. I am very thankful to my supervisor **Prof. Dr. Ishtiaq Hassan** for his timely guidance and support whenever i needed. His motivation and encouragement able me to complete numerous tasks. I am also very grateful to the faculty, and administration of Department of Civil Engineering, Capital University of Science and Technology, Islamabad, for their continuous help, guidance and support.

I am very thankful to my parents who always prayed for me and provided every kind of assistance to achieve my goals. It is their aspiration to complete my PhD degree. I am thankful to my brother Dr. Hammad Zaffar, who motivated me though out this research work. I am also thankful to my wife for being so patient during the research period.

I also extend my gratitude to the management of University of Chenab, Gujrat, for their continuous support to pursue my PhD degree. I am very thankful to Prof. Dr. Zulfiqar Ali and Dr. Kaleem Sarwar for their support in providing the research data and FLOW-3D training. I am thankful to my colleagues, friends and relatives for their prayers. I also am thankful to Mr. Younus, Engr. Muhammad Yasir and Engr. Muhamamd Husnain for helping me to obtain relevant data from the barrage site. Last but not the least, i am very grateful to my mother for her never-ending prayers for my health and success.

**(Muhammad Waqas Zaffar)**

---

## *Abstract*

Hydraulic structures are used for water supply and power generation. Downstream of these structures, different shapes of stilling basins are designed and constructed. Barrages are low head hydraulic structures which are built across rivers to divert required flow into the canals. In Pakistan, such structures are built about 50 to 100 years ago, and the stilling basins of these barrages are jump-type which include impact baffle and friction blocks. The stilling basin of Taunsa barrage was constructed in 1958 and soon after its operation several issues were occurred i.e., lowering of tail water, uprooting of baffle blocks, and downstream bed retrogression. These issues remained unresolved till 2004, and during the years 2005 to 2008, the barrage's basin was remodeled. For the remodeling, the results of model study were employed which focused the investigation of tail water effects on hydraulic jump. In the remodeling process, old basin's appurtenances were dismantled and new energy dissipation arrangements were made. Even after the remodeling, during 2010 flood, the previous studies indicated large scour pits downstream of the new basin, and block filter floor in front of some bays was also found sinking. On the other hand, previous studies have also showed that due to the flow reattachment on the sides, vertical face baffle block reduces wake area and drag force, whereas wedge-shaped baffle block (WSBB) creates large wake region, thereby produces more drag force. However, the literature is lacking the use of WSBB for the stilling basins of open channel hydraulic structures.

The aim of present study is to develop FLOW-3D hydraulic and scour for different basins of Taunsa barrage. By employing hydraulic and scour models, the study also investigates the suitability of WSBB downstream of river diversion barrage. For the hydraulic modelling, three gated flows i.e., 2.44 m<sup>3</sup>/s/m, 4.88 m<sup>3</sup>/s/m, 7.22 m<sup>3</sup>/s/m are employed downstream of different investigated basins. Under the hydraulic investigation, sequent depths, free surface profiles, velocity profiles, roller lengths, hydraulic jump efficiency, and turbulent kinetic energy (TKE) are the main investigated parameters. In the hydraulic models, to capture the turbulence, RNG K- $\epsilon$  model is employed while volume of Fluid (VOF) method is used for

free surface tracking. For the assessment of hydraulic models, volume flow rates obtained from the present models are compared with the prototype data. For the scour models, the mesh blocks, and boundary conditions are employed similar to the hydraulic models. However, the third mesh block is extended due to the inclusion of 30 m long sediment bed. It is worth mentioning that the sediment beds studied in the present models are completely made of fine sand which has contained the physical properties (i.e., diameter and density) similar to that is obtained from the prototype barrage. The present scour models are developed for designed and flood discharge of  $24.30 \text{ m}^3/\text{s}/\text{m}$  and  $18 \text{ m}^3/\text{s}/\text{m}$ , respectively. The flow fields downstream of the scoured and retrogressed beds are captured by three different turbulence models whereas for the sediment transport rate, Van Rijn equation is employed. The scour profiles downstream of remodeled basin (Type (B)) are used for models' validation and their results are compared with probing data of prototype barrage.

The results of volume flow rate in different stilling basins have indicated acceptable errors for the tested discharges which ranged between -3% to 14%, respectively. At all the investigated gated flows, as compared to modified USBR basin (Type (A)) and remodeled basin (Type (B)), the lengths of hydraulic jump (HJ) in wedge-shaped baffle blocks basins (Type (C) & (D)) are found to be less, however, distances of HJ starting locations from the toe of downstream glacis are found to be less in WSBB basins. In the studied basins, sequent depth ratios are decreased as the flow is increased and the maximum sequent depth ratio is noticed in the Type (D) basin. Similar to the sequent depths, the dimensionless roller lengths in the studied basins are decreased as flows is increased. At the studied discharges, the maximum relative energy loss is observed at  $4.88 \text{ m}^3/\text{s}/\text{m}$  discharge in Type (D) basin which reached 26%. However, as the discharge is increased, the relative energy loss is found to be decreased in the studied basins. In Type (A), (C) & (D) basins, the patterns of velocity profiles in the HJ regions are found to be a jet-like structures which showed agreement with the literature. Furthermore, at lower flows, the minimum velocity at the basin's end is found in Type (C) & (D) basins which indicates that these basins are decaying the velocity more

efficiently than Type (A) and (B) basins of the studied barrage. At lower flow, the maximum TKEs and turbulent intensity (TI) at the basin's end are found in Type (B) basin, whereas in Type (A), (C) & (D) basins their values were found to be close. However, the near basin's floor, due to the development of large wake regions, the TKEs in Type (C) & (D) basins are found less than Type (A) and (B) basins. As compared to the lower discharges, at higher discharges, the values of TKEs and TI are found higher. However, near the basins' floor, the minimum TKEs and TI are observed in WSBB basins (Type (C) & (D)).

The bed profiles downstream of Type (B) basin have shown good agreement with field data for which  $R^2$  reached 0.908, 0.909 and 0.953 in LES, RNG and Standard K- $\epsilon$  models, respectively. As compared to other turbulence models, the results of RNG K- $\epsilon$  model are found more promising when compared with field data. The results of flow field on scoured and retrogressed indicate a large flow re-circulation zone near the rigid floor of Type (B) basin which showed scour hole. On the contrary, a forward velocity profiles are observed on retrogressed beds downstream old and Type (C) & (D) basins. At the designed discharge ( $24.30 \text{ m}^3/\text{s}/\text{m}$ ), upon use of LES model, the sediment bed downstream of Type (B) is completely expose near the rigid floor and at the end of sediment bed, whereas downstream of Type (A), (C) & (D) basins only beds retrogression is noticed. At designed discharge, the net change of erodible bed downstream of Type (A) basin is reached to 65% in LES model, however, the maximum change of beds downstream of Type (C) & (D) are reached to 67% and 68% in RNG and LES models, respectively. On the other hand, at the flood discharge ( $18 \text{ m}^3/\text{s}/\text{m}$ ), the minimum change in the bed is noticed downstream of Type (C) basin which reaches to 37% (at Y/4 section) whereas the maximum change is witnessed downstream of Type (B) which reaches 89% (at Y/4 section).

Based on the results, it is concluded that the present Type (B) of studied barrage is dissipating less energy and producing highly turbulent flow on the riverbed. The results further confirm that WSBB with vertex angle of  $150^\circ$  and cutback angle of  $90^\circ$  can be implemented downstream of river diversion barrage up to the discharge  $18 \text{ m}^3/\text{s}/\text{m}$ . The study further confirms that both RNG K- $\epsilon$  and Vin Rijn

transport rate equations are efficient for hydraulic and scour modelling, respectively. However, as the present numerical models are limited to gated flow of  $7.22 \text{ m}^3/\text{s}/\text{m}$  and flood flow of  $18 \text{ m}^3/\text{s}/\text{m}$ , therefore, the study recommends employing other discharges to investigate the hydraulic and scour modeling downstream of studied and other barrages of Pakistan. The study also suggests employing other vertex and cutback angles for WSBB to check their suitability downstream of open channel flow structures.

Keywords:

FLOW-3D, Barrage, Hydraulic Modelling, Scour Models, Wedge-Shaped Baffle Block (WSBB)

# Contents

<b>Author’s Declaration</b>	<b>v</b>
<b>Plagiarism Undertaking</b>	<b>vi</b>
<b>List of Publications</b>	<b>vii</b>
<b>Acknowledgement</b>	<b>viii</b>
<b>Abstract</b>	<b>ix</b>
<b>List of Figures</b>	<b>xvii</b>
<b>List of Tables</b>	<b>xxii</b>
<b>Abbreviations</b>	<b>xxiv</b>
<b>Symbols</b>	<b>xxvi</b>
<b>1 Introduction</b>	<b>1</b>
1.1 Background . . . . .	1
1.2 River Indus and Barrages . . . . .	3
1.3 Hydraulics of Punjab Barrages . . . . .	4
1.4 Impacts of Floods on Barrages . . . . .	4
1.5 Research Motivation and Problem Statement . . . . .	5
1.6 Novelty of the Research . . . . .	6
1.7 Research Objectives . . . . .	9
1.8 Scope and Research Limitations . . . . .	9
1.8.1 Research Scope . . . . .	9
1.8.2 Research Limitations . . . . .	10
1.8.2.1 General Limitations . . . . .	10
1.8.2.2 Models’ Limitations . . . . .	11
1.9 Dissertation Organization . . . . .	12
<b>2 Literature Review</b>	<b>14</b>
2.1 Introduction . . . . .	14

---

2.2	Hydraulic Jump and its Usefulness . . . . .	15
2.3	Significance of Stilling Basins and Appurtenances . . . . .	17
2.3.1	Function of Chute Blocks in Stilling Basins . . . . .	18
2.3.2	Effects of Baffle Blocks on Flow Characteristics . . . . .	18
2.3.2.1	Summary . . . . .	20
2.3.3	Sill-controlled and Multiple-steps Stilling Basins . . . . .	21
2.3.3.1	Summary . . . . .	22
2.3.4	Effects of Tail Water Depth (TWD) on Hydraulic Jump and Energy Dissipation . . . . .	22
2.3.4.1	Summary . . . . .	24
2.4	Wedge-Shaped Baffle Block (WSBB) Stilling Basins . . . . .	25
2.4.1	Summary . . . . .	26
2.5	Computational Fluid Dynamics (CFD) and Hydraulic Modelling . .	27
2.5.1	Application of Turbulence Models . . . . .	33
2.5.2	Summary . . . . .	36
2.5.3	Mesh Blocks and Cell Size Effects on CFD Models . . . . .	36
2.5.4	Comparison of Numerical Models . . . . .	39
2.5.5	Summary . . . . .	40
2.6	Sediment Scour Models . . . . .	42
2.6.1	Summary . . . . .	46
2.7	Overall Summary . . . . .	46
<b>3</b>	<b>Study Area &amp; Methodology</b> . . . . .	<b>48</b>
3.1	Background . . . . .	48
3.2	Study Area . . . . .	48
3.2.1	Taunsa Barrage and the Hydraulic Concerns . . . . .	52
3.3	Identification of Critical Hydraulic Parameters (CHPs) . . . . .	54
3.4	Selection of CFD Software . . . . .	57
3.5	Numerical Modeling Technique . . . . .	58
3.5.1	Direct Numerical Simulation (DNS) . . . . .	60
3.5.2	Large Eddy Simulation (LES) . . . . .	60
3.5.3	Reynolds-Averaged Navier-Stokes Equations (RANS) . . . . .	61
3.6	Closure Problems and Turbulence Models . . . . .	62
3.6.1	Standard K- $\epsilon$ Model . . . . .	63
3.6.2	Renormalization Group (RNG K- $\epsilon$ ) Model . . . . .	63
3.7	Numerical Solution Methods . . . . .	64
3.7.1	Finite Volume Method (FVM) . . . . .	64
3.8	Free Surface Tracking . . . . .	65
3.9	Pressure-Velocity Coupling . . . . .	66
3.10	Fluid-Solid Interface Reconstruction . . . . .	66
3.11	Computation Grid . . . . .	67
3.11.1	Unstructured Grid-meshing . . . . .	68
3.11.2	Structured Grid-meshing . . . . .	68
3.12	Sediment Scour Model . . . . .	69

3.12.1	Critical Shields Number	69
3.12.2	Bed-Load Transport	70
3.12.2.1	Meyer, Peter and Müller Equation	70
3.12.2.2	Nielsen Equation	70
3.12.2.3	Van Rijn Equation	70
3.12.3	Maximum Packing Fraction	71
3.12.4	Bed Shear Stress	71
3.13	Data Requirement for Numerical Models	71
3.13.1	Models Drawings, Hydraulic Data and Models Operation	71
3.13.2	Hydraulic Data and Models' Operation	74
3.13.2.1	Free and Gated Flow Analysis	75
3.14	Hydraulic Investigation	77
3.14.1	Meshing and Boundary Setup	78
3.15	Scour Modelling and Investigation	80
3.15.1	Geometry and Meshing for Scour Models	81
3.15.2	Boundary Conditions for Scour Models	83
3.15.3	Simulation Time for Scour Stability Conditions	83
3.15.4	Performance Assessment of Scour Models	87

<b>4</b>	<b>Identification of Hydraulic Parameters &amp; Performance of Stilling Basins</b>	<b>88</b>
4.1	Background	88
4.2	Identification of Critical Parameters	89
4.3	Hydraulic Modelling	93
4.3.1	Results of Gated and Free Flow	93
4.4	Results of Hydraulic Parameters for Gated Discharge	94
4.4.1	Free Surface Profiles (FSPs)	94
4.4.2	Sequent Depths	101
4.4.3	Roller Lengths	102
4.4.4	Relative Energy Loss	104
4.4.5	Velocity Profiles (VPs)	106
4.4.6	Turbulent Kinetic Energy (TKE) and Turbulent Intensity (TI)	118
4.5	Results of Hydraulic Parameters for Free Flow Discharges	129
4.5.1	Free Surface Profiles (FSPs) at Flood and Design Discharges	129
4.5.2	Velocity Field and Patterns at Flood and Design Discharges	132
4.5.2.1	Velocity Field and Patterns at Flood Discharge	132
4.5.2.2	Velocity Field and Patterns at Design Discharge	135
4.5.3	Turbulent Kinetic Energies	138
4.5.3.1	Turbulent Kinetic Energies (TKEs) at Flood Discharge	138
4.5.3.2	Turbulent Kinetic Energies (TKEs) at Design Discharge	141
4.6	Tail Water Rating Curves and Locations of Hydraulic Jumps ( $HJ_s$ )	143



---

<b>5</b>	<b>Flow Field, Local Scour and Bed Retrogression</b>	<b>148</b>
5.1	Background . . . . .	148
5.2	Validation on Scour Models . . . . .	148
5.3	Flow Field . . . . .	155
5.3.1	Velocity Distribution at Designed Discharge . . . . .	155
5.3.2	Velocity Field at High Flood Discharge . . . . .	165
5.3.3	Bed Shear Stress on Sediment Beds at Designed Discharge . . . . .	172
5.3.4	Bed Shear Stress on Sediment Beds at High Flood Discharge . . . . .	176
5.4	Local Scour and Bed Retrogression . . . . .	181
5.4.1	Scour and Retrogression Pattern at Designed Discharge . . . . .	181
5.4.2	Scour and Retrogression Pattern at High Flood Discharge . . . . .	186
5.4.3	Longitudinal Bed Profiles at Designed Discharge . . . . .	190
5.4.4	Longitudinal Bed Profiles at High Flood Discharge . . . . .	193
5.5	Economic Analysis . . . . .	196
<b>6</b>	<b>Conclusions &amp; Recommendations</b>	<b>198</b>
6.1	General . . . . .	198
6.2	Conclusions . . . . .	199
6.3	Research Significance and Implications . . . . .	202
6.4	Recommendations . . . . .	203
	<b>Bibliography</b>	<b>205</b>
	<b>Annex-3A</b>	<b>236</b>
	<b>Annex-3B</b>	<b>238</b>

# List of Figures

3.1	Flow Chart of Research Methodology . . . . .	49
3.2	Location map of study area . . . . .	50
3.3	Taunsa barrage irrigation system . . . . .	51
3.4	Longitudinal cross section of Taunsa barrage (Study area) . . . . .	52
3.5	Dismantling of Baffle blocks [43] . . . . .	53
3.6	Existing appurtenances of barrage [43] . . . . .	53
3.7	Process for identification of CHPs . . . . .	57
3.8	Detailed methodology for hydraulic and scour modelling . . . . .	59
3.9	Geometries and dissipation arrangements in different stilling basins, (a) Type (A), (b) Type (B), (c) Type (C), and (d) Type (D) . . . . .	72
3.10	(a) USBR block, (b) USBR block, Isometric view, (c) WSBB (d) WSBB, Isometric view . . . . .	73
3.11	Unit discharge during the years at Taunsa barrage . . . . .	76
3.12	Minimum, mean and maximum flows during years 2013-2020 at Taunsa barrage . . . . .	76
3.13	Model operation for gated flow . . . . .	77
3.14	Meshing setup for solid and flow domains . . . . .	79
3.15	Boundary conditions for different mesh blocks to govern the solution domain . . . . .	80
3.16	Geometry and three dimensional schematic setup of rigid and scour bed . . . . .	82
3.17	Hydraulic stability through MAFKEs in Type (A) basin . . . . .	84
3.18	Hydraulic stability through MAFKEs in Type (B) basin . . . . .	85
3.19	Hydraulic stability through MAFKEs in Type (C) basin . . . . .	86
3.20	Hydraulic stability through MAFKEs in Type (D) basin . . . . .	86
4.1	FSPs in different basins at 2.44 m <sup>3</sup> /s/m . . . . .	96
4.2	FSPs in different basins at 4.88 m <sup>3</sup> /s/m . . . . .	97
4.3	FSPs in different basins at 7.22 m <sup>3</sup> /s/m . . . . .	97
4.4	Schematic diagram showing the components of dimensionless FSP of HJ . . . . .	99
4.5	Dimensionless FSPs of HJ at 2.44 m <sup>3</sup> /s/m discharge . . . . .	99
4.6	width=0.8 . . . . .	100
4.7	Dimensionless FSPs of HJ at 7.22 m <sup>3</sup> /s/m discharge . . . . .	100
4.8	Roller length of HJ in different stilling basins at unit discharge of 2.44 m <sup>3</sup> /s/m . . . . .	103

4.9	Roller length of HJ in different stilling basins at unit discharge of 4.88 m <sup>3</sup> /s/m	104
4.10	Roller length of HJ in different stilling basins at unit discharge of 7.22 m <sup>3</sup> /s/m	104
4.11	Vertical distribution of velocity in HJ for different stilling basins at 2.44 m <sup>3</sup> /s/m, (a) <b>Type (A)</b> , (b) <b>Type (B)</b> , (c) <b>Type (C)</b> , and (d) <b>Type (D)</b>	107
4.12	2-D illustration of VPs in Y-Z plane at at 2.44 m <sup>3</sup> /s/m in <b>Type (A)</b> (a&b), <b>Type (B)</b> (c&d), <b>Type (C)</b> (e&f), and <b>Type (D)</b> (g&h) basins	108
4.13	Vertical VPs in different stilling basins at 4.88 m <sup>3</sup> /s/m, (a) <b>Type (A)</b> , (b) <b>Type (B)</b> , (c) <b>Type (C)</b> , and (d) <b>Type (D)</b>	110
4.14	2-D illustration of VPs in Y-Z plane at at 4.88 m <sup>3</sup> /s/m in <b>Type (A)</b> (a&b), <b>Type (B)</b> (c&d), <b>Type (C)</b> (e&f), and <b>Type (D)</b> (g&h) basins	112
4.15	Vertical distribution of velocity in HJ for different stilling basins at 7.22 m <sup>3</sup> /s/m, (a) <b>Type (A)</b> , (b) <b>Type (B)</b> , (c) <b>Type (C)</b> , and (d) <b>Type (D)</b>	114
4.16	2-D illustration of VPs in Y-Z plane at 7.22 m <sup>3</sup> /s/m in <b>Type (A)</b> (a&b), <b>Type (B)</b> (c&d), <b>Type (C)</b> (e&f), and <b>Type (D)</b> (g&h) basins	116
4.17	2-D representation of TKEs and TI at 2.44 m <sup>3</sup> /s/m discharge, <b>Type (A)</b> (a & b), <b>Type (B)</b> (c & d), <b>Type (C)</b> (e & f), and <b>Type (D)</b> (g & h) basins	120
4.18	Distribution of TI at 2.44 m <sup>3</sup> /s/m flow in <b>Type (A)</b> (a&b), <b>Type (B)</b> (c&d), <b>Type (C)</b> (e&f), and <b>Type (D)</b> (g&h) basins after the HJ and at the basins' end	122
4.19	2-D representation of TKEs and TI at 4.88 m <sup>3</sup> /s/m discharge, <b>Type (A)</b> (a & b), <b>Type (B)</b> (c & d), <b>Type (C)</b> (e & f), and <b>Type (D)</b> (g & h)	123
4.20	Distribution of TI at 4.88 m <sup>3</sup> /s/m flow in <b>Type (A)</b> (a&b), <b>Type (B)</b> (c&d), <b>Type (C)</b> (e&f), and <b>Type (D)</b> (g&h) basins after the HJ and at the basins' end	125
4.21	2-D representation of TKEs and TI at 7.22 m <sup>3</sup> /s/m discharge, <b>Type (A)</b> (a&b), <b>Type (B)</b> (c&d), <b>Type (C)</b> (e&f), and <b>Type (D)</b> (g&h)	127
4.22	Distribution of TI at 7.22 m <sup>3</sup> /s/m flow in <b>Type (A)</b> (a&b), <b>Type (B)</b> (c&d), <b>Type (C)</b> (e&f), and <b>Type (D)</b> (g&h) basins after the HJ and at the basins' end	128
4.23	Comparison of FSPs in different basins at flood discharge of 18 m <sup>3</sup> /s/m	131
4.24	Comparison of FSPs in different basins at flood discharge of 24 m <sup>3</sup> /s/m	131
4.25	2-D Illustration of velocity distribution downstream of different basins at flood discharge of 18 m <sup>3</sup> /s/m, (a) Type (A), (b) Type (B), (c) Type (C) and (d) Type (D)	134

4.26	2-D Illustration of velocity distribution downstream of different basins at design discharge of $24.30 \text{ m}^3/\text{s}/\text{m}$ , (a) Type (A), (b) Type (B), (c) Type (C) and (d) Type (D) . . . . .	137
4.27	2-D Illustration of turbulent kinetic energies in different basins at flood discharge of $18 \text{ m}^3/\text{s}/\text{m}$ , (a) Type (A), (b) Type (B), (c) Type (C) and (d) Type (D) . . . . .	139
4.28	2-D Illustration of turbulent kinetic energies in different basins at design discharge of $24.30 \text{ m}^3/\text{s}/\text{m}$ , (a) Type (A), (b) Type (B), (c) Type (C) and (d) Type (D) . . . . .	142
4.29	Tail water rating curves of the studied basins at gated and free flow discharges . . . . .	144
4.30	Comparison of hydraulic jump locations at gated and free flow discharges for the studied basins . . . . .	145
5.1	Comparison of modelled scour profiles using different turbulence schemes with bay 33 of Prototype . . . . .	150
5.2	Comparison of modelled scour profiles using different turbulence schemes with bay 34 of Prototype . . . . .	150
5.3	Comparison of modelled scour profiles using different turbulence schemes with bay 55 of Prototype . . . . .	151
5.4	Comparison of scour profile of Bay 33 with the numerical models, (a) LES, (b) RNG $k-\epsilon$ , and (c) Std $K-\epsilon$ model . . . . .	152
5.5	Comparison of scour profile of Bay 34 with the numerical models, (a) LES, (b) RNG $k-\epsilon$ and (c) Std $K-\epsilon$ model . . . . .	153
5.6	Comparison of scour profile of Bay 55 with the numerical models, (a) LES, (b) RNG $k-\epsilon$ and (c) Std $K-\epsilon$ model . . . . .	154
5.7	2-D Illustration of velocity distribution downstream of Type (A) basin at $24.30 \text{ m}^3/\text{s}/\text{m}$ , (a) RNG $K-\epsilon$ , (b) Std $K-\epsilon$ model, and (c) LES model . . . . .	158
5.8	2-D Illustration of velocity distribution downstream of Type (B) basin at $24.30 \text{ m}^3/\text{s}/\text{m}$ , (a) RNG $K-\epsilon$ , (b) Std $K-\epsilon$ model, and (c) LES model . . . . .	160
5.9	2-D Illustration of velocity distribution downstream of Type (C) basin at $24.30 \text{ m}^3/\text{s}/\text{m}$ , (a) RNG $K-\epsilon$ , (b) Std $K-\epsilon$ model, and (c) LES model . . . . .	162
5.10	2-D Illustration of velocity distribution downstream of Type (D) basin at $24.30 \text{ m}^3/\text{s}/\text{m}$ , (a) RNG $K-\epsilon$ , (b) Std $K-\epsilon$ model, and (c) LES model . . . . .	164
5.11	2-D Illustration of velocity distribution downstream of Type (A) basin at $18 \text{ m}^3/\text{s}/\text{m}$ , (a) RNG $K-\epsilon$ , (b) Std $K-\epsilon$ model, and (c) LES model . . . . .	166
5.12	2-D Illustration of velocity distribution downstream of Type (B) basin at $18 \text{ m}^3/\text{s}/\text{m}$ , (a) RNG $K-\epsilon$ , (b) Std $K-\epsilon$ model, and (c) LES model . . . . .	168

5.13	2-D Illustration of velocity distribution downstream of Type (C) basin at 18 m <sup>3</sup> /s/m, (a) RNG K- $\epsilon$ , (b) Std K- $\epsilon$ model, and (c) LES model . . . . .	171
5.14	2-D Illustration of velocity distribution downstream of Type (D) basin at 18 m <sup>3</sup> /s/m, (a) RNG K- $\epsilon$ , (b) Std K- $\epsilon$ model, and (c) LES model . . . . .	172
5.15	Shear stress distribution downstream of Type (A) basin at designed discharge, (a) RNG K- $\epsilon$ , (b) Std K- $\epsilon$ model, and (c) LES model . . . . .	173
5.16	Shear stress distribution downstream of Type (B) basin at designed discharge, (a) RNG K- $\epsilon$ , (b) Std K- $\epsilon$ model, and (c) LES model . . . . .	174
5.17	Shear stress distribution downstream of Type-C basin at designed discharge, (a) RNG K- $\epsilon$ , (b) Std K- $\epsilon$ model, and (c) LES model . . . . .	175
5.18	Shear stress distribution downstream of Type-D basin at designed discharge, (a) RNG K- $\epsilon$ , (b) Std K- $\epsilon$ model, and (c) LES model . . . . .	176
5.19	Shear stress distribution downstream of Type (A) basin at Flood discharge, (a) RNG k- $\epsilon$ , (b) Std K- $\epsilon$ model, and (c) LES model . . . . .	177
5.20	Shear stress distribution downstream of Type (B) basin at Flood discharge, (a) RNG k- $\epsilon$ , (b) Std K- $\epsilon$ model, and (c) LES model . . . . .	178
5.21	Shear stress distribution downstream of Type (C) basin at Flood discharge, (a) RNG k- $\epsilon$ , (b) Std K- $\epsilon$ model, and (c) LES model . . . . .	180
5.22	Shear stress distribution downstream of Type (D) basin at Flood discharge, (a) RNG k- $\epsilon$ , (b) Std K- $\epsilon$ model, and (c) LES model . . . . .	181
5.23	3-D representation of scoured bed below Type (A) basin at designed discharge, (a) RNG k- $\epsilon$ , (b) Std K- $\epsilon$ model, and (c) LES model . . . . .	182
5.24	3-D representation of scoured bed below Type (B) basin at designed discharge, (a) RNG k- $\epsilon$ , (b) Std K- $\epsilon$ model, and (c) LES model . . . . .	183
5.25	3-D representation of scoured bed below Type (C) basin at designed discharge, (a) RNG k- $\epsilon$ , (b) Std K- $\epsilon$ model, and (c) LES model . . . . .	185
5.26	3-D representation of scoured bed below Type (D) basin at designed discharge (a) RNG k- $\epsilon$ , (b) Std K- $\epsilon$ model, and (c) LES model . . . . .	185
5.27	3-D representation of scoured bed below Type (A) basin at 18 m <sup>3</sup> /s/m, (a) RNG k- $\epsilon$ , (b) Std K- $\epsilon$ model, and (c) LES model . . . . .	187
5.28	3-D representation of scoured bed below Type (B) basin at 18 m <sup>3</sup> /s/m, (a) RNG k- $\epsilon$ , (b) Std K- $\epsilon$ model, and (c) LES model . . . . .	188
5.29	3-D representation of scoured bed below Type (C) basin at 18 m <sup>3</sup> /s/m, (a) RNG k- $\epsilon$ , (b) Std K- $\epsilon$ model, and (c) LES model . . . . .	189
5.30	3-D representation of scoured bed below Type (D) basin at 18 m <sup>3</sup> /s/m, (a) RNG k- $\epsilon$ , (b) Std K- $\epsilon$ model, and (c) LES model . . . . .	190
5.31	Longitudinal scour profiles at 24.30 m <sup>3</sup> /s/m discharge using RNG K- $\epsilon$ model . . . . .	192
5.32	Longitudinal scour profiles at 24.30 m <sup>3</sup> /s/m discharge using Std K- $\epsilon$ model . . . . .	192
5.33	Longitudinal scour profiles at 24.30 m <sup>3</sup> /s/m discharge using LES model . . . . .	193

---

5.34	Longitudinal scour profiles at 18 m <sup>3</sup> /s/m discharge using RNG k- $\epsilon$ model . . . . .	194
5.35	Longitudinal scour profiles at 18 m <sup>3</sup> /s/m discharge using Std k- $\epsilon$ model . . . . .	194
5.36	Longitudinal scour profiles at 18 m <sup>3</sup> /s/m discharge using LES model	195
1	Time rate change of discharge at 2.44 m <sup>3</sup> /s/m, <b>(a)</b> Type (A), <b>(b)</b> Type (B), <b>(c)</b> Type (C), and <b>(d)</b> Type (D) basins . . . . .	239
2	Time rate change of discharge at 4.88 m <sup>3</sup> /s/m, <b>(a)</b> Type (A), <b>(b)</b> Type (B), <b>(c)</b> Type (C), and <b>(d)</b> Type (D) basins . . . . .	240
3	Time rate change of discharge at 7.22 m <sup>3</sup> /s/m, <b>(a)</b> Type (A), <b>(b)</b> Type (B), <b>(c)</b> Type (C), and <b>(d)</b> Type (D) basins . . . . .	241

# List of Tables

1.1	History of floods at Taunsa Barrage, Punjab, Pakistan . . . . .	5
2.1	Utilization of two equations turbulence models for HJ and flow fields	35
2.2	Different mesh blocks and cell sizes employed in numerical models for HJ and energy dissipators . . . . .	38
2.3	Comparison of numerical model for hydraulic investigation . . . . .	41
3.1	Salient Features of Taunsa Barrage . . . . .	52
3.2	Hydraulic parameters from the experimental studies and their sources . . . . .	55
3.3	Hydraulic parameters from the numerical studies and their sources .	56
3.4	List of strongly desired feature for selection of CFD software . . . . .	58
3.5	Models operation and HJ conditions . . . . .	75
3.6	Details of mesh blocks and cell sizes . . . . .	78
3.7	Quality indicators for different mesh blocks . . . . .	79
3.8	Physical properties of sediment packed/scour bed. . . . .	82
3.9	Mesh boundary setup for scour modelling . . . . .	83
4.1	Parameters' Frequency, RII and ranking in numerical studies. . . . .	89
4.2	Parameters' Frequency, RII and ranking in experimental studies . . .	90
4.3	RII and ranking of parameters after combining numerical and ex- perimental studies. . . . .	91
4.4	Relative % score and ranking based on frequency of occurrence of parameters in literature [223], [225], [226] . . . . .	92
4.5	Relative position of parameters from literature using different sta- tistical methods . . . . .	93
4.6	Comparison of gated discharges with Prototype discharge of year 2010 ([43]) . . . . .	95
4.7	Length of HJs in the studied basins . . . . .	101
4.8	Sequent depths ratio in the studied basins . . . . .	102
4.9	Energy loss in different basins at various gated flows . . . . .	105
4.10	Summarized results of Critical Hydraulic parameters (CHPs) in Type (A), (B), (C) and (D) basins at gated flows . . . . .	146
4.11	Summary of Hydraulic parameters in Type (A), (B), (C) and (D) basins at flood and design discharges . . . . .	147

---

5.1	Maximum scour depths at different Y-sections downstream of studied basins at designed discharge . . . . .	195
5.2	Maximum scour depths at different Y-sections downstream of studied basins at flood discharge . . . . .	196
1	Strongly desired features of three dimensional (3-D) numerical codes and their comparison . . . . .	237



# Abbreviations

<b>AIC</b>	Akaike information criterion
<b>CFD</b>	Computational Fluid Dynamic
<b>CHJ</b>	Classical hydraulic jump
<b>DNS</b>	Direct numerical simulation
<b>DSJ</b>	Deflected surface jet
<b>DNN</b>	Descriptive neural network
<b>Fr</b>	Froude number
<b>FVM</b>	Finite Volume Method
<b>FAVOR</b>	Fractional area/volume obstacle representation
<b>GMRES</b>	Generalized Minimum Residual Solver
<b>HJ</b>	Hydraulic jump
<b>LES</b>	Large Eddy simulation
<b>MSE</b>	Mean square error
<b>MAE</b>	Mean absolute error
<b>NSE</b>	Naiver Stokes equation
<b>PID</b>	Punjab Irrigation Department
<b>PI</b>	Performance index
<b>RNG</b>	Re-normalization group theory
<b>RII</b>	Relative importance index
<b>RWJ</b>	Reattaching wall jet
<b>R<sup>2</sup></b>	Coefficient of determination
<b>RANS</b>	Reynolds-Averaged Naiver-Stokes Equations
<b>Stl</b>	Stereo Lithography

<b>USBR</b>	United States Bureau of Reclamation
<b>USU</b>	Utah State University
<b>VOF</b>	Volume of fluid
<b>WSBB</b>	Wedge-Shaped baffle block

# Symbols

$y_1$	Supercritical flow depth
$y_2$	Sub-critical flow depth
$Fr_1$	Froude number before hydraulic jump
$g$	Acceleration due to gravity
$C_d$	Discharge coefficient
$R_f$	Relative frequency
$V_F$	Partial volume of flow
$RPA$	Relative portion of party affected
$R_{SOR}$	Mass source
$R_{DIF}$	Diffusion term of turbulence
$\rho$	Fluid density
$u, v,$ and $w$	Velocity components in x, y and z directions
$A_x, A_y,$ and $A_z$	Flow areas in x, y and z directions
$G_x, G_y,$ and $G_z$	Body accelerations in x, y and z directions
$f_x, f_y,$ and $f_z$	Viscous acceleration in x, y and z directions
$P$	Pressure
$P_T$	Shear production
$G$	Buoyancy production
$F$	Fluid fraction
$C_{1\epsilon}, C_{2\epsilon},$ and $C_{3\epsilon}$	Model constants
$A$	Average flow area
$S_m$	Fluid physical mass term
$K$	Turbulent kinetic energy

---

$\epsilon$	Dissipation rate
$\mu$	Dynamic viscosity
$\mu_t$	Turbulent dynamic viscosity
$\theta_{cr,i}$	Critical shield number
$\tau_{cr}$	Minimum bed shear stress
$d_i$	Diameter of sediment particle
$d_{*i}$	Dimensionless grain size
$\rho_i, \rho_f$	Sediment and fluid densities
$V_f$	Kinematic fluid viscosity
$\beta_{MPM,i}$	Dynamic bed load coefficient
$\Theta_i$	Bed load transport
$C_{rough}$	User-defined coefficient
$k_s$	Nikuradse roughness
$d_{50}$	Median grain diameter
$C_{bi}$	Fractional volume of species $i$
$h_e$	Effective head
$H_d$	Design head
$h_c$	Center-line head
$Q$	Flow rate
$q$	Unit discharge
$D$	Gate opening
$X_{min}, X_{max}$	Boundaries limit in $X$ -direction
$Y_{min}, Y_{max}$	Boundaries limit in $Y$ -direction
$Z_{min}, Z_{max}$	Boundaries limit in $Z$ -direction
$T_a$	Actual time
$T_s$	Simulation time
$H_1$	Specific head upstream of hydraulic jump
$H_2$	Specific head downstream of hydraulic jump
$L_r$	Roller length of hydraulic jump
$L_r/d_1$	Dimensionless roller length
$SS_{res}$	Sum of square of residuals between observed and predicted data

$SS_{tot}$	Total sum of squares between observed and mean of observed data
$X_1, X_2$	Function of variable X
$\eta$	Relative energy loss
$u_{rms}, v_{rms}, w_{rms}$	Root mean square velocities in x, y and z directions

# Chapter 1

## Introduction

### 1.1 Background

Hydraulic structures are classified into two categories i.e., high head, and low head [1]. Dams are the high head hydraulic structures [2][3] built to create reservoirs for water storage and power generation, while barrages are the low head hydraulic structures [4] [5] [6] constructed across the rivers to regulate water for irrigation system.

Flow over these hydraulic structures is very complicated [7] [8] [9] which is associated with turbulence and three-dimensional secondary currents [10] [11]. Downstream of these hydraulic structures, energy dissipation arrangements/stilling basins [12] [13] are provided to reduce kinetic energy of the upstream flow. Based on numerous model studies on different type of stilling basins, the United State Bureau of Reclamation (USBR) recommended to employ Type-II [14] [15] [16] and Type-III [17] [18] [19] basins downstream of high and low head hydraulic structures, respectively. The primary objectives of these stilling basins were to enhance the performance of hydraulic jump (HJ), and to minimize the stilling basin's length [20][21][22][23].

Primarily, these stilling basins were studies on reduced scaled models and their performance was also evaluated on prototypes. All around the world, the USBR

Engineering Monograph No. 25 “Hydraulic Design of Stilling Basins and Energy Dissipators” [24][25][26] is applied as a manual for modelling of energy dissipators design. The performance of any hydraulic structure is said to be compromised when: discharging capacity is reduced, hydraulic jump is not contained properly, and the energy dissipation within the stilling basin is lessened.

Conventionally, physical models of hydraulic structures are built in the laboratory to investigate their flow behavior. However, such kind of modelling technique is very expensive and time consuming [27], and associated with scaling effects i.e., models’ and measurement effects [28][29][30] [31][32]. These models also face difficulties in terrain and concrete roughness, and measurement tools also create hindrance to flow which alters the hydraulic behavior [33]. Additionally, in case of turbulent flow, it is very difficult to notice the streamline, and measurement can only be carried at certain locations. Furthermore, to carry out testing on different size and dimension of models, old ones must be demolished, and new models are developed which put additional cost.

On the contrary, with the advancement in computer technology, and more efficient computational fluid dynamic (CFD) tools, it is possible to investigate the hydraulic modelling of full-scale spillways and barrage bays [34] [35]. The first CFD model was developed in 1970, and during the years 1990 to 2000, an increase in the use of CFD models was noticed in the research institutes. Additionally, with the upgraded turbulence models i.e., Re-normalization group theory (RNG) [36] [37], Standard K- $\epsilon$  [38], and large eddy simulation model [39], an insight view of hydraulic jump, free surface, pressure variation, velocity fluctuations, turbulent kinetic energy, and sediment transport can be established.

On the other hand, whenever a hydraulic structure is built on the pathway of environmental flows, it not only changes the riverbed but also affects the flow patterns. Subsequently, these interventions lead to local scouring downstream of the structures [40][41]. Therefore, predicting of local scour at the design stage is an essential research field because if not properly addressed, it can damage the entire foundation of the structure [42].

In Pakistan, all most, all existing hydraulic structures i.e., barrage, are designed on basis of physical modelling. These structures were designed about 50 to 100 years ago and require rehabilitation. In 2004, a model study on rigid bed suggested to remodel the stilling basin of Taunsa barrage and from 2005 to 2008, the basin was remodelled [43][44][45]. For the remodelling process, the model study was limited to investigation of tail water and the location of hydraulic jumps. Even after the remodelling, during the year 2010, the literature revealed large scour pits, damages to basin's floor & stone apron and block floor in-front of some of bays was also found to be launched downstream of the barrage. In view of the above mentioned, presently, numerical models using FLOW-3D [46] [47] are developed to investigate hydraulic behavior downstream of Taunsa barrage by implementing different energy dissipation arrangements. The study further implemented scour models to assess the performance of different dissipation systems.

## 1.2 River Indus and Barrages

The Indus is one of the world's mightiest rivers, which traverses through Tibet, Kashmir, and Pakistan before falling into the Arabian Sea.

After traversing downstream, it meets the first Barrage, known as Jinnah Barrage, and further going downstream about 48.28 km, the Kurram tributary joins at Chashma Barrage. The barrage transfers water from river Indus to river Jhelum through a link canal known as Chashma-Jhelum Link Canal.

After traveling 249.5 km downstream, the river flows from the Suleman Ranges at the foot of Taunsa Barrage, the 3<sup>rd</sup> barrage in the chain of head works. Spurs are constructed on both sides of the barrage upstream to maintain the river approach.

On its course, the river Indus crosses, Guddu barrage near Khashmor, Sukkar barrage, and Kotri barrage near Hyderabad, where vast agricultural land is irrigated before discharging into the Arabian Sea. In short, barrages play a crucial in Pakistan's irrigation network. After diverting the water into the canals, a large



area of agriculture land is irrigated by these barrages. They also serve for road transport, rail lines and provide crossings for oil, gas, and power transmission.

### 1.3 Hydraulics of Punjab Barrages

Barrage/Weirs in the Punjab, Pakistan are constructed about 50 to 100 years ago. Such hydraulic structure falls into the category of low head hydraulic structures. They are constructed across the rivers to raise the upstream water levels to supply the required amount of water for agricultural purposes. The hydraulic designs of these structures are such that the maximum kinetic energies of the upcoming flows must be dissipated within the designed length of the stilling basins [48].

In the plane areas of the Pakistan, these hydraulic structures are designed as the jump-type stilling basin which are assisted with energy dissipators [49]. These arrangements not only stabilize the hydraulic jump (HJ) but also stop the excessive energies to travel on downstream of the stilling basin (Chanson, [50]; Hamedi et al. [32], Hamedi et al. [51]). Approximately all the stilling basins of Punjab barrages have auxiliary devices/appurtenance to keep the HJ at glaciis even though the tail water levels are less than the required conjugate depths [52]. These hydraulic structures are built on alluvial soil which usually experience retrogression and scouring on their downstream. If such downstream problems are not controlled properly, the safety of these structures can be jeopardized. Therefore, to secure these hydraulic structures from local scour, flexible aprons, i.e. stone in gabions and loose stone aprons are provided [53].

### 1.4 Impacts of Floods on Barrages

Floods cause about 40% of deaths worldwide and also damage the environment [54]. In Pakistan. Floods occur due to heavy rainfall in river catchments areas. Snow melt flows further supplement them during the monsoon season, especially

from the Bay of Bengal and the Himalayan foothills. The historical record of the floods damages occurred in Pakistan are shown in Table 1.1. As mentioned earlier, River Indus has a significant catchment area which also feed all other rivers. The monsoon period during 2010 came out to be the most devastating flooding year in the past 80 years, which caused heavy flood in River Indus.

Table 1.1 shows maximum peak discharges on the Indus River in Punjab Province, especially at Taunsa barrage during the unprecedented monsoon rainfall within the last week of July 2010. Except Taunsa barrage, all other head works and barrages had safely passed the super flood of year 2010 which led to an uncontrolled breach on its left marginal bund. The flood had not only damaged the downstream stilling basin of the barrage but also developed deep scour hole washed away the whole stone apron and concrete floor and inverted filter blocks [49].

TABLE 1.1: History of floods at Taunsa Barrage, Punjab, Pakistan

River	Head work /Barrage	Designed Capacity ( $\text{m}^3/\text{s}$ )	Historical Peak flood		2010 Peak Flood	
			Flood	Year	Flood	Year
Indus	Tarbela Dam	42469	14440	1989	23584	2010
	Jinnah	26897	26897	1942	26541	2010
	(Kala Bagh)	26897	22270	1976	29351	2010
	Chashma	26897	22239	1958	27180	2010
	Taunsa	28313				

## 1.5 Research Motivation and Problem Statement

All over the world, dams spillways, barrages, weirs, sluice gates and other hydraulic structures with enormous dimensions are widely used to control and manage the flows of streams and rivers [55][56][57] [58]. Barrages are the low head hydraulic structures to divert the required amount of water into the canals. Downstream of these hydraulic structures, i.e., stilling basins are constructed to dissipate the

potential and kinetic energies of the upstream flows thereby minimizing the adverse effects on the downside riverbed [59][49][60]. Usually, the performance of these stilling basins is assessed by USBR monograph No.25 which provides a wide range of design criteria for different stilling basins of various hydraulic structures [61][62] [63] [64] [65] [52] [66] [61] [64] [67] [68] [69][26] [62] [66][70] [63][71] [72]. However, if such structures are not designed and operated carefully, it can affect the downstream generating problem such as uprooting of appurtenances (baffle and friction blocks) and scouring [73] [74] [75] [49] [54].

Hence, during the design stage, it is very important to focus all the critical hydraulic parameters which have dominant role. These parameters are required to be determined on the basis of various physical and numerical studies in the literature. There is also need to investigate geometrical changes in the appurtenances of stilling basins for the hydraulic and scour behaviour by employing critical hydraulic parameters.

1. For low head hydraulic structures, apart from the hydraulic models, the performance of these structures needs to be investigated for local scouring.
2. In addition, due to the advancement in computer technology, transport and turbulence models, full-scaled numerical models of barrage should be employed along with the reduced scale modeling.

## 1.6 Novelty of the Research

Barrages in the plain areas of Pakistan are built about a century ago for the uninterrupted water supply and power generation. With the passage of time, these barrages started facing structural and hydraulic issues. Similarly, Taunsa barrage on the mighty river Indus was constructed about 65 years ago for a designed discharge capacity of 28,313 m<sup>3</sup>/s. The stilling basin of barrage was designed according to the USBR Type-III basin which consisted of baffle and friction blocks. Soon after the barrage construction in 1958, multiple problems were seen i.e.,

lowering of tail water and consequently uprooting of baffle blocks, riverbed retrogression, and damages to basin's floor. From years 1958 to 2004, these regular issues were addressed by the partial repairs. After so much repair work, during the years 2004 to 2008, based on the model study of 1:50 scale, the barrage's basin was changed in which the old baffle and friction blocks were replaced with chute blocks and end sill, and it was concluded that the old basin was not retaining the tail water levels as per the hydraulic jump (HJ) requirements. In the remodelling, the basin's floor level was also changed from 126.79 m to 127.10 m [44] [45] [76]. In addition, in the model study, only the effects of tail water levels on various discharge were investigated, however, the study didn't investigated the the performance of new basin for local scouring, therefore, even after the remodelling, the probing data of years 2010 to 2014 showed large scour pits on the barrage downstream. The data also revealed that the flexible apron in front of the bays was also sinking [49]. In addition, the literature also revealed that after the remodelling, on the downstream, the river also changed its route towards the left side. After the remodelling of Taunsa barrage, the literature showed only one study [77] that investigated the hydraulics of two different stilling basins before and after remodeling using Hydrologic Engineering Center River Analysis System (HEC-RAS).

On the contrary, numerous investigations have been conducted on the shapes of energy dissipators (Hager and Li [26], Hamedi and Kitabdar [32], Mohammed et al. [53], Tiwari et al. [62], Habibzadeh et al.[67], Maci'an-P'erez et al.[78], Tiwari et al. [79], Guardio and Marion [80], Mansour et al. [81], Alikhani et al. [82], Grimaldi et al. [83], Eloubaidy et al. [84], Omid et al.[85], Babaali et al. [86], Elsaeed et al.[87] and Armenio et al.[88]) downstream of graded control structures, i.e., spillways, diversion structures, canal falls, and pipe outlets. However, the use of wedge-shaped baffle blocks (WSBB) (Goel [66], Pillai et al. [70], Goel [72], Verma et al. [89], Verma and Goel [90], Verma and Goel [91]), has been found limited downstream of open channel flow. Previously, these dissipators have only been investigated downstream of pipe-outlets basins, i.e., square, and circular outlets. In those investigations, WSBB with different vertex and cutback

angles were examined, however, the results of WSBB with vertex angle of  $150^0$  and cutback angle of  $90^0$  was found to be promising which decreased the local scour and overall length of the studied basins. Additionally, in those studies, the WSBB were investigated for the initial Froude number of 4.5.

Conventionally, the above mentioned hydraulic investigations have been carried on reduced scaled models. Such modelling techniques are not only time consuming but also associated with scaling effects, e.g., models' effect. In addition, the flow and other measuring devices also hinder the flow which consequently comprise the results of output parameters. In contrast, since last few decades, due to advancement in computer technology and turbulence models, the use of numerical codes, i.e., FLOW-3D, has become prevalent in the hydraulic and scour modeling. These models have provided significant opportunities for the hydraulic experts to understand the inherent characteristics of flow over the full-scaled hydraulic structures [92]. In addition, because of the high processors computers, the use of coarse meshes (one-dimensional) for hydraulic modelling is now limited and has been replaced with the three-dimensional (3-D) fine meshes which provide stable and accurate hydraulic modelling without any further need of the simplified assumptions [93],[94]. Many numerical researches [52], [57],[58], [71], [82], [85], [88], [95], [96], [41], [97], [98], [99], [100], [101], [102], [103], [104],[105], [106], [107] employed numerical models to investigate HJ, energy dissipation, and scouring downstream of different hydraulic structures but the literature lacks to provide any data on Taunsa barrage (presently investigated).

From the literature review, it is noted that construction and remodelling of studied barrage experiences multiple issues on its downstream. The present study is novel in term of: a) to identify the critical hydraulic parameters which had not been considered in the above two stages of barrage construction and are the most relevant one to minimizing the problem and (b) to make modification in the baffle blocks regions by changing the shape of baffle blocks geometry that help to increase the energy dissipation near the basins' floor and improved flow characteristics in the basin. Therefore, this study has developed FLOW-3D hydraulic and scour models to investigate the hydraulics of different stilling basins downstream of the studied

barrage. Primarily, the study investigates four different stilling basins, i.e., modified USBR Type-III basin, remodelled basin (USBR-Type-III basin), and WSBB basins. In the WSBB basins, the WSBB with vertex angle of  $150^\circ$  and cutback angle of  $90^\circ$  is employed to confirm the suitability of such dissipators downstream of diversion structures.

## 1.7 Research Objectives

This research study intends to investigate hydraulic parameters that are critical for hydraulic modelling and energy dissipation. The study implements WSBB and other energy breaking appurtenance previously used on Tuansa barrage to investigate hydraulic and scouring behavior on the barrage downstream. The specific objectives of the present study are;

1. Identification of critical hydraulic parameters (CHPs) from the literature and implementation of 3-D numerical models to investigate these CHPs with WSBB and other shapes of appurtenances which are previously used downstream of the studied barrage.
2. To determine the shapes and configuration of appurtenances using 3-D numerical models that help to increase the energy dissipation process downstream of the studied barrage.

## 1.8 Scope and Research Limitations

### 1.8.1 Research Scope

The present study developed numerical models to investigate hydraulic and scour phenomena downstream of Taunsa barrage using FLOW-3D software. The study focused four different type energy dissipation arrangement for hydraulic and scour models. For the hydraulic models, different parameters were studied for three

gated flows using the most suitable turbulence model. The models input data, i.e., pond and tail water levels were gathered from the barrage site, while to replicate the actual conditions of the barrage gate openings were computed. To resolve the geometry and basin's appurtenance, different mesh blocks were employed, and suitable finish time was assigned to obtain the steady state solution for the models.

For the scour models, the present study focused uncontrolled free flows condition using three different turbulence models. For the scour models, sand bed was employed downstream of the different stilling basin, and Van Rijn sediment transport rate equation was applied. The present numerical models were validated with the probing/scour data of year 2015.

## 1.8.2 Research Limitations

The present study developed FLOW-3D numerical models downstream of Taunsa barrage. The modelling of environmental flows in a computer based models bears some assumptions and limitations. Similarly, the present study has also some limitations which are further divided into two categories, i.e., general limitation and models' limitations as listed below.

### 1.8.2.1 General Limitations

1. For the gated flows, the present study has only focused three discharge values, i.e., 2.44, 4.88 and 7.22 m<sup>3</sup>/s/m. Similarly, for the validation of models' flow values, the study only employed three free flows such as designed, 90% and 75% of designed flow.
2. As the barrage under study was remodelled during the year 2008, which also consisted of subsidiary weir on its downstream. However, at present, the focus is only made downstream of main weir where the basin appurtenances are remodelled. Subsequently, the investigation of different hydraulic and scour parameters are also examined downstream of the main weir.

3. Presently, to run the simulations, operational conditions, i.e., tail water depths, and pond levels of year 2010 flood are employed while minimum and maximum hydraulic jump conditions are yet to be explored for hydraulic and scour processes.

### 1.8.2.2 Models' Limitations

1. Only one bay of the barrage is modelled from hydraulic and scour models. For the hydraulic modelling, the present study only focuses lower flows, and due to the absence of field and laboratory data, for all the investigated flows, the performance of hydraulic models is ensured by volume flow rates at the inlet and outlet boundaries.
2. Due to the non-availability of river bed data, for the scour models, the study employed sand bed downstream of the studied basins, and only Van Rijn transport rate equation is employed. Additionally, the scour models were studied for two uncontrolled free flow conditions i.e., 24.30 and 18 m<sup>3</sup>/s/m discharges.
3. Presently, the dimensions of different energy dissipators such as impact baffle and friction blocks are kept constant, and for the WSBB, the vertex and cutback angles were restricted to 150<sup>0</sup> and 90<sup>0</sup>, respectively.
4. The main focus of this study is to investigate the affects of different energy dissipating system downstream of low head hydraulic structure, and to check the suitability of WSBB for open channel hydraulic structures.
5. It is worth mentioning here that the present study has only investigated the geometry of different energy dissipators to check their suitability for river diversion barrages.
6. Presently, to investigate the turbulent flow regions,i.e., hydraulic jump and near the scour beds, mainly two equation RANS models, such as RNG K- $\epsilon$  and Standard K- $\epsilon$  models are employed, whereas the effects of other models



like SST  $K-\omega$  and Reynolds stress models (RSM) are yet to be studied for hydraulic and scour patterns downstream of the investigated barrage.

## 1.9 Dissertation Organization

The dissertation consists of six chapters as detailed below:

The Chapter first begins with brief of hydraulic structure and their modelling concepts. The chapter highlights the importance of hydraulic structure, and includes the use of numerical modelling. The chapter also includes the brief of barrage design in Pakistan, and the affects of flooding on these structure. After that, research motives, problem statement, research novelty and scope & limitations are outlined.

The Chapter two provides the literature review for this research work. The literature review starts with the brief background of turbulent flow behavior over hydraulic structures and highlights the significance of hydraulic jump (HJ). The literature review also includes the role of stilling basin appurtenances, i.e., chute blocks, baffle blocks, and end sills for energy dissipation. The literature review further illustrates physical and experimental studies on HJ, energy dissipators and local scour downstream of hydraulic structure. Furthermore, the literature review provides background for use of computational fluid dynamic in hydraulic and scour modeling and, describes numerical studies relevant to this research work. Lastly, the literature review provides a summary for problem statement, research gap and motives for the present study.

The Chapter three presents the methodology carried out for the current study. At start, methodology displays the study area on which research motives are focused. Keeping in view the research objectives, methodology is divided into three main phases. In the first phase, critical hydraulic parameters are identified from the literature and their ranking is done using Frequency analysis and relative importance index (RII). During the first phase, from the available literature, a detailed

comparison of different numerical codes is also performed, and FLOW-3D code is selected to conduct hydraulic and scour modelling. For the second phase, methodology explains numerical modelling techniques, turbulence closure models, solution methods, computational grids, free surface tracking, and fluid solid interface to carry out hydraulic modelling of the identified critical hydraulic parameters. In the third phase, the methods and techniques selected for hydraulic modelling and scour models are explained. In the end, the methodology also presents input data, initial and boundary conditions i.e., drawings, discharge, and sediment data.

The Chapter four presents the results in two parts. In the first part, results of ranking of different hydraulic parameters are displayed, and based on the methodology defined in chapter 3, critical hydraulic parameters are identified. In the second part, initially, performance of present FLOW-3D numerical models is assessed by gated and free flow analysis, and then the comparison of hydraulic parameters such as free surface profiles, sequent depths ratio, roller lengths, hydraulic jump efficiency, velocity profiles and turbulent kinetic energy is done for the studied stilling basins. The results of hydraulic parameters in the studied stilling basins are also compared with the relevant experimental and numerical studies of the literature.

The Chapter five shows the results of local scour and bed retrogression downstream of the studied stilling basins using different turbulence schemes i.e., RNG  $K-\epsilon$ , Standard  $K-\epsilon$  and Large Eddy simulation (LES) as described in chapter 3. Before representing the scour results, the scour results downstream of Type (B) basin are validated with field data. Using the field data, the scour results downstream of Type (B) basin are also assessed by statistical method i.e., Coefficient of Determination ( $R^2$ ). After the validation, the results of flow field over the scour/retrogressed beds of investigated basins are presented and their discussion is made accordingly. Lastly, the chapter 5 displays and discusses the 3-D illustrations of scoured/retrogressed bed downstream of studied stilling basins.

The Chapter six provides the overall conclusions and recommendations of the present study. The chapter also provides the practical implications of the study.

# Chapter 2

## Literature Review

### 2.1 Introduction

Flow characteristics over the hydraulic structures are very complicated, highly turbulent which develop secondary currents and reattachment on the bodies of the structures [70][108]. The grade-control structure across rivers and canals are used to calculate flow, raise upstream water levels, reduce velocity, and help to limit the excessive channel degradation on their downstream [33]. Barrages and weirs are the low head hydraulic structures constructed across the river to divert water into the canal for a regular water supply for irrigation and control the released water [68], [109], [110], [111]. These structures operate under low Froude numbers, and their floor levels are kept so that the hydraulic jump (HJ) must be formed on the downstream toe of the glacis. The leftover energy from the HJ must be dissipated within the downstream stilling basin using different structural arrangements. Furthermore, a flexible apron is also provided downstream side of stilling basin to dissipate the residual energies. Thus, such structures improve the river approach and navigation conditions. However, if the flow conditions are not properly developed, the safety of the whole system can be jeopardized [112]. From the history, it is found that physical modelling has played crucial role to understand the process, testing and optimization of the hydraulic structures at various stages

i.e. design and prototype construction [113],[114]. In most of the situations, environmental flow are turbulent in nature, and to control the turbulence, HJs are developed in the stilling basin of these hydraulic structures. The physical experimentation to study HJ in term of energy dissipation, free surface profiles (FSP<sub>s</sub>), velocity profiles (VP<sub>s</sub>), pressure and the behaviour of HJ in different types of stilling basin with various appurtenances have been reviewed presently and discussed in the proceeding sections.

## 2.2 Hydraulic Jump and its Usefulness

Hydraulic jump (HJ<sub>s</sub>) are occurred in the rivers, canals, and below the industrial, industrial discharge outlets [115], [116], [113]. Civil and hydraulic engineers develop such conditions to create this phenomenon for efficient and effective energy dissipation [24], [117], [118], [119], [120] downstream of hydraulic structures. This chaotic phenomenon happens when a supercritical flow transforms into the subcritical flow. The Belanger equation is employed to compute the sequent depths of free HJ [83], [41], [121], [100], [122].

$$\frac{y_2}{y_1} = \frac{1}{2}(\sqrt{1 + 8Fr_1^2} - 1) \quad (2.1)$$

where  $y_1$  and  $y_2$  are the supercritical and subcritical flow depths, respectively, and  $Fr_1$  is the incoming Froude number from the upstream which equals to;

$$Fr_1 = \frac{v}{\sqrt{gy_1}} \quad (2.2)$$

where,  $v$  is supercritical flow velocity, and  $g$  is acceleration due to gravity. Various studies are carried out on HJ characteristics but only few of the most relevant ones are discussed in the proceeding section.

A mathematical model was developed to investigate the characteristics of HJ to assess the performance of prototypes and physical models. The integral strip method, which uses the velocity shape function and allows the partial integration

of the equation of motion was used. The results showed that the value of Froude Number greater than 4 increased the pressure and centrifugal force. The results further indicated that flow bulking was the main reason for entrained air.

Misra et al. [120] investigated mean and turbulent structure of weak HJ. A recirculating tilting flume was used to carry out experiments and undershot weir was used to develop the flow conditions. The results showed a thick curved shear layer near the bed which was parallel to the free surface. This shear layer produced the turbulence, and its intensity was decreased from the HJ toe towards downstream. The results further showed that Reynolds shear stress was found to be negative in the shear layer, which indicated the momentum diffusion beneath the shear layer and its value was positive just beneath the free surface.

Pagliara et al. [123] conducted experiments in horizontal rectangular flume on the homogeneous and non-homogeneous rough beds to investigate the HJ characteristics. The results indicated that in the nature bed, the correlation coefficient was not only dependent on sequent depths and roughness coefficient but also on uniformity of the roughness.

Abbaspour et al. [122] conducted experimental in a metal glass flume to investigate the effects of sinusoidal corrugated bed on HJ characteristics. The discharge was measured by triangular weir which was placed at the end of flume. The results indicated that as compared to the smooth bed, tail water depth (hereafter called TWD) and HJ length were reduced in corrugated bed. The results of shear stress on the corrugated bed was 10 times more than that of smooth.

Zobeyer et al. [124] investigated flow turbulence from the end of HJ to open channel flow. Discharge, upstream water and tail water depths were controlled by magnetic flow meter, sluice gate and tail water gate, respectively. The results showed that length of turbulence region in transition zone was about 10 times of sub critical depth.

Mignot and Cienfuegos [125] conducted experiments to investigate turbulence production and energy dissipation for weak HJ. In case of undeveloped inflow jumps,

the results indicated that turbulence production and turbulence kinetic energy were confined within the shear layers of upper fluid column. However, in case of partially developed jump, peaks of turbulence production and turbulence kinetic energy were observed in upper shear layer as well as near the wall region.

Macián-pérez et al. [78] conducted laboratory investigation on USBR-II stilling basin to study the HJ characteristics. The efficiency of HJ was reached from 70% to 75% for  $Fr_1=9$ . The roller length of the HJ was reached to 1.25 m which was less than the roller length calculated from the classical HJ equation. The velocity decay was found slow as compared to the classical HJ equation.

Stojnic et al. [126] conducted experiments to investigate the HJ on a stepped spillway. The results revealed 17% more HJ length than that was found in Petreka (1958) results. Due to the curvilinear flow behavior near the upstream jump toe, high-pressure fluctuations was found in that region.

## 2.3 Significance of Stilling Basins and Appurtenances

Energy dissipation is the most common issue faced in the design of hydraulic structures. The potential and kinetic energies typically come from the upstream of the dams, spillways, chute, sluice gates, and weirs which are further induced by the HJ and its turbulent structure [87]. To dissipate the excessive energy of the water, stilling basins [26], [63],[72],[52], [24] [50], [127], [89], [90], [91], [25] are constructed downstream of these hydraulic structures. There are various types of stilling basin designs i.e., United States Bureau of Reclamation (USBR) stilling basins [24], [25],[61], manifold stilling basins [128], Utah State University (USU) energy dissipators [129], Mahakaal stilling basins [63], [62], and wedge-shaped stilling basins [89], [91]. Furthermore, performance of these basin is also affected by their size and geometry which develops different flow patterns [83]. In the stilling basin, various geometrical arrangements such as chute blocks [52], baffle blocks

[67], [65], [80], [32], friction blocks, [45], [76], end sill, [44],[81],[130], and vertical sill [82], and splitter blocks [91] are made to uniformly distribute the kinetic energy and turbulence. Numerous studies are carried on the design of stilling basins but only a few of them are briefly discussed in the proceeding section.

### 2.3.1 Function of Chute Blocks in Stilling Basins

Chaudary and Sarwar [76] studied the two different stilling basins of Taunsa Barrage. The old basin was changed in which chute blocks and sill were placed at the start and end of basin, respectively. It is reported that after 2010, the barrage was unable to pass the flood and downstream of the barrage, the river changed its route. After comparing the pre and post dissipation systems, the results indicated that the remodeling of basin was not rational.

Padulano et al. [127] conducted experiments on USBR-II stilling basin and investigated different types of HJs. The study focused pressure and forces on the stilling basin and identified free and submerged HJs. The results showed that energy dissipation and HJ efficiency were increased as the submergence increased. In the submerged jumps, maximum efficiency was achieved for the negative submergence as the values of  $(Fr_1)$  increased. In case of submerged HJ, the results further showed at 0.5 pressure coefficient, the pressure fluctuation were high as the HJ changed from C-type to Spray-type.

Farhoudi [130] investigated flow behavior on ogee spillway with chute blocks. The flow depths were controlled by tail water gate which was installed at the end of flume. The results further showed a second-order polynomial function between the Froude number and pressure fluctuation.

### 2.3.2 Effects of Baffle Blocks on Flow Characteristics

Stilling basins are design to accommodate a wide range of flows without damaging the components of the hydraulic structures [68]. Various shapes of auxiliary

devices/energy dissipators are developed within the stilling basins to stabilize and reduce the turbulence. These devices also control the HJ length and enhance energy dissipation within the basins [131]. These dissipators are placed on downstream of the gates and can be of various shapes and sizes. Numerous studies are carried out on the sizes and shapes of baffle blocks but only a few of them are briefly discussed below.

Nettleton and McCorquodale [61] conducted a total of 120 experiments to investigate characteristics of HJ in the radial stilling basin. The study further implemented multiple regression analysis to developed equations for the hydraulic parameters such as location of baffle blocks, flows, gate openings and tail water levels. The results showed that radial basin created less sequent depths than that of rectangular channel basin. The results further showed that the dimensionless length of forced HJ in the radial stilling basin was found equal to the free HJ.

Grimaldi et al. [83] investigated curve baffle blocks and developed dimensionless equations for the investigated hydraulic parameters. As compared to regular straight blocks, results indicated that curve baffle blocks produced more energy dissipation which increased from 3.2% to 33.3%. The results further showed that increase in the effective height ratio ( $h/Y$ ) produced 36% more energy dissipation than conventional baffle blocks.

Habibzadeh et al. [64] investigated the performance of submerged HJ with baffle blocks. The results showed two regimes, namely deflected surface jet and reattaching wall jet flows. For small submergence values, deflected surface jet was found to be more efficient in energy dissipation as compared to the reattaching wall jet.

Habibzadeh et al. [67] investigated submerged HJ for baffle walls and blocks. The results showed that  $Fr_1$  and submergence were the functions of energy dissipation in the submerged HJs. The results further showed that the energy dissipation increased as the submergence was increased. However, as the tail water depths increased the energy dissipation was decreased. Upon use of baffle blocks with the same values of  $Fr_1$ , the results revealed that in the submerged HJs energy dissipation was found high than that was observed in free HJs.



Abbas et al. [68] investigated different shapes of baffle blocks in rectangular flume. For different HJs, the values of  $Fr_1$  were ranged from 3.99 to 7.48. The result showed that Type-D block reduced the sequent depths ( $y_2/y_1$ ) and hydraulic jump length ( $y_j/y_1$ ) ratio and up to 26% and 37%, respectively. The results further indicated that two rows of D-type baffle block produced 28.6% energy loss on smooth bed.

Bestawy [132] studied different shapes of baffle piers within the stilling basin of spillway. Discharge was measured with orifice meter, and point gauges were installed to measure the flow depths. The scour length and depth were measured with a scale mounted on side of the flume. The experiments were conducted for 5 to 9 values of  $Fr_1$ . The results showed that models which produced vertical circulation and roller along the transverse direction were more efficient for energy dissipation which also reduced the scour. Among various models, the vertical semi-circular and vertical trapezoidal sections baffle blocks showed better hydraulic performances as compared to other models.

Al-Mansori et al. [133] studied V-shaped baffle blocks to investigate energy dissipation downstream of ogee spillway. As Compared to the normal baffle blocks, upon use of V-shaped, the results showed 9.31% increase in the energy dissipation while a 38.6% decreased in the HJ length was also observed. In comparison to the standard baffle blocks, 98.6% increase of drag force ratio was also observed in V-shaped baffle blocks.

### 2.3.2.1 Summary

From the previous studies, it is found that the baffle blocks have improved the flow conditions and stabilize the HJs downstream of different hydraulic structures. It is also reported that using different energy dissipators, the dissipation rate within different stilling basin is also increased. Additionally, few of the studies also highlighted that in comparison to the vertical face baffle blocks, the other shapes of baffle blocks such as V [132], Curve [133] increased the energy dissipation and decayed kinetic energies more efficiently.

### 2.3.3 Sill-controlled and Multiple-steps Stilling Basins

Sills are HJ-type energy dissipator and are placed at various locations in the stilling basin. They are of various shaped and size such as Un-dentated and dentated sills which control sequent depths and stabilize the HJ [69]. However, on flat apron to control the length of submerged HJs [85] sudden drop, rise, and multiple steps are also provided in the stilling basin. Primarily, these arrangements are made to dissipate excessive kinetics energies which are released from sluice gates, pipe outlets, and spillways. Numerous studies are conducted on sill and multiple steps within the stilling but the most relevant are discussed in the following section.

Hager and Li [26] conducted laboratory experimentation to investigate the effects of end sills on tail water and scour depth. The results showed that due to formation of strong rollers around the end sill, erodible bed was less scoured as compared to the results of scour in classical hydraulic jump. Similarly, results also showed that the stilling basin with end sill controlled HJ length and tail water depths as compared to the results of classical HJ without end sill.

Alikhani et al. [82] conducted experiments on five different heights of vertical sills to investigate the characteristics of HJ without tail water depth. The results indicated that upon increase of sill height, the free surface profile of HJ was increased while smaller sequent depths was observed. As compared to free HJ without end sill, upon use of sill, the results indicated 30% reduction in stilling basin length .

Tiwari et al. [63] conducted experiments on different heights of intermediate sill downstream of non-circular pipe outlets. The experiments were conducted for three different value of  $Fr_1$  such as 3.85, 2.85, and 1.85. The performance of the investigated models were monitored by a non-dimensional performance index (PI). As compared to other models, triangular blocks of 0.5d height and base width of d showed less scour.

Elsaeed et al. [87] investigated the effects of negative steps of bed on the pressure fluctuation in HJ. The upstream and downstream flows were controlled by pressure tabs while Transamerica Instruments was attached to the computer to

collect pressure data. The results showed that pressure fluctuation was found to be maximum in at the impingement point. The dimensionless pressure coefficient was found varying with the change of step shape and dimension. On comparison, the results further revealed that the maximum pressure fluctuations were smaller than the classical HJ, and its values were confined within 20% of the classical HJ.

Ali and Mohamed [112] conducted experiments to investigate the HJ characteristics for different stilling basins downstream of radial gates. The results showed that the stilling basin with multiple step at the apron's end produced smaller length of submerged HJ. In comparison to other stilling basins, multi-steps stilling basin also reduced velocity and scour.

#### **2.3.3.1 Summary**

From the studies related to end sill and multiple step basin, it is revealed that these arrangements have increased the energy dissipation in the basins and controlled the HJs length. However, before employing such arrangements, the size and geometry of these dissipators need special attention. Additionally, in the the literature these type of setup are found to be applied for submerged HJ conditions whereas their employment downstream of the open channel i.e., river diversion barrage need special care.

#### **2.3.4 Effects of Tail Water Depth (TWD) on Hydraulic Jump and Energy Dissipation**

Free surface profiles (FSPs) downstream of the hydraulic structures produce convective acceleration and deceleration of the flows. This acceleration or deceleration of the FSPs is called tail water when the flow becomes subcritical [134] [135]. For a specific flow rate, distinct tailwater levels are developed downstream of the hydraulic structures and any increase or decrease in tail water depths produces effects downstream of channel and river [136] [137] [138]. The effects of tail water depths

downstream of hydraulic structures are investigated in many studies but only a few them are highlighted in the proceeding section.

Matooq et al. [139] investigated the effects of tail water depths for Diyala weir. The results indicated that to form the HJ, available tail waters on downstream of the Diyala weir were less than the required sequent depth. The results further showed that an oscillating HJ was formed within the stilling basin which caused hydraulic issues on downstream of the Diyala weir. The study recommended to increase the downstream floor level to cater the problems.

Ead and Rajaratnam [137] investigated the effect of tail water shallowness on plane turbulent wall jet. The results indicated that in the developed region, the rate of velocity decay was independent of TWD while velocity profiles in developing and developed regions were found to be similar.

Ali and Kaleem [140] studied energy dissipation for two different stilling basins of Tuansa barrage. It was reported that the old basin was functioning properly while the new remodelled basin dissipated less energy in the basin. The study further showed that the remodelled basin also launched the stone apron in front of some bays, and drifted the river toward left side of the barrage.

Chaudhry [45] investigate the tail water effects for various discharges on the downstream of Taunsa barrage. The results showed that the existing tail water level were appropriate for HJs which further indicated no sweeping on HJs. The study revealed that the two different basins of the barrage produced different hydraulic behaviour which might be studied further for local scour and other hydraulic parameters.

Mosaa et al.[141] conducted experiments to investigate the effects of tail water levels on the vertical drop downstream of spillway. By varying the  $TWD_s$ , five different flow conditions, A-jump, wave jump, wave train, B-jump with plunge condition and limited jump were noticed. The analysis revealed quasi-periodically flow configuration for oscillating jumps. In addition, due to oscillating effects, the free surface profile, pressure and velocity values were also found to be changed.

The results further indicated that for a constant  $Fr_1$ , as the step ratio was increased the TWD ratio were also increased. The study also developed a flow regime chart for a wide range of discharges, step ratio and  $TWD_s$ , and suggested to employ these guidelines for the vertical drop basins downstream of spillways.

Bhuiyan et al. [142] studied the effects of shallow  $TWD_s$  for the characteristics of plane turbulent offset jet on rough beds. The momentum analysis revealed that due to increase of  $TWD_s$ , the water surface near the offset jet dropped and results further showed that for a similar bed roughness, the effects of bed roughness in offset jet were found to be less than wall turbulent jet. Under shallow  $TWD_s$ , The results further showed as compared to wall jet, the momentum and velocity decay were found to be higher on downstream side which further accelerated the bed roughness was increased.

Espa and Sibilla [143] studied intermediate  $TWD_s$  to investigate local scour downstream of apron. The study indicated three different scour regimes, i.e., surface jet regime, bed jet regime and an intermediate regime ranged from bed to surface. The results indicated that in surface jet regime, the scour hole and dune was formed horizontally while in bed jet regime, the shorter scour hole and dune were noticed, however, the vertical dimensions of the scour hole and dune found to be higher than surface jet regime. On the contrary, in the intermediate regime, the water jet was found to be switching between bed and surface which indicated unsteady scour hole and dune. The results further indicated that to understand intermediate scour regime, densi-metric Froude number, dimensionless apron length and dimensionless  $TWD_s$  were the dominating parameters.

#### 2.3.4.1 Summary

Based on the literature review, it is found that the tail water downstream of hydraulic structures plays a crucial role in the development of HJs. In case of less tail water levels, the HJ phenomena can be changed which further have implications on the river bed, i.e., bed retrogression and local scour. A very few studies have been found which investigated the tail waters effects on the HJ whereas the

literature is lacking to provide the effects of tail water on different parameters of HJ and flow behaviour within the stilling basins' of barrage. Therefore, the effects of tail water in different stilling basins downstream of river diversion barrages are yet to be explored.

## 2.4 Wedge-Shaped Baffle Block (WSBB) Stilling Basins

Different types of stilling basins have been designed downstream of the hydraulic structures, as mentioned in the 2.3 section. However, none of the designs have mentioned the optimal length of these stilling basins. This section has focused WSBB which are preciously used downstream of pipe outlets to reduce the length of the basins.

Goel [66] investigated different shapes of stilling basin appurtenance downstream of circular pipe outlet. The study conducted seventy-four (74) experiments in the rectangular flume and the performance of different models was assessed by local scour. Out of the investigate models, M-71 model showed less scour. In M-71 model, WSBB produced maximum drag on either sides of baffle blocks, and created discontinuity in fluid layer. The results also showed large number of eddies on either sides of WSBB which increased energy dissipation.

Pillai et al. [70] investigated the role of chute and WSBB for the design of short stilling basins. The WSBB at the vertex angle of  $150^{\circ}$  and a cutback angle of  $90^{\circ}$  were used in the stilling basin. The experiments were performed for inflow Froude number ( $Fr_1$ ) of 2.85. The results showed that newly proposed basin produced less scour than the USBR-IV stilling basin. The study recommended to develop such stilling basin for ( $Fr_1$ ) ranging from 3.75 to 4.57.

GOEL [72] conducted experiments to investigate different shapes and sizes of energy dissipators such as end sills, baffle blocks, WSBB, impact walls, and intermediate sills for square pipe outlets. The results showed that WSBB spread the

water jet in a wider area and improved the flow behavior and head loss. The results also showed that WSBB produced more drag force and wake areas which increased eddies of either side of blocks. On comparison with USBR-IV stilling basin, the stilling basin with WSBB enhanced energy dissipation and reduced the of length of basin up to 15%.

Verma and Goel [91] carried out experiments to investigate WSBB on downstream the for pipe outlet. The invert level of the pipe was kept on the floor level and the values of  $Fr_1$  were ranged from 1.70 to 5.50. The results showed that WSBB spread the fluid across the full length in lateral direction. Upon use of WSBB, the results indicated more energy loss due to the entrainment of the surrounding fluid which distributed by momentum to the greater mass. Additionally, the WSBB also increased small eddies on either sides and developed more drag forces which increased energy dissipation. Overall, compared to USBR-IV basin, the WSBB basin reduced basin length up to 25% reduction.

Verma and Goel [90] investigated the flow characteristics downstream of the circular pipe outlets and implemented WSBB. The tests were conducted for 1.70 to 5.50 values of  $Fr_1$ . The WSBB with a vertex angle of  $150^\circ$  and cut back at  $90^\circ$  produced larger drag force and less scour. As compared to USBR-IV stilling basin, SB-34 model with length of  $6d$  generated less scour.

### 2.4.1 Summary

Based on available literature of WSBB, it is found that the previous studies lack to provide the use of WSBB downstream of the open channel/low head hydraulic structures such as barrages. Therefore, to fill this gap, the present study investigated the WSBB downstream of open channel flow, i.e, river diversion barrage. Based on results of studies [66], [72], [70], [91], [90], for the investigated WSBB, the vertex angle of  $150^\circ$  and cutback angle of  $90^\circ$  is still to study for diversion barrages.

## 2.5 Computational Fluid Dynamics (CFD) and Hydraulic Modelling

Physical modelling and on-site-measurements are usually expensive and time consuming. Therefore, the use of numerical modelling for hydraulic characteristics of grade-control structures is becoming popular. Such modeling tools are useful, especially when the basic fundamental equations cannot be useful such as in case of multifaceted geometries [59].

In the former section, a wide range of literature on the experimental studies is discussed, which could be assisted by CFD models e.g., investigation of hydraulic jumps (HJs) and energy dissipation [98] [100]. Flow over the hydraulic structures is very complex and associated by secondary currents which characterized it highly turbulent in three dimensions. Hence, it is usually hard to accurately measure the free surface profile, pressure variations, velocities, secondary currents and turbulent kinetic energy over these hydraulic structures (Jothiprakash et al. [33]). With the development of CFD in 1970, numerous studies were conducted with different numerical tools which opened new dimensions to model the above mentioned hydraulic issues. Also, the rapid development of computer technologies and turbulence models, these numerical techniques provide an insight view of the hydrodynamic downstream of graded controlled structures [97]. Additionally, these numerical models are also capable of solving fluid equations, and facilitate civil engineers and hydraulic experts for performances evaluation of dissipation mechanism [144] [145] [146] [147] [148]).

Several hydraulic modellings tools are available in the market to address the multi-surface problems of hydraulics, such as FLOW-3D [149], Fluent CFD [150], Open Foam [151], REEF3D [152], HEC-RAS [153], Phoenics [154] and STAR-CMM+ [155]. All the above-mentioned tools use Finite Volume Method (FVM) to discretize the Reynolds Averaged Navier Stokes (RANS) equation and implement turbulence models to solve the closure problems. Numerous studies are carried



out on the hydraulics of spillways, sluice gates, weirs, and barrages. A brief review of the few numerical studies on the hydraulic investigations is presented here.

Chaudhry [77] investigated FSPs downstream of barrage's stilling basins using two dimensional HEC-RAS models. The results revealed acceptable values of FSPs in which the locations of HJs were found at the glacis. Similarly, the result also showed that in the old basin, the velocities were within the acceptable limits while higher values were noticed in the remodelled basin. Furthermore, it was also reported that as compared to old basin, the remodeled basin was developing higher flow depths and due to that reason, the locations of HJ toe were found to be shifting above on the glacis.

Mishra [156] used Fluent CFD to investigate energy dissipation on flexible apron downstream of the barrage. The study investigated hydraulic parameters on two bed i.e, horizontal and inclined flexible aprons. In comparison to the horizontal apron, the results showed that TKE downstream of the inclined apron was found less. Similarly, as compared to horizontal apron, no velocity currents and flow concentration was noticed on the downstream of inclined bed.

Cassan and Belaud [157] used Fluent CFD to investigate large gate openings and gate submergence, and compared results with the experiments. The results indicated that the numerical model slightly overestimated velocity values in the longitudinal direction. The results further revealed that maximum turbulence energy and dissipation were found in the mixing region, particularly near the contracted stream.

Bayon-Barrachina et al. [99] conducted numerical investigation on rectangular smooth horizontal channel to study characteristics of HJ using 3-D Open Foam software. The turbulence was captured by Standard K- $\epsilon$ , RNG K- $\epsilon$ , and SST K- $\omega$ . The free surface was tracked by volume of fluid (VOF) method. The results showed that multiple sizes of bubble were found in the recirculating and turbulent shear region of HJs. The mesh sensitivity analysis showed that all models results showed less than 2% error but the results of RNG K- $\epsilon$  were found to be in close

agreement with the roller length. For the FSP, the value of  $R^2$  reached 0.996 which indicated better performance than other models.

Lopes et al. [106] investigated the hydraulic characteristics of stepped spillways. Two different width of spillway models i.e., 0.5 m and 0.3 m were investigated for skimming flow patterns using Open Foam code. The results revealed a seesaw flow pattern over the consecutive steps of the spillway. The results further showed that this pattern was found because of complex nature of cross waves along the spillway, and alternating skimming flow was more profound at cavities than that of free-stream flow. The results also showed that near spillway crest, turbulent kinetic energy (TKE) was high due to the development of the boundary layer. The results showed that the free surface velocity increased when the distance was increased towards the spillway crest.

Nguyen [107] carried out investigation on the free surface flow analysis for rivers and natural channels using Open Foam code. The study used two different methods to track the free surface such as front tracking and front capturing. The results showed that in  $180^\circ$  curved channel, the front tracking method failed to produce the water surface profile on the inner side while the results of outer side were found promising. In case of the dam break phenomena, again the front tracing method failed to capture the complex free profiles, while front capturing method produced a good shape of complex breaking surface at  $t=0.25s$  and  $t=0.50s$ . Similarly, the simulation results of the free surface over the Kostheim Weir showed breaking surface of HJ which indicated that the results of front tracking method deviated from the experimental data. However, the front capturing with use of dense meshes produced the HJ characteristics which agreed with the experiments.

Liu and García [158] used Open Foam code to investigate the local scour downstream of turbulent wall jet and around circular cylinder. The results indicated flow circulation at three different location which caused scour on movable bed. In near jet region, the results were agreed with experiments, however, in the far region the model overestimated the velocity distribution. At equilibrium, the maximum

scour depth reached 0.63 m while maximum deposition depth was found about 0.4 m which agreed with the experimental observations.

Parson et al. [154] conducted numerical study on aeolian dune of different geometry to investigate wind flow structure using 2-D PHOENICS models. The pressure velocity coupling was carried out by Simpler method, while turbulence was captured using RNG K- $\epsilon$  model. The results indicated that upon increase of dune height, flow at the dune's crest and in the streetwise direction was increased, while at the toe of leeward side the flow was decreased. The study further highlighted that the steeper dunes with the same aspect ratio affected the flow field especially on the leeward side of dunes.

Sergeenko et al. [159] used STAR CMM+ models to investigate the flow over broad crested spillway. The study used realizable K- $\epsilon$  to capture the turbulence downstream of the spillway. The results indicated air injection at the hydraulic jump initial location and the maximum velocity was observed before the HJ and at downstream floor. The results further indicated that the maximum turbulence intensity were at the locations of maximum velocities. Upon comparison of results of numerical model with experiments, the study showed that STAR CMM+ produced agreeable results, however, due to the absence of air entrainment model, the results of numerical models showed deviation at the flow impingement location.

Babaali et al. [86] investigated the HJ characteristics on stilling basin with converging sidewall using FLOW-3D. The study implemented four convergence angles such as  $5^0$ ,  $7.5^0$ ,  $10^0$  and  $12.5^0$  for the USBR-II stilling basin. VOF, RNG and Standard K- $\epsilon$  models were utilized to track free surface and turbulence within the HJ, respectively. The results showed that in the HJ region, the basin's end, because of low turbulence, the pressure distribution was found to be hydro-static. The results further showed that near the bottom, velocity distribution was found to be consistent, while at top, due to fluid circulation, adverse velocity profile was noticed. Using both K- $\epsilon$  models, except in the HJ region, the water profiles showed good agreement with the experiments. The results also showed that at the convergence angles of  $5^0$ , the HJ efficiency was found to be maximum.

Ghaderi et al. [98] implemented FLOW-3D to investigate the geometrical effects of Trapezoidal–Triangular Labyrinth weirs (TTLW) on the characteristics of HJ. Free surface and turbulence were modeled by VOF and RNG K- $\epsilon$  models, respectively. The results showed that for the higher value of hydraulic head/weir height ( $H/P$ ), as the angles of sidewall decreased, the discharge coefficient was also decreased due to the collision of the falling jet. The results further showed that maximum energy was dissipated due to the colliding nappes in the upstream apex angle while on the downstream side, it was noticed in circulation region behind the nappe. Additionally, the results also showed that energy dissipation was reduced as angles of sidewall and weir height increased.

Ghaderi et al. [101] conducted experiments on triangular macro-roughness for the characteristics of submerged HJ and compared the results with FLOW-3D models. The results showed reduction in the HJ length, and maximum turbulent kinetic energies were found on the free surface. The results of bed shear stress coefficient and energy loss within the submerged HJ using triangular micro-roughness were more significant as compared to the results of smooth bed.

Savage and Johnson [104] conducted experiment to investigate the FSPs and discharge coefficient over the standard ogee spillway. The study also compared results with FLOW-3D numerical models. The results showed close agreement of discharge coefficients ( $C_d$ ) with the experimental data. The results further revealed that at the crest, a small change in pressure produced different magnitude of pressure forces.

Wang [160] conducted experimental and numerical investigation to study the effects of separated and compound stilling basins. The turbulence was captured by four different turbulence models. The free surface was tracked by VOF method. The validation of the models were carried out using flow rates with the prototype data of Lotus Temple hydro power station on Gourd River, China. As compared to separated basin, the compound stilling basin decayed more velocity which decreased from 1.5 to 2 m/s. Additionally, the results higher showed energy dissipation rate in compound basin than the separated stilling basin.

FLOW-3D models were used to study the flow pattern at flood discharge downstream of multipurpose Soyang dam [145]. As compared to the scaled model and field data, the numerical model overestimated the discharge up to 4%. The value of maximum velocity was found on the spillway glacis which reached 43 m/s. Additionally, the result of flow reattachment were agreed with the scaled model.

Nikmehr and Aminpour [161] investigated the HJ characteristics over the rough bed using FLOW-3D numerical models. For calibration of the models, experimental data was used. The RNG K- $\epsilon$  turbulence model was used to observe the sequent depth ratio, surface profiles, length of the jump, and velocity distribution. The location of the free water profiles was identified by VOF method. The results indicated that after reducing the roughness height and its distance, the sequent depths ratios and HJ lengths at all value of Froude number were also decreased. Additionally, velocities profile near the bed decreased as the roughness height and its distance was increased.

Chen [162] employed FLOW-3D models to study the flow characteristics on rectangular sharp-crested weir with varying upstream and downstream slopes. The study further investigated the effects of weir slopes on coefficient of discharge ( $C_d$ ). VOF and RNG K- $\epsilon$  models were implemented to capture the FSPs and turbulence, respectively. The results showed that after increasing the energy heads, the discharge coefficient was also found to be increased, which slightly overestimated the  $C_d$  values from the compared studies.

Valero et al. [163] developed FLOW-3D models to study the flow characteristics on smooth and stepped spillway. RNG K- $\epsilon$  and VOF models were implemented to captured turbulence and FSPs, respectively. In case of stepped spillway, results showed more turbulent flow behavior on the spillway in which turbulent kinetic energy was contained between the basin's inlet and appurtenances. The maximum velocity was found at the sloping region while maximum velocity decay was found downstream of the baffle blocks. Upon use of lower tail water levels and  $Fr_1$ , the study indicated that baffle blocks increased the total force, which stabilized the HJ.

Macián-Pérez et al. [164] developed FLOW-3D models to analyze the flow characteristics in USBR-II stilling basin. RNG K- $\epsilon$  and VOF methods modeled the turbulence and FSPs, respectively. The results showed that the modelled sequent depths were less than the Classical hydraulic jump (CHJ), and HJ efficiencies for the physical and numerical models reached to 0.516 and 0.505, respectively. The stream wise VPs showed higher values in the upper region of flow depths while effects of energy dissipation devices were visible in the VPs.

Viti and Gualtieri [165] investigated HJ characteristics with FLOW-3D RANS models, large eddy simulation (LES), and direct numerical simulation (DNS) methods. The results of the detailed review showed that RNG K- $\epsilon$  models produced more accurate results when compared with the results of published data. However, as compared to the rest of implemented turbulence models, Standard K- $\epsilon$  model produced more reliable results of free surface and lengths of HJ.

Valero et al. [166] employed FLOW-3D to study the FSPs and turbulence with the chute blocks on spillway. To capture the free surface and turbulence, VOF and RNG K- $\epsilon$  models were implemented, respectively. Four different mesh blocks were implemented to examine the flow characteristics on the sloping area and in the basin. The results indicated that entrained air was in the bottom region while air entrapment was noticed on the free surface. The study indicated that as the submergence increased, the HJ efficiency increased. Furthermore, on the lower submergence, velocity decay was found between the HJ region and wall jet.

### 2.5.1 Application of Turbulence Models

The flow over the weir's crest and on the downside is very turbulent in nature. Due to the change in gradient, HJs occur on the downstream side of graded control hydraulic structures and flow passes through certain conditions, i.e., subcritical, critical, and supercritical. In these conditions, three-dimensional turbulent currents are generated. In addition, around the basin's appurtenance and on the

scoured beds, large number of re-circulation, eddies and wake zones are developed, thereby, it is very essential to study the characteristics of turbulent flow including secondary flow patterns for the basins.

In the preceding section, a detailed review of numerical studies is performed which employed different 1-D, 2-D, and 3-D codes. In these models, RANS equations are employed to solve the turbulent flow which find closure using turbulence models. Number of turbulence models, i.e., Standard K- $\epsilon$ , RNG K- $\epsilon$  model, K- $\omega$ , RSM, K-large eddy simulation (LES), and realizable K- $\epsilon$  models are developed to examine the turbulent flow behavior downstream of open and close channels. Because of the simplicity and low computation cost, the two-equation standard K- $\epsilon$  is mostly widely used turbulence model in hydraulic applications. Similarly, RNG K- $\epsilon$  model is also known to describe the flows more accurately in strong shear regions which only differs in formulation from the standard K- $\epsilon$  model, especially for values of models' parameters. In addition, due to the less computation cost, the model is recommended to be used for strained flow. On the other hand, due to the problems of flow separation under adverse pressure gradient, the standard (Std) K- $\epsilon$  models fail to accurately measure the free surface, thereby, by adding transport effects in the eddy viscosity, K- $\omega$  models are considered to be the more accurate model for adverse pressure nears wall regions. However, for output precision, finer meshes are recommended near the wall regions which makes this model computationally un-affordable.

Numerous researchers have employed turbulence models to investigate secondary flow [167] [150], river flows [168], discharge measurement [169], air entrainment in hydraulic jump (HJ) [170], submerged HJs [171][172] and flow fields on spillway and within stilling basins [173][174][175] using different numerical codes. These studies examined different hydraulic parameters and compared the performance of the mostly widely used two equations turbulence models, i.e., Std K- $\epsilon$ , RNG K- $\epsilon$  and K- $\omega$  models. A detailed comparison of different turbulence models is provided in Table 2.1.

TABLE 2.1: Utilization of two equations turbulence models for HJ and flow fields

Reference	Focus	Study parameters	Turbulence Models			Accurateness
			Std K- $\epsilon$	RNG	K- $\omega$	
Tajnesaie et al.[167]	Secondary flow in Trapezoidal channel	Water surface, depth averaged velocity, shear stress	✓	X	✓	Std K- $\epsilon$
Rodriguez et al.[168]	Sinuuous River Reach	Depth-averaged velocity, bed velocity, free surface velocity	✓	✓	X	RNG K- $\epsilon$
Ma et al.[170]	Air entrainment in HJs	Water surface, void fraction, vortex Structure in roller	✓	X	✓	K- $\epsilon$ /k- $\omega$
Azeez and Azzubaidi[173]	Spillway under gated condition	Velocity profiles, volume fraction, discharge, pressure	X	X	✓	K- $\omega$
Heyrani et al.[169]	Flow modeling in venturi flume	Water level, velocity profile	✓	✓	✓	Std K- $\epsilon$
II and Rao[150]	Open channel flow with HJs	Stationary water depth, bottom roughness effective on HJ location	✓	✓	✓	RNG K- $\epsilon$
Behnamtalab et al.[174]	Turbulent flow in USBR Type-IV basin	Velocity profiles, turbulent dissipation, turbulent kinetic energy (TKEs),	X	✓	X	RNG K- $\epsilon$
Shekari et al.[171]	Turbulence in Submerged HJs	Water surface, velocity profiles, near bed velocity,	✓	✓	X	Std K- $\epsilon$
Moroni et al.	Dam spillway and basin	Rating curve, velocity profiles, volume fraction	✓	X	✓	Results Matched
Jesudhas et al.[172]	Symmetrical Submerged HJ	Water surface, velocity profile, TKEs	X	X	✓	K- $\omega$



### 2.5.2 Summary

Based on the literature review, it is found that researchers have employed number of turbulence models to investigate HJ and energy dissipation. However, out of the various options, two equation turbulence models are found to be efficient, and due to less computational cost, relative courser meshes, and computational time Std K- $\epsilon$ , and RNG K- $\epsilon$  models are more preferred for hydraulic simulation. However, in case of adverse pressure gradient, cavitation effects and shear boundary layer K- $\omega$  models are employed

### 2.5.3 Mesh Blocks and Cell Size Effects on CFD Models

In RANS models, the simulation domains are discretized into sub domains to solve the Navier-Stokes equations. In each sub domain, mesh cells are employed to store the required information on their nodes and center. Two different approached such as Lagrangian and Eulerian are applied in the present-day numerical codes. In term of HJ and turbulence model, Lagrangian method can produced the free surface profiles with higher accuracy because of less dependence on mesh. On the other hand, RANS models compromised the accuracy of HJ profile and to accommodate these problems, finer meshes and shorter time-steps are employed in the HJ regions. In addition, to reduce the uncertainly, many researchers have employed multiple mesh blocks of various cell sizes for HJ and around the basin's appurtenances.

Mirzaei and Tootoonchi [57] employed different meshing arrangement to study the HJ characteristics on bump using DNS, LES and RNG K- $\epsilon$  model. Upon use of DNS and LES model, as compared to RNG K- $\epsilon$  model, the results of finer meshes indicated more turbulence and small-scale eddies near the sluice gate. Similarly, in fine meshing, using DNS and LES models, the dimensionless free surface profiles from sluice gate to bump was found to be agreed with experimental data.

Macián-Pérez et al.[176] investigated HJ and energy dissipating effects of negative step by employed two different size of mesh blocks in FLOW-3D models. The

study employed a fine meshes of 0.01, 0.015, and 0.025 m on upstream of the HJ while 0.02, 0.03, and 0.05 m mesh sizes in the subcritical regions. The results indicated lesser values of sequent depths as compared to the previous which allowed for the shorter stilling basin's length. The results further indicated a decrease in the stream-wise pressure and upon use of negative step, the effects of pressure fluctuations on the HJ were also found to be reduced.

Bryant and Ng [177] investigated HJ characteristics with mesh based ANSYS FLUENT models and compared the results with Lagrangian moving grid methods. The study employed two different mesh blocks in which the finer mesh grid was set near the HJ region which ranged from 0 to 2 m. However, after the HJ, a relatively, coarse mesh grid was employed to study the velocity profiles and other flow fields i.e., turbulent kinetic energy and dissipation. The results showed that in the HJ region, as compared to RANS model, i.e., RNG K- $\epsilon$  and SST K- $\omega$ , the Lagrangian standard K- $\epsilon$  model overestimated the free surface profiles and overall water depth. However, near the sluice gate, the Lagrangian model captured the turbulence better than Eulerian models.

Numerous numerical models have been developed to the HJ and energy dissipation downstream of graded control structures using different mesh blocks and cell size. These studies have developed scales models of the prototype and tested them in the laboratory. Due to the less dimension of these scaled models, finer meshes are employed in the interest region, i.e., flow measurements using venturi meter [178], nappe impingement jet on spillway [179], submerged and classical HJs downstream on the spillway basins [99][160], flow field over spillway[111], river morphology [180] and scouring [181]. However, a few of the models investigated HJ and energy dissipation using full-scale of prototype structure such as energy dissipators for spillways geometries [52][182][183]. The Table ?? highlights a few of the most relevant reduced and full scaled models' studies which employed different mesh blocks and cell sizes.

TABLE 2.2: Different mesh blocks and cell sizes employed in numerical models for HJ and energy dissipators

Reference	Study Focus	Models Detail		Mesh Block	Mesh Size (m)
		Reduced Scale	Full Scale		
Pourshahbaz et al. [180]	River morphology around groynes	✓	X	Two	0.012, 0.025
Welahettige et al.[178]	Flow in venturi meter	✓	X	One	0.003, 0.020
Castillo et al.[179]	Nappe impingement jet on spillway	✓	X	One	0.01
Mukha et al. [184]	Classical HJ	✓	X	One	0.001
Chanel and Doering [183]	Spillway modeling	X	✓	Two	0.5, 1
Moroni et al.[175]	Dam spillway and stilling basin	✓	X	One	0.005, 0.02
Bayon-Barrachina et al.[99]	Spillway HJ	✓	X	One	0.124, 0.12, 0.10
Zhou and Wang[160]	Spillway HJ and stilling basins	✓	X	Three	0.20, 0.25, 0.30
Soori et al.[52]	Energy dissipators for Spillway basin	X	✓	one	3
Rovesht et al.[182]	Spillway geometry and energy dissipators	X	✓	Two	0.2, 0.4
Le et al.[181]	Scour downstream of box culvert	✓	X	Two	0.01, 0.015, 0.02
Macián-Pérez et al.[176]	HJ and energy dissipation	✓	X	Two	0.136, 0.18
Simşek et al.[185]	B-Type HJ and energy dissipators	✓	X	Multi-blocks	0.00016, .0007
Valero et al.[163]	HJ and energy dissipators under adverse TWD	✓	X	Two	0.012
Kumcu [111]	Flow field over spillway	✓	X	Two	0.50, 0.25
Present study	Energy dissipation using different baffle blocks and scour modeling	X	✓	Three	0.125, 0.25

## 2.5.4 Comparison of Numerical Models

Selecting the most reliable numerical model is not an easy task, as criterion are always found to be case dependent. There are many numerical models available in the market which are employed in hydraulic and scour modelling, i.e., FLOW-3D, Open FOAM, IBER, HEC-RAS, Fluent CFD, and River-2D etc. At present, a brief comparison among the different numerical models is made, and based on the results and models limitations, the suitability of the different models is assessed. Table 2.3 compares various numerical model which conducted investigations for open channel flow. Further selection criteria using strongly desired features can be in seen in Chapter 3, section 3.4.

Vasquez et al. [4] reported that FLOW-3D models predicted better results of the Free surface profile, Vertical velocity profiles, solid fluid interaction and water profile over triangular sill. The study further reported that due to the problem lies in ground model of River-2D model, the results of flow depths were not capturing accurately while using real time topographic data, FLOW-3D results were found to promising within the limited computational cost. Similarly, Vargas at al. [186] employed HEC-RAS, IBER, and FLOW-3D numerical models to the flow dynamics in the meandering river and studied Channel Bank erosion, secondary currents, Velocity distribution, flow depths, and velocity profiles. The results indicated that as compared to IBER and HEC-RAS models, FLOW-3D results of the investigated parameters were found to be agreed with the experimental and field data. The study further stated that IBER and HEC-RAS model were limited in the computation of flow depths and velocity distribution. Shademan et al. [187] evaluated the performance of OpenFOAM software for the complex geometries, i.e., flow over the bluff bodies. The study investigated Velocity distribution, pressure, and mass flow rates near the bluff bodies. The results indicated the Open FOAM successfully captured all the investigated parameters for the complex geometries. The study further stated to employed the Open FOAM code using LES turbulence model, as the other RANS models were limited to capture the wake zone and vortex shedding using LES model.

In contrast, Rajaa et al. [188] employed Fluent-2D and FLOW-3D numerical models to investigate velocity profiles, free surface profiles; pressure and the turbulent kinetic energy over and downstream of over spillway. The results indicated that both the models predicted the hydraulic parameters in a good agreement to the experimental data. However, as compared Fluent-2D, the results of pressure profile were found to good in FLOW-3D models. The study further highlighted due to limitation of uniform mesh cell size, the computational cost in Fluent-2D model was found much higher than FLOW-3D models. Bayon et al. [103] compared Open FOAM and FLOW-3D soft wares to investigate characteristics of HJ of low Reynolds number. The study mainly investigated Sequent depths, roller length, mean velocity, HJ location, and free surface profiles. The results indicated that both the models predicted good results which showed agreement with the experimental data. However, the results of hydraulic parameters in supercritical and subcritical, i.e., sequent depth were found to promising in FLOW-3D model, while for the roller lengths and velocity profiles, Open FOAM results agreed well with the compared data. In addition, the results of velocity decay in stilling basin was well predicted by the FLOW-3D.

### 2.5.5 Summary

From the literature, it is found that due to the limitation of groundwater model, River-2D is unable to capture free surface profile, vertical velocity profiles, and solid fluid interaction at high flood discharges. Similarly, as IBER and HEC-RAS models are limited in flow depth computation, these models can not produce good result for HJ and its associated parameters. On the contrary, because of the limitation in uniform grid development, the computational cost of Fluent-2D is very high. On the other hand, the results of FLOW-3D and Open FOAM are found to be promising in HJ and flow investigations, however, due to advantage of uniform mesh size and FAVOR method, FLOW-3D is widely used for investigation of hydraulic structures which have simple geometries.

TABLE 2.3: Comparison of numerical model for hydraulic investigation

<b>Authors</b>	<b>Study Focus</b>	<b>Numerical Model</b>	<b>Parameters investigated</b>	<b>Model Accuracy</b>
Vasquez et al. [4]	Dam beak waves	River-2D, FLOW-3D	Free surface profile, vertical velocity profiles, solid fluid interaction, water profile over triangular sill	FLOW-3D
Vargase et al. [186]	Meandering rivers	HEC-RAS, IBER, FLOW-3D	Channel Bank erosion, secondary currents , elocity distribution , flow depths, velocity profiles	FLOW-3D
Shademan et al. [187]	Flow bluff bodies	Open FOAM	Velocity distribution, pressure, mass flow rates, Flow over Bluff Bodies	OpenFOAM in complex geometries
Rajaa et al. [188]	Flow over ogee spillway	Fluent-2D, FLOW-3D	Velocity, free surface profiles, pressure, turbulent kinetic energy	FLOW-3D
Bayon et al. [103]	HJ in horizontal bed Channel	Open FOAM, FLOW-3D	Sequent depths, roller length, mean velocity, HJ location, free surface profiles	Both

## 2.6 Sediment Scour Models

Scouring is the process of sediments removal from downstream end of graded control structures such as weir, barrage and spillways [48], [69]. Therefore, kinetic energy of flowing water over these structures must be dissipated within the stilling basins to prevent excessive bed degradation. Ample protection measures i.e., such as location of hydraulic jump; energy dissipators, and downstream tail water depths are required to limit the size and location of scour. The scouring process starts from downstream end of stilling basin when bed shear stresses increase beyond the critical limits. Due to the significant values of hydraulic structure, prediction of scour in open channel is a challenging research field [189] for which many experimental and numerical investigations have carried downstream of open channel flow, culvert, and around the bridge piers. Before, highlighting the studies, a brief description on the sediment scour models is presented below.

Sediment scour or local scouring is usually governed by three dimensional characteristics of packed and suspended particles [190]. The packed sediment bed does not move as they are bounded by the surrounding particles and due to the zero permeability, the fluid flow on these beds stops. Due to the local pressure gradient, as the bed shear stress by the flowing fluid increases from the critical shear stress, the sediment bed starts eroded and particles begin to be suspended. Such motion is governed by drifting models, in which the particle advects and drifts in the modeling domain [191]. On the other hand, at the interface on fluid and packed bed, as sediment bed starts eroded and begins to be suspended which motion is called lifting of the sediment.

In the sediment scour models, the rate of erosion mainly depends on fluid shear stress, critical shear stress, sediment and fluid densities and mean diameter. In CFD models, the shear stress on the beds is usually computed by critical shield number (CSN) which defines the amount of shear stress required to lift a sediment particle from the packed bed [192], and for the present study, further details are given in Chapter 3, section 3.12. Another the important aspect of sediment models is to define the maximum packing fraction in all sediments cells which effects and

viscosity and densities. The sediment bed fraction is the ratio of volume occupied by the sediment to the total volume, i.e., sum of sediment in suspension and remaining packed concentration is divided by density of that sediment ( $\rho$ ) [193]. In numerical model, the solid and liquid fraction should be equal to unity as presented by expression (2.3);

$$f_s + f_f = 1 \quad (2.3)$$

In addition, in the scouring phenomena, the processes of entertainment and settling of particles occur simultaneously. This process define the overall rate of packed and suspended sediments. In the entertainment, the lift velocity is required to move the sediment particle from the packed bed [194]. In contrast, when the velocity of suspended load particles decrease, the particles start settling down on the sediment bed. According to bed load transport rate equations, different values of entertainment coefficients are utilized in CFD models.

On the critical parameter of scouring is the angle of repose which affects the lifting velocity [195]. As the natural riverbeds are not flat, thereby, in CFD models, user can also define a number of angles for different species according to particular problem under investigation.

Balachandar et al. [196] investigated the effects of TWD on the dynamic of local scour downstream of sluice gate. The study reported that even after 96 hrs, asymptotic bed profiles were not attained on the investigated conditions. During digging phase, the results of stream-wise and transverse velocity components indicated that flow moved towards the bed, while, in the refilling process, it was reflected toward the free surface.

Mohammed et al. [53] investigate local scour for different curvature of end sill downstream of spillway. End sills of different angles such as  $10^0$ ,  $20^0$ ,  $30^0$ ,  $45^0$ , and  $60^0$  were experimented in the spillway models. After changing the angle from  $10^0$  to  $60^0$ , results showed 18% decrease in scour. The results further showed that when the flow was increased up to 320%, bed was completely exposed within 13 min and 5.25 minutes for models with end sill's angle of  $60^0$  and  $10^0$ , respectively.



Wüthrich et al. [197] conducted experiments to investigate the local scour after placing randomly distributed concrete prisms in the plunge pool of Chancy-Pougny barrage. The results indicated flow re-circulation and eddies due to the asymmetry of plunge pool which was controlled by vertical wall. The results showed that prism concrete blocks dissipated energy which further reduced local scour downstream of the studied barrage.

Güven [40] developed multi-output descriptive neural network (DNN) to study the local scour below the hydraulic structures. Scour depth and location were the main investigated parameters. For scour depth, DNN produced better results compared to the published equations which showed  $AIC = -61.921$ ,  $MAE = 0.341$ ,  $MSE = 0.030$  and  $R^2 = 0.819$ . Similarly, DNN also produced better results in terms of location of scour ( $X_m$ ) for which values of different performance indicators such as MAE, MSE,  $R^2$ , and AIC reached to 0.109, 0.364, 0.907 and -9.232, respectively.

Elsayed et al. [198] investigated local scour by employing multi-gate operation downstream of hydraulic structure. The results showed that gate opening affected the flow pattern and due to that different scour patterns were noticed. The results further showed that as Froude number and tail water increased maximum scour depth and length were also increased. Similarly, as the upstream water head increased, the maximum scour depth and maximum scour length was also increased. In case of the operation of side gate, the results showed high value of maximum scour depth while in all gates operation the values were found to be less.

Amin [48] investigated local scour downstream of Fayoum type weir. A sand bed with mean diameter  $d_{50}=0.70$ -mm was laid on downstream. The results showed that upon increase of flow, the relative scour depth and length were reduced while on decrease of Froude number, relative scour depth and length were also decreased. The results further showed that at relative jet position ( $L_j/L_f$ ) of 0.7 and relative jet discharge ( $Q_j/Q$ ) of 0.15, the net scour depth and length was reduced up to 68% and 76%, respectively.

Scour models were developed to investigate the local scour downstream of the box culvert using FLOW-3D software [199]. Because of the meandering effects, results

indicated local scour on concave-side and sand deposition on the convex-side. The results further indicated that the higher value of bed roughness/ $d_{50}$  ratio produced deeper and larger bed deformation.

Local scour around the three tandem piles was studied using FLOW-3D numerical models [200]. The results indicated that local scour was affected due to down flow horseshoe vortex, which was driven by downstream pressure gradient, high bed shear stress, flow circulations in front of piles and flow acceleration. The results further indicated that the maximum scour was near the first tandem pile.

Daneshfaraz et al. [201] employed FLOW-3D scour models around the circular piles. The results showed that in comparison to the front piles, the highest scour was found near the downstream piles. To minimize scour effect of harvesting material, the study altered the shape of front piles, and then results showed 29% decline in the scour depth. Due to the inclusion of new shaped piles, the results also showed decline in the velocity magnitude around the other piles.

Taha et al. [202] employed FLOW-3D scour models to study the local scour downstream of blocked culvert. The results showed that 70% of the blockage in the culvert increased water depth and flow velocity to 2.3 and 3 times, respectively. However, small effects on scour downstream of culvert were also observed for which the models developed scour equations.

Shamohamadi and Mehboudi [203] developed FLOW-3D scour models to study influencing parameters of scour for confluence channels. It was found that the ratio of discharge of main to secondary channels, and ratio of width of main to secondary channel width were causing the local scour. The results further showed that upon increasing the ratio of discharge of main to secondary channels, the scour also found to be increased in the main channel, while increase in ratio of width of main to secondary channels width developed the scour hole in the secondary channels.

### 2.6.1 Summary

From the literature review, it is found that apart from examining the HJs and flow characteristics on rigid bed, the study of local scour downstream of these structures is also very crucial for the assessment of stilling basin's design. On the other hand, bibliographical analysis showed that in the plane area of Pakistan, based on physical model studies on rigid bed, the stilling basins of diversion barrages are remodelled. These studies didn't apply erodible bed on the downstream. However, scouring downstream of any hydraulic structure is an important research area to investigate the performance of any stilling basin. Therefore, to draw comparison between the different stilling basins of barrage, scour investigation is presently focused for the uncontrolled designed flow conditions.

## 2.7 Overall Summary

In Pakistan, barrages are essential for irrigation and power generation but many of them are suffered because of ageing, hydraulic, structural and retrogression issues which have endangered their overall stability [43]. Taunsa barrage is an important diversion barrage which was built on Indus River for the discharge capacity of 28,313 m<sup>3</sup>/s. The barrage's basin was modified form of USBR Type-III basin which consists of two staggered rows of baffle and friction blocks. After the completion of barrage in 1958, many problems appeared in the barrage's basin such as uprooting of baffle blocks and retrogression. After many repairs till 2004, from years 2005 to 2008 the energy dissipating system within the basin of Taunsa barrage was changed in which chute blocks and end sill were placed at the downstream glacis and at the basin's end, respectively. From the literature review, it is found that only few studies [76], 44, [45], [77] have investigated the the basins' of Taunsa Barrage which mainly focused the influences of tail water levels on the locations of HJs. Additionally, the probing data from years 2010 to 2014 also indicated that even after the remodelling of barrage's basin, in front of many bays, the blocks floor, flexible apron and inverted filter blocks are washed away. However, the

past studies are lacking to provide the justification of damages occurred after the remodelling and did not investigate important hydraulic parameters such as roller lengths of HJ, velocity distribution in the basin, free surface profile of HJ, sequent depths, energy loss in the HJ and TKEs in two different basins of the studied barrage.

On the contrary, the use of WSBB downstream of the river diversion barrage was found limited in the literature. Therefore, the aim of the present study is to investigate various hydraulic parameters in different basins' of Tuansa barrage for three different discharges using FLOW-3D numerical models. The study also investigated WSBB with different setup downstream of the studied barrage. The present study also developed FLOW-3D scour models to investigate the performance of different shapes of stilling basin's appurtenances i.e., USBR baffle block basin, remodelled basin with chute blocks and end sill, WSBB basin, and composite basin using WSBB and USBR baffle block. Based on the results of maximum energy dissipation, appropriate baffle blocks shape and configuration are determined for diversion barrage i.e., Taunsa barrage.

# Chapter 3

## Study Area & Methodology

### 3.1 Background

The methodology has three phases in which first phase identifies the critical hydraulic parameters from the literature and selects 3-D numerical codes. In second phase, the identified critical parameters are numerically investigated downstream of Taunsa barrage for different stilling basin using the selected numerical code. In the third phase, the study compares the performance of different stilling basins, i.e., Modified USBR stilling basin (Type (A)), chute blocks and end sill stilling basin (Type (B)), Wedge-shaped baffle block stilling basin (Type (C)), and composite baffle block stilling basin (Type (D)). After hydraulic analysis, the study further performed scour analysis to investigate the performance of above mentioned stilling basins. The general flow chart of the research is presented in Fig. [3.1](#).

### 3.2 Study Area

Taunsa Barrage is an important diversion structure which is located across the River Indus to supply arid zone of Southern Punjab. The barrage is about 18 Kilometers away from Kot Addu Town, a Tehsil of District Muzaffargarh. The

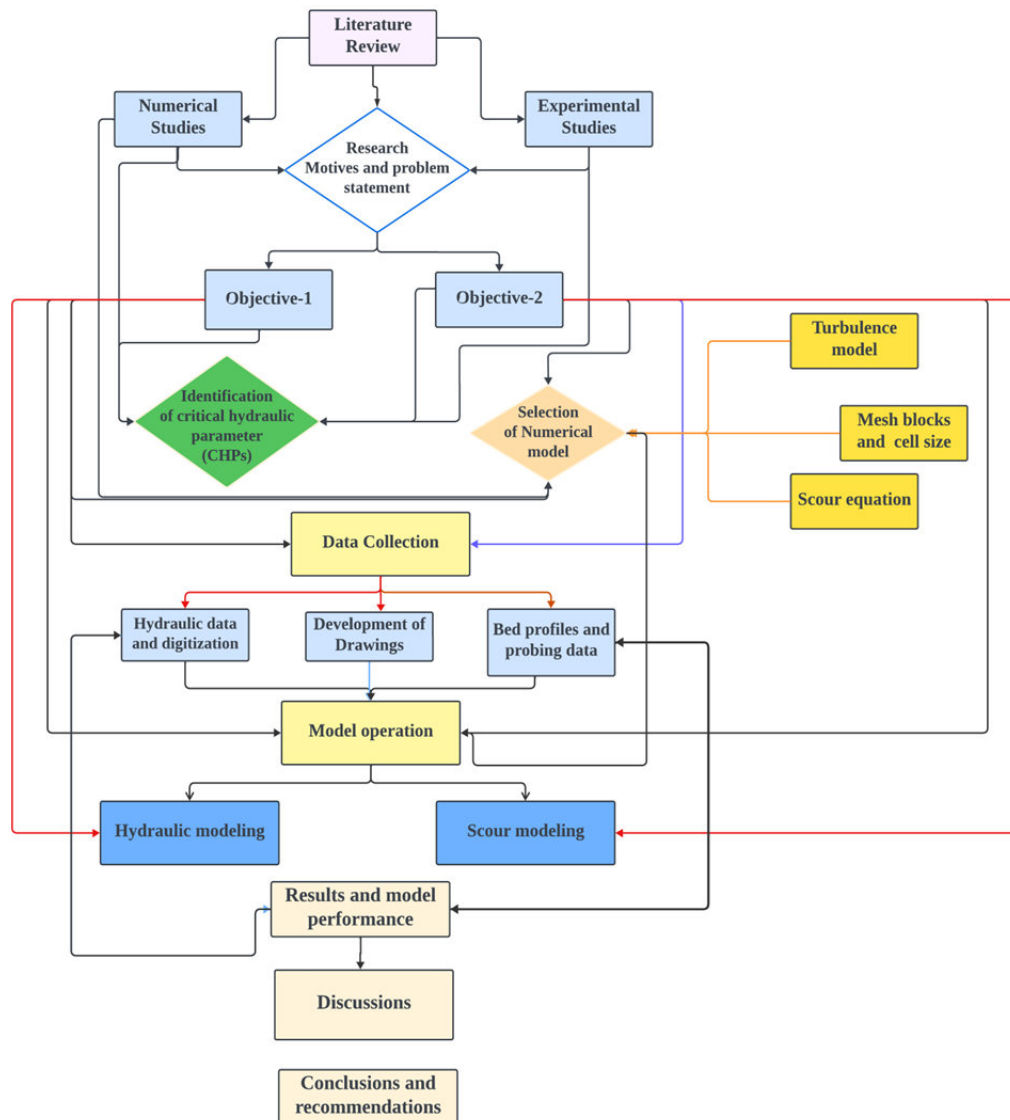


FIGURE 3.1: Flow Chart of Research Methodology

barrage's name was emanated from a Town "Taunsa Sharif," which is situated 30 km upstream of right bank of the River Indus [75] [43]. The location of Taunsa Barrage is show in Fig. 3.2 below.

The story of Taunsa barrage was started back in 1936 by Mr. J.D. Bed ford, who had initiated irrigation scheme for the area of Districts D.G. Khan and Muzaf-fargarh. At that time, many inundation canals operated in these districts from River Indus but the supplies from these canals were indecisive, especially during the sowing and maturing times.

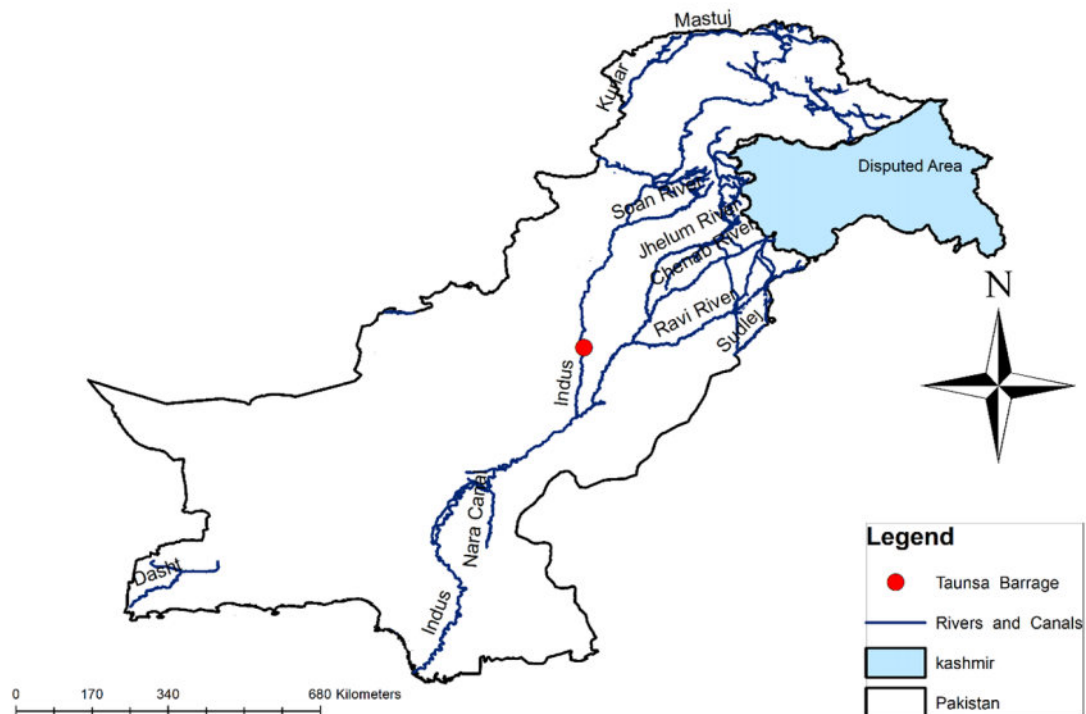


FIGURE 3.2: Location map of study area

Therefore, regulation of these canals was to be made by weir control structures. In 1943, a new "Project Circle" was opened in the Punjab Irrigation Department (PID), which carried out the preparation works of taunsa barrage project. The Project was started in 1953 and barrage was completed in 1958 [76].

The barrage is more than a traditional diversion structure because it also accommodates transportation energy infrastructure, i.e., railroad crossing, an oil pipeline, gas pipeline, transmission lines, and serves as an arterial road bridge.

Furthermore, the barrage also supplies uninterrupted flows to four canals that take off from its upstream, i.e., Muzaffargarh (command area (2)), TP-Link, DG Khan (Command area (1) and (3)), and Kachhi canal. Taunsa Punjnad (TP) Link canal (command area (4)) supplies water to the Chenab River to meet irrigation requirement of command area (5) of the Panjnad Barrage. The general layout of the barrage irrigation system is shown in Fig. 3.3.

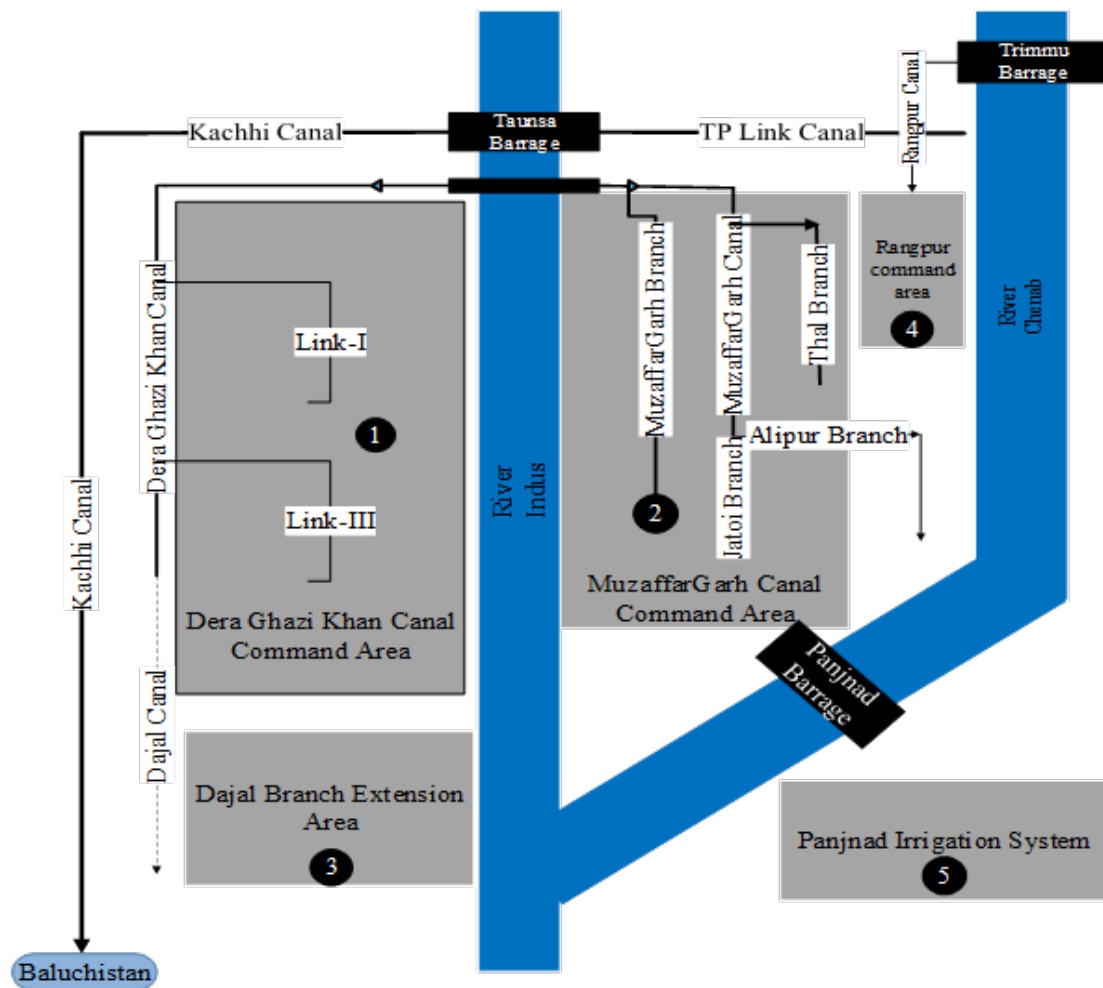


FIGURE 3.3: Taunsa barrage irrigation system

Rules and Regulations for Maintenance and Working of Taunsa barrage (1979) report that  $28313 \text{ m}^3/\text{s}$  is the maximum design discharge of the barrage [74]. The below Table 3.1 shows salient features of the the barrage originally, a 38.10 m long stilling basin was designed to dissipate excessive kinetic energy of the upstream flows. Energy dissipators/appurtenances were also installed in the basin to dissipate the surplus energy from the HJ.

The two rows of baffle blocks were also installed about 3 m from the two of the downstream glacis while two rows of friction blocks are placed at the basin's end. Such devices were provided to increase the turbulence and also stabilize the HJs in case of less tail water levels [76],[77], [45], [44]. The fall height was fixed to 3.66 m. Fig. 3.4 shows longitudinal cross-section of the barrage.



TABLE 3.1: Salient Features of Taunsa Barrage

Sr. No.	Description	Design values	Sr. No.	Description	Design Value
1	Maximum design discharge capacity	28313 m <sup>3</sup> /s	8	Crest width	1.83 m
2	Total width between abutments	1324.60 m	9	Crest level	130.44 m
3	Water way	1177.08 m	10	Upstream floor level	128.31 m
4	Maximum upstream pond level	136.24 m	11	Downstream floor level	126.79 m
5	Maximum downstream tail water level	135.32 m	12	Maximum design head of gates	6.86 m
6	Normal pond level	135.93 m	13	Gate Width	18.29 m
7	No. of bays	64	14	One Bay Width	18.29 m

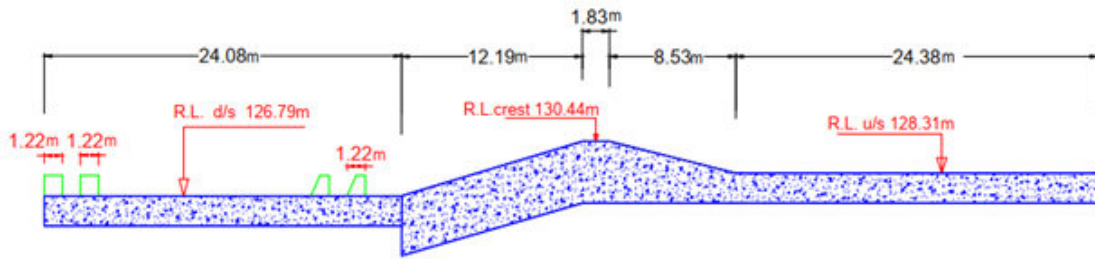


FIGURE 3.4: Longitudinal cross section of Taunsa barrage (Study area)

### 3.2.1 Taunsa Barrage and the Hydraulic Concerns

Barrages in the Indus Basin are built about 50 to 100 years ago. Due to the change in river hydrology, river bed downstream of these hydraulic structure are usually eroded which generates stability issues.

Apart from the erosion, “piping” also causes soil loss from the foundation which speed up the bed erosion on the downstream. Soon after the barrage completion in 1958, the barrage’s basin faced many problem i.e., riverbed retrogression, and damage to the basin’s floor. To cater the above mentioned problems, during 1959-1962, repairs works were carried out for stilling basin of Taunsa barrage but problems remained unresolved and the issue continued to aggravate.

The Government of Pakistan engaged the consultant firm to review the hydraulic and structural integrity of six existing barrages which were built between 1890 and 1958. After feasibility study, the consultants reported to rehabilitate the barrage and some major works were recommended to prevent the sudden collapse of entire structure.



FIGURE 3.5: Dismantling of Baffle blocks [43]



FIGURE 3.6: Existing appurtenances of barrage [43]

Based on the criteria mentioned above, Taunsa Barrage was put in the first place to be rehabilitated. Based on the barrage history, it was clear that the barrage was suffering from erosion problems on its downstream and can be failed in case of high floods [75], [73].

After The World Bank willingness to fund the Project, during the year 2004, the the feasibility study for Taunsa Barrage Emergency Rehabilitation and Modernization Project was completed. Consequently, the remodelling of barrage's stilling basin was completed from June 2005 to December 2008 [75].

In the rehabilitation, old stilling basin's appurtenance were changed with chute blocks and end sill as shown in Fig. 3.5 and 3.6.

Soon after the remodelling, during super-flood of 2010, the probing data showed that the inverted filter blocks floor in-front of some of the bays moved away from its original location and the flexible apron was also found to be sinking downstream of the stilling basin [140], [44], [77].

### 3.3 Identification of Critical Hydraulic Parameters (CHPs)

A systematic review of previous studies was carried out and all those articles were retrieved which addressed hydraulic parameters on the downstream of hydraulic structures such as spillway, barrage, sluice gate, weirs, and falls. The retrieved articles were divided into two categories i.e, experimental and numerical studies. By doing so, eighty (80) research articles were retrieved and after detailed analysis, 42 experimental and 24 numerical articles were further analysed to identify the CHPs.

Tables 3.2 and 3.3 show the sources of experimental and numerical studies, respectively. The statistical methods used for the identification of parameters are explained below. For parameter ranking, Relative percentage score of the parameters was carried out by Eq. (3.1). [204], [205], [206].

$$PercentScore = R_f \times RPA \quad (3.1)$$

where  $R_f$  is relative frequency of a parameter, and RPA is Relative Portion of the Party Affected. In the present investigation, experimental and numerical articles were taken as parties.

TABLE 3.2: Hydraulic parameters from the experimental studies and their sources

Sr. No.	Hydraulic Parameters	Relevant studies
1	Velocity profile (VP)	[207][196][109][198][208][148][95][209][119][189][210][105][87][211][122][112][124][45][125][146][44][212][86][213]
2	Froude Number (Fr)	[207][122][86][214][82][211][215][140][216][64][189][67][124][83][217][45][117][137][119][105][210][213]
3	Tail water (TWL)	[196][105][189][210][122][140][123][218][80][83][45][212][57][137][138][148][104][105][209][76]
4	Stilling basin shape (SS)	[86][138][107][83][112][64][82][123][67][215][76][104][105][209][44][218]
5	Surface profile (FSP)	[207][210][117][138][219][83][95][209][189][122][125][126][45][140][218][212][86][109][146][80]
6	Bed Profile (BP)	[210][105][117][138][216][126][189][219][83][45][122][125][86][197]
7	Scour profile (SP)	[208][196][83][69][210][189][209][80][214][212][110][66]
8	Energy dissipation (ED)	[123][122][86][125][146][216][211][214][218]
9	Turbulent energy (TKE)	[146][123][122][86][125][105]
10	Pressure profile (PP)	[210][95][209][80][86][146]
11	Bed Shear Stress (BSS)	[208][117][213][217][68][105][44]
12	Reynolds stress (RSS)	[217][119][124][209][44]
f13	Turbulent intensity (TI)	[217][119][124][209][44]
14	Submergence (SM)	[140][67][64][189]
15	Retgression (RG)	[105][107][140]
16	HJ efficiency ( $\eta$ )	[122][125][87]
17	Momentum flux (MF)	[117][137]
18	Volume flux (VF)	[117][137]
19	Length of HJ (LHJ)	[207][112][212][80]
20	Turbulent production (TP)	[125]
21	Power spectra (PS)	[119]
22	Sequent depth ( $y_2/y_1$ )	[109][148]
23	Energy loss ( $\Delta E/E_1$ )	[122]

TABLE 3.3: Hydraulic parameters from the numerical studies and their sources

Sr. No.	Hydraulic Parameters	Articles Cited
1	Velocity profile (VP)	[99][86][220][157][156][221][107][97][57][164][158][148][65][222][161][121]
2	Surface profile (FSP)	[220][86][99][222][65][97][158][164][161][221][52][156][107][95][147]
3	Pressure profile (PP)	[99][86][164][147][158][103][104][105][148][222][52]
4	Turbulent energy (TKE)	[99][156][97][121][220][157][221][222]
5	Air volume value (AV)	[99][86][156][97][164][147][221]
6	Discharge measurement(DM)	[104] [86][105][222][65][52]
7	Stilling basin shape (SS)	[219][119][220][104]
8	Froude Number (Fr)	[221][107][57][158][97][86]
9	HJ efficiency ( $\eta$ )	[86][164][103][148][222]
10	Reynolds stress (RSS)	[99][121][158]
11	Tail water (TWL)	[105]
12	Contraction coefficient (CC)	[157]
13	Head loss (HL)	[157]
14	Frictional forces (FF)	[157]
15	Momentum coefficient (MC)	[157]
16	Energy coefficient (EC)	[220]
17	Discharge coefficient (DC)	[220]
18	Wall shear stress (WSS)	[148][99]
19	Sequent depth ( $y_2/y_1$ )	[158][161][148][99]
20	Length of HJ (LHJ)	[158][161][148]
21	Scour profile (SP)	[158]
22	Bed profile (BP)	[97]
23	Energy dissipation (ED)	[220]
24	Bed shear stress (BSS)	[220] [148]

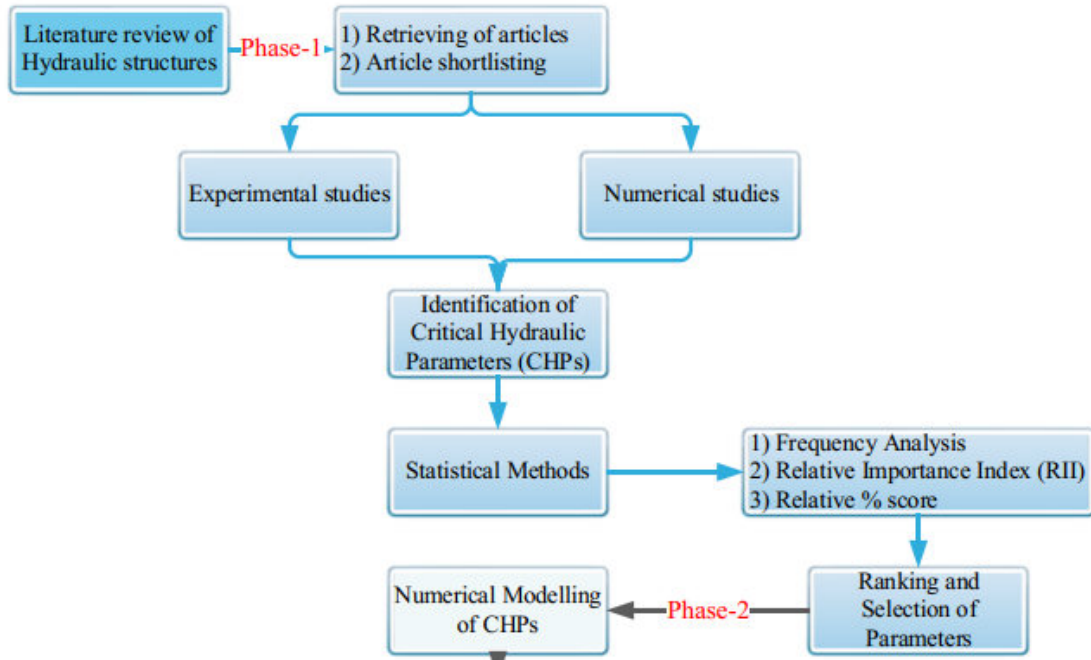


FIGURE 3.7: Process for identification of CHPs

To find relative importance of the parameters, Relative Importance Index (RII) (Muneeswaran et al.[223]; Gündüz e al. [224]; Ahmad et al. [225]; Siddique et al. [226]) was applied which was calculated by Eq. (3.2):

$$RII = \sum_{(i=0)}^n (W_i)/(A_x N) \quad (3.2)$$

where, RII = Relative importance index;  $W_i$  = Weight given to each parameter by research; A= Highest weight and N = Total number of researches. The RII value ranges from 0 to 1. Any of the identified parameters whose values approaches to 1 was considered as the critical parameters.

### 3.4 Selection of CFD Software

Based on the objectives defined, the list of strongly desired features from various CFD software were studied and divided into various groups i.e., modelling capabilities, pre and post processing capacities, the solver, user friendliness and

support. On the basis of literature review, five different software were selected for comparison. Table 3.4 the strongly desired features of the different CFD codes.

TABLE 3.4: List of strongly desired feature for selection of CFD software

FEATURE	Open FOAM	FLOW-3D	FLUENT CFD	PHOENICS	STAR-CD
Discretization technique	FVM	FVM	FVM	FVM	FVM
Mesh type	STR	STR	STR	STR	UNS
2D and 3D	Yes	Yes	Yes	Yes	Yes
Friendly interface	No	Yes	No	Yes	Yes
Body-fitted coordinates	Yes	Yes	Yes	Yes	N/A
Turbulence models	Yes	Yes	Yes	Yes	Yes
Multi- phase/ species	Yes	Yes	Yes	Yes	Yes
Access to Fortran user- routines	Yes	Yes	Yes	Yes	Yes

From Table 3.4, four leading software were selected for further analysis and detailed comparison was performed as shown in Table-1 of Annex-3A.

### 3.5 Numerical Modeling Technique

In second phase of the research, CHPs were numerically investigated using FLOW-3D models. Before, implementing the models, data related for the FLOW-3D models were studied, and suitable methods & techniques were selected, as described in the proceeding paragraphs. The detailed process for the numerical models is shown in the flow chart (Fig. 3.8).

All environmental flows are governed by physics laws such as law of conversation of mass, momentum, and energy. However, for the open-channel flows, mass and

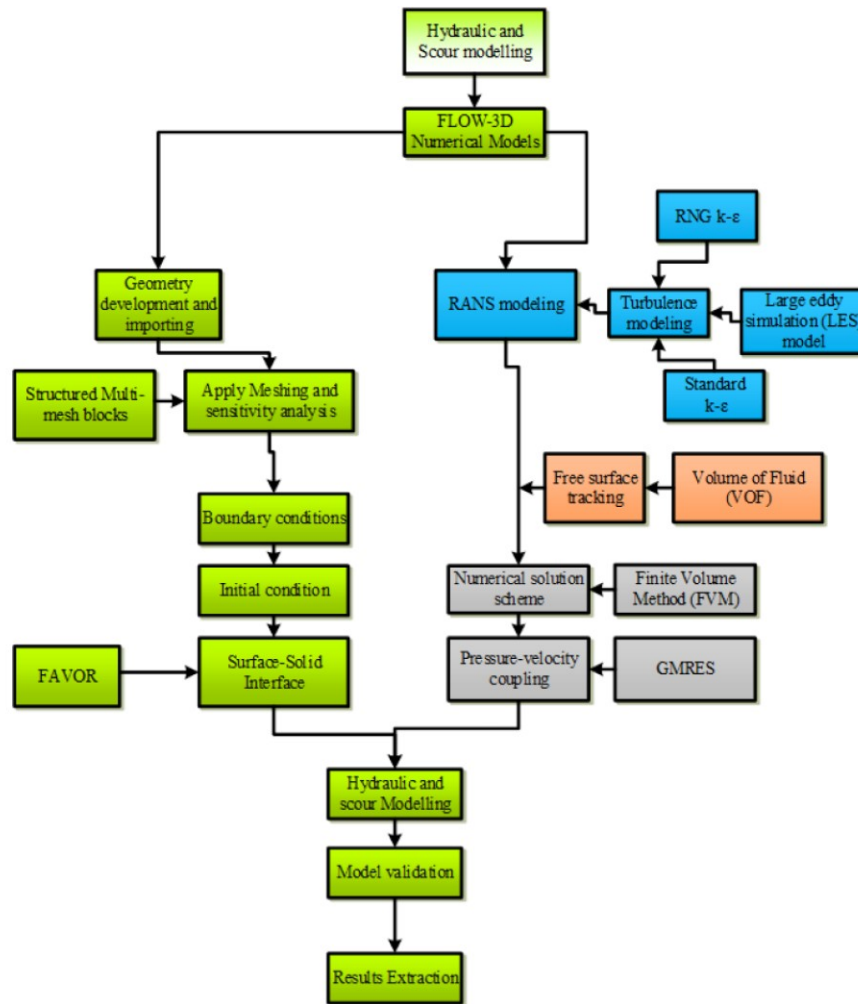


FIGURE 3.8: Detailed methodology for hydraulic and scour modelling

momentum equation are more dominating. For these flows, Navier Stokes equation (NSEs) is termed as the momentum equation [165]. These equations are partial differential schemes and can be solved analytically for one and two-dimensional flows. However, in case of three-dimensional flows, NSEs do not concede with analytical methods and need numerical techniques to accumulate their solutions.

With the advent of high computer technologies and evolving algorithms, Computation Fluid Dynamic (CFD) and numerical modelling techniques are beneficial for stimulation of the above-mentioned fluid complexities [227] [228]. CFD is the branch of numerical modelling which solves the problems of flow physics [228] [92]. In the CFD modelling, flow equations i.e., NSEs and continuity equation are discretized in each cell. Generally, these models start with a mesh which further contain multiple interconnected cells in the employed mesh blocks. These meshes



subdivide the physical space into small volumes which are associated with several nodes. The values of unknown parameters are stored on these nodes, such as velocity, temperature, and pressure. In CFD modelling, before the outputs, the particular models are calibrated with most reliable parameters, however, the calibrating parameters are usually case-dependent and varies as per the investigation. Different numerical techniques are used to discretize the Naiver Stokes equations, as discussed below.

### 3.5.1 Direct Numerical Simulation (DNS)

The continuity and Naiver-Stokes equations (NSEs) have four unknowns, i.e.,  $p$ ,  $u$ ,  $v$ , and  $w$ . The DNS technique uses these equations to solve the unknown directly without using the turbulence models [33]. DNS provides a more accurate turbulence structure and calculates mean flow velocity and turbulent intensity from the smallest to the largest scale on the spatial grid, but computational costs involved in this technique are completely un-affordable [33] [99]. DNS technique works only for the low Reynolds Number and requires sufficiently fine meshes to resolve the Kolmogorov micro scales and a much smaller time-step to resolve the fastest fluctuations. DNS method requires the most powerful high-performance computers to calculate high Reynolds numbers, which further escalates the cost. Therefore this method is often avoided in river and hydraulic engineering [160].

### 3.5.2 Large Eddy Simulation (LES)

Despite efforts of researchers over the last three decades, no specific turbulence model has been developed which can develop the turbulence flow features for all the hydraulic investigations. The primary reason behind the above-mentioned issue is the difference in the behavior of small and large-scaled eddies in which the small eddies usually are isotropic. However, the large-scale eddies are found as an isotropic. In the large eddy simulation (LES) method, the small and large eddies are separated by the filter that applies cutoff width in which large eddies

are calculated directly as carried out in DNS [229], [230]. Implementing LES in river engineering for high Reynolds numbers requires fine meshing near the wall and thin boundary because the flow domain has to be divided into sub-grid to apply filtering function for the core and near-wall flow to calculate for large and small eddies [231]. As compared to other modeling technique, LES produces a more reliable prediction of problems, especially in strong shear, separation, and vortex regions. However, due to the high computational cost, LES models are not used readily.

### 3.5.3 Reynolds-Averaged Naiver-Stokes Equations (RANS)

These days, Reynolds-Averaged Naiver-Stokes Equations (RANS) is the most widely used technique to solve the NSEs, continuity and momentum equations, which also simulates the turbulent flows. After adding averaged and fluctuating values, RANS method also solves instantaneous velocity and pressure [164], [152]. As compared to other models, these models also offer less computational cost and employ less time for flow resolution. Upon use of RANS models, two additional variables are generated for which turbulence closure models are usually employed [100]. In the present numerical model, RANS models are implemented using FLOW-3D. The equations (3.3) is the momentum equation.

$$(V_F \rho) / \partial t + \frac{\partial}{\partial x}(\rho u A_x) + R \frac{\partial}{\partial y}(\rho v A_y) + \frac{\partial}{\partial z}(\rho w A_z) + \xi \rho u A_x / x = R_{sor} + R_{DIF} \quad (3.3)$$

where  $V_F$  is partial volume of flow,  $\rho$  is the fluid density,  $R_{SOR}$  is the mass source, and  $R_{DIF}$  is diffusion term of turbulence. In case of Cartesian coordinates, R is equal to unity and  $\xi$  is set as zero. For in compressible flow simulation, using constant value of density ( $\rho$ ), the above equation is transformed for turbulent flow as shown in Eq. (3.4).

$$\frac{\partial}{\partial x}(u A_x) + R \frac{\partial}{\partial y}(v A_y) + \frac{\partial}{\partial z}(w A_z) + \xi \frac{\partial u}{\partial x} A_x / x (u A_x) = R_{SOR} / \rho \quad (3.4)$$

The fluid velocities components in x, y and z directions are in the RANS Eq. (3.5), (3.6), and (3.7), respectively.

$$\frac{\partial u}{\partial t} + \frac{1}{V_F} (uA_x \frac{\partial u}{\partial x} + vA_y \frac{\partial u}{\partial y} + wA_z \frac{\partial u}{\partial z}) = -\frac{1}{\rho} \frac{\partial p}{\partial x} + G_x + f_x \quad (3.5)$$

$$\frac{\partial v}{\partial t} + \frac{1}{V_F} (uA_x \frac{\partial v}{\partial x} + vA_y \frac{\partial v}{\partial y} + wA_z \frac{\partial v}{\partial z}) = -\frac{1}{\rho} \frac{\partial p}{\partial y} + G_y + f_y \quad (3.6)$$

$$\frac{\partial w}{\partial t} + \frac{1}{V_F} (uA_x \frac{\partial w}{\partial x} + vA_y \frac{\partial w}{\partial y} + wA_z \frac{\partial w}{\partial z}) = -\frac{1}{\rho} \frac{\partial p}{\partial z} + G_z + f_z \quad (3.7)$$

where, u, v, w, are the velocities in x, y and z directions;  $A_x$ ,  $A_y$ , and  $A_z$  are the areas in x, y and z directions,  $G_x$ ,  $G_y$ , and  $G_z$  are body accelerations in x, y and z directions;  $f_x$ ,  $f_y$ ,  $f_z$  are the viscous acceleration;  $\rho$  and P are the fluid density and pressure, respectively.

### 3.6 Closure Problems and Turbulence Models

The turbulent flows are associated with the fluctuation of velocity components, and these fluctuations (Turbulence) are transported through mass, energy and momentum. In practical engineering problems, due to the small scale and high frequencies, these fluctuations can't be solved directly [111]. Therefore, RANS equations are implemented to solve time-averaged small scale fluctuations and add additional unknown variables which are solved by the turbulence closure models [232].

Six different turbulence models are available in FLOW-3D such as one-equation Prandtl mixing length model, two equations Standard K- $\epsilon$ , RNG- K- $\epsilon$  and K- $\omega$  and LES model. In these models, different equations are employed to resolve the closure issues, however, two-equation models, i.e., Std K- $\epsilon$  and RNG-K- $\epsilon$ , are used widely in civil engineering and are also discussed below.

### 3.6.1 Standard K- $\epsilon$ Model

Because of the simplicity and lesser computation time, Std K- $\epsilon$  model is widely used in engineering applications and employs two-equation ( i.e., K and  $\epsilon$ ). This model derives its coefficients empirically [165] [166]. The model assumes Reynolds stress to be proportional to the time-averaged strain, and in case of fully turbulent flow this model ignores the molecular viscosity and overlooks the historical effects in the stream wise direction. However, in case of large curvature, standard K- $\epsilon$  comprises the performance [107]. For turbulent kinetic energy (k) and its dissipation rate  $\epsilon$  the model implements Eq.(3.8) and (3.9) [83].

$$\frac{\partial k}{\partial t} + \frac{1}{V_F} [U A_x \frac{\partial k}{\partial x} + V A_y \frac{\partial k}{\partial y} + w A_z \frac{\partial k}{\partial z}] = P_T + G + D_{iff} + \epsilon \quad (3.8)$$

$$\frac{\partial \epsilon}{\partial t} + \frac{1}{V_F} [U A_x \frac{\partial \epsilon}{\partial x} + V A_y \frac{\partial \epsilon}{\partial y} + w A_z \frac{\partial \epsilon}{\partial z}] = C_{1\epsilon} \frac{\epsilon}{k} (P_T + C_{3\epsilon} G) + D_{iff} - C_{2\epsilon} \frac{\epsilon^2}{k} \quad (3.9)$$

where  $P_T$ , G,  $D_{iff}$  and  $D_{dif}$  are shear production, buoyancy production and diffusion parameters, respectively, while  $C_{1\epsilon}$ ,  $C_{2\epsilon}$ , and  $C_{3\epsilon}$  are the model constants and the values of  $C_{1\epsilon}$  and  $C_{2\epsilon}$  are 1.44 and 1.92, respectively.

### 3.6.2 Renormalization Group (RNG K- $\epsilon$ ) Model

Due to progressive development in CFDs, the researcher have continually modified by turbulence models and considering the turbulence vortex, Re-normalization Group (RNG K- $\epsilon$ ) model deduced the turbulent kinetic energy (K) and its dissipation rate ( $\epsilon$ ) through re normalization theory methods [233]. This model is considered for low turbulence and high shear area which showed better results than Standard K- $\epsilon$  model [148]. The model also adds an addition term for dissipation rate which increases its performance [234],[235]. In the RNG model, Eqs. (3.10) and (3.11) are used for turbulent kinetic energy (K) and its dissipation( $\epsilon$ ), respectively.

$$\frac{\partial}{\partial t} (\rho \times k) + \frac{\partial}{\partial x_i} (\rho \times k u_i) = \frac{\partial}{\partial x_j} \left[ \mu + \frac{\mu_t (\rho \times k)}{\sigma \times k} \frac{\partial k}{\partial x_j} \right] + p_k + \rho \epsilon \quad (3.10)$$

$$\frac{\partial}{\partial t}(\rho\epsilon) + \frac{\partial}{\partial x_i}(\rho\epsilon \times u_i) = \frac{\partial}{\partial x_j}[\mu + \frac{\mu_t}{\sigma\epsilon}(\rho \times k) \frac{\partial\epsilon}{\partial x_j}] + c_1\epsilon(\frac{\epsilon}{p_k}) + c_2\epsilon(\frac{\epsilon^2}{k}) \quad (3.11)$$

where  $x_i$ ,  $\mu$ ,  $\mu_t$ ,  $P_k$  are coordinate in i-axis, dynamic viscosity, turbulent dynamic viscosity, and TKE production, respectively, and the terms  $\sigma k$ ,  $\sigma\epsilon$ ,  $C_{1\epsilon}$ , and  $C_{2\epsilon}$  are the model parameters [233]. As compared to Standard  $K-\epsilon$  model, due to the difference in the model formulation essentially in the values  $C_{1\epsilon} = 1.42$  and  $C_{2\epsilon} = 1.68$ , the RNG K- $\epsilon$  models showed better results in the hydraulic applications. On the recommendation [236] and results presented in [83], [98], [103], [157], [99], [237] the present study has implemented RNG K- $\epsilon$  model for the turbulence modelling in various cased studied here.

## 3.7 Numerical Solution Methods

The process in which the partial differential equations are converted into sets of non-linear algebraic equations is called discretization. The solution of these equations is flow-dependent. In the case of steady flow, pseudo-time iteration schemes are used. However, in unsteady flow, the non-linear algebraic equations are converted into linear equations by iteration schemes, and numerical methods solve these equations. In general, most of the present 3-D hydraulic models use these solution methods. In FLOW-3D, finite volume method (FVM) is implemented for discretization of partial differential equations as discussed below:

### 3.7.1 Finite Volume Method (FVM)

Finite Volume Method (FVM) is a discretization scheme which is used for various types of flows and has been used extensively in fluid mechanics and other engineering fields. FVM is also known as a robust and cheap method for discretizing the law of conservation [238].

In CFD, the spatial discretization of Navier Stokes Equations (NSE) is carried out by replacing the continuous variable with the control volume [237] for which

FVM is gaining popularity because it offers less flexibility during the discretization process [239]. In FVM, initial differential equations are integrated into a spatial form which are then solved by the numerical methods such as FLOW-3D. More precisely, in FVM, conservation equations, i.e., mass, momentum, energy, and volume fraction are integrated and discretized over the control volume and are solved on each iterative time step.

In FLOW-3D numerical models, equations of the controlled volume are formulated with area and volume porosity functions. This formulation is called the ‘fractional area/volume obstacle representation’ (FAVOR) method and is efficiently used in complex geometries and around the solid regions [240].

### 3.8 Free Surface Tracking

In CFD, a considerable free surface tracking or capturing methods, e.g., the marker and cell (MAC) and level set method (LSM), are available to be used in the numerical simulation [58], but the extensively used method is the volume of fluid (VOF).

It was initially adopted by [241] to yield the turbulence and free surface tracking of mean flow and the method uses donor-acceptor formulation [163]. The method is designed for two or more immiscible fluids in which one fluid is compressible (i.e., air). The technique uses a fixed Eulerian mesh with a transport equation to define the relative fraction volume of different fluids in each computational mesh cell [106]. In the present study, the VOF transport equation (3.12) is employed

$$\frac{\partial F}{\partial t} + \frac{1}{V_F} \left[ \frac{\partial F}{\partial x} A_x u + \frac{\partial F}{\partial y} A_y v + \frac{\partial F}{\partial z} A_z w \right] = 0 \quad (3.12)$$

where,  $A_x$ ,  $A_y$ ,  $A_z$  are the average flow areas in x, y, and z directions, and u, v, and w are the average velocities in x, y, and z directions, respectively. In the above equation, F is fluid fraction, which ranges from 0 to 1. If  $F = 0$ , it represents air in

the cell, and ( $F = 1$ ) shows the cell is full of water. However, ( $F = 0.5$ ) represents the free surface.

### 3.9 Pressure-Velocity Coupling

The approximation of NSEs is highly case-dependent, and the performance of algorithms is generally assessed by computation requirements, stability, and convergence. Due to the additional variable, pressure converge is a main problem in the continuity equation which puts an additional constraint on the velocity field [184]. For stability and convergence of pressure and velocity fields, pressure-velocity coupling algorithms are implemented, i.e., SIMPLE, SIMPLER, SIMPLEC, and PISO [150], [242], [208], [243]. However, FLOW-3D uses the Generalized Minimum Residual Solver (GMRES) method to implicitly approximate the NSEs and find pressure and velocity fields in highly efficient and accurate manners [183]. GMRES contains good speed, convergence, and symmetry and does not apply over and under relaxation factors. GMRES also possesses an additional algorithm, “Generalized Minimum Residual Solver (GCG),” to treat the viscous terms [244].

### 3.10 Fluid-Solid Interface Reconstruction

For advection and interface reconstruction, traditional techniques such as Simple Line Interface Calculation (SLIC) [245][246], Piece-wise Linear Interface Calculation (PLIC) [247], and Flux line-segment model (FLAIR) [248] were applied in the past. These methods used volume fractions of the neighboring cell to reconstruct the interface line. However, FLAIR uses the cell face volume fraction to develop the line segments. The main problem of these techniques is the “stair-stepping” [249].

In FLOW-3D, Fractional Area-Volume Obstacle Technique (FAVOR) [250] is used to resolve the solid and flow regions. The developed curved and complicated

geometries are embedded in the computation grids by the pre-processor. This method consists of special algorithms to compute inter facial areas, wall stress evaluation, enhance stability and solve advection along with the obstacles [52], [236], [251]. All the governing equations in FLOW-3D are also framed as area/volume porosity function [147], [59], [71] [103], [104], [163], [240]. As compared to transitional techniques in other CFD codes, the FAVOR method in FLOW-3D is simple and accurate in resolving the complex geometries without the requirement of body-fitted grids [148]. In FLOW-3D, the FAVOR method also allows structured grids [165] for the whole flow domain, especially in case of rounded geometries [98], [183].

Additionally, in case of a larger flow domain, the technique allows more fine mesh and multiple blocks to resolve the geometry and capture more details of flow . This technique removes the "stair-stepping" effect typically connected with rectangular grids and replaces it with short, straight-lined segments [101], [107], [252]. The technique utilizes the "law of wall" to accurately simulate the flow near the obstacle [253]. In this numerical study VOF-FAVOR method with structured rectangular hexahedral meshes of various sizes is used to resolve the flow domain and solid geometries. The general form of equation (3.13) for in-compressible fluid based on FAVOR is given below;

$$\Delta(uA) = \left[ -\frac{\partial V_F}{\partial t} + \frac{S_m}{\rho} \right] \quad (3.13)$$

where,  $S_m$  is the fluid physical mass term,  $V_F$  and  $A$ , are the volume and area fractions, respectively.

### 3.11 Computation Grid

In numerical codes, to solve the partial differential equations, the flow domain is subdivided into cells and elements which is called computational grid. These meshes further divide the physical space into small volumes with many nodes which store the value of essential parameters such as pressure, velocity, and temperature [103]. Two category of grids are used in CFDs problems, as described below.



### 3.11.1 Unstructured Grid-meshing

The computation grids usually consist of geometrical primitives such as triangle, quadrilateral, tetrahedral and hexahedral [254]. The unstructured grid and mesh do not have a definite and uniform pattern and are usually made of triangles and tetrahedral. This meshing system is used for complex geometry because of the flexibility and minor closures and skewness issues [114]. Unstructured grids allow the use of computational cells of any arbitrary shape such as hexahedral, tetrahedral, triangle and prism which reduce simulation time. In most aerodynamic and complex environmental flows, unstructured meshes provide a convenient framework for local refinement [253]. One of the disadvantages of using unstructured meshing is that the repeating local refinement leads to poor mesh quality, disparate element sizes, high vertex and large face angles, which lead to poor flow fields.

### 3.11.2 Structured Grid-meshing

Regular connectivity of cells and meshes in 2D (quadrilateral) and 3D (hexahedral) is characterized as structured grids. This type of grid and meshing are easy to create, has defined shapes, and is easy to implement [33]. As compared to unstructured mesh grids, it is believed that structured meshing [98], [164] produces better results, and is faster to perform in CFD problems than the unstructured meshing. These grids consume less computational memory and create fewer latency issues [121], [253].

Furthermore, the problems of an-isotropic in the thinner sections are also catered by the structured meshing such as hexahedral. In FLOW-3D, these structured meshes are easy to develop, and this code is compelling in generating complicated meshes. The code also offers to create multiple grid blocks that can be linked and nested. Furthermore, the software allows the pre-processor to check the meshing quality and analyze it by the FAVOR method [183]. In this numerical study, the geometry of the models is straightforward, which allows to implement structured

meshing, therefore, for the studied stilling basins, presently, multiple structured mesh blocks are employed.

## 3.12 Sediment Scour Model

In sediment scour modelling, number of sediment species can modelled with various characteristics such as grain size, density, bed load transport rate, critical shear stress, entrainment coefficients and angle of repose. FLOW-3D models predict the sediment scouring in two different ways such as packed and suspended sediment which further include advection, erosion, settlement and deposition.

In FLOW-3D, several parameters are required to model the scour such as bed load transport rate equation, maximum packing, fraction critical shield number definition, and various sediment properties. For the sediment transport models, following equations are used in the present study.

### 3.12.1 Critical Shields Number

Critical shield parameter ( $\theta_{cr,i}$ ) is the minimum bed shear stress  $\tau_{cr}$  required to move sediment species from the packed bed. The rate of erosion on the sediment packed bed depends on size, density and forces acting on the sediment particle.

$$\Theta_{cr,i} = \frac{\tau_{cr,i}}{gd_i(\rho_i - \rho_f)} \quad (3.14)$$

where  $g$ ,  $\tau_{cr,i}$ ,  $d_i$ ,  $\rho_i$  and  $\rho_f$  are acceleration due to gravity, critical shear stress, sediment diameter, sediment and fluid densities, respectively.

In FLOW-3D, the critical shield number can be computed by the software automatically for which prescribed values are selected while its value can also be calculated by Soulsby-White house equations (3.15 and 3.16) as described below;

$$\Theta_{cr,i} = \frac{0.3}{1.2d_{*i} + 1} + 0.055[1 - \exp(-0.02d_i)] \quad (3.15)$$

$$d_{*i} = d_i[g(s_i - 1)/V_f]^3 \quad (3.16)$$

where  $d_{*i}$  is the dimensionless grain size,  $S_i = \rho_i/\rho_f$  and  $V_f$  is the kinematic fluid viscosity. In FLOW-3D models, a default value of 0.05 can be assigned as a critical shields number.

### 3.12.2 Bed-Load Transport

The mode of transport of sediment particle from the surface of packed bed is defined as bed load transport ( $\Theta_i$ ). In FLOW-3D, three different equations for the volumetric sediment transport rate per bed width are used as described below;

#### 3.12.2.1 Meyer, Peter and Müller Equation

$$\Theta_i = \beta_{MPM,i}(\Theta_i - \Theta_{cr,i})1.5C_{b,i} \quad (3.17)$$

where  $\beta_{MPM,i}$  is the bed-load coefficient which ranges from 5.0 to 5.7 for low transport, 8.0 for intermediate transport, and 13.0 is used for very high transport [255].

#### 3.12.2.2 Nielsen Equation

$$\Theta_i = \beta_{Nie,i} \Theta_i^{1.5} (\Theta_i - \Theta_{cr,i}) C_{b,i} \quad (3.18)$$

where  $\beta_{Nie,i}$  is the bed-load coefficient with a default value of 12.0 [256].

#### 3.12.2.3 Van Rijn Equation

$$\Theta_i = \beta_{VR,i} d_{*i} (\Theta_i/\Theta_{cr,i} - 1)^{2.1} C_{b,i} \quad (3.19)$$

$\beta_{VR,i}$  is the bed load coefficient which has 0.053 default value while for equation (3.17), (3.18), and (3.19)  $C_{b,i}$  is the fractional volume of species  $i$  in packed sediment bed [181][257][258].

### 3.12.3 Maximum Packing Fraction

The maximum packing fraction is the ratio of fraction of all sediment species to open volume in a cell and the cells are considered as packed in which drag function reached to infinity (No fluid). The maximum packing fraction ranges from 0.55 to 0.7 while 0.64 is the default value of packing fraction which is automatically selected by FLOW-3D [201].

### 3.12.4 Bed Shear Stress

For turbulent flow, the bed shear stress applied on the surface of packed sediment is computed by standard wall function.  $C_{rough}$  is the user-defined coefficient which is obtained by ratio of Nikuradse roughness  $k_s$  to median grain diameter ( $d_{50}$ ) in packed sediment for which 2.5 value is recommended [200][199].

## 3.13 Data Requirement for Numerical Models

To operate the numerical models, the following geometries and flow data were supplied to FLOW-3D.

### 3.13.1 Models Drawings, Hydraulic Data and Models Operation

The solid geometries of investigated models were designed in AutoCAD and converted into stl files. Before employing the files in FLOW-3D, the files were tested in Netfabb-basic software to remove holes, facets, and boundary edges. Three-Dimensional (3-D) geometries of USBR baffle block, remodelled basin's appurtenances, and WSBB basins are shown in Fig. 3.9.

In Type (A) basin, floor level is fixed at 126.79 m whereas in Type (B) basin, it is changed to 127.10 m. The weir crest in both basins is fixed at 130.44 m.

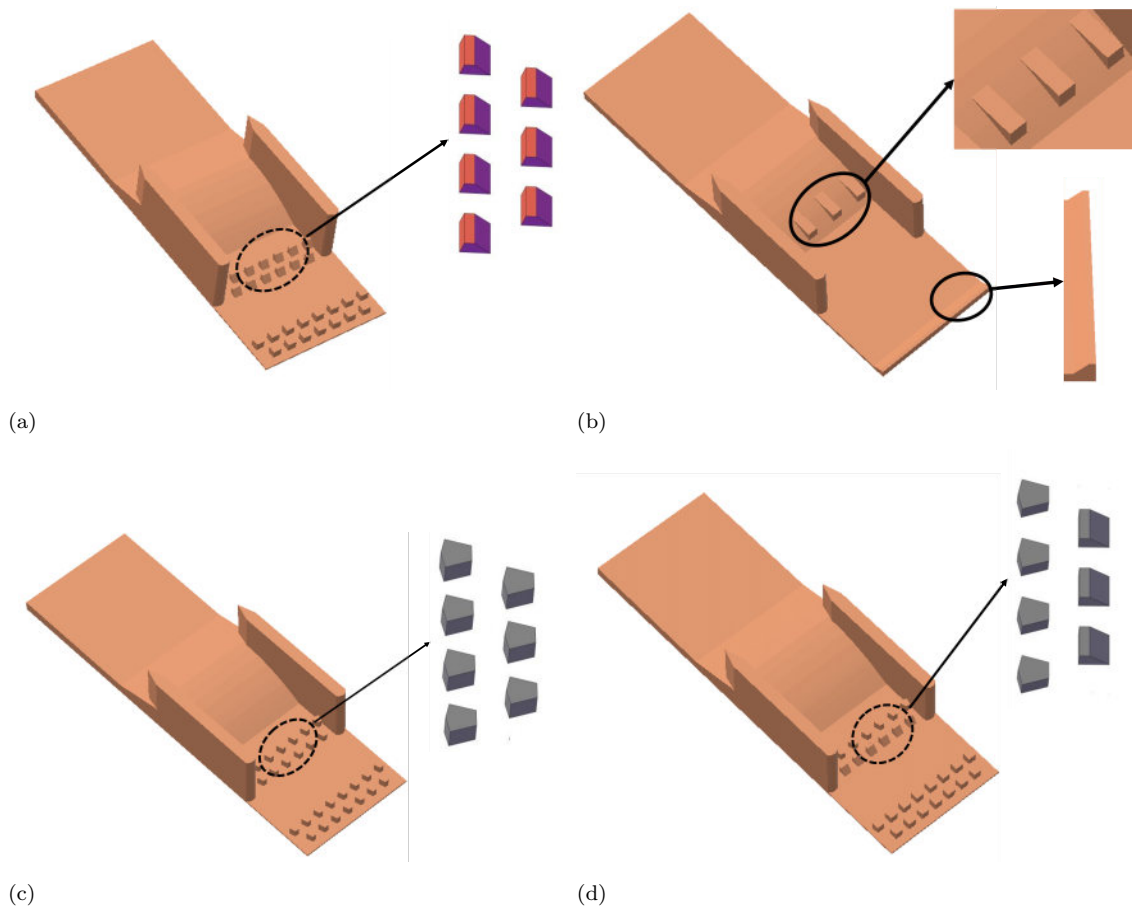


FIGURE 3.9: Geometries and dissipation arrangements in different stilling basins, (a) Type (A), (b) Type (B), (c) Type (C), and (d) Type (D)

In Type (A) and (B) basins, the slopes of upstream and downstream glacis are maintained at 1:3 and 1:4 (H:V), respectively. In Type (A) basin, the USBR blocks are installed 14.63 m away from the center-line of the crest which are placed in a staggered position.

The overall length and height of the blocks is 1.37 m whereas its width is 1.22 m. Additionally, between the two staggered rows of baffle blocks a 1.37 m distance is maintained while the top width of all the USBR blocks is 0.46 m which are angled at  $45^{\circ}$  from the rear side. Furthermore, in Type (A) basin, two staggered row of friction blocks are also placed at the basin's end about 28.95 m away from the weir's crest. These friction blocks are 1.37 m long, 1.22 m wide, and 1.37 m high. The top surface of these blocks is identical to their bottom.

On the contrary, in remodelled basin (Type (B)), chute blocks are made on the

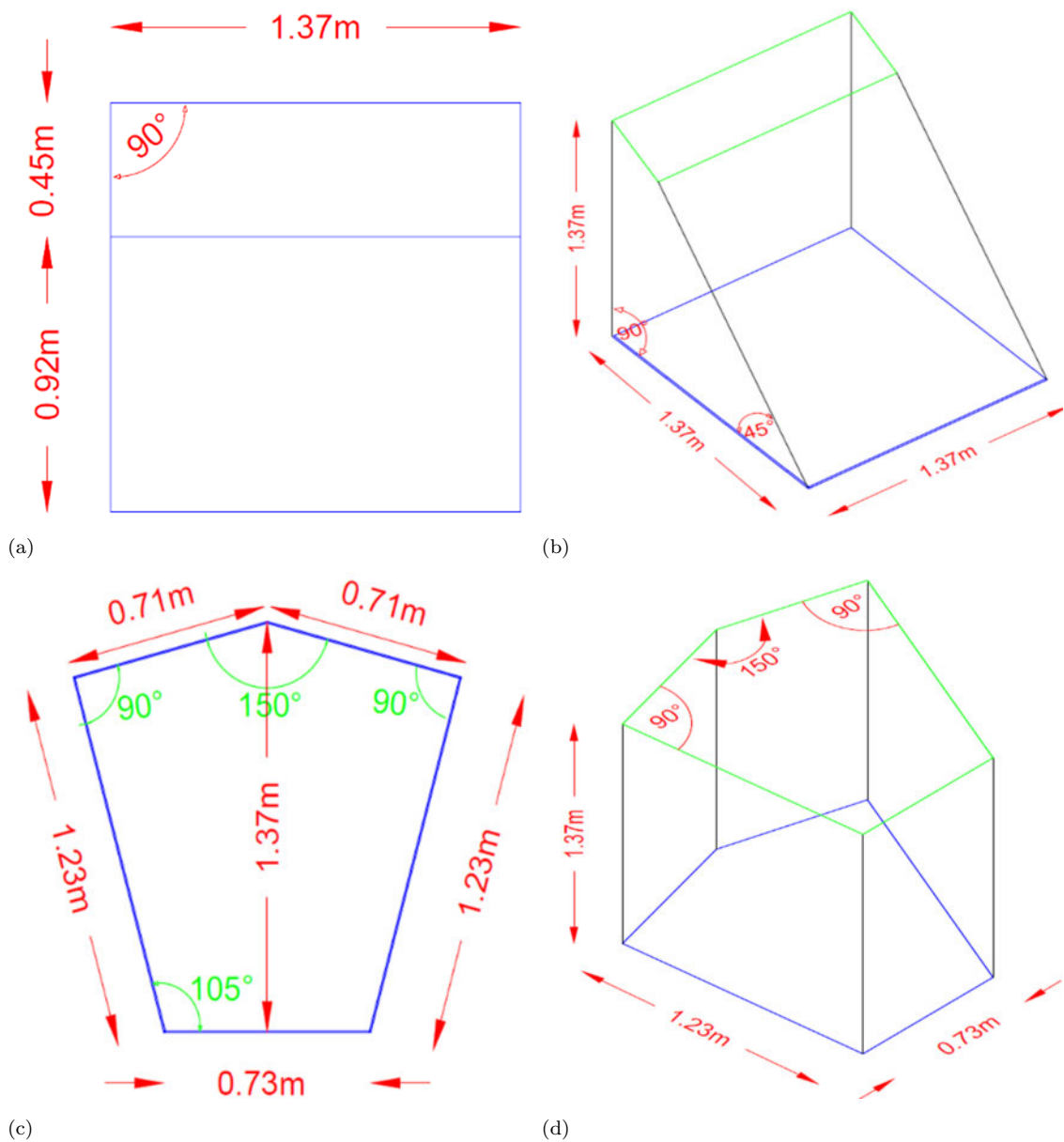


FIGURE 3.10: (a) USBR block, (b) USBR block, Isometric view, (c) WSBB (d) WSBB, Isometric view

downstream glacis whereas at the basin's end, a sill replaced the friction blocks. The overall length, width and height of chute block are 4.82 m, 1.70 m, and 1.70 m, respectively. From the top, these chute blocks are 5% inclined in the downward direction, and 3.45 m distance is maintained between the two consecutive chute blocks.

The height of end sill is 1.52 m while its width is stretched along the width of modelled bay. The end sill is sloped from the upstream side which is fixed to 2:1

(H:V), while the top width of the sill is fixed to 0.30 m.

In Type (C) basin, the WSBB are placed at the locations of impact USBR blocks. The overall length, width and height of the wedge-shaped block is kept to 1.37 m.

In the present models, for the investigated WSBB, a vertex angle of  $150^{\circ}$  and cutback angle of  $90^{\circ}$  is employed. However, in Type (C) basin, the friction block is used of the sizes as described in Type (A) basin. In Type (D) basin, only first row of impact USBR blocks is replaced with WSBB, while the rest of basin geometry is kept identical to the Type (A) basin. The top and isometric views of impact and WSBB are shown in Fig.3.10.

All the models are treated as concrete elements for which roughness coefficient of 0.013 is assigned.

### 3.13.2 Hydraulic Data and Models' Operation

For the hydraulic investigation of different stilling basins, boundary and initial conditions were provided to the models. During the run time, for a particular flow, the pond and tail water levels were maintained to develop the conditions of HJ. For all the investigated stilling basins, discharge, pond and tail water level data of year 2010 was used to run the models as displayed in Table 3.5.

For the investigation of different stilling basins on various discharges, hydro-graphs are developed from year 2013 to 2020 as shown in Fig. 3.11. The hydro-graphs trends indicated that the maximum discharge at Tuansa barrage was from mid-June to September, while in rest of the months low flows were noticed. The box plot in Fig. 3.12 shows the minimum, maximum and mean values of a year.

From the box plot analysis, the minimum value of discharge during a year was ranged between 0.25 to 0.37  $\text{m}^3/\text{s}/\text{m}$  while the maximum value was found between 4.90 to 7  $\text{m}^3/\text{s}/\text{m}$ . However, the mean value of discharge was found between 1.94 to 2.64  $\text{m}^3/\text{s}/\text{m}$ . Based on the flow analysis, it is found that during the year, the

TABLE 3.5: Models operation and HJ conditions

Discharge (m <sup>3</sup> /s/m)	Pond Levels (m)	Minimum TWLs for Jump formation (m)	Maximum TWLs for Jump formation (m)	TWLs during 2010 Flood (m)
2.44	136.24	129.08	132.28	130.40
4.88	136.24	130.14	132.89	131.23
7.22	136.24	130.75	133.34	131.91
18	134.60	132.73	134.56	133.65
21.7	135.63	133.5	135.08	133.86
24.3	135.93	133.8	135.32	134.00

mean flow in river Indus at Taunsa barrage was remained up to 2.1 m<sup>3</sup>/s/m, while the mean of upper box plot values was found up to 6.2 m<sup>3</sup>/s/m.

Therefore, to accommodate any error within the discharge data, the gated flow models were operated up to the maximum discharge value of 7.22 m<sup>3</sup>/s/m with an equal increment of 2.44 m<sup>3</sup>/s/m. However, for validation and performance assessment of FLOW-3D, investigated models were also run for the free flow discharges of 24.3, 21.7 and 18 m<sup>3</sup>/s/m. The detailed operations of gated and free flow analysis are described in 3.13.2.1 and 3.13.2.2 sections.

### 3.13.2.1 Free and Gated Flow Analysis

The hydraulic performance of present numerical models was assessed with  $H_e/H_d$  values of 0.998 and 0.996, whereas  $H_d$  and  $H_e$  are designed and effective heads, respectively. These values are designed and high flood discharge of the studied barrage. Therefore, the modelled free flow discharge values were compared with the designed (24.3, 21.7 and 18 m<sup>3</sup>/s/m) values. The illustration of  $H_e$  and  $H_d$  can be seen in Fig. 3.13.

For hydraulic modelling, discharge computation is very crucial. However, in routine, openings of the barrage gates are not same, and are usually set according



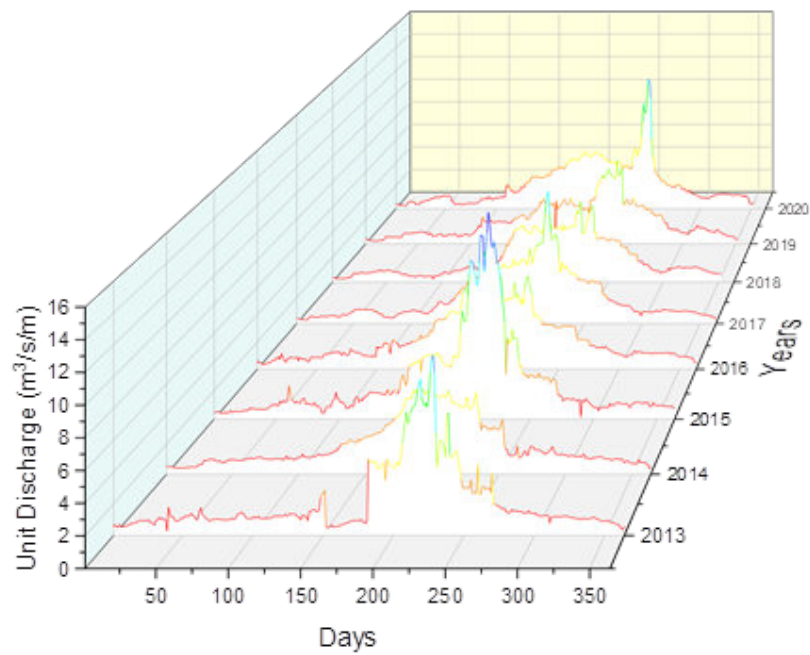


FIGURE 3.11: Unit discharge during the years at Taunsa barrage

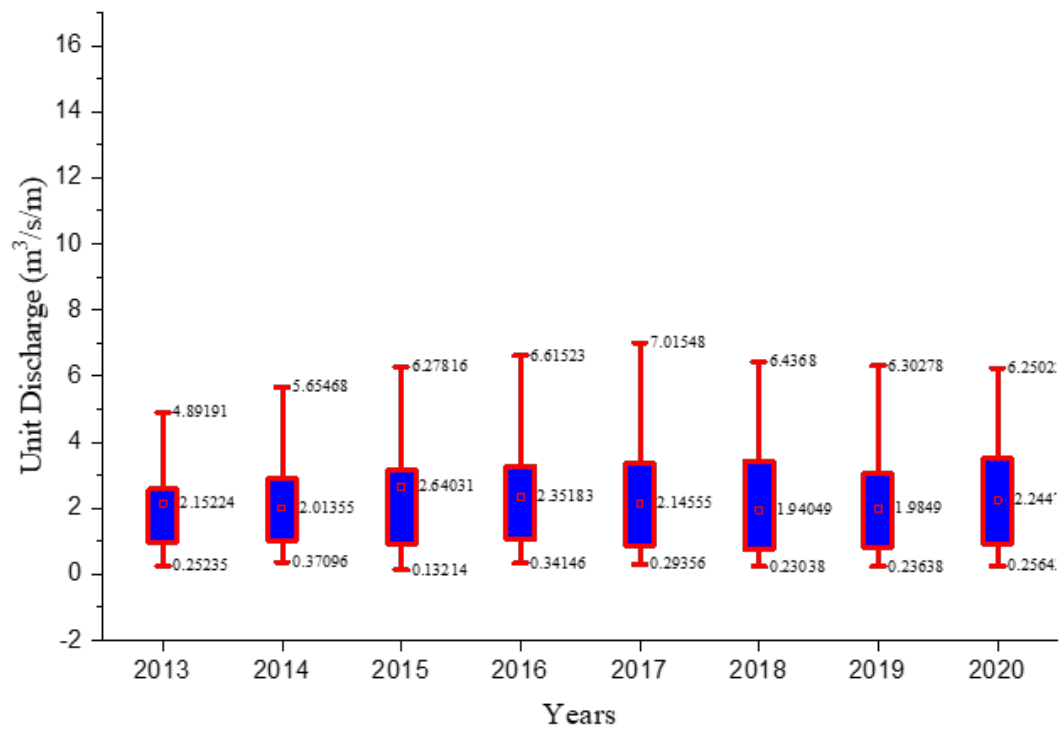


FIGURE 3.12: Minimum, mean and maximum flows during years 2013-2020 at Taunsa barrage



FIGURE 3.13: Model operation for gated flow

to the flows in rivers. Presently, one bay of the studied barrage was modelled, and discharge computed from single bay was used to replicate actual condition of the barrage. Table 3.5 shows the initial condition to run these models. To compute discharge for the gated flow, the equation was used to estimate the gate openings ( $D$ ). Fig. 3.13 shows the typical cross section of gated flow operation for the studied models.

$$Q = \frac{2}{3}C_d(A)\sqrt{2gh_c} \quad (3.20)$$

where  $Q$  is known and measured in ( $\text{m}^3/\text{s}$ ),  $A$  is the area of gate opening in ( $\text{m}^2$ ),  $b$  is width of the bay in ( $\text{m}$ ),  $D$  is the gate opening in ( $\text{m}$ ),  $g$  is acceleration due to gravity, and ( $h_c = H_d - D/2$ ) is the center-line head which is measured in ( $\text{m}$ ).

In the numerical models, the flux surface (porosity=1) was set up at  $X_{max}$  of the mesh, and a movable probe was assigned to measure the free surface profile and other essential parameters in the studied stilling basins. The flow calculated for the modelled domain was used to calculate the discharge from the barrage, thereby the actual flow conditions were generated for free and gated flows. Based on the flow analysis, all the models were operated for gated flow of 2.44, 4.88 and 7.22  $\text{m}^3/\text{s}/\text{m}$ . The total length of the simulation domain was 55.50 m, in which hydraulic investigations were carried out on 38.10 m of downstream side.

### 3.14 Hydraulic Investigation

Presently, the performance of different stilling basins is assessed different hydraulic. NSEs, continuity and momentum equations were used by RANS Eq. 3.3, Eq. 3.4, Eq. 3.5, Eq. 3.6, and Eq. 3.7, while turbulence was captured by Eq. 3.10 using

RNG K- $\epsilon$  models. The modelling domain was discretized by FVM method while the free surface was tracked by VOF method using Eq. 3.12. Pressure-velocity coupling was solved using GRMES, while solid-fluid interface was constructed by the FAVOR method using Eq. 3.13.

### 3.14.1 Meshing and Boundary Setup

After importing the models' geometries into FLOW-3D, meshing was applied to the models. A 3D uniform-structured mesh blocks were employed to resolve the solution domain, in which 1<sup>st</sup> mesh block was initiated from  $X_{min}=15$  m (Upstream) and was ended at  $X_{max}=51$  m (downstream). However, the 2<sup>nd</sup> mesh block was started from  $X_{min}=51$  m and ended  $X_{max}=56$  m. Lastly, the 3<sup>rd</sup> block was started from  $X_{min}=56$  m and extended up to the end of basin (Rigid floor,  $X_{max}=71$  m).

It is worth mentioning here that the purpose of three mesh blocks is resolve the baffle block because the hydraulic investigations are focused within the hydraulic jump, especially in the baffle block region. Overall, 56 m long, 22.5 m wide and 11 m high models were simulated and a total of approximately 196,5600 cells were used in the modelling domain. The details of each mesh block, cell sizes and their quality indicators are provided in the Table-3.6 and Table 3.7, respectively. To

TABLE 3.6: Details of mesh blocks and cell sizes

Mesh blocks and cell sizes	Mesh Block (1)	Mesh Block (2)	Mesh Block (3)
Cell size (m)	$\Delta x \Delta y \Delta z$ 0.25 0.25 0.25	$\Delta x \Delta y \Delta z$ 0.125 0.125 0.125	$\Delta x \Delta y \Delta z$ 0.25 0.25 0.25
Total Cells	777,600	950,400	324,000

reduce the simulation time, a domain-removing section was added to deactivate unused cells and ensured that the component was not containing the flow. For gated flow analysis, a vertical gate of 18.5 m wide, 0.53 m long, and 6.10 m high

TABLE 3.7: Quality indicators for different mesh blocks

Mesh Block	Number of cells	Maximum adjacent ratio			Maximum aspect ratio		
		X	Y	Z	X-Y	Y-Z	Z-X
Block (1)	X=144, Y=90, Z=60	1.00	1.00	1.00	1.016	1.016	1.061
Block (2)	X=40, Y=180, Z=120	1.00	1.00	1.00	1.00	1.00	1.00
Block (3)	X=60, Y=90, Z=60	1.00	1.00	1.00	1.00	1.00	1.00

was mounted upstream of the weir crest. Fig. 3.14 shows the meshing setup for solid and flow domain.

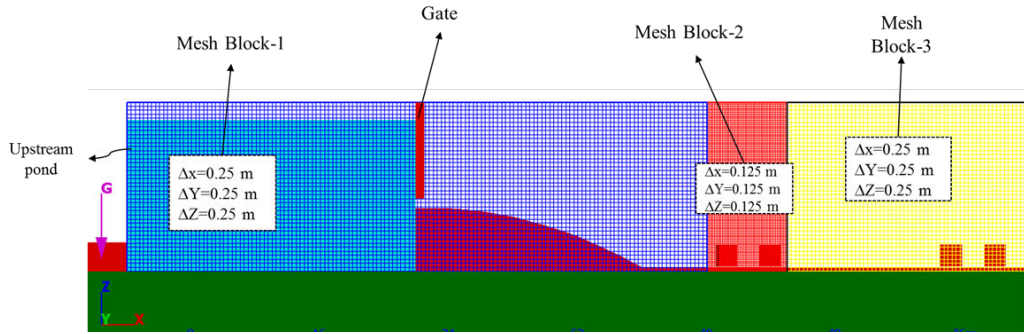


FIGURE 3.14: Meshing setup for solid and flow domains

Fig. 3.15 illustrates that both  $X_{max}$  and  $X_{min}$  were set as pressure (P) boundaries while  $y_{max}$ ,  $y_{min}$  and  $z_{min}$  were set as wall (W) boundaries which represents no-slip, zero tangential and normal velocities to the walls. Expect pressure which was set to zero, for all other variables  $Z_{max}$  was set to atmospheric pressure. For the 2<sup>nd</sup> block,  $X_{min}$  and  $X_{max}$  boundaries were set as symmetry (S). The boundaries conditions governing the present models are shown in Fig. 3.15.

To run models for various discharges, upstream pond and tail water levels were provided while gate opening (D) was computed from the equation (3.20).

For controlling the time step at each iteration, a courant number stability criterion was employed. At every iteration, the step step was monitored by stability and convergence both for free (0.0023 to 0.0025) and gated flow (0.015 to 0.0025). To achieve the steady state of models, discharge was monitored at the inlet and outlet

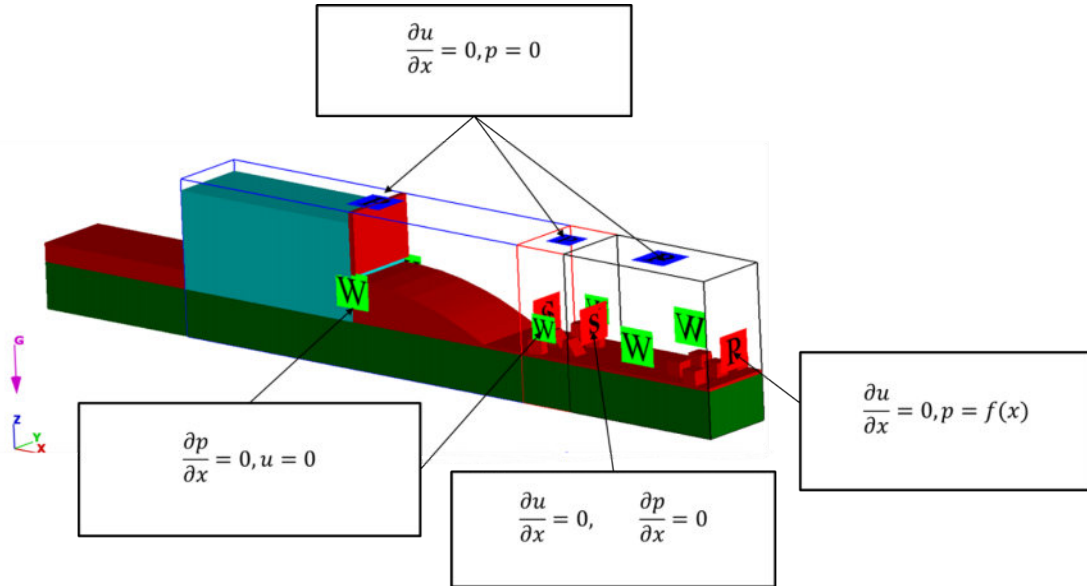


FIGURE 3.15: Boundary conditions for different mesh blocks to govern the solution domain

boundaries. The steady state solution of the models was varied between  $T=100$  s to 165 s.

The analysis indicated that for the free flow discharge, the model achieved steady state at the averaged time of  $T=60$  s, while the gated flow models achieved steady state after longer periods of time, i.e., between  $T=150$  s to 165 s. However, to accommodate fluctuations/oscillations in the flows,  $T=170$  s (finish time) was provided to the free and gated flow models. In the Annex-3B, Figs. 1, 2 and 3 show the time rate change of gated (2.44, 4.8 and  $7.22 \text{ m}^3/\text{s}/\text{m}$ ) flow at the inlet and outlet boundaries of different stilling basins.

### 3.15 Scour Modelling and Investigation

For scour modelling, numerical models for different stilling basins' geometries were developed. A fully in-compressible and clear water of  $20^\circ \text{ C}$  was supplied to the tested models for various free and gated flow condition as described in Table 3.8.

The total length, width and height of the modelling domain was 85 m, 22.5 m and 11 m, respectively. Out of the total length, 15 m was upstream pond level and

70 m was downstream side where hydraulic and scour investigations were carried out. Out of 70 m on downstream, 30 m of the bed was laid as erodible (Sediment Packed Bed) where scour was studied.

Before carrying out scour modelling, models were set for hydraulic characteristics, and for the free surface tracking and turbulence modelling, volume of Fluid (VOF) method and RNG K- $\epsilon$ , Standard K- $\epsilon$  and LES models were implemented, respectively. Generalized Minimum Residual Method (GMRES) was used to pressure velocity couple while for the spatial discretization of the flow domain was solved by Finite Volume Method (FVM).

In the present study, only one sediment specie was considered for modelling of scour for which maximum packing fraction of 0.64 was used. User prescribed value for critical shield number was used while Van Rijn equation (3.19) were implemented for bed load transportation.

After calculation of the critical shield number, bed load coefficient was computed using Van Rijn equation (3.19). The drag on settlement of sediment species was computed by Richardson-Zaki coefficient and a value equal to 1 was assigned. The diffusion of suspended sediment was controlled by turbulent diffusion and molecular diffusion coefficients, and they were assigned values equal 1 and 0, respectively.

The entertainment coefficient controlled the rate of scour modelling and its default value selected by FLOW-3D was used in the models. The value of 2.5 was used for ratio of bed roughness/ $d_{50}$ . The other physical specifications of the sediment packed bed are provided in Table 3.8.

### 3.15.1 Geometry and Meshing for Scour Models

The solid .Stl files of models were imported in FLOW-3D. A 30 m long, 18.29 m wide and 4.78 m deep erodible bed downstream of the stilling basin was created in FLOW-3D which was defined a sediment packed bed as 100 % sand component. Fig.3.16 indicates the geometrical setup for the different models under scouring modelling.

TABLE 3.8: Physical properties of sediment packed/scour bed.

Sr. No.	Sediment Characteristics	Modelling Value
1	Bed Load species	Fine sand
2	Species diameters ( $d_{50}$ )	0.0002 m
3	Sediment density	1692 kg/m <sup>3</sup>
4	Critical Shield number	0.05
5	Entrainment coefficient	0.018
6	Bed load coefficient	0.053
7	Angle of repose (Degree)	32 <sup>0</sup>

Three mesh blocks were applied to the modelling domain. The first mesh block was started from  $X_{min}=15$  m and ended at  $X_{max}=51$  m, while the second mesh block started from  $X_{min}=51$  m and end at  $X_{min}= 56$  m.

These two blocks were implemented to investigate the hydraulic jump and flow in the baffle blocks regions, while the third mesh block was started after baffle blocks' region and ended after the sediment packed bed which ranged from  $X_{min}= 56$  m to  $X_{max}= 100$  m.

Within the mesh blocks, structured rectangular hexahedral mesh cells were employed to resolve the solid and flow domains. A total of 259,2000 mesh cells were used for the modelling domain.

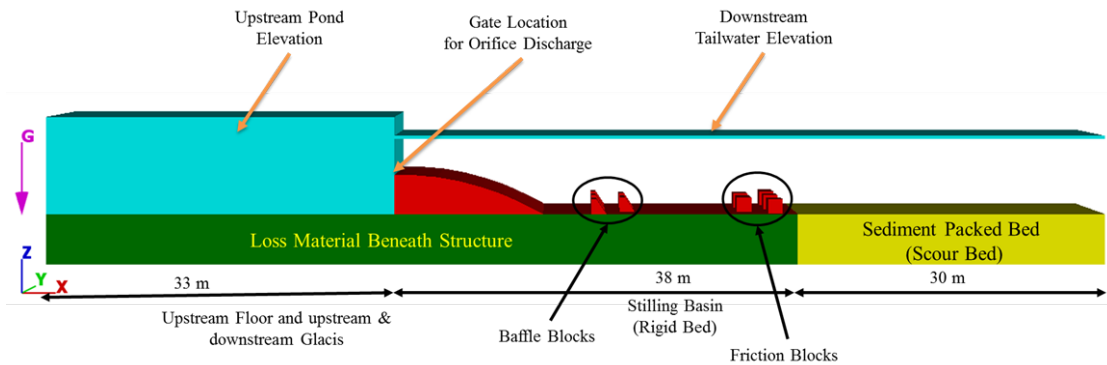


FIGURE 3.16: Geometry and three dimensional schematic setup of rigid and scour bed

### 3.15.2 Boundary Conditions for Scour Models

Like the hydraulic modelling as discussed in section (3.14.1), three mesh blocks were implemented to investigate the hydraulic and scour behaviour downstream of the studied stilling basins. However, in case of third mesh blocks, the block was extended to the end sediment packed bed with bottom ( $Z_{min}$ ) as Wall (W) boundary. Table 3.9 shows the boundary condition for rigid and sediment packed bed.

TABLE 3.9: Mesh boundary setup for scour modelling

Mesh Blocks	Xmin	Xmax	Ymin	Ymax	Zmax	Zmin
Block (1)	P	P	W	W	P	W
Block (2)	S	S	W	W	P	W
Block (3)	S	P	W	W	P	W

### 3.15.3 Simulation Time for Scour Stability Conditions

For scour and bed retrogression, the models' stability and convergence at each time step was monitored by courant number. It is important to mention that for free flow analysis of higher unit discharge such as 24.3 and 18  $\text{m}^3/\text{s}/\text{m}$ , the steady state solution can only be achieved by mass-averaged fluid kinetic energies (MAFKE) and volume flow rates at inlet and outlet boundaries.

Therefore, time (T) at which MAFKEs values reached to steady state was assigned as simulation time ( $T_s$ ). Based on the hydraulic stability criterion mentioned above, models were run for  $T_s=500$  s. However, the average actual time ( $T_a$ ) of the simulations was reached to 96 hrs.

To investigate the patterns of scour and bed retrogression, three turbulence models such as LES and two equation turbulence (K- $\epsilon$ ) models were applied.



Using LES model, in Type (A) stilling basin, hydraulic stability was achieved at different intervals of time i.e,  $T_s= 81$  s, 111 s, 141 s, 171 s, 200 s, 231 s, 261 s, 291 s, 3.35 s, 3.85, 435 s and 485 s. However, upon use of K- $\epsilon$  models no hydraulic stability was observed even at  $T_s=500$  s. Such conditions occurred because: downstream bed continued to be retrogressed, fluctuations in MAFKEs, and the formulation of turbulence models.

At  $T_s= 500$  s (Finish time), the maximum MAFKEs reached 8.32, 8.55 and 8.35  $\text{m}^2/\text{s}^2$  in LES, Standard K- $\epsilon$  and RNG K- $\epsilon$  models, respectively as shown in Fig 3.17.

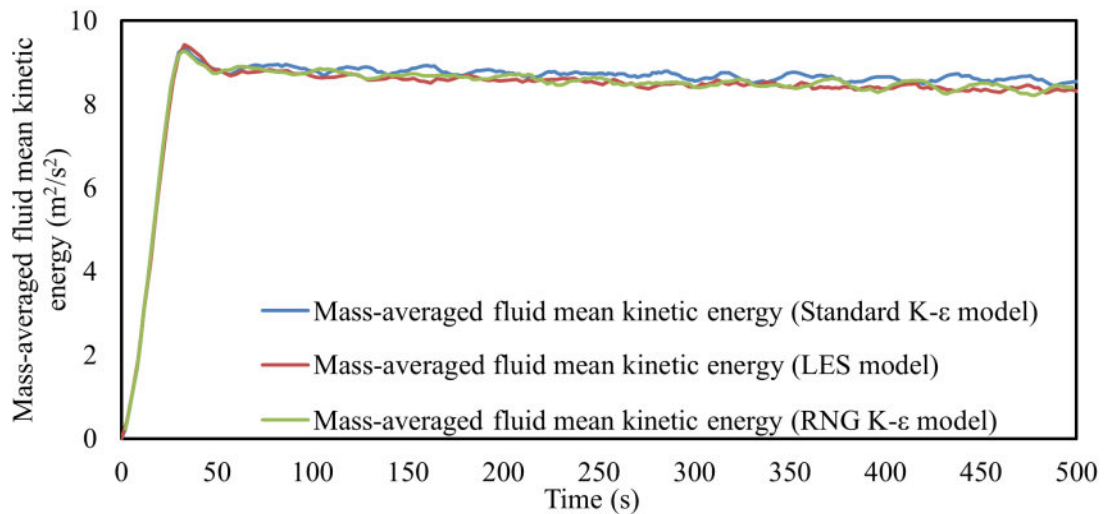


FIGURE 3.17: Hydraulic stability through MAFKEs in Type (A) basin

In Type (B) stilling basin, upon use of LES model, model achieved hydraulic stability at  $T_s= 68$  s, 93 s, 118 s, 143 s, 168 s, 193 s, 218 s, 243 s and 3.35 s. As compared to Type (A) basin, in Type (B) basin the hydraulic stability was achieved earlier, however, upon use of Standard and RNG K- $\epsilon$  models, the initial stability conditions were noticed at  $T_s=121$  s, and  $T_s= 222$  s, respectively.

At  $T_s=500$  s, the maximum MAFKE in Type (B) stilling basin was reached to 8, 8.67, and 8.56  $\text{m}^2/\text{s}^2$  in LES, Standard K- $\epsilon$  and RNG K- $\epsilon$  models, respectively as shown in Fig 3.18.

In the case of K- $\epsilon$  models, the MAFKEs in Type (B) basin were higher than that were observed in Type (A) basin. The higher values in Type (B) basin were

because: there were no basin's appurtenances due to which velocity was higher on the basin's floor, and higher bed degradation.

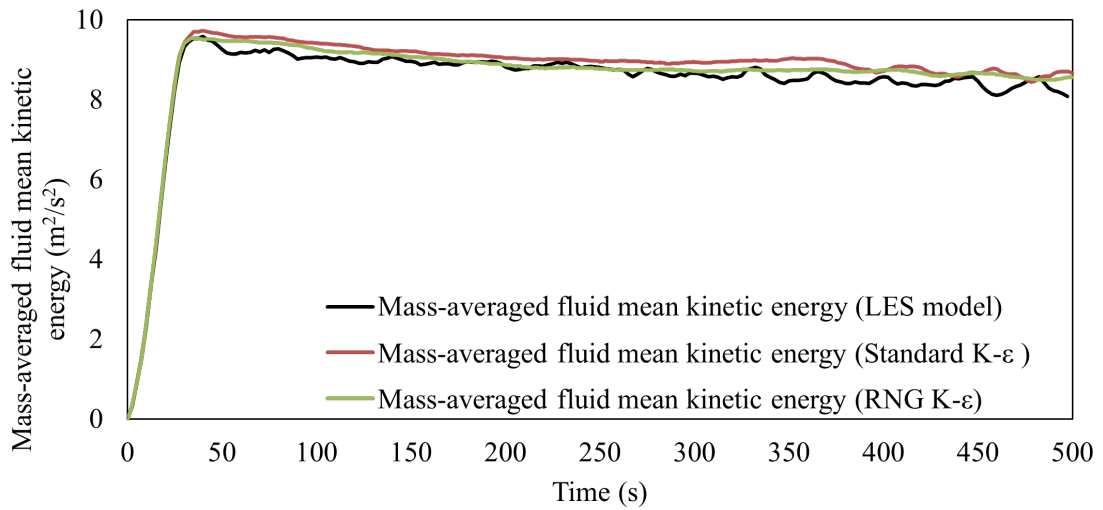


FIGURE 3.18: Hydraulic stability through MAFKEs in Type (B) basin

Using LES model, in Type (C) and D stilling basins, the model indicated hydraulic stability at 93 s, 1.18 s, 1.43 s, 193 s, and 243 s while no stability condition appeared in K- $\epsilon$  models. The maximum MAFKEs in Type (C) stilling basin were reached 8.46, 8.40 and 8.64  $\text{m}^2/\text{s}^2$  in LES, Standard K- $\epsilon$  and RNG K- $\epsilon$  models, respectively as shown in Fig 3.19. In case of Type (D) stilling basin, the maximum MAFKEs were reached 8.52, 8.77, 8.53  $\text{m}^2/\text{s}^2$  in LES, Standard K- $\epsilon$  and RNG K- $\epsilon$  models, respectively as shown in Fig 3.20.

Additionally, besides fluctuations in MAFKEs values, results also indicated fluctuations in free surface profiles because of the retrogressed bed which continued up to finish time. Due to the change in the geometry of baffle blocks, upon use of K- $\epsilon$  models, fluctuation in different hydraulic parameters were found more in Type (C) and (D) basin than that were observed in Type (A) basin .

However, even at  $T_s=500$  s, scour in Type (A), (B), (C) and (D) stilling basins didn't achieve stability, and the sediment bed was found to be eroded even after actual averaged time of 96 hrs. In fields at such a higher discharge rate, similar conditions of free surface profiles and bed retrogression take place downstream of river diversion hydraulic structures. Additionally, under such flow rate sometime

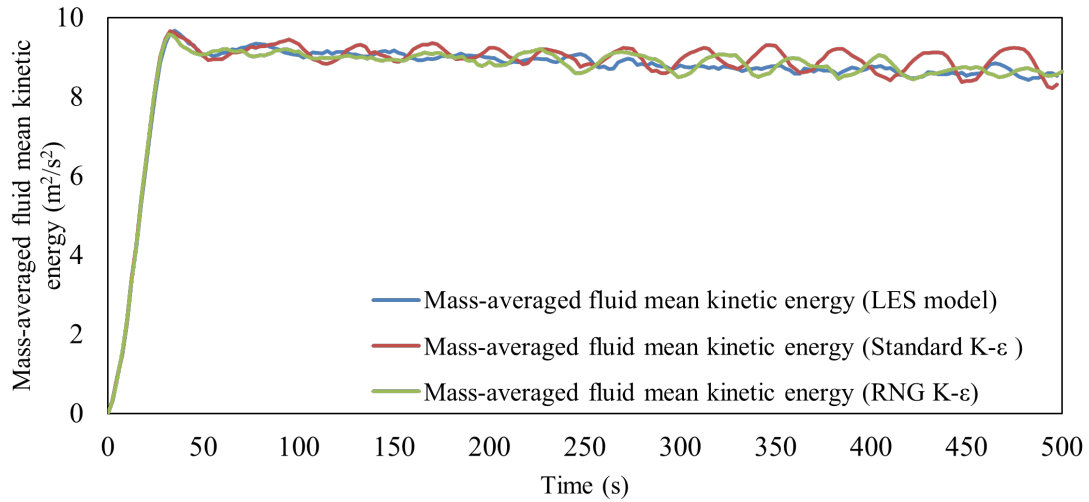


FIGURE 3.19: Hydraulic stability through MAFKEs in Type (C) basin

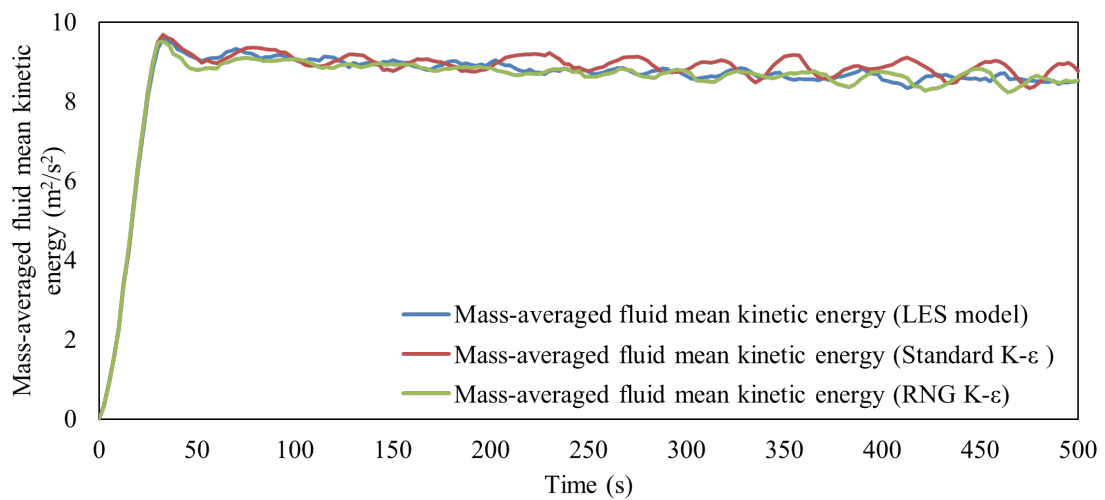


FIGURE 3.20: Hydraulic stability through MAFKEs in Type (D) basin

large scour pits are formed as witnessed downstream of Type (B) basin. Based on the results of hydraulic and scour stability, LES turbulence scheme showed hydraulic stability in the tested basins, while no hydraulic and scour stability was noticed in rest of tested turbulence models.

Therefore, to assess the performance of different basins, the simulation time  $T_s$  at which the sediment bed completely exposed was fixed to highlights various results i.e., flow field, scour and retrogression patterns, longitudinal and lateral bed profiles. Initially, at  $T_s=380$  s, sediment packed bed downstream of Type (B) basin was found fully eroded at the end and soon after the rigid bed. However, models were further run for extra 120 s to observe the maximum scour depth

downstream of Type (A), (C) and (D) stilling basin. The details of scour pattern and depths are provided in the chapter 5.

### 3.15.4 Performance Assessment of Scour Models

The performance of present scour models is assessed by the Coefficient of determination ( $R^2$ ), which can be measured by the expression (3.21).

$$R^2 = 1 - \frac{SS_{res}}{SS_{tot}} \quad (3.21)$$

where,  $SS_{res}$  is sum of square of residuals between the field observation and predicted data and  $SS_{tot}$  shows total sum of squares between the field observations and mean of field data. The model shows the perfect agreement between the observed and predicted data when the  $R^2$  values reached 1, however,  $R^2$  value higher than 0.70 is considered to good. For the present models, upon use of different turbulence models, the scour profiles downstream of Type (B) basin are used for comparison with the observed field data. In addition to  $R^2$ , the study also employed the Nash-Sutcliffe efficiency (NSE) Coefficient to measure the relative residual variance of the simulated data as compared to the observed data. The model performance is believed to perfect if the value reaches to 0 while it is said to poor when the values become negative. The expression (3.22) is applied to draw comparison between riverbed and the modelled scour profiles.

$$NSE = 1 - \frac{\sum_{i=1}^n (obs_i - sim_i)}{\sum_{i=1}^n (obs_i - \overline{obs})} \quad (3.22)$$

where,  $obs_i$ ,  $sim_i$  are the field and models' value, respectively while  $\overline{obs}$  is the mean of field values.

## Chapter 4

# Identification of Hydraulic Parameters & Performance of Stilling Basins

### 4.1 Background

The critical hydraulic parameters from the literature are identified using frequency analysis and relative importance index (RII). Velocity, Froude number, free surface profile, shape of stilling basin, turbulent kinetic energy, and tail water were found as the most investigated parameters in the literature. To investigate above mentioned hydraulic parameters on various discharges i.e., 2.44, 4.88, and 7.22 m<sup>3</sup>/s/m, different stilling basin's appurtenances were installed downstream of studied barrage. The performance of different stilling basins was assessed on the basis of free surface profile, sequent depths, roller lengths, relative energy loss in hydraulic jump, VPs and turbulent kinetic energy.

## 4.2 Identification of Critical Parameters

The hydraulic parameters in Chapter 3 (see Tables 3.2 & 3.3) are placed according to their frequency of occurrence and the total number of parameters in numerical, and experimental studies were found to be twenty-four (24) and twenty-three (23), respectively.

After analysis, it was found that fifteen (15) parameters were common in both types of studies (numerical and experimental). After adding all the extracted parameters (numerical and experimental), in total thirty-three (33) parameters were found from published data as shown in Table 4.3. In Table 4.1, relative Impor-

TABLE 4.1: Parameters' Frequency, RII and ranking in numerical studies.

Parameters	Frequency	RII	Rank	Parameters	Frequency	RII	Rank
VP	16	0.155	1st	WSS	2	0.019	10th
FSP	15	0.146	2nd	BSS	2		
PP	11	0.107	3rd	TWL	1		
TKE	8	0.078	4th	CC	1		
AV	7	0.068	5th	HL	1		
DM	6	0.058	6th	FF	1		
$Fr_1$	6	0.058		MC	1	0.010	11th
$\eta$	5	0.049	7th	EC	1		
SS	4	0.039	8th	DC	1		
SDHJ	4	0.039		SP	1		
RSS	3	0.029	9th	BP	1		
LHJ	3	0.029		ED	1		

tance Index (RII) showed that Velocity Profile (VP), Free Surface Profile (FSP), Pressure Profile (PP), Turbulence Kinetic Energy (TKE), Air Volume Value (AV), Discharge Measurement (DM), Shape of Stilling Basin (SS),  $Fr_1$  and HJ efficiency

( $\eta$ ) were found to be the most critical parameters which were studied in numerical researches.

From Table 4.2, it was found that VP,  $Fr_1$ , TWL, SS, FSP, BP, SP, and ED were the most critical parameters on which several numerous experimental works were carried out during the past years. After combining parameters from experimental and numerical studies, the RII showed that VP, FSP,  $Fr_1$ , SS, TWL, PP, BP, TKE, SP, and ED were found to be the most critical parameters based as shown in Table 4.3.

TABLE 4.2: Parameters' Frequency, RII and ranking in experimental studies

Parameters	Frequency	RII	Rank	Parameters	Frequency	RII	Rank
VP	24	0.125	1st	TI	5	0.026	11th
$Fr_1$	24	0.125		SM	4	0.021	12th
TWL	20	0.104	2nd	LHJ	4	0.021	
FSP	19	0.099	3rd	RG	3	0.016	13th
SS	17	0.089	4th	$\eta$	3	0.016	
BP	14	0.073	5th	MF	2	0.010	
SP	13	0.068	6th	VF	2	0.010	14th
ED	9	0.47	7th	SDHJ	2	0.010	
BSS	7	0.036	8th	TP	1	0.005	
TKE	6	0.031	9th	PS	1	0.005	15th
PP	6	0.031		$(\Delta E/E_1)$	1	0.005	
RSS	5	0.026	10th				

The results of relative percentage score were categorized in three different levels as shown in Table 4.4.

Parameters which were positioned above 5%, were found to be highly significant; 3-5 % were moderately significant, and below 3% were less significant [103], [99], [208], [45]. The significance of the parameters was based on their occurrence in

TABLE 4.3: RII and ranking of parameters after combining numerical and experimental studies.

Parameters	Frequency	RII	Rank	Parameters	Frequency	RII	Rank
VP	40	0.14	1st	SDHJ	6	0.021	14th
FSP	31	0.11	2nd	TI	5	0.017	15th
$Fr_1$	30	0.1	3rd	SM	4	0.014	16th
SS	21	0.08	4th	RG	3	0.01	17th
TWL	21	0.07	5th	MF	2	0.007	
PP	17	0.05	6th	VF	2	0.007	18th
BP	15	0.06		WSS	2	0.007	
TKE	14	0.06	7th	CC	1	0.003	
SP	14	0.06		HL	1	0.003	
ED	10	0.04	8th	FF	1	0.003	
BSS	9	0.03		MC	1	0.003	
RSS	8	0.03	9th	EC	1	0.003	19th
$\eta$	8	0.02	10th	DC	1	0.003	
AV	7	0.03	11th	ES	1	0.003	
LHJ	7	0.01	12th	TP	1	0.003	
DM	6	0.02	13th	PS	1	0.003	
				$(\Delta E/E_1)$	1	0.003	

literature as investigated by many researchers. Based on the results of relative percentage score, in total nine (9) parameters were found to be highly significant, while 2, and 22 parameters were moderately and less significant, respectively.



TABLE 4.4: Relative % score and ranking based on frequency of occurrence of parameters in literature [223], [225], [226]

Parameters	Frequency	Relative Frequency	PA	RPA	% score	Relative % score	Parameters	Frequency	Relative Frequency	PA	RPA	% score	Relative % score
VP	40	0.137	2	1	0.137	14.71	TI	5	0.017	1	0.34	0.006	0.63
FSP	31	0.106	2	1	0.106	11.40	SM	4	0.014	1	0.34	0.005	0.50%
$Fr_1$	30	0.103	2	1	0.103	11.04	RG	3	0.010	1	0.34	0.003	0.38
SS	21	0.072	2	1	0.072	7.72	MF	2	0.007	1	0.34	0.002	0.25
TWL	21	0.072	2	1	0.072	7.72	VF	2	0.007	1	0.34	0.002	0.25
PP	17	0.058	2	1	0.058	6.25	WSS	2	0.007	1	0.66	0.005	0.49%
BP	15	0.051	2	1	0.051	5.52	CC	1	0.003	1	0.66	0.002	0.24
TKE	14	0.048	2	1	0.048	5.15	HL	1	0.003	1	0.66	0.002	0.24
SP	14	0.048	2	1	0.048	5.15	FF	1	0.003	1	0.66	0.002	0.24
ED	10	0.034	2	1	0.034	3.68	MC	1	0.003	1	0.66	0.002	0.24
BSS	9	0.031	2	1	0.031	3.31	EC	1	0.003	1	0.66	0.002	0.24
RSS	8	0.027	2	1	0.027	2.94	DC	1	0.003	1	0.66	0.002	0.24
$\eta$	8	0.027	2	1	0.027	2.94	ES	1	0.003	1	0.66	0.002	0.24%
AV	7	0.024	1	0.66	0.016	1.70	TP	1	0.003	1	0.34	0.001	0.13
LHJ	7	0.024	2	1	0.024	2.57	PS	1	0.003	1	0.34	0.001	0.13
DM	6	0.021	1	0.66	0.014	1.46	$(\Delta E/E_1)$	1	0.003	1	0.34	0.001	0.13
SDHJ	6	0.021	2	1	0.021	2.21							

Based on frequency analysis, RII and relative % score, the overall relative position of CHPs is shown in Table 4.5. Table 4.5 shows that, except VP, all other parameters were changing their position literature. Table 4.5 further showed that VP,  $Fr_1$ , FSP, SS, TKE and TWL were found to be the most significant parameters in the literature, and therefore, for hydraulic investigation the focus of the present numerical study was made to these parameters for the studied stilling basins.

TABLE 4.5: Relative position of parameters from literature using different statistical methods

Parameters	Ranking from Table-4.1	Ranking from Table-4.2	Ranking from Table-4.3	Ranking from Table-4.4	Overall occurrence
(1)	(2)	(3)	(4)	(5)	(6) = 2)+(3)+(4)+(5)
VP	1st	1st	1st	1st	4
$Fr_1$	6th	1st	3rd	3rd	4
FSP	2nd	NA	2nd	2nd	3
SS	NA*	4th	4th	4th	3
TKE	4th	NA	7th	8th	3
TWL	NA	2nd	5th	5th	3

### 4.3 Hydraulic Modelling

#### 4.3.1 Results of Gated and Free Flow

For the investigated basins, the models' accuracy was checked by the discharge rating curves of free and gated flow at the outlet boundaries (Johnson and Savage [105]; Savage and Johnson [104]; Chanel and Doering [183]). The models results were compared with the flow rates of the prototype. For gated flow of 2.44 m<sup>3</sup>/s/m discharge, the present models produced 2.70, 2.50, 2.57 and 2.50 m<sup>3</sup>/s/m discharge in Type (A), (B), (C) and (D) basins, respectively, as shown in Table 4.6.

Similarly, at 4.88 m<sup>3</sup>/s/m unit discharge, the models values reached to 5, 5.10, 5.50, and 5.40 m<sup>3</sup>/s/m in Type (A), (B), (C) and (D) basins, respectively as presented in Table 4.6. For 7.22 m<sup>3</sup>/s/m discharge, the models underestimated the discharge values in Type (A) and (B) basins while overestimation of discharge was noticed in Type (C) and (D) basins.

The overall percentage errors for the investigated discharges were found to be between -3 to 14.5 % which showed that the present models produced acceptable results of discharge rating curves.

Additionally, upon comparison with field data, 83.33 % of the models' results are found to be higher than the compared values. However, in all basins, % errors on higher discharge were found to be less than the lower discharge. For free flow analysis, the present models were run for 100 %, 90% and 75 % of the designed discharge capacity of the barrage.

As compared to 2010 flood data, the results indicated that about 87.5 % of present models showed a little overestimation of the free flows as shown in Table 4.6.

## **4.4 Results of Hydraulic Parameters for Gated Discharge**

### **4.4.1 Free Surface Profiles (FSPs)**

VOF method was used to obtain FSPs within different stilling basins at various discharges. In the beginning with change of time step and due to the inlet velocity, the FSPs were changed which stabilized when the models reached to the steady state.

In all the models, from gate opening to hydraulic jump (HJ) initiating point, the FSPs in the supercritical region followed a similar trend. However, locations of the

TABLE 4.6: Comparison of gated discharges with Prototype discharge of year 2010 ([43])

<b>Gated Flow (m<sup>3</sup>/s/m)</b>									
Stilling basins									
	Actual	Predicted	% Error	Actual	Predicted	% Error	Actual	Predicted	% Error
Type (A)	2.4	2.7	12.5	4.8	5	4	7.22	7	-3
Type (B)	2.4	2.5	4	4.8	5.1	6	7.22	6.9	-4.4
Type (C)	2.4	2.57	7	4.8	5.5	14.5	7.22	7.4	2
Type (D)	2.4	2.5	4	4.8	5.4	12.5	7.22	7.4	2

<b>Free Flow (m<sup>3</sup>/s/m)</b>									
Stilling basins									
	100 %	Predicted	% Error	90 %	Predicted	% Error	75 %	Predicted	% Error
Type (A)	24.3	24.5	0.8	21.7	22.3	2.7	18	17	-5
Type (B)	24.3	23.33	3	21.7	21.23	-2	18	18.4	2
Type (C)	24.3	24.85	2.2	21.7	22.94	5	18	18.6	3
Type (D)	24.3	25.6	5	21.7	22	1	18	18.33	2

hydraulic jumps (HJ) were found to be different which also varied as the discharges were changed.

Fig 4.1 shows FSPs within different stilling basins at 2.44 m<sup>3</sup>/s/m discharge. In the supercritical flow region, flow pattern was observed similar while locations of the hydraulic jump were found different.

However, locations of the HJs were found at the downstream glacis. Fig. 4.1, in Type (A), Type (B), Type (C), and Type (D) basins, distances of the HJs initiating points from toe of the glacis were 4.90 m, 4.67 m, 4.66 m, and 4.50 m, respectively. In HJ regions, except Type (B) basin, trends of the FSPs were observed identical.

However, within the HJ region, a small fall of free surface was also observed in Type (A) basin while Type (C), and Type (D) basins showed similar FSPs.

After the jump initiating point, in Type (B) basin, the free surface profile remained supercritical which was found to be raised as the distance from the HJ initial location was increased. The results of FSP in Type (B) basin further indicated an undulating free surface within the HJ region which showed deviation from the other studied basins as shown in Fig. 4.1. After the HJ, the FSPs in all the basins followed a similar pattern, however, small fluctuations were observed in the FSPs because of the types of HJ profiles produced by different basins.

In comparison to the other stilling basins, after the HJ in Type (B) basin, a dropped FSP was observed in the subcritical flow region.

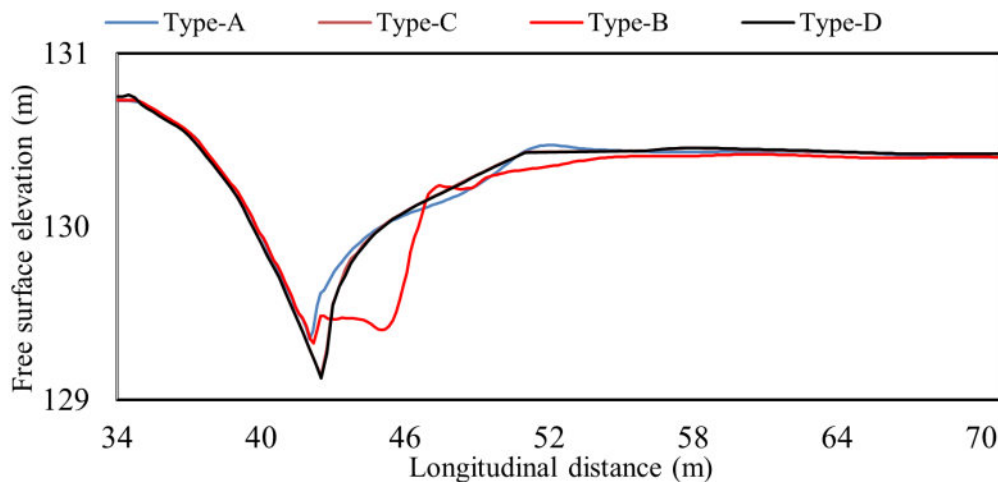


FIGURE 4.1: FSPs in different basins at 2.44 m<sup>3</sup>/s/m

Fig 4.2 illustrates FSPs in different basins at 4.88 m<sup>3</sup>/s/m discharge. In the supercritical region, the FSPs followed the similar trend while variations were seen in the HJ region.

The results of the FSPs indicated different locations and lengths of HJ in different basins. In Type (A), (B), (C), and (D) basins, the distances of the HJs initiating points from toe of the glacis were 6.10 m, 5.23 m, 5.19 m, and 4.86 m, respectively. However, in all the basins, the locations of HJ were noticed on the downstream glacis.

In sub critical region, the basin with WSBB such as Type (C), and Type (D) showed a similar trend of FSPs while different trends were noticed in Type (A)

and (B) basins. After HJ, the FSP in Type (B) basin showed deviation from the rest of investigated basins as shown in Fig. 4.2.

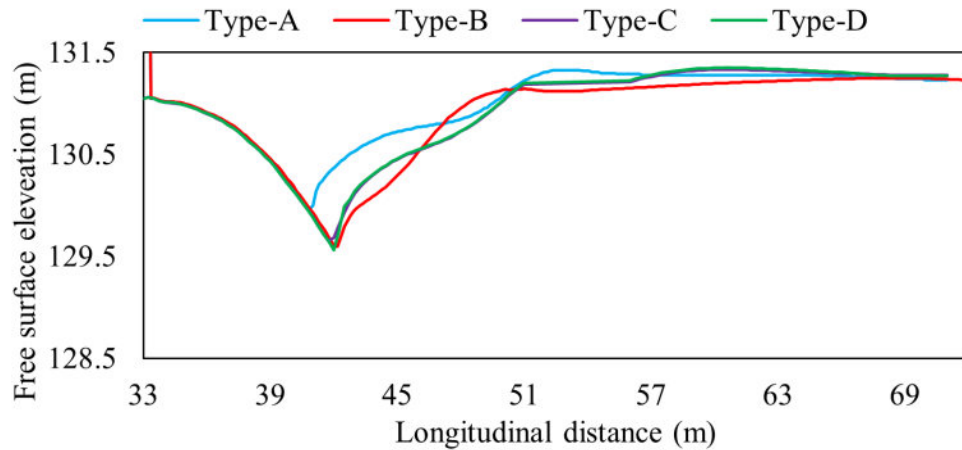


FIGURE 4.2: FSPs in different basins at 4.88 m<sup>3</sup>/s/m

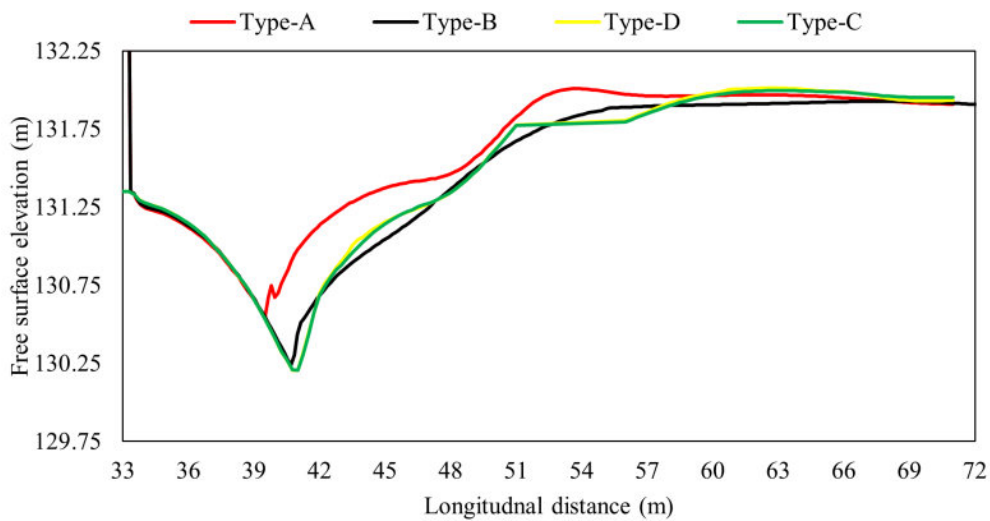


FIGURE 4.3: FSPs in different basins at 7.22 m<sup>3</sup>/s/m

Fig. 4.3 shows the FSPs in different basins at 7.22 m<sup>3</sup>/s/m discharge. In all the investigated basins, identical flow behaviors were noticed in the supercritical flow regions. Except Type (B) basin, similar flow patterns were observed in the HJ region, however, deviations were noticed in the supercritical region as shown in Fig. 4.3.

The location of HJ in the tested basins were noticed at the glaxis while their lengths and distances from the toe glaxis were found to be different. The basins with WSBB showed similar trend of flow in the subcritical region. However, Type

(A) basin showed higher free surface elevation after the HJ which gradually level off at the end of the basin.

In Type (B) basin a curvilinear flow pattern was observed from jump initiating to termination locations and the flow became steady after the HJ. Additionally, in Type (B) basin, the elevation of the FSPs in the subcritical region was less than that was observed in other basins.

Bakhmeteff and Matzke [259] developed hydraulic jump similarity models and proposed dimensionless Eq. 4.1 for FSP of HJs.

$$\Gamma(X) = \tan(h(1.5.X)) \tag{4.1}$$

where,  $\Gamma(X)$  is flow depth at  $X(h_i)$  in which variable  $X$  is the dimensionless longitudinal coordinates, as shown in the dimensionless Eq. 4.2 and 4.3, respectively.

$$\Gamma(X) = \frac{(h_i - h_1)}{(h_2 - h_1)} \tag{4.2}$$

$$X = \frac{(X_i - X_1)}{(X_2 - X_1)} \tag{4.3}$$

where  $h_1$  and  $h_2$  are the flow depths in supercritical and subcritical regions, respectively.  $X_1$  and  $X_2$  are functions of variable  $X$ , and their values can be calculated at the toe of HJ and end of the roller region, respectively. The components of Eqs. 4.2 and 4.3 are shown in the below schematic diagram 4.4 .

Fig. 4.5 compares results of FSPs with Bayon-Barrachina et al. [99] (RNG K- $\epsilon$ ) and Wang and Chanson [115] at 2.44 m<sup>3</sup>/s/m. Except, Type (B) basin, the FSPs in all other basin were found close to the compared studies. Out of the present basins, FSPs produced by Type (D) basin showed more accurate results when compared with Bayon-Barrachina et al. [99] (RNG K- $\epsilon$ ). After comparing results with Wang and Chanson [115], except Type (B) basin, the FSPs in all other basin showed close agreement.

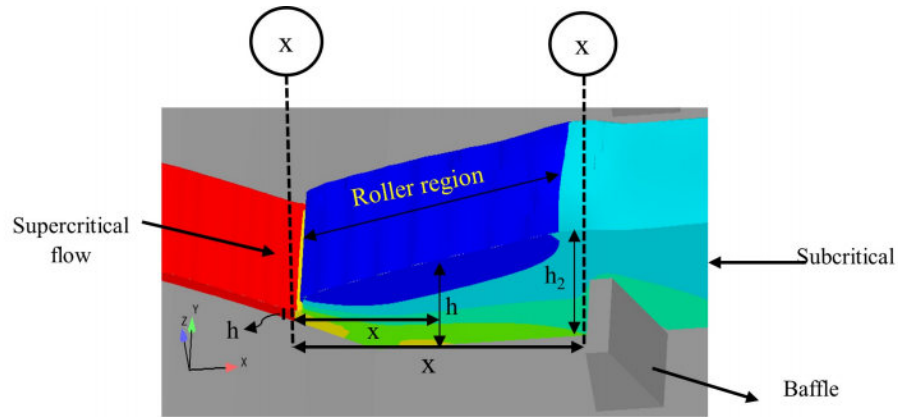


FIGURE 4.4: Schematic diagram showing the components of dimensionless FSP of HJ

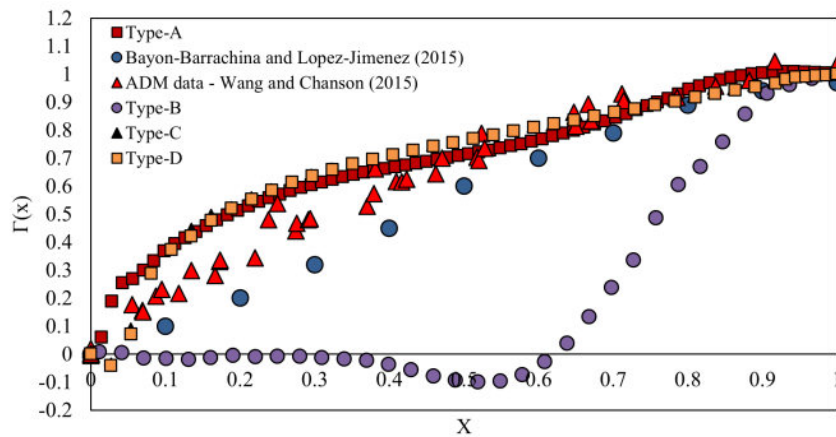


FIGURE 4.5: Dimensionless FSPs of HJ at 2.44 m<sup>3</sup>/s/m discharge

Like 2.44 m<sup>3</sup>/s/m discharge, the FSPs within the investigated stilling basins at 4.88 m<sup>3</sup>/s/m followed the trends of Bayon-Barrachina et al. [99] (RNG K-ε) and Wang and Chanson [115].

As compared to the lower discharge, the FSPs within Type (B) basin at 4.8 m<sup>3</sup>/s/m discharge showed improvement and its trend was found identical to the compared studies as shown in Fig.4.6. Except for the result of FSP in Type (B) basin, all other FSPs showed a close agreement with Wang and Chanson [115].

Fig. 4.7 shows the dimensionless FSPs in Type (A), B, C, and D basins at 7.22 m<sup>3</sup>/s/m discharge. In the tested basins, all the FSPs showed identical trend and agreed with the compared with numerical study of Bayon-Barrachina et al. [99] (RNG K-ε) and experimental study of Wang and Chanson [115].



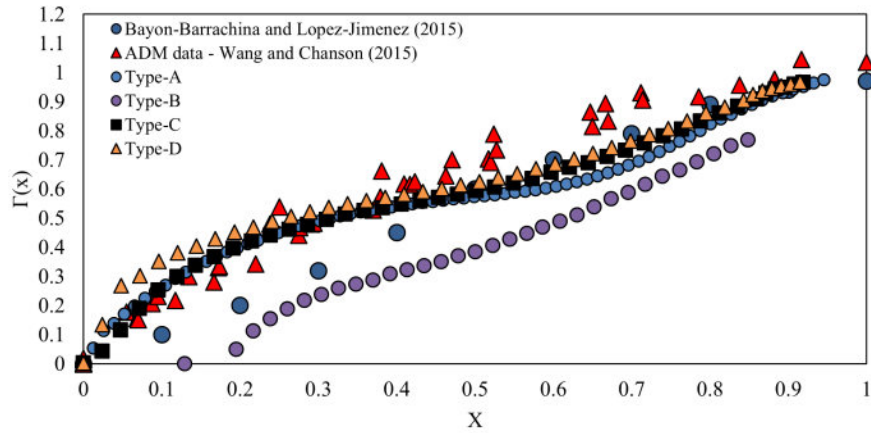


FIGURE 4.6: Dimensionless FSPs of HJ at 4.88 m<sup>3</sup>/s/m discharge

However, the FSPs in the Type (B) stilling basin showed more promising results when compared with the literature data. Furthermore, at the HJ Initiating locations, the results of the FSPs in Type (B) and (D) basins showed a small deviation than the compared studies and found to be agreed as the distance from HJ initiating location was increased.

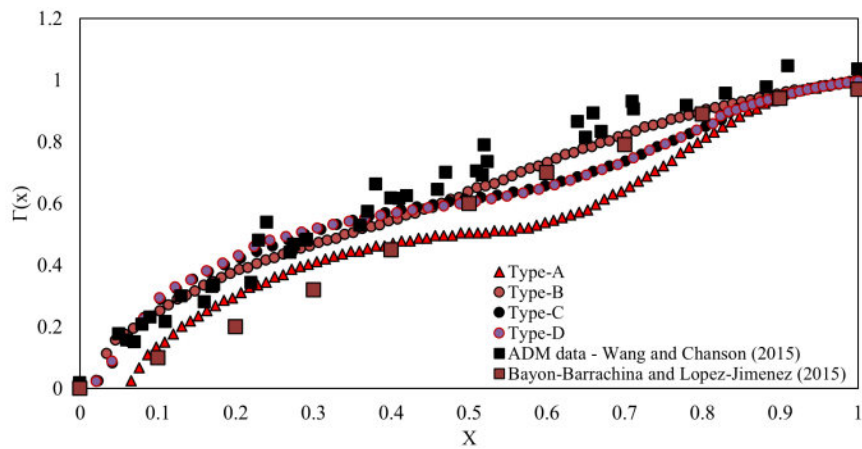


FIGURE 4.7: Dimensionless FSPs of HJ at 7.22 m<sup>3</sup>/s/m discharge

The analysis of FSPs of HJ in different basins indicated that at the lower discharge, the basin with USBR baffle block (Type (A)) and WSBB (Type (C) & (D)) showed identical patterns of FSPs. However, the basins with wedge shaped baffle block (Type (C) & (D)) reduced the lengths of the HJ while a complex flow phenomenon was observed in the basin with chute and end sill (Type (B)).

After increasing the flow, the lengths of HJ in wedge-shaped baffle block basins (Type (C) & (D)) were found to be reduced while their locations on the glacis were found below than that was observed in USBR baffle block basin (Type (A)).

On the other hand, in chute and end sill basin (Type (B)), the FSPs were improved which matched with other basins. Like the lower flows, at the higher flow, the HJ lengths in Type (C) & (D) basins were less than Type (A) & (B) basins. However, FSPs within and after the HJ were found to be similar in all the basins.

Table 4.7 shows lengths of HJ in different basins at the studied discharges. In Type (A) and (B) basins, results showed a linear trend between discharge and length of the HJ, however, in Type (B) basin, at higher discharge (7.22 m<sup>3</sup>/s/m), increase in the HJ length was found higher than Type (A) basin.

In Type (C), and (D) basins, a linear trend between discharge and HJ length was observed, and the results further showed that at higher discharge, the length of HJ was increased than that was found at the lower discharge.

TABLE 4.7: Length of HJs in the studied basins

Discharge (m <sup>3</sup> /s/m)	Type (A)	Type (B)	Type(C)	Type (D)
<b>Length of Hydraulic Jump (m)</b>				
2.44	9.7	5.0	9.5	9.3
4.88	11.5	7.0	10.7	10.5
7.22	12.9	13.0	12	12.1

#### 4.4.2 Sequent Depths

Table 4.8 shows the sequent depths ratio within different basins at various discharges i.e., 2.44, 4.88, and 7.22 m<sup>3</sup>/s/m.

At the lower discharge (2.44 m<sup>3</sup>/s/m), minimum and maximum sequent depth ratio was 11.18 and 13.88 in Type (D) and (B) basins, respectively. At higher

discharge (7.22 m<sup>3</sup>/s/m), the minimum and maximum sequent depths ratio was obtained in Type (B) and Type (C) basins, respectively.

It is worth mentioning here that that in all the basins, as the discharge was increased , the sequent depths ratio was gradually decreased which indicated a linear trends.

TABLE 4.8: Sequent depths ratio in the studied basins

Discharge (m <sup>3</sup> /s/m)	Type (A)	Type (B)	Type (C)	Type (D)
	<b>Sequent depths ratio</b>			
2.44	12.17	13.88	12.8	11.18
4.88	7.41	7.60	8.13	8.30
7.22	5.82	5.55	5.70	5.85

### 4.4.3 Roller Lengths

Carollo et al.[260] indicated that the roller length, which is measured between the HJ toe and end of the rollers is found to be a better length parameter as compared to HJ length. The literature further described that the roller length was easy to measure, observe and can properly be specified for steady flow conditions [123]. However, on the contrary, due to flow oscillations, turbulence, and surface waves, length of HJ is difficult to measure.

Figs. 4.8, 4.9, 4.10 show the comparison of dimensionless roller lengths ( $L_r/d_1$ ) with initial Froude number ( $Fr_1$ ) at various discharge in the different stilling basins, whereas  $L_r$  is the length of rollers in HJs and  $d_1$  is the flow depth in supercritical region before the HJ.

At the lower discharge (2.44 m<sup>3</sup>/s/m) as shown in Fig. 4.8, except in the Type (B) basin, the present model showed larger roller lengths which showed deviation from the compared experimental studies ([261] [262] [115]). On the contrary, in

Type (B) basin, the model underestimated the roller length when compared with the previous studies and other investigated basins.

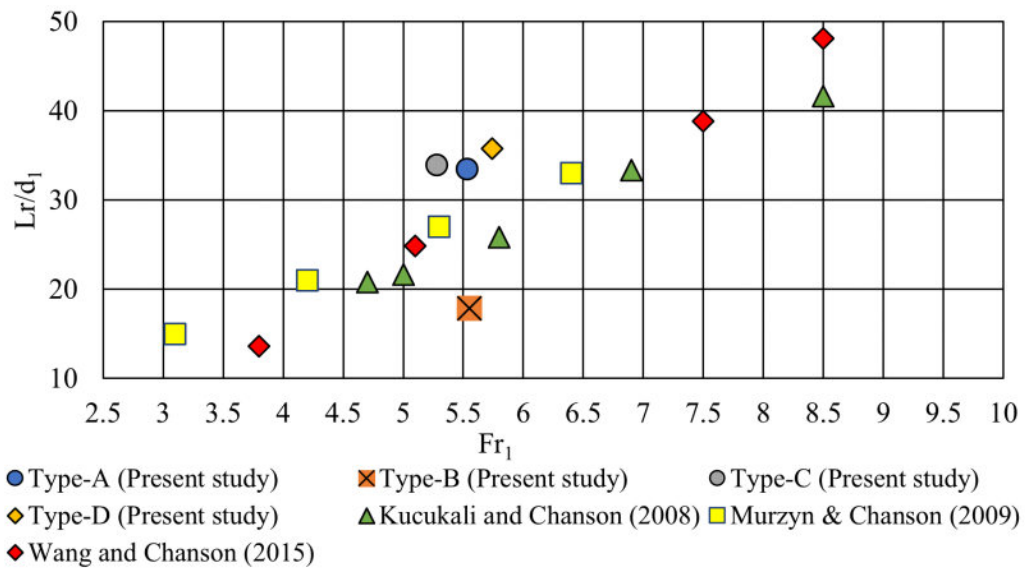


FIGURE 4.8: Roller length of HJ in different stilling basins at unit discharge of  $2.44 \text{ m}^3/\text{s}/\text{m}$

At  $4.88 \text{ m}^3/\text{s}/\text{m}$  discharge, Except Type (B) basin, all basin produced approximately identical roller lengths, however, small difference can be seen due to change of shape of baffle blocks which controlled these roller lengths as shown in Fig. 4.9. On the contrary, the roller length in Type (B) basin was about 50 % less than other investigated models and showed deviation from the compared experimental studies.

At  $7.22 \text{ m}^3/\text{s}/\text{m}$  discharge, like the lower discharge, the basins with USBR and WSBB (Type (A), (C), and (D), respectively) showed the identical roller lengths which agreed with the literature studies, while in Type (B) basin, the roller length was found higher than the other models. Out of the compared experimental data, the model showed close agreement with [262]. Furthermore, the results showed that as the flow was increased, the roller length within Type (A), (C) and (D) basins were found to be decreased while opposite behavior was noticed in Type (B) basin as can be seen in Fig. 4.10.

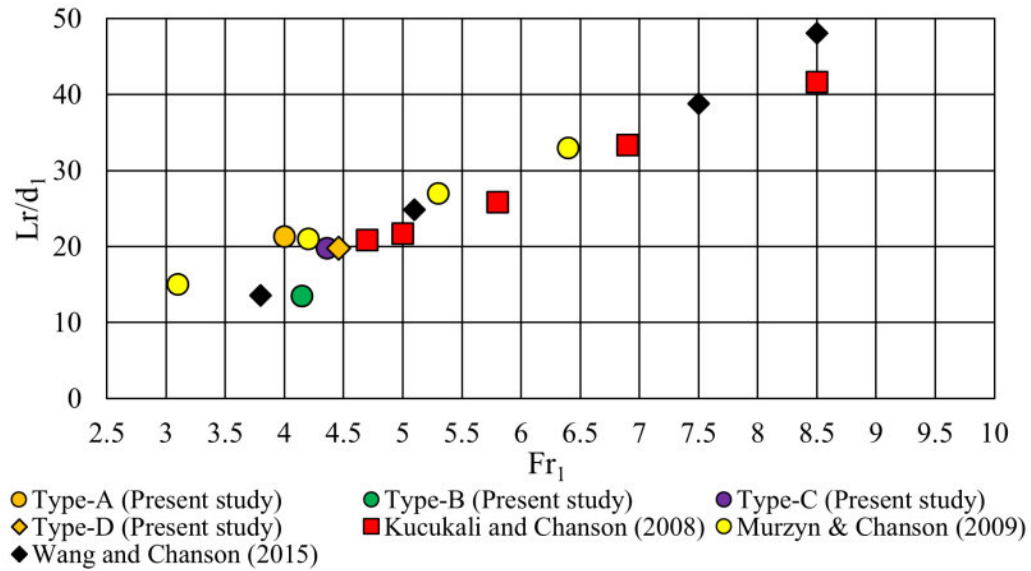


FIGURE 4.9: Roller length of HJ in different stilling basins at unit discharge of 4.88 m<sup>3</sup>/s/m

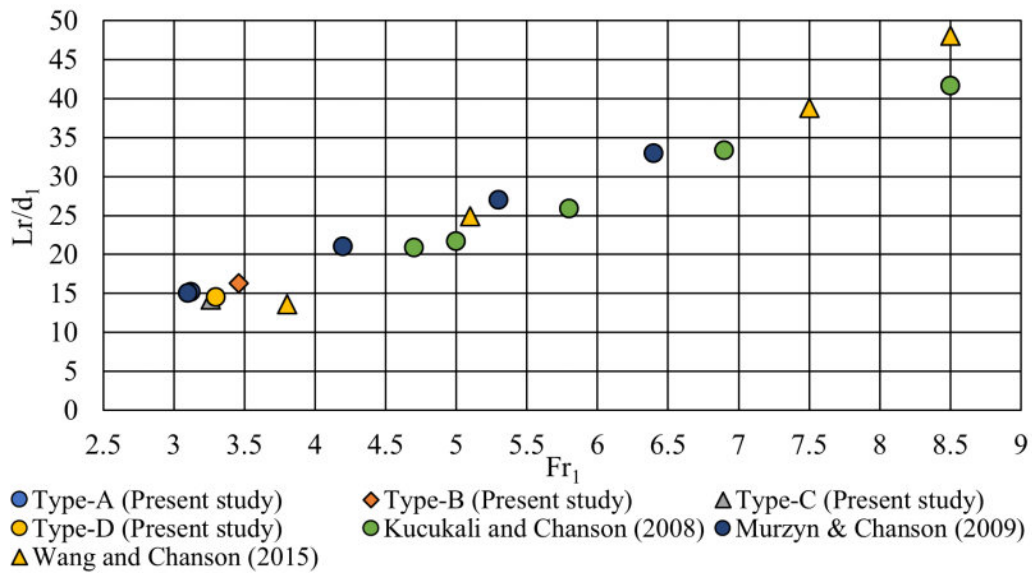


FIGURE 4.10: Roller length of HJ in different stilling basins at unit discharge of 7.22 m<sup>3</sup>/s/m

#### 4.4.4 Relative Energy Loss

The relative energy loss within the HJs was calculated by the following expression (4.4). It states that relative loss is the ratio of energy loss between the two different sections (upstream and downstream heads) of HJ to the upstream hydraulic head. Whereas,  $h_i$ ,  $v_i$  and  $g$  are the variables of relative energy loss in the HJs.

$$\eta = \frac{\Delta H}{H_1} = \frac{H_2 - H_1}{H_1} \tag{4.4}$$

where,  $H_1$  and  $H_2$  are the energy heads of two different sections (upstream and downstream) of HJs.

Table 4.10 shows the relative energy loss of the investigated Type (A), (B), (C), and (D) basins at different discharges i.e., 2.44, 4.88, and 7.22 m<sup>3</sup>/s/m. From Table 4.10, it is noted that as the flow was increased, the relative energy loss of HJs was found to be decreased in the studied basins. In Type (A) and (B) basins, a decreasing linear trends of energy loss was observed while a nonlinear trends were observed in Type (C), and (D) basins.

TABLE 4.9: Energy loss in different basins at various gated flows

Discharge (m <sup>3</sup> /s/m)	Stilling basins	Energy at ( $E_1$ )	Energy at ( $E_2$ )	Relative energy loss (%)
2.44	Type (A)	4.39	3.54	19
	Type(B)	4.00	3.23	19
	Type(C)	4.50	3.70	18
	Type(D)	4.54	3.68	19
4.88	Type(A)	4.79	4.38	8
	Type(B)	4.99	4.31	14
	Type(C)	5.64	4.56	19
	Type(D)	5.10	3.78	26
7.22	Type(A)	5.15	5	3
	Type(B)	5.15	4.96	4
	Type(C)	5.37	5.15	4
	Type(D)	5.42	5.23	3

At the investigated flows, the maximum energy loss with HJ was noticed at 4.88 m<sup>3</sup>/s/m discharge in Type (C) and (D) basins which reached 19 and 26 %, respectively. As compared to other basins, Type (C) basin showed higher relative energy loss at the studied gated discharges.

#### 4.4.5 Velocity Profiles (VPs)

To obtain vertical VPs, velocity was measured before, within, and after the HJ at different flow depths in the studied stilling basins. In Type (A), (B), (C), and (D) basins, the maximum value of forward velocity was observed after the toe of HJ (at  $X=2$  m), and their values reached to 5.31, 7.53, 5.17, and 5.46 m/s, respectively as shown in Figs. 4.11 (a), (b), (c), and (d), respectively. As the distances from the HJ increased, the values of vertical velocity were found decreased which decayed before the end of basins as noted in [138][137].

As compared to other basins, after the HJ, at  $X=12$  m, the minimum velocities were observed in Type (A) basin while maximum velocity was observed in Type (B) basin which reached 2.2 m/s. The forward velocity profile from the HJ initiating to the termination point showed the identical trends in Type (A), (C), and (D) as noted in [161][117], while a different patterns of VPs were observed in Type (B) basin.

At  $X=12$  m, the basins with WSBB (Type (C) & (D)) showed different VPs which indicated two forward regions i.e., near the bed, and at  $Z=1.5$  m as shown in Figs. 4.11 (c) and (d). At  $2.44 \text{ m}^3/\text{s}/\text{m}$ , as compared to the other basin, due to the less roller length in Type (B) basin, the velocity in the upper region started level off at  $X=10$  m, while up to  $X=10$  m, backward VPs were observed in other basins.

Fig. 4.12 illustrates velocity plots in Y-Z plane at horizontal sections i.e., after the HJ (At  $X=12$  m), and at the basin's end (At  $X=28$  m) in Type (A), (B), (C), and (D) basins. In all basins, after the HJ, the maximum values of velocity were observed at the bottom surface of the downstream glacis. However, the values were found to be different because the HJs initiating locations for the different basins were different. Except Type (B) basin, velocities in the other basins were found low at bottom and free surface.

In Type (B) basin, velocity values were found higher which reached to 8.5 m/s at top surface of the chute blocks, and 7.3 m/s between the chute blocks. On the

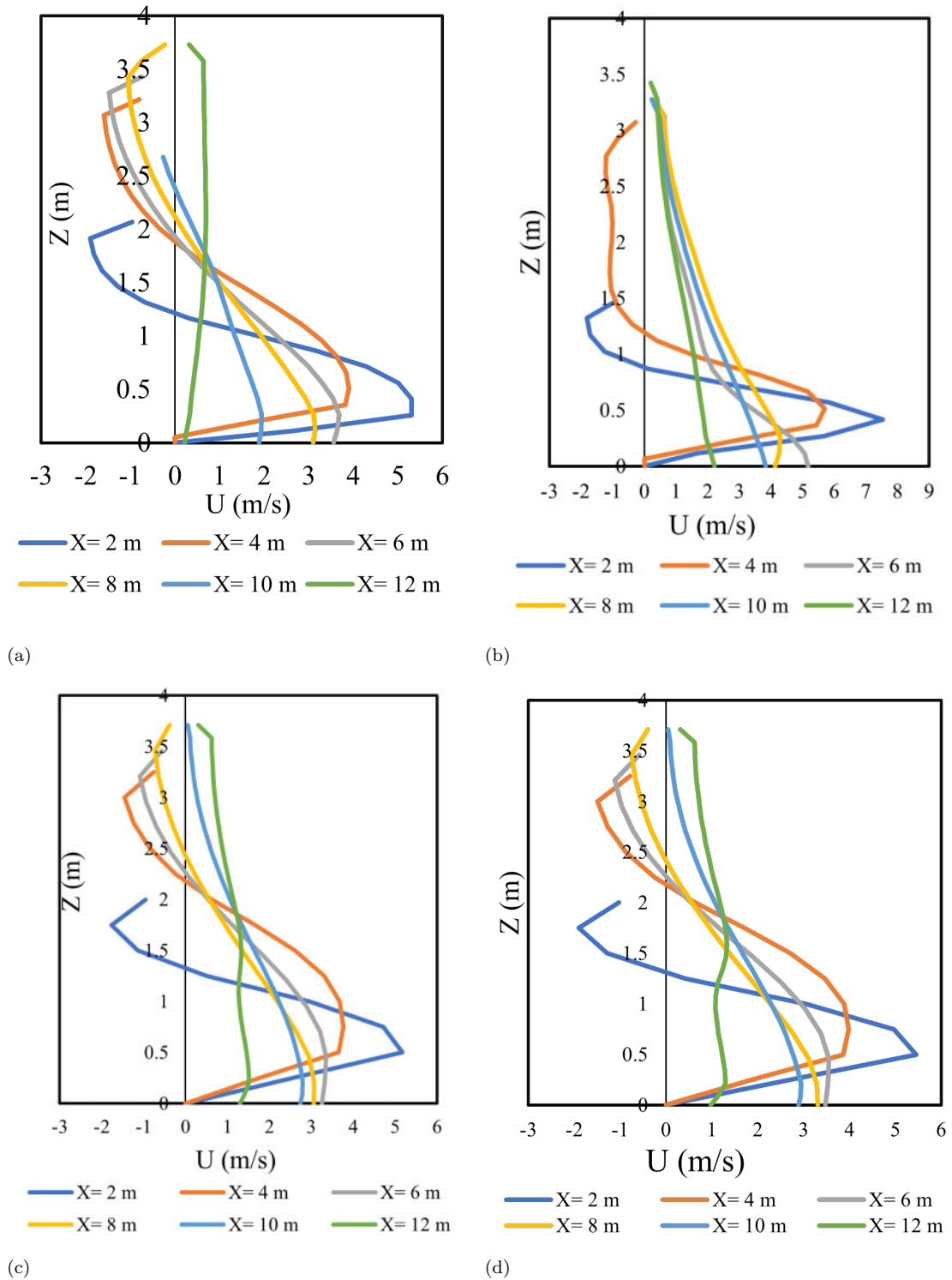


FIGURE 4.11: Vertical distribution of velocity in HJ for different stilling basins at  $2.44 \text{ m}^3/\text{s}/\text{m}$ , (a) **Type (A)**, (b) **Type (B)**, (c) **Type (C)**, and (d) **Type (D)**



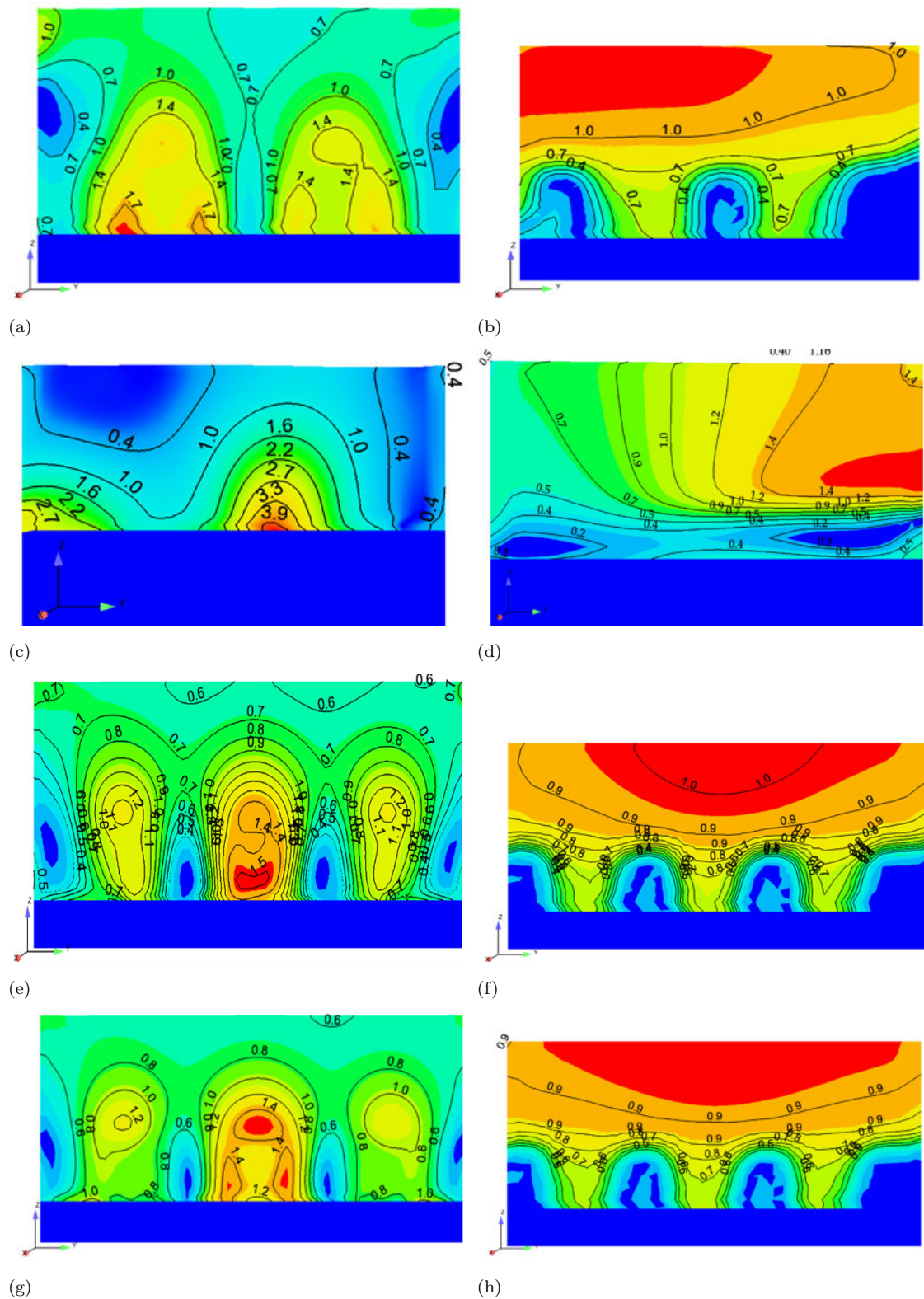


FIGURE 4.12: 2-D illustration of VPs in Y-Z plane at at  $2.44 \text{ m}^3/\text{s}/\text{m}$  in **Type (A)** (a&b), **Type (B)** (c&d), **Type (C)** (e&f), and **Type (D)** (g&h) basins

other hand, in Type (A), (C), and (D) basins, the velocity ranged from 4.8 to 5.5 m/s at bottom, and 1.3 to 1.8 m/s at the free surface.

At X= 12 m, the velocity in Type (A), (C), and (D) basins ranged between 1.2 to 1.7 m/s in the lower fluid depths as shown in Figs 4.12 (a), (e), and (g), however the maximum velocity was observed in Type (A) basin. Additionally, after the baffle blocks in Type (A), (C), and (D) basins, the velocity values were found decreased while between the baffle blocks comparatively higher values were noticed.

On the contrary, different ranges of velocity magnitude were observed in Type-B stilling basin which reached to 3.90 m/s and were higher than the rest of studies stilling basin as shown in Fig 4.12 (c). The reason for such higher velocity values was the absence energy dissipation arrangements in the basin. At the basin's end, the maximum velocities of 1.0, 1.40, 1.0, and 0.90 m/s were observed at the free surface in Type (A), (B), (C), and (D) basins, as shown in Figs 4.12 (b), (d), (f) and (h), respectively.

Fig 4.13 shows the vertical VPs at 4.88 m<sup>3</sup>/s/m discharge in Type (A), (B), (C) and (D) basins. As compared to the other basins, the maximum forward velocity was found soon after the HJ (At X=2 m) in Type (B) basin which reached to 9.45 m/s as shown in 4.13 (b). Similar to 2.44 m<sup>3</sup>/s/m discharge, the velocity pattern at 4.88 m<sup>3</sup>/s/m discharge showed identical trends. However, compared to the lower discharge, at 4.88 m<sup>3</sup>/s/m discharge, the velocities were higher at various sections within the HJ in all the stilling basins.

In comparison to 2.44 m<sup>3</sup>/s/m, at 4.88 m<sup>3</sup>/s/m, after the HJ (at X=14 m), the velocities near the bed in Type (C), and (D) basins were found less than Type (A) and (B) basins as shown in Figs. 4.13 (c) and (d). Although, in the central part of flow depths (Z= 1.5 to 2.5 m) the velocities were found higher in Type (C) and (D) basins as shown in Figs. 4.13 (c) and (d). Fig 4.13 (b) in Type (B) basin, the velocity near bed reached to 4.24 m/s compared to 2.55, 0.42, and 0.15 m/s in Type (A), (C), and (D) basins. Near the bed, the change in velocity values was due to the difference of energy dissipating arrangements, i.e., USBR blocks, WSBB, and Chute blocks & end sill etc.

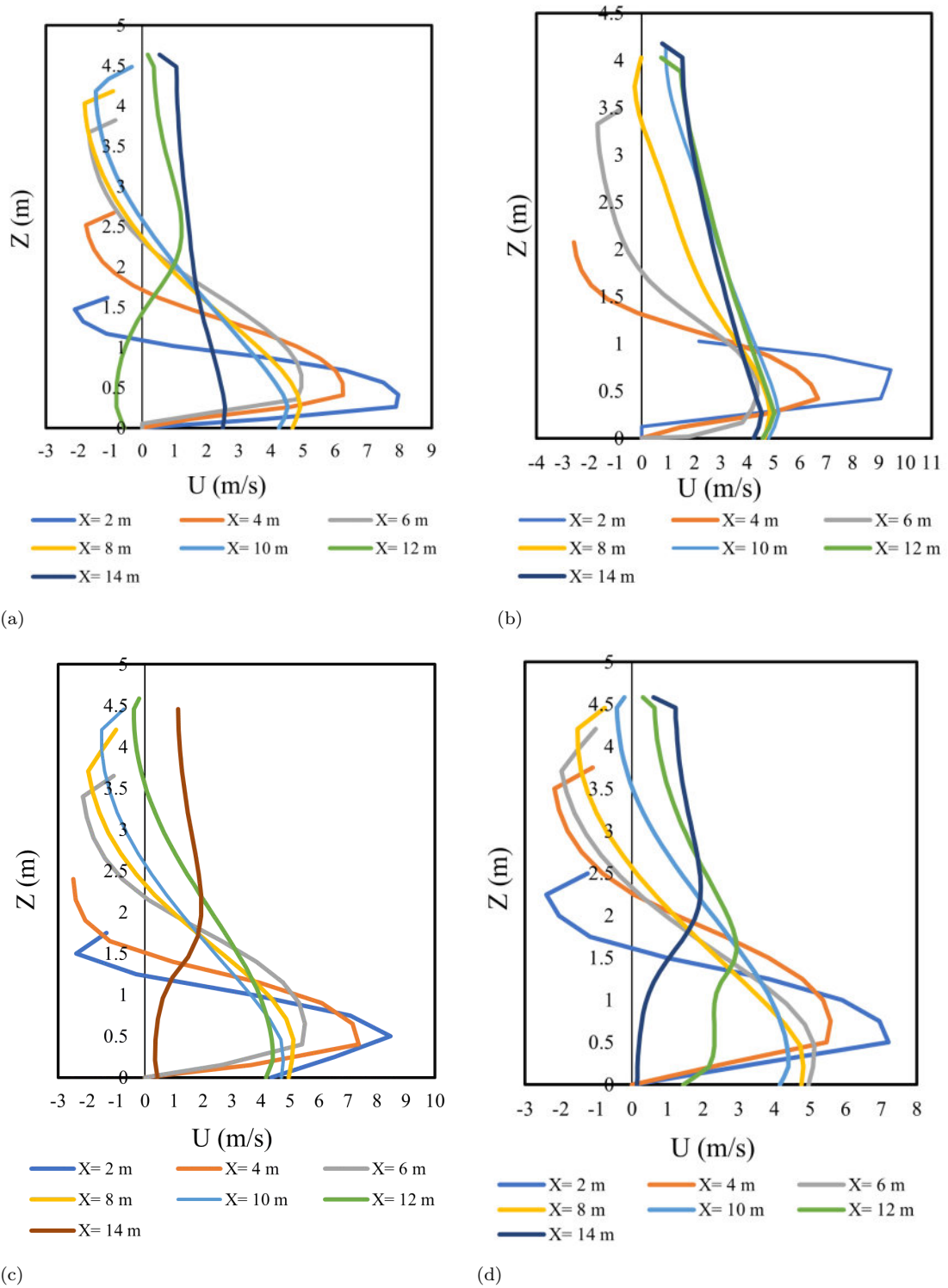


FIGURE 4.13: Vertical VPs in different stilling basins at  $4.88 \text{ m}^3/\text{s}/\text{m}$ , (a) **Type (A)**, (b) **Type (B)**, (c) **Type (C)**, and (d) **Type (D)**

Fig. 4.14 shows velocity contours in Y-Z plan at various sections in Type (A) basin. After the HJ, the maximum velocity values were found near the bed which gradually declined as the distance from the HJ initiating location was increased. The maximum velocity contours were noticed from the bed to central part of fluid depths. After the baffle blocks, the velocity values were found to be declined which reached 1.20 m/s behind the blocks, while higher values were noticed between the blocks which reached 1.90 m/s as shown in Fig 4.14 (a).

In the HJ region, higher velocities were observed near the basin's floor while fluid re-circulations were noticed near the free surface which reduced the velocities up to 1.20 m/s as shown in Fig 4.14 (a). Compared to the lower discharge ( $2.44 \text{ m}^3/\text{s}/\text{m}$ ), at  $4.88 \text{ m}^3/\text{s}/\text{m}$  discharge, velocities both at floor and free surface were found higher at the end of the basin. At the end of Type (A) basin, the maximum velocity was found in the central fluid depths which reached 1.60 m/s as shown in Fig. 4.14 (b).

In Type (B) basin, from the HJ initial location to termination point ( $X=14 \text{ m}$ ), velocity near bed remained between 9 m/s to 4.10 m/s. In the chute blocks region, velocity near and above the chute blocks remained between 5.80 to 8.70 m/s as. In Type (B) basin after the HJ (at  $X=12 \text{ m}$ ) more concentrated flow was observed between the chute blocks, and at the same regions velocity were found higher than the sides and upper fluid depths as shown in Fig. 4.14 (c). On right side of the bay, below the chute blocks, re-circulations and eddies were observed due to which velocity values were declined and remained between 0.70 to 0.60 m/s as shown in Fig. 4.14 (c). At the end of Type (B) basin, the velocity at the basin's floor reached 4.10 m/s while 1.50 m/s was noticed at the free surface as shown in Fig. 4.14 (d).

Close to the basin's floor, the velocity values were found to be declined in Type (C) basin and identical pattern was found as was noticed in Type (A) basin. Due to the larger wake areas around WSBB, the velocity after the HJ was found to be less than Type (A) basin as shown in Fig. 4.14 (e). Soon after the WSBB, value of velocity were found between 1.20 to 1.50 m/s behind the baffle blocks while

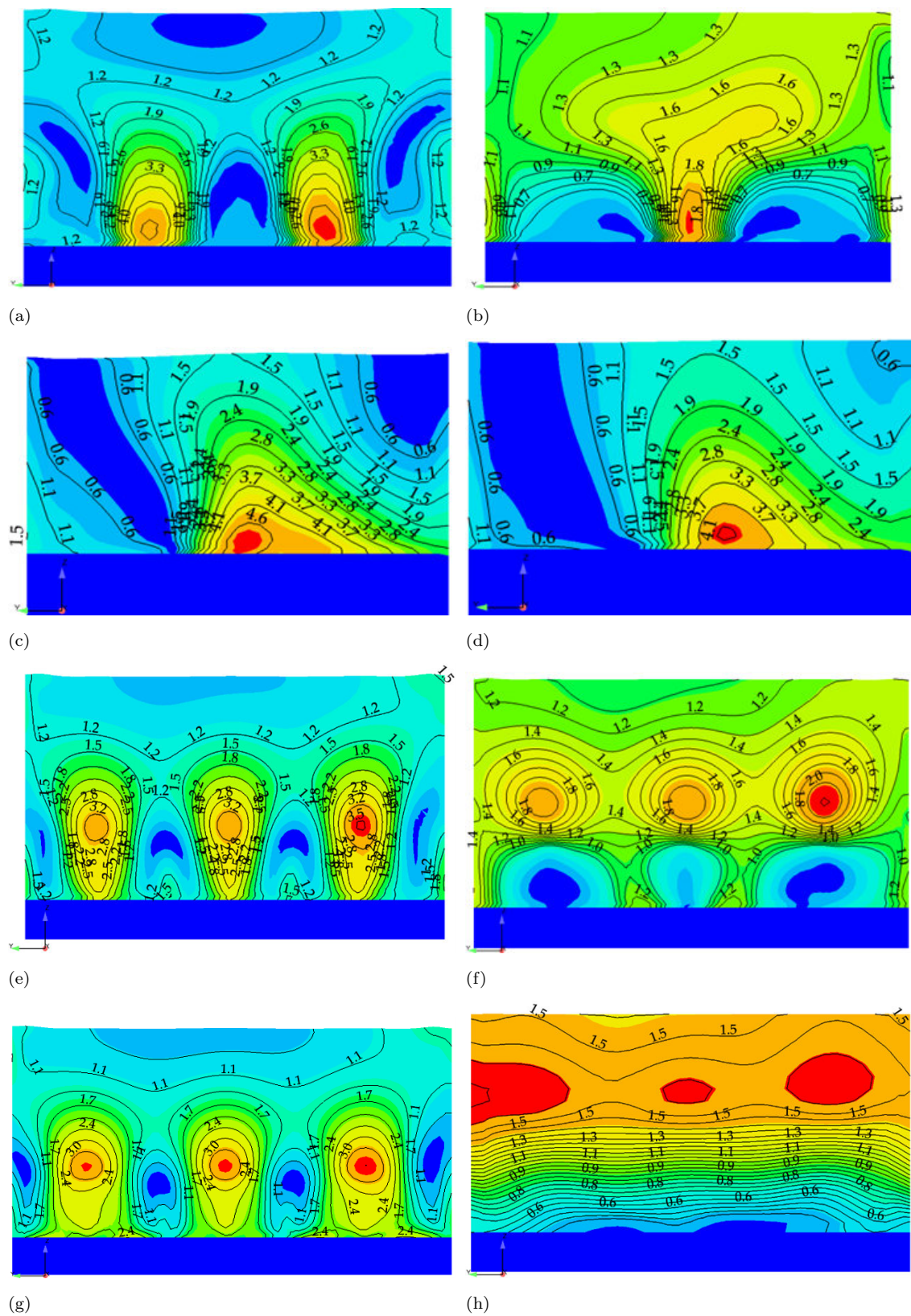


FIGURE 4.14: 2-D illustration of VPs in Y-Z plane at  $4.88 \text{ m}^3/\text{s}/\text{m}$  in **Type (A)** (a&b), **Type (B)** (c&d), **Type (C)** (e&f), and **Type (D)** (g&h) basins

between the WSBB the maximum velocity values reached 2.80 m/s as shown in Fig. 4.14 (e). At the basin's end the higher velocities were noticed in the central fluid region which reached 1.80 m/s while near the basin's floor and at the free surface it reached to the maximum values of 1.20 m/s as shown in Fig. 4.14 (f).

Figs. 4.14 (g) and 4.14 (h) show VPs in Type (D) basin, and after the HJ and baffle blocks (At X=12 m), velocity were found to be declined from floor to the central fluid region while value was slightly increased at the free surface which reached to 1.10 m/s as shown in Fig. 4.14 (g). At the end of Type (D) basin, maximum velocity was reached 1.50 m/s at the free surface while near the floor 0.60 m/s velocity values were observed as shown in Fig. 4.14 (h).

In comparison to the lower flow, at 7.22 m<sup>3</sup>/s/m discharge, forward VPs from the HJ were found more due to larger roller and length of HJs. In Type (A), (C), and (D) basins, at X=8 m, results of vertical profiles showed fully developed region of HJ as shown in Fig. 4.15 (a), (c) and (d). However, upon comparison with other basins, in Type (B) basin, the boundary layer growth were found to increased as the distance from the HJ was increased as shown in Fig. 4.15 (b).

Additionally, as compared to Type (A), (C), and (D) basins, due to larger HJ length in Type (B) basin and the absence of baffle blocks, the vertical VPs showed higher values near the bed at all horizontal sections. In Type (B) basin even at X=16 m, near the bed, the results showed a developing HJ which indicated more boundary growth layers compared to the rest of investigated basins as shown in Fig. 4.15 (b). At X=2 m from the HJ, the maximum value of velocity in Type (A), (B), (C), and (D) basins were reached to 7.56, 8.21, 7.79, and 7.70 m/s, respectively.

Figs. 4.16 (a) and (b) show velocity contours in Type (A) basin at 7.22 m<sup>3</sup>/s/m discharge. The velocity contours were drawn at two different sections, i.e., after the HJ and at the basin's end. The results showed that as the distance from the HJ jump initial location was increased, the velocity on the basin's floor was found to be reduced. After the HJ (at X=12), maximum velocity was found in the gully flows of baffle blocks which ranged from 3.10 to 3.60 m/s, while behind

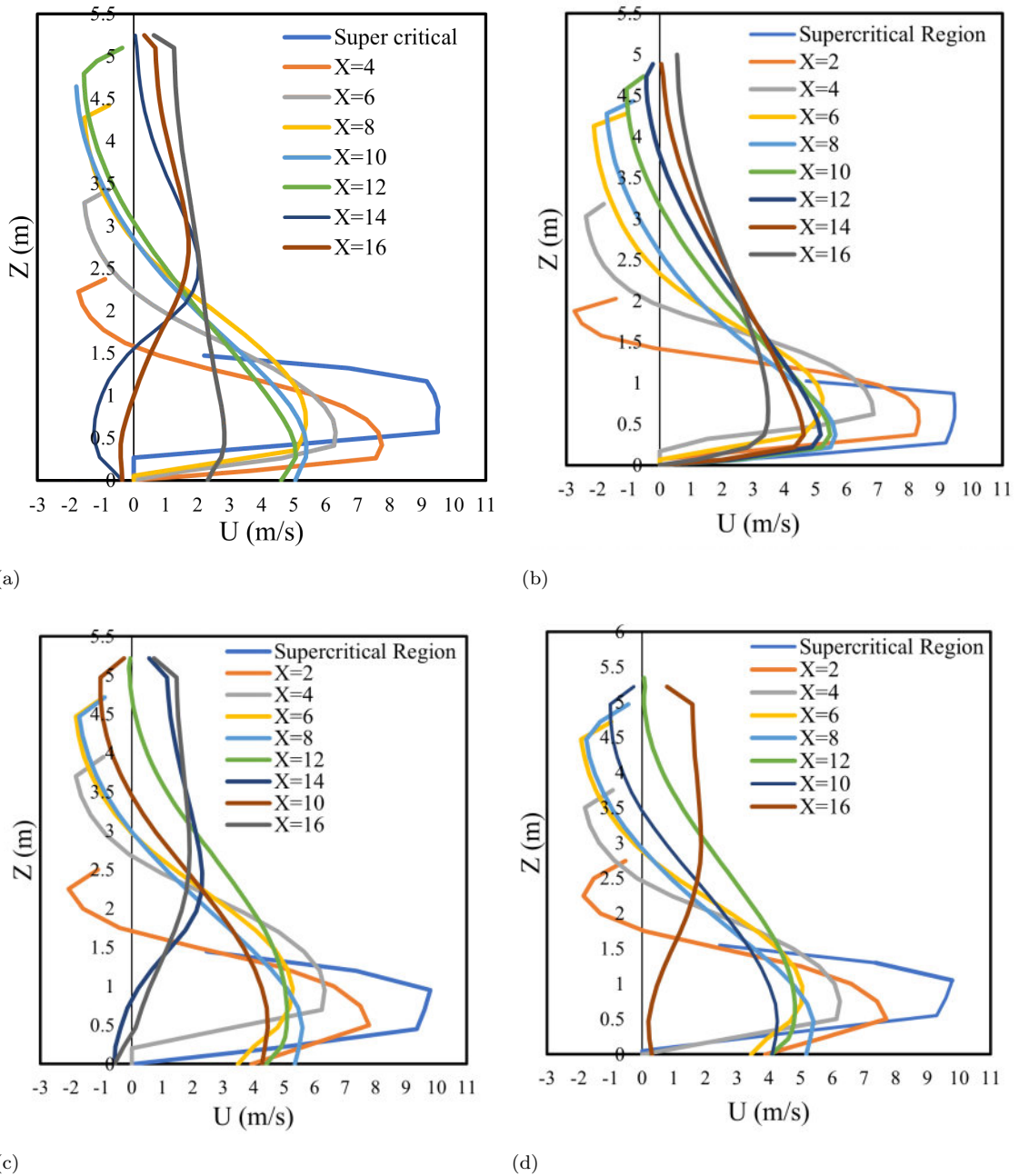


FIGURE 4.15: Vertical distribution of velocity in HJ for different stilling basins at  $7.22 \text{ m}^3/\text{s}/\text{m}$ , (a) **Type (A)**, (b) **Type (B)**, (c) **Type (C)**, and (d) **Type (D)**

baffle blocks the velocity values reached  $1.10 \text{ m/s}$  as shown in Fig. 4.16 (a). At the basin's end after the friction blocks, lower velocity values were seen near the floor while at the free surface the velocity reached  $1.80 \text{ m/s}$  as shown in Fig. 4.16 (b).

Figs. 4.16 (c) and (d) show the velocity contours in Type (B) basin at  $7.22 \text{ m}^3/\text{s}/\text{m}$

discharge. After the HJ (At X=12 m), velocity values were reached to 4.40 m/s at the floor, while from central fluid region to free surface the values were ranged from 3.10 to 1.20 m/s as shown in Fig. 4.16 (c). After the end sill, at basin's end, velocity from lower fluid region to the top surface were found between 1.20 to 2 m/s, while at the floor 0.70 m/s velocity value was observed as shown in Fig. 4.16 (d).

It worth mentioning here that the increase of velocity from lower fluid depth to free surface was due to the fluid deflection created by end sill.

In Type (C) basin, after the HJ (At X=12 m), in the WSBB region, the maximum value of velocity contours was found in between the spaces which showed similar values as were seen in Type (A) basin as shown in Fig. 4.16 (e). However, the pattern of velocity contours was found to be different.

At this section, the maximum velocity was reached to 3.10 m/s and found less than Type (A) basin, while at surface it reached up to 1.20 m/s. After the WSBB, higher velocities were observed in the gully flows which moved in the central part of fluid depths and gradually reduced towards the free surface, while behind the baffle blocks, velocity values were reduced 1.20 m/s. After the rectangular friction blocks, 2 m/s was the maximum velocity observed at the end of basin as shown in Fig. 4.16 (f).

In Type (D) basin, after the HJ (at X=12 m). the velocity values were seen similar to that found in Type (C) basin, however, their pattern was found to be different. The maximum values of velocity contour and their values were found similar to the Type (A) and (C) basins which reached 2.70 m/s as shown in Fig. 4.16 (g).

After the baffle blocks, higher velocity was shifted to upper fluid depths and their values ranged from 2.70 to 2.10 m/s. On the free surface, these values reached 1.40 m/s. At the end of stilling, similar to Type (A) and (C) basin, the velocity was reached 2 m/s at the free surface, and 0.80 m/s was observed at the floor level, as shown in Fig. 4.16 (h).



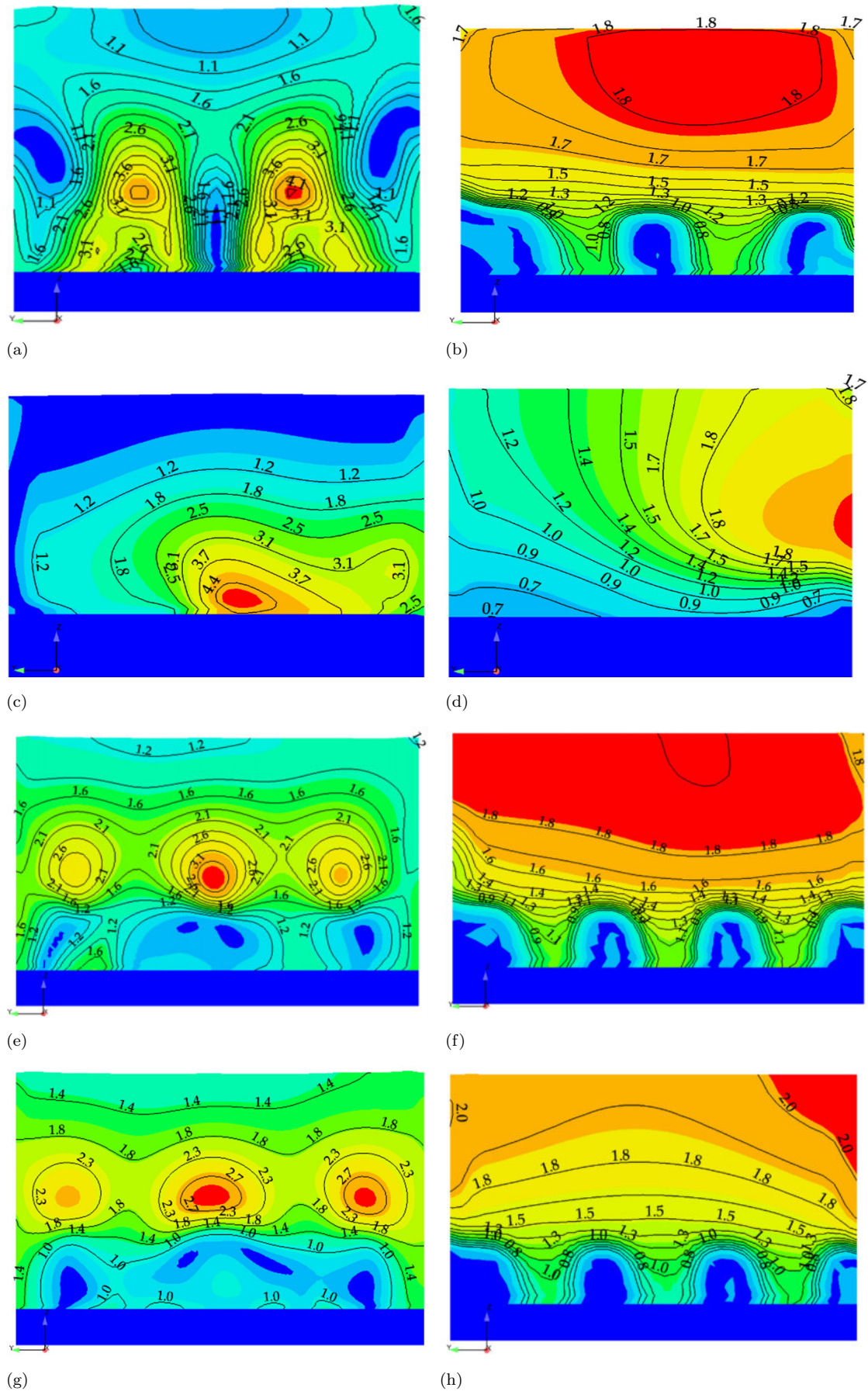


FIGURE 4.16: 2-D illustration of VPs in Y-Z plane at  $7.22 \text{ m}^3/\text{s}/\text{m}$  in **Type (A)** (a&b), **Type (B)** (c&d), **Type (C)** (e&f), and **Type (D)** (g&h) basins

At the studied discharges, from supercritical regions to HJ termination points, the VPs in Type (A), (C) and (D) basins showed the wall jet-like structure which showed agreement with the previous studies (Ead and Rajaratnam [117]; Nikmehr and Aminpour [161]).

The analysis of VPs using the similar operation and boundary conditions indicated that due to the changes in energy dissipation arrangements i.e., baffle and chute blocks, different pattern, and values of VPs were observed in the different stilling basins.

Conclusively, on low flows ( $2.44 \text{ m}^3/\text{s}/\text{m}$ ), at basins' end, the minimum velocity at the free surface was noticed in Type (D) basin, while minimum value of velocity profile after the HJ was found in Type (A) basin. After increasing flow up to  $4.88 \text{ m}^3/\text{s}/\text{m}$ . after the HJ, the velocity values near the basin's floor were less in Type (C) and (D) basins.

Additionally, as compared to Type (B) basin, the minimum velocity values at the basin's end were noticed in Type (D) basin. However, on high flow ( $7.22 \text{ m}^3/\text{s}/\text{m}$ ), as compared to Type (A) basin, at the end of basins, a slight increase in the velocity values was observed in Type (C) & (D) basins which approximately reached 10 %.

Convincingly, the analysis of vertical and lateral velocity profile indicated the WSBB basins (Type (C) & (D)) were found to be efficient in decaying the velocity at lower flow while the decay rate was found to be decreased as the flow was increased.

On the other hand, analysis revealed that at all the investigated flows, the maximum velocity after the HJ and at end of basin was noticed in Type (B) basin, which further indicated that the Type (B) basin was dissipating less energy within the HJ, thereby higher velocity values were noticed at the basin's end.

### 4.4.6 Turbulent Kinetic Energy (TKE) and Turbulent Intensity (TI)

The flow turbulence between the two measured sections is represented by Turbulent kinetic energy (TKE) which is also an important indicator of energy dissipation. It is a function of averaged velocity values in different directions i.e., x, y and z, and can be measured by taking the root mean-square of velocities fluctuations as expressed in (4.5).

$$U_{rms} = \sqrt{\frac{1}{n}(u_1^2 + u_2^2 + u_3^2 + \dots + u_n^2)} \tag{4.5}$$

where,  $u_1$ ,  $u_2$  and  $u_3$  are the velocities, and their values can be utilized to compute the TKEs as expressed below (4.6).

$$TKE = \frac{1}{2}(u_{rms}^2 + v_{rms}^2 + w_{rms}^2) \tag{4.6}$$

where  $u_{rms}$ ,  $v_{rms}$  and  $w_{rms}$  are the root mean square velocities in x, y and z directions, respectively. Under various investigated discharges i.e., 2.44, 4.88, 7.22 m<sup>3</sup>/s/m, the turbulent kinetic energy is shown from the center line of Type (A), (B), (C), and (D) basins.

Fig. 4.17 (a) shows the 2-D plots of TKE in Type (A) basin at 2.44 m<sup>3</sup>/s/m discharge. It was noticed from Fig. 4.17 (a) that the maximum amount of TKE were found in fore side of HJ at the contracted jet of supercritical velocity. The maximum amount of TKE was reached to 3.10 m<sup>2</sup>/s<sup>2</sup> which gradually reduced up to X=18 m from the HJ initiating location. Fig. 4.17 (a) further indicates that the maximum amount of TKE were observed in the HJ region from lower fluid depths (Z= 1.22 m) to the free surface. At the basin’s end, the maximum TKE reached below 0.21 m<sup>2</sup>/s<sup>2</sup>. Fig. 4.17 (b) indicates TI in Type (A) basin at 2.44 m<sup>3</sup>/s/m discharge. From the results, it was found that the maximum TI was located at the locations of maximum TKE and was found within the HJ region which was ranged from 171 to 115 %. After the basin’s baffle blocks, the TI was gradually

reduced. In Type (A) basin, 26 % TI was observed at the basin's end, as can be seen in Fig. 4.17.

Figs. 4.17 (c) and (d) show TKE and TI in Type (B) basin. In comparison to Type (A) basin, in Type (B) basin the TKE travelled up to X=22 m from the HJ initiating location, and its value reached  $1 \text{ m}^2/\text{s}^2$ . Fig. 4.17 (c) also shows that after end sill, the TKE was between 0.40 to  $0.80 \text{ m}^2/\text{s}^2$ . Similar to the Type (A) basin, the maximum TKE was noted in the central fluid depths of HJ, however, it was found further on the downstream. In Type (B) basin, 0.80 to  $1.10 \text{ m}^2/\text{s}^2$  values of TKEs were noticed at the floor surface which travelled about 24 m from the HJ initiating location as can be seen in Fig. 4.17 (c). Fig. 4.17 (d) illustrates TI in Type (B) basin at  $2.44 \text{ m}^3/\text{s}/\text{m}$ . As compared to Type (A) basin, in Type (B) basin, the intensity and distance was found more after the HJ which travelled long way to the basin's end. The maximum TI was observed in the HJ region, and its value was reached to 175 %, However, at the basin's end TI was reached up to 50 %. The increase of TI at end of stilling basin was due to the absence of baffle blocks.

Figs. 4.17 (e) and (f) show the TKE and TI in Type (C) basin at  $2.44 \text{ m}^3/\text{s}/\text{m}$ . Following the similar pattern as seen in Type (A) and (B) basins, the maximum TKE was found within, and fore side of the HJ as shown in Fig. 4.17 (e). In Type (C) basin, the maximum TKE was reached  $3 \text{ m}^2/\text{s}^2$  and after the WSBBs in upper layer of the flow depth, its values reached below  $0.23 \text{ m}^2/\text{s}^2$ . In Type (C) basin, maximum TKE were found to be diminished before the basin's end. Upon comparison with Type (A) and (B) basins, less TKEs were witnessed at the end of Type (C) basin as shown in Fig. 4.17 (e).

Fig. 4.17 (f) represents TI in Type (C) basin. The maximum TKEs were found in the HJ and baffle block region, as was noticed in Type (A) and (B) basins and the maximum values found at the contracted jet of supercritical flow. The TI values in the HJ region was reached 180.7 % and after the WSBBs these values reduced to 100 %. Upon comparison with Type (A) and (B) basins, at the end of Type

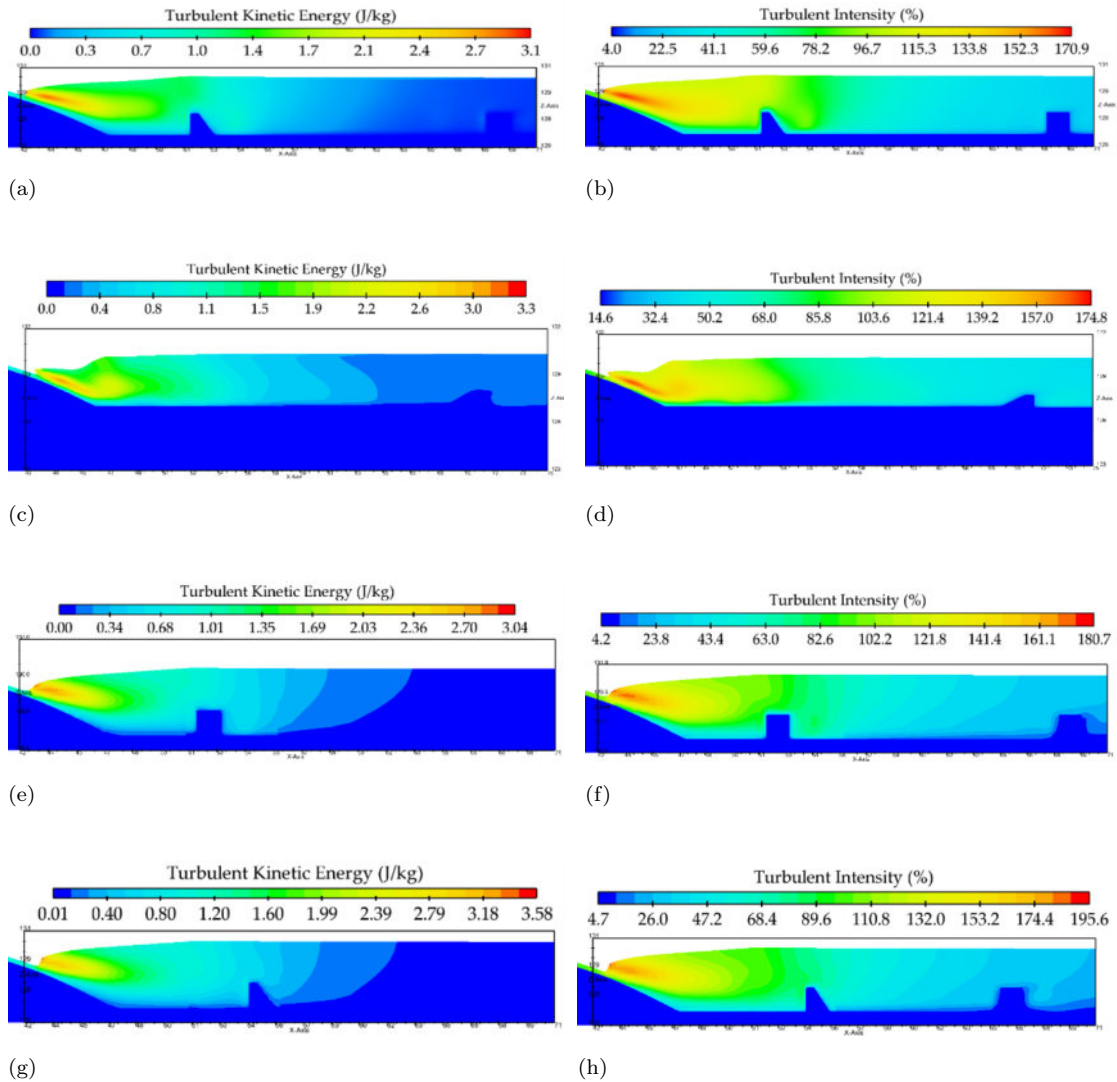


FIGURE 4.17: 2-D representation of TKEs and TI at 2.44 m<sup>3</sup>/s/m discharge, **Type (A)** (a & b), **Type (B)** (c & d), **Type (C)** (e & f), and **Type (D)** (g & h) basins

(C) basin, TI was found less and its value reached 26 % which was 24 % less than that was observed in Type (B) basins.

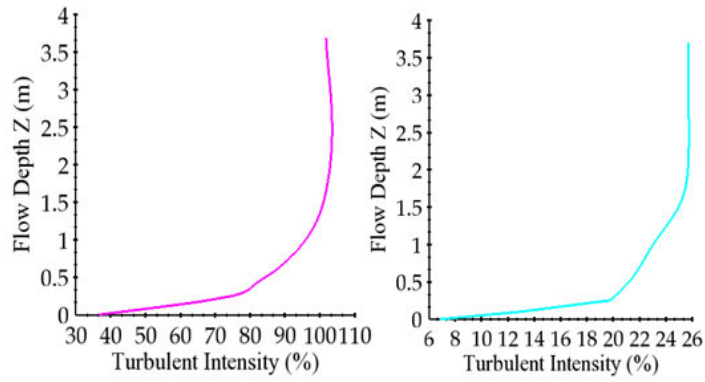
Fig. 4.17 (g) shows TKE in Type (D) basin at 2.44 m<sup>3</sup>/s/m discharge. The maximum TKE was found at HJ initiating location which reached to 3.60 m<sup>2</sup>/s<sup>2</sup> and was observed higher than Type (A), (B) and (C) basins. However, from the HJ to X=18 m the TKE travelled were found to be less in Type (D) basin than Type (A), (B) and (C) basins. At X=18 m, the maximum TKE was reached below 0.20 m<sup>2</sup>/s<sup>2</sup>. Similar to Type (C) basin, the TKE was found to be declined

before the basin's end. Fig. 4.17 (h) shows TI in Type (D) basin at 2.44 m<sup>3</sup>/s/m discharge. In the HJ region, TI in Type (D) basin was more than other basins and the maximum value in Type (D) basin was reached 195 %. However, the  $TI_s$  reduced in basins' appurtenances region and were ranged between 68 to 90 %. From the baffle region to friction blocks region, the  $TI_s$  were found to be between 20 to 68% and further low  $TI_s$  were noted at the basin's end.

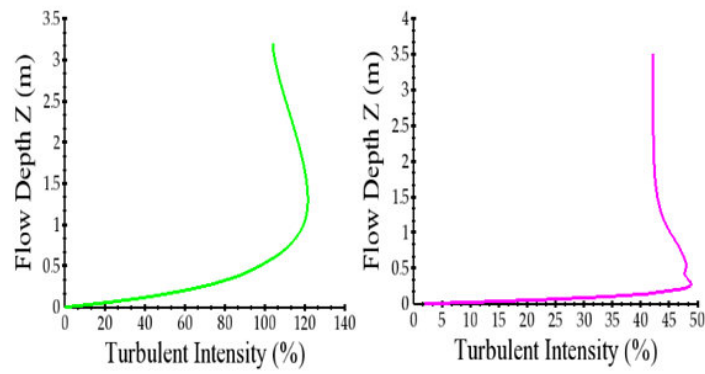
Fig. 4.18 shows the vertical distribution of TI after HJ and end of the basins at 2.44 m<sup>3</sup>/s/m. Figs. 4.18 (a) and (b) show the vertical distribution of TI in Type (A) basin. After the HJ, the TI was reached 38 % in lower fluid depths ( $Z=1.5$  m), while from middle to free surface, the TI gradually increased up to 110 % as shown in Fig. 4.18 (a). The maximum TI at the end of Type (A) basin was found in upper fluid region which reached to 26 %.

In Type (B) basin, after HJ, TI was found higher in the lower fluid depths (At,  $Z=1$  m) which reached 120 %, while a small reduction was notice at the upper fluid depths. After the HJ, in the lower fluid depth, especially near the floor ( $Z=0.5$  m), TI was reached 50 % as shown in Fig. 4.18 (c). At the basin's end, in the upper fluid region, TI reached to 45 % as shown in Fig. 4.18 (d).

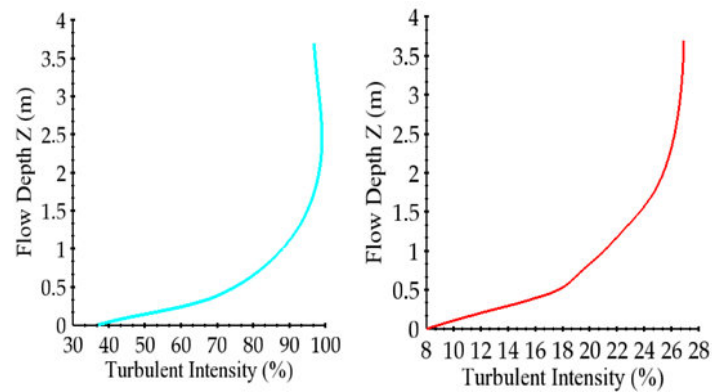
In Type (C) basin, the distribution of  $TI_s$  was different than that was noted in Type (A) and (B) basins. After HJ, maximum TI was reached 100 % at  $Z=2$  m, while further reduction in  $TI_s$  was noticed in upper fluid depths as shown in Fig. 4.18 (e). The maximum TI at the end of Type (C) basin was reached 26 % at the free surface, while in lower fluid depths ( $Z=0$  to 3 m) TI was found between 8 % to 26 % as shown in Fig. 4.18 (f). The trends of TI in Type (C) basin were found similar to Type (A) basin. Fig. 4.18 (g) and (h) show TI intensity in Type (D) basin at the two vertical sections i.e., after the HJ and at the basin's ( $X=70$  m). The overall trend of  $TI_s$  at the investigated two sections was similar to that was noted in Type (A) and (C) basins. The maximum TI after the HJ was reached to 100 % (At  $Z=2.25$  m) which gradually reduced in upper fluid regions as shown in Fig. 4.18 (g). The maximum TI at the end of Type (D) basin was reached to



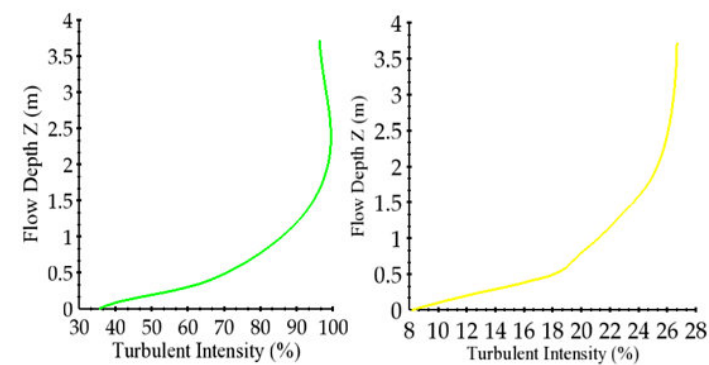
(a)



(b)



(c)



(d)

FIGURE 4.18: Distribution of TI at  $2.44 \text{ m}^3/\text{s}/\text{m}$  flow in **Type (A)** (a&b), **Type (B)** (c&d), **Type (C)** (e&f), and **Type (D)** (g&h) basins after the HJ and at the basins' end

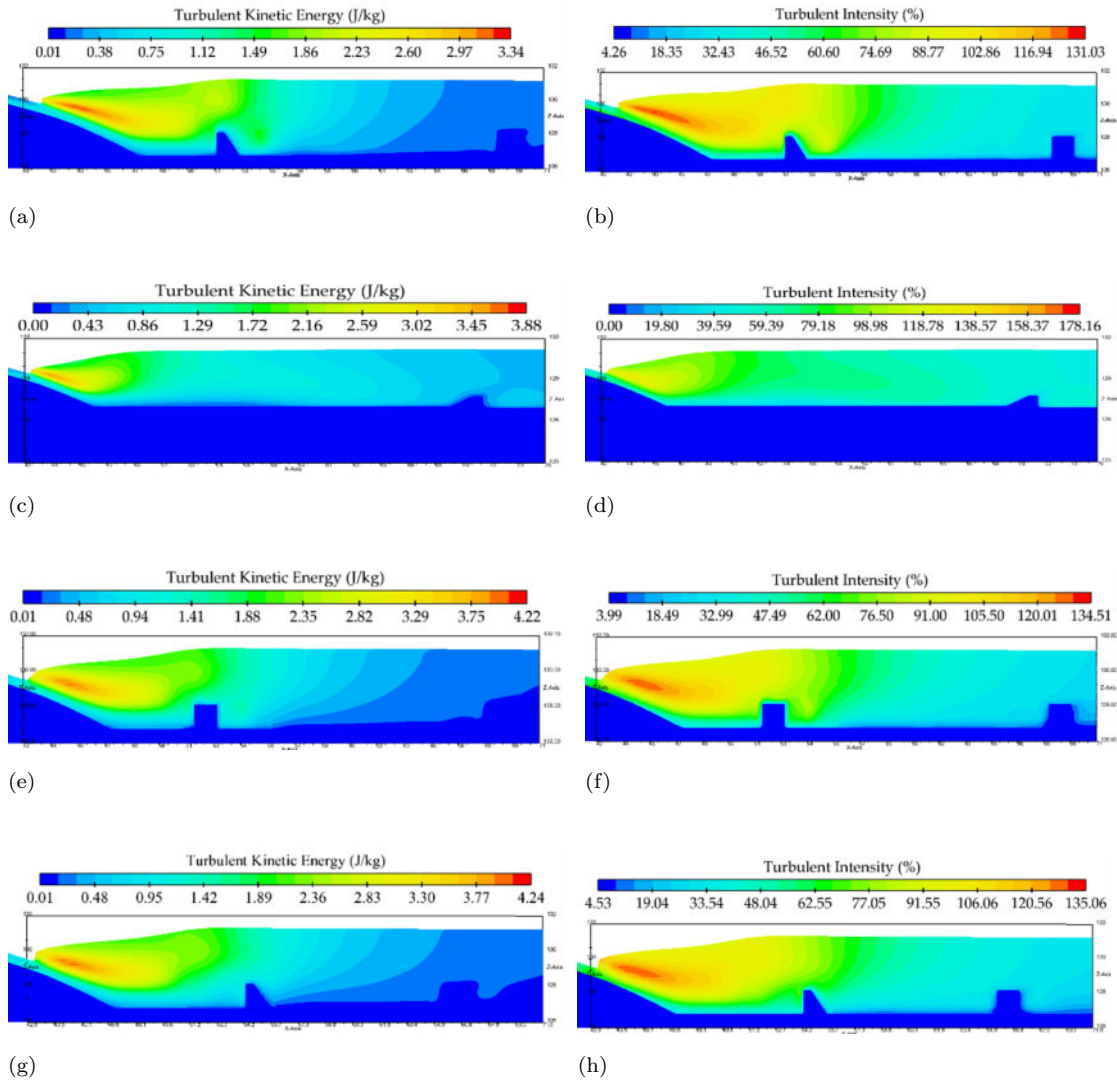


FIGURE 4.19: 2-D representation of TKEs and TI at  $4.88 \text{ m}^3/\text{s}/\text{m}$  discharge, **Type (A)** (a & b), **Type (B)** (c & d), **Type (C)** (e & f), and **Type (D)** (g & h)

26 % at the free surface, while from the floor level to  $Z= 2.5 \text{ m}$ ,  $TI_s$  were ranged between 8 to 26 % as shown in Fig. 4.18 (h).

Figs. 4.19 (a) and (b) show the distribution of  $TKE_s$  and  $TI_s$  in Type (A) basin at  $4.88 \text{ m}^3/\text{s}/\text{m}$  discharge, respectively. The values are taken at X-Z plane at  $Y/2$ . Fig. 4.19 (a) shows that maximum TKE was at the fore side of HJ which reached to  $3.34 \text{ m}^2/\text{s}^2$ . The TKEs were decreased in the lower and upper regions of fluid re-circulation. Additionally, further decrease of TKEs was also noticed after the baffle blocks region to  $X=64$  which showed  $0.38 \text{ m}^2/\text{s}^2$  of TKE. The decrease was

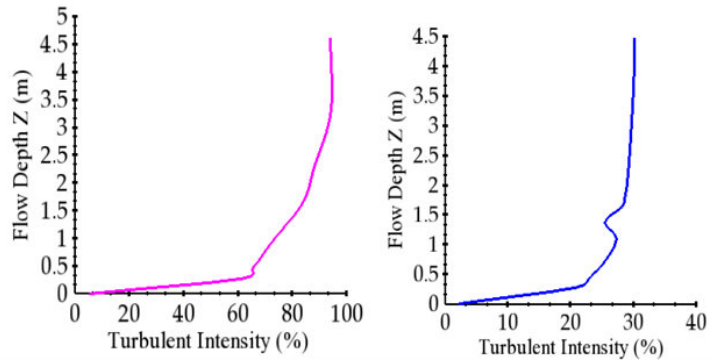


due to influence of baffle blocks as they dissipated the residual energy from the HJ. From Fig. 4.19 (b), it was noted that the maximum TI occurred at the locations where maximum TKEs existed which were found to be decreased after the HJ initiating location towards downstream of the HJ.

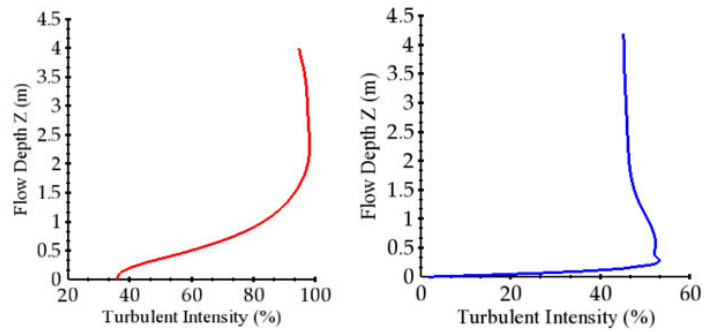
Figs. 4.19 (c) and (d) show the variation of TKE and TI in Type (B) basin at 4.88 m<sup>3</sup>/s/m discharge. In Type (B) basin, due to the smaller HJ length, lesser amount of TKE was dissipated in the HJ region. However, In comparison to Type (A) basin, the amount TKE was higher in HJ region which reached to 3.88 m<sup>3</sup>/s/m. On the other hand, more TKE was observed at the end of the basin. The higher TKE at the end of basin was due to the absence of baffle blocks in Type (B) basin.

Figs. 4.19 (e) and (f) show the TKE and TI in Type (C) basin. The maximum TKE was noticed at contracted jet of supercritical flow and its value reached 4.22 m<sup>2</sup>/s<sup>2</sup>. In Type (C) basin,  $TKE_s$  were restricted between the HJ and baffle blocks region which declined towards downstream as the distance from the HJ initiating point was increased. After comparing with Type (A) basin,  $TKE_s$  were noted above the top level of WSBBs and their values were reduced after the baffle blocks. In addition, the results indicated that the  $TKE_s$  at the end of Type (C) basin were fully decayed in the lower fluid layers. At 4.88 m<sup>3</sup>/s/m discharge, Fig 4.19 (e) shows TI intensity at Y/2 in Type (C) basin. Maximum amount of TI was noticed at the locations of maximum  $TKE_s$  which reached to 134.5 %.

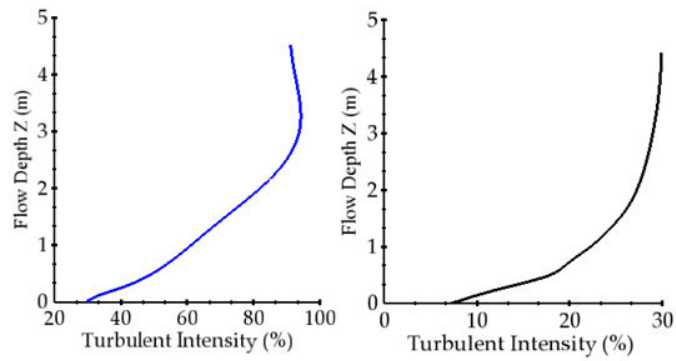
Following the similar trend of Type (A) and (C) basins, maximum amount of  $TKE_s$  and TI in Type (D) basin were noted in the fore side of the HJ which were found to be declined towards downstream from the HJ toe as shown in Fig. 4.19 (g) and (h). Because of the different geometry of the basin's appurtenances, the pattern of  $TKE_s$  in the HJ and baffle block region were dissimilar to that was observed in Type (C) and D basins. From Fig. 4.20 (a), soon after the HJ in Type (A) basin, it can be seen that maximum amount of  $TI_s$  was found at free surface, while at the basin's end (X=70 m),  $TI_s$  at the free surface was reduced to 30 % as shown in Fig. 4.20 (b).



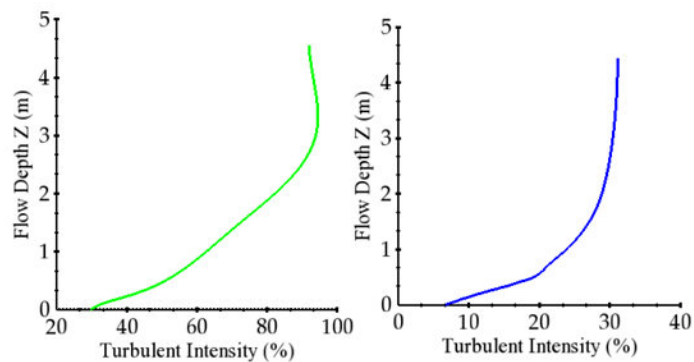
(a)



(b)



(c)



(d)

FIGURE 4.20: Distribution of TI at  $4.88 \text{ m}^3/\text{s}/\text{m}$  flow in **Type (A)** (a&b), **Type (B)**(c&d), **Type (C)** (e&f), and **Type (D)** (g&h) basins after the HJ and at the basins' end

After the HJ, 98 % TI was observed at  $Z= 2.5$  m, while at the free surface TI reached 94 % as shown in Fig. 4.20 (a). The maximum TI at basin's end was found near the floor which reached 52%, while at the free surface its value reached 45 % as shown in Fig. 4.20 (c). After comparing with Type (A) basin, more TKE and TI were noticed at end of Type (B) basin as shown in Fig. 4.20 (d).

Figs. 4.20 (e) and (f) show  $TI_s$  in Type (C) basin at two different sections (After HJ, and at basin's end). After the HJ, maximum TI was reached 94% at  $Z=3.25$  m which gradually reduced to 91 % at the free surface shown in Fig. 4.20 (e). At the end of Type (C) basin, TI was reduced to 30 % at the free surface as shown in Fig 4.20 (f).

After the HJ, the maximum  $TKE_s$  in Type (D) basin was noticed at  $Z=3.4$  m which showed that the Type (D) basin deflected  $TKE_s$  towards free surface as shown in Fig 4.20 (g). At the end of Type (D) basin, TI near the floor was reached to 29 %, while its value reached to 30% at the free surface ( $Z=4.5$  m) as can be seen in Fig 4.20 (h).

Fig. 4.21 shows the distribution of  $TKE_s$  and  $TI_s$  at  $7.22 \text{ m}^3/\text{s}/\text{m}$  discharge in Type (A), (B), (C) and (D) basins. The trend of the  $TKE_s$  and  $TI_s$  in Type (A) basin was found to be similar as was noticed at  $4.88 \text{ m}^3/\text{s}/\text{m}$  discharge. The maximum  $TKE_s$  and  $TI_s$  was observed at the fore side of the HJ which decreased as distance from the HJ was increased.

In Type (A) basin, the maximum TKE and TI reached to  $3.22 \text{ m}^2/\text{s}^2$  and 122.4 %, respectively, as shown in Fig. 4.21 (a) and (b), respectively. At  $7.22 \text{ m}^3/\text{s}/\text{m}$  discharge in Type (B) basin, the maximum of TKE and TI were reached to  $3.88 \text{ m}^2/\text{s}^2$  and 122 %, respectively, as shown in Figs. 4.21 (c) and (d), respectively.

In Type (C) basin, the maximum TKE was reached to  $4.20 \text{ m}^2/\text{s}^2$  at the contracted jet as shown in Fig. 4.21 (e), which showed growth in the upper and lower fluid depths as was observed in Type (A) basin. Due to concentration of TKE at the contracted jet, its value was found to be higher than that was noticed in Type (A) basin. The maximum amount of TI was reached up to 116.2% as shown in Fig.

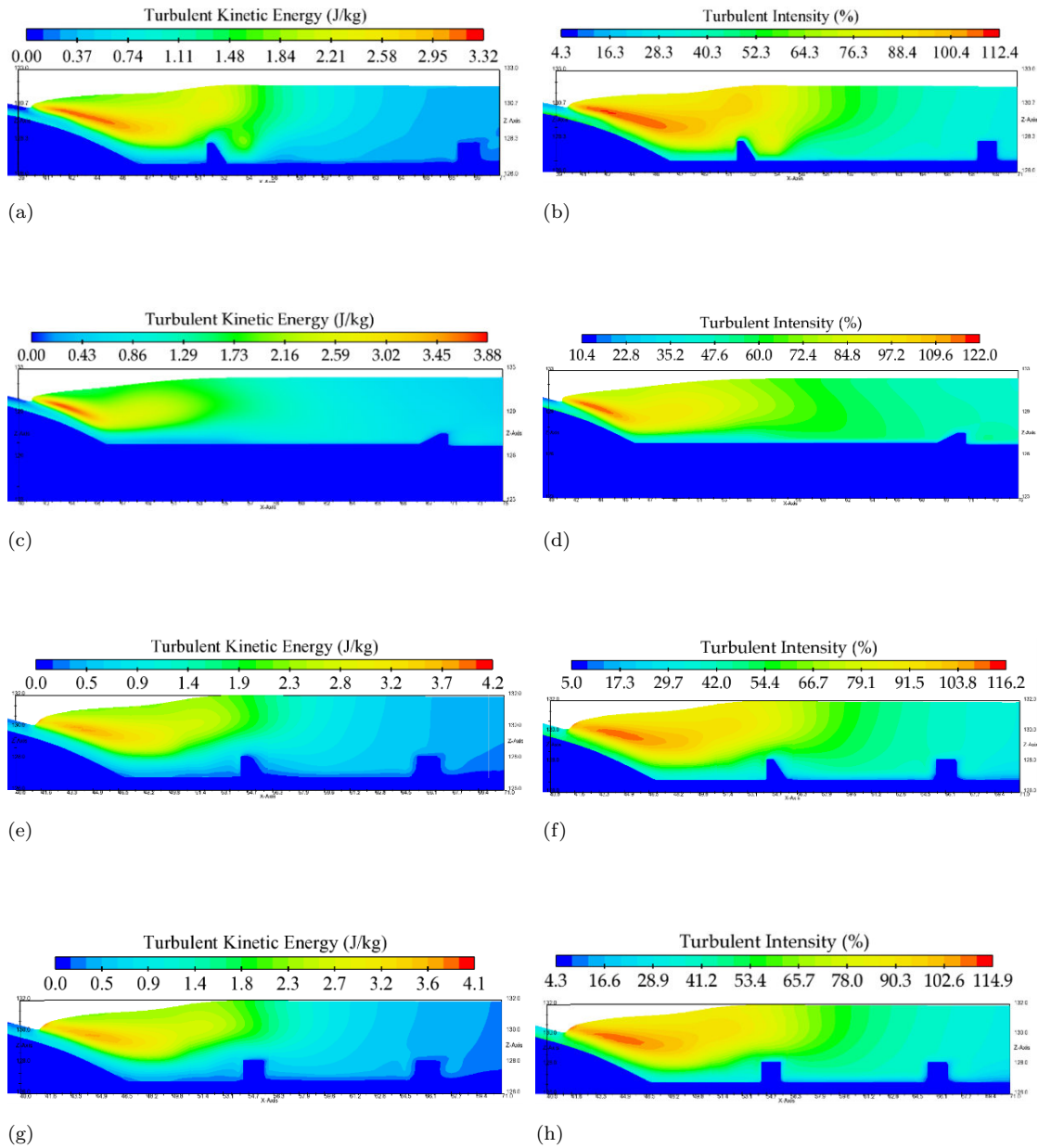


FIGURE 4.21: 2-D representation of TKEs and TI at  $7.22 \text{ m}^3/\text{s}/\text{m}$  discharge, **Type (A)** (a&b), **Type (B)** (c&d), **Type (C)** (e&f), and **Type (D)** (g&h)

4.21 (f). At  $7.22 \text{ m}^3/\text{s}/\text{m}$  discharge, the maximum TKE and TI in Type (D) basin were reached to  $4.1 \text{ m}^3/\text{s}/\text{m}$  and  $114.9 \%$ , respectively as shown in Figs. 4.21 (g) and (h), respectively.

Due to resemblance of baffle blocks, trends of  $TKE_s$  and  $TI_s$  in Type (D) basin were found to be similar as noticed in Type (C) basin. Fig. 4.22 shows vertical distribution of TI in different basin after the HJs and at the basin's end. In Type

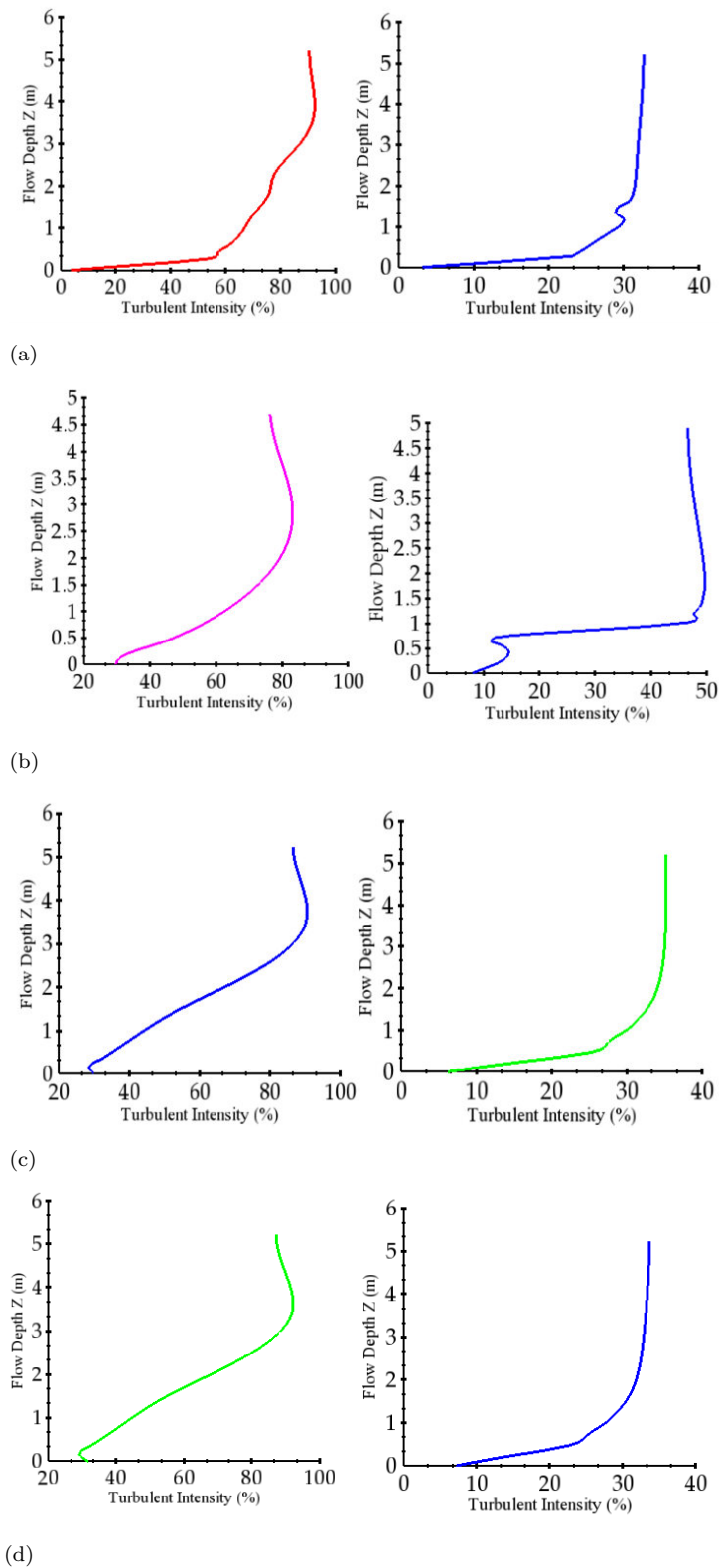


FIGURE 4.22: Distribution of TI at  $7.22 \text{ m}^3/\text{s}/\text{m}$  flow in **Type (A)** (a&b), **Type (B)** (c&d), **Type (C)** (e&f), and **Type (D)** (g&h) basins after the HJ and at the basins' end

(A) basin, the maximum  $TI_s$  were reached 90% and 32% after the HJ and at the basin's end, respectively as shown in Figs. 4.22 (a) and (b), respectively. In Type (B) basin, the maximum  $TI_s$  after the HJ and at the basin's end were 77% and 46%, respectively, as shown in Figs. 4.22 (c) and (d), respectively. However, near the bed, the TI was found even more than the free surface which reached 53%. On the other in Type (C) basin, the pattern and distribution of TI was found to be different than Type (A) and (B) basins. The TI near the basin's floor was less while relatively higher values were noticed at the free surface as can be seen in Fig. 4.22 (e) and (f). The maximum TI after the HJ and at the end of Type-C basin was 88% and 32%, respectively, as shown in Fig. 4.22 (e) and (f), respectively.

In Type (D) basin, the maximum TI after the HJ and at the basin's end was reached 86% and 32%, respectively as shown in Fig. 4.22 (g) and (h), respectively. It is important to mention here that in Type (D) basin, the TI near the floor was found to be less than that was observed in Type (A) and (B) basins.

In conclusion, the pattern of TI in WSBB basins were found to be different than that was observed in USBR baffle block (Type (A)) and remodelled basins (Type (B)). Additionally, the TI near the floor of Type (C) and (D) basins were considerably less than the other investigated basins.

## 4.5 Results of Hydraulic Parameters for Free Flow Discharges

### 4.5.1 Free Surface Profiles (FSPs) at Flood and Design Discharges

Fig. 4.23 shows free surface profiles within Type (A), (B), (C) and (D) basins at flood discharge of  $18 \text{ m}^3/\text{s}/\text{m}$ . The plots are drawn from the center line of the models. From Fig. 4.23, due to different basins' geometries, the results indicated dissimilar profiles in supercritical, HJ and subcritical regions. In Type (A) basin,

the results indicated that up to HJ initial location, the free surface declined and followed the glacis slope while within the HJ large undulations and fluctuations were noticed which travelled up to  $X=67$  m. After  $X=67$  m, the free surface became stable. In addition, after the jump termination, a sudden drop in the free surface was noted which developed a large wavy surface.

At flood discharge, the HJ initiating point in Type (B) was found close to that noted in Type (A) basin. In addition, within the HJ, large fluctuations were observed which indicated that even at the steady state, the water surface profiles were still fluctuating. Furthermore, in comparison to Type (A), (C) and (D) basins, the free surface profile of HJ was also found to be lower which gradually raised as the distance from the HJ was increased. From the Fig. 4.23, the results indicated a gradually increasing trend of water profile in Type (B) while at  $X=60$  m, the free surface profiles were found to be close with the profiles of other basins.

On the other hand in Type (C) and (D) basins, the results indicated a similar trends of free surface profiles and the HJ initiating locations were also found to be closed which were well above on the glacis. The results further revealed a smooth transition of HJ into the subcritical flow conditions as shown in Fig. 4.23. After the HJ, the free surface in Type (C) and (D) basins were found to be stable as the flow travelled towards the downside of the basins. In conclusion, from the results, it can be believed that Type (C) and (D) basins are holding the HJs well above on the downstream glacis while the HJ location in Type (A) and (B) basins were found on the downside of the glacis. In addition, as compared to Type (A) and (B) basins, at high flood discharge of  $18 \text{ m}^3/\text{s}/\text{m}$ , the transition of HJs into the subcritical region is found to be good in Type (B) and (C) basins. Furthermore, the results also showed a large wave on downstream of Type (A) basin which ended just 4 m before the basin's end. Fig. 4.24 shows free surface profile on the studied basins at the design discharge. In comparison to the flood discharge, results indicated different water surface profiles in Type (A), (B), (C) and (D) basins. In comparison to flood discharge, due to the nature of highly turbulent flow, the free surface downstream of Type (A) was found to be unstable and revealed large waves which travelled up to the basin's end.

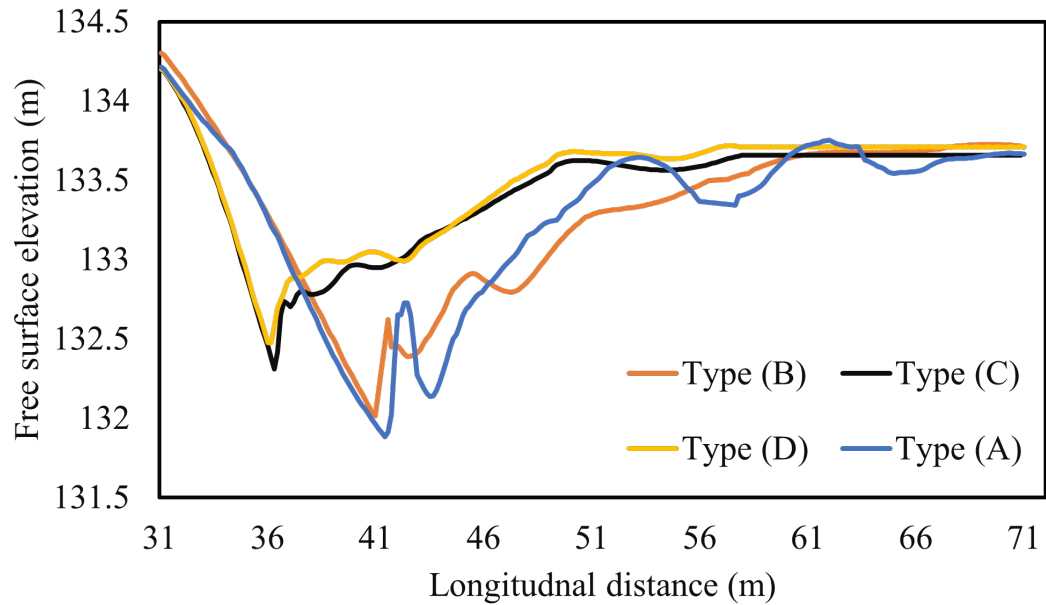


FIGURE 4.23: Comparison of FSPs in different basins at flood discharge of 18 m<sup>3</sup>/s/m

In Type (B) basin, the HJ initial location moved further on the downside of glacis while a smooth free surface in the supercritical region was noticed as shown in Fig. 4.24. After the initial location of HJ, a gradually raising profile was noted which became levelled after at X=63.4 m.

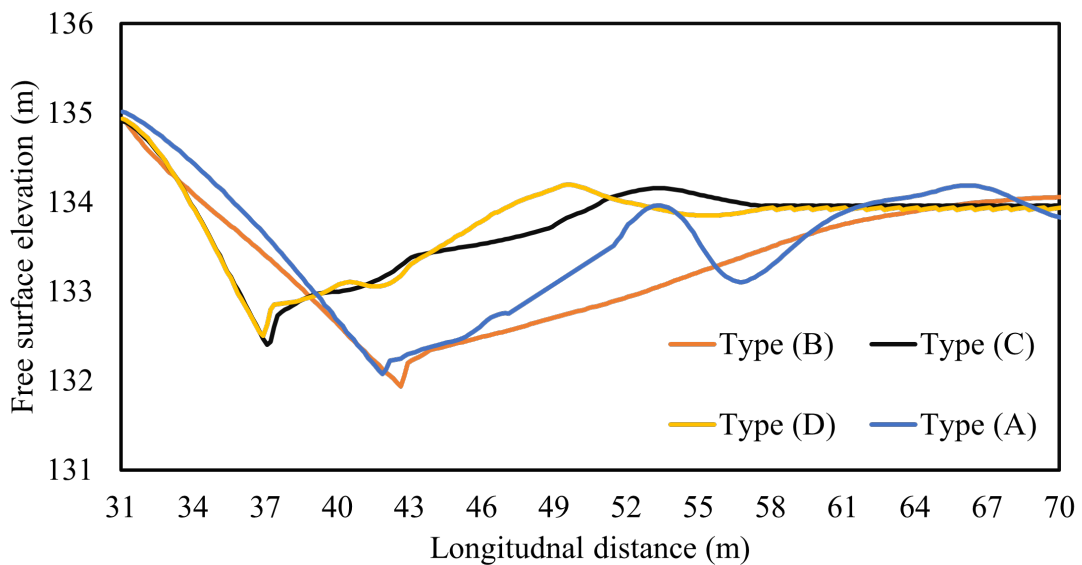


FIGURE 4.24: Comparison of FSPs in different basins at flood discharge of 24 m<sup>3</sup>/s/m

On the contrary, in Type (C) and (D) basin, the results indicated an identical free



surface profiles in the supercritical regions while dissimilar profiles were noticed in the HJ regions. In addition, at design discharge, the results showed different HJ termination locations in Type (C) and (D) basins. Furthermore, after the HJs, a fluctuating free surface profiles were noted in Type (C) and (D) basins as shown in Fig.4.24. However, after  $X=58$  m, the free surface profiles were found to be stable with little fluctuations. It is important to mention that at such higher discharges, i.e., 18, and  $24.30 \text{ m}^3/\text{s/m}$ , the free surface profiles downstream of prototype barrages are always found to be wavy and fluctuating.

From the analysis of free surface profiles, it is concluded that out of the studied basins, the newly proposed Type (C) and (D) basins are holding the HJs well above from floor level and toe of the downstream glacis. However, as compared to Type (C) and (D) basins, in Type (A) and (B) basins, the locations of HJs and its distances are found to be less from the glacis toe.

## **4.5.2 Velocity Field and Patterns at Flood and Design Discharges**

### **4.5.2.1 Velocity Field and Patterns at Flood Discharge**

Fig. 4.25 (a) shows velocity field downstream of Type (A) at flood discharge. The maximum velocity was found on the top surface in the supercritical region. Near the floor, from glacis toe to baffle blocks region, a large wake zone was noted which seemed to dissipate the upcoming supercritical jet. The depth of this wake zone was increased as the flow moved towards downstream. After the baffle blocks, near the floor, re-circulation's were noted which continued up to the end of the basin. In Type (A) basin, after impacting with the baffle blocks, the flow moved towards the upper fluid region and due to this reason, the boundary growth layers near the floor were found to be instantly reduced. However, after the baffle blocks, two different forward vertical velocity profiles were noted which indicated that the fluid was highly turbulent in nature, as usually notice downstream of prototype barrages. In addition, the results also indicated eddies and reserve velocity field

in the HJ region as can be seen in Fig. 4.25 (a). At flood discharge, in Type (A) basin, the maximum velocity at the basin's end reached to 3.8 m/s.

Fig.4.25 (b) shows 2-D velocity field downstream of Type (B) basin at 18 m<sup>3</sup>/s/m discharge. From the plots, it can be seen that the supercritical flow was impinging on the basin's floor. The results indicated three velocity zones on the Type (B) basin, i.e., 1) high velocity zone; 2) intermediate zone, and lower velocity zone. From the downstream glaucis to the end the basin's floor, the depths of these zones were found to be consistent. The results of velocity field also indicated that due to the absence basin's appurtenances, higher velocity is striking on floor which travelled to the end of basin. However, on the free surface, a small re-circulation region was also notice within the HJ while after the HJ a forward velocity profiles were observed as shown in Fig. 4.25 (b). From the vertical velocity profiles, it can be observed as the flow moved towards the basin's end the boundary growth layer remained unchanged that indicated the velocity was not properly decayed within basin. At 18 m<sup>3</sup>/s/m discharge, the maximum velocity was found in the supercritical region which reached 7.22 m/s whereas at the basin's end the maximum velocity reached 3 m/s.

Fig. 4.25 (c) shows velocity field on the Type (C) basin at 18 m<sup>3</sup>/s/m discharge. From the Fig. 4.25 (c), the results indicated that the supercritical flow was striking on basin while after impacting with wedge-shaped baffle blocks (WSBB), the high velocity vectors moved toward the middle fluid region which travelled to the end of basin. After the baffle blocks, large wake zone and eddies were generated which travelled up to the basin's end as shown in Fig. 4.25 (c). From the velocity field, it can be said that after impacting the WSBB, the fluid velocity was significantly decreased near the basin. In addition, at the free surface, large re-circulation was noticed within the HJ which showed that a large amount energy was also dissipated in the HJ region, thereby, after the HJ, lower low velocity fluid moved toward the downstream side. The results indicated maximum velocity at in the supercritical region which reached 6.96 m/s, however, on the basin's end the velocity value was reached to 2.71 m/s.

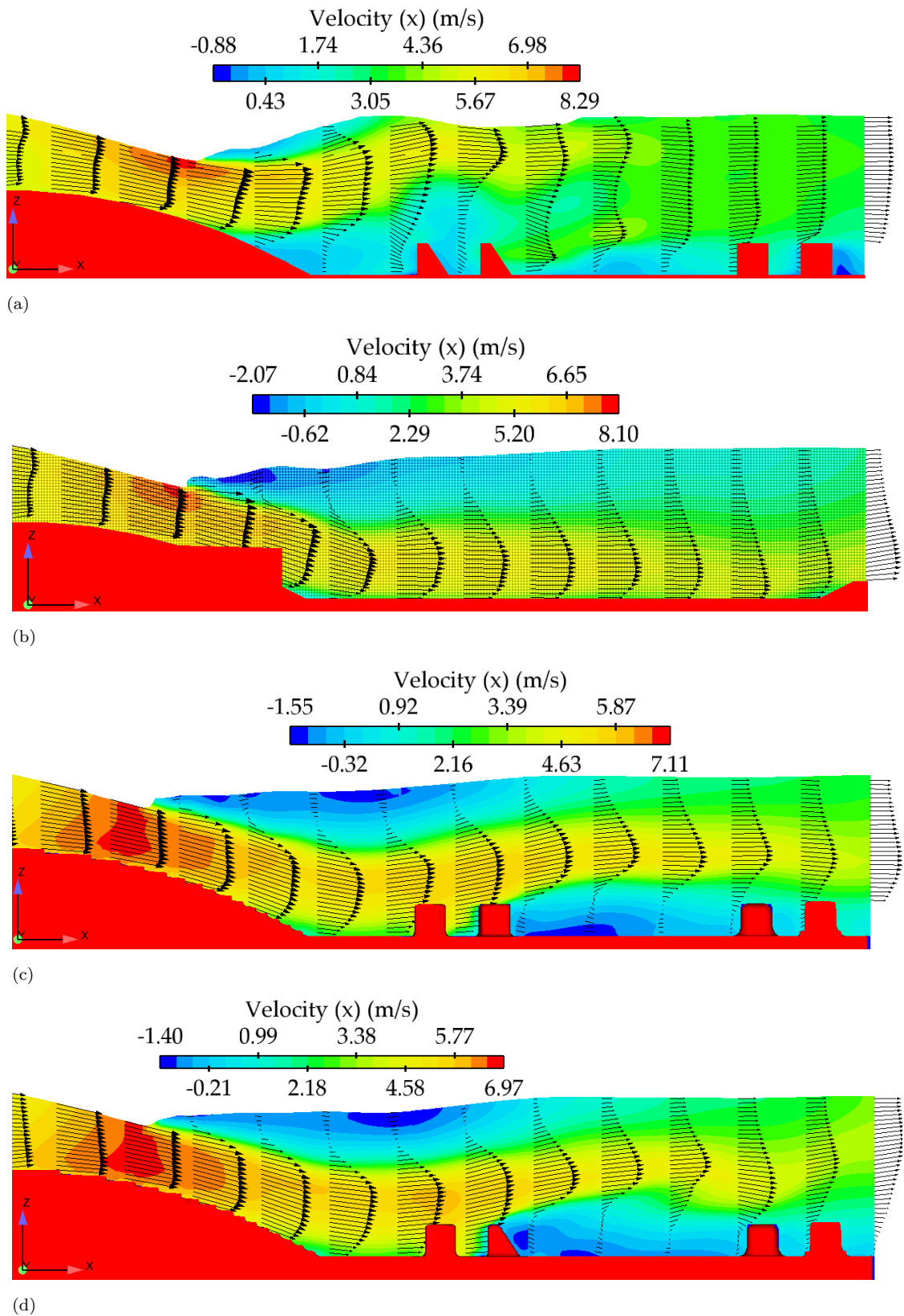


FIGURE 4.25: 2-D Illustration of velocity distribution downstream of different basins at flood discharge of  $18 \text{ m}^3/\text{s}/\text{m}$ , (a) Type (A), (b) Type (B), (c) Type (C) and (d) Type (D)

Fig.4.25 (d) shows velocity field on Type (D) basin at 18 m<sup>3</sup>/s/m discharge. The overall pattern of velocity field on Type (D) basin was found similar to that was observed in Type (C) basin. However, after the baffle blocks, the pattern of wake zone was found to be different than Type (C) basin and was lesser than that was noted in Type (C) basin. From the vertical velocity profiles in Type (D) basin, the results indicated that after impacting the baffle blocks, the distance of maximum velocity vectors from the bed was large than that was noticed in Type (C) basin. In addition, at the free surface, a large re-circulation was also noticed, and after the HJ, the backward negative velocity vectors converted into the forward velocity profile as can be seen in Fig.4.25 (d). In Type (D) basin, the maximum velocity values at the downstream glacis and basin's end reached to 6.87 m/s and 2.47 m/s, respectively.

In conclusion, based on the analysis of velocity field at the flood discharge, the resulted showed that out of studies basins, Type (C) and (D) are producing less velocity in the basin which indicated that these basin's appurtenances are significantly decaying the velocity magnitude in three dimensions. However, out of studied basins, at the flood discharge, the maximum velocity was found in Type (A) basin.

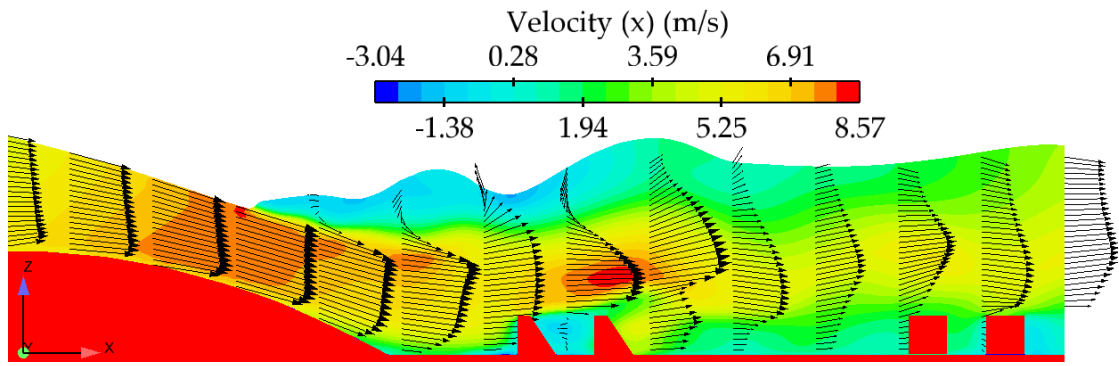
#### **4.5.2.2 Velocity Field and Patterns at Design Discharge**

Fig. 4.26 (a) shows velocity pattern in Type (A) basin at design discharge. The maximum velocity magnitude was found in the supercritical region on the downstream glacis which reached to 8.1 m/s. The results indicated that a highly turbulent flow was impinging on the basin's floor which was shortly deflected by the baffle blocks to the upper fluid layer. At design discharge, the results revealed three different velocity zones, i.e., 1) a weak velocity zone from floor to the top surface of basin's appurtenances; 2) high velocity zone in the central fluid depths, and free surface velocity zone with fluctuating velocity magnitude. From the velocity field, the results showed that as the flow travelled towards downstream, the depth of high velocity zone was found to be increased which further indicated that

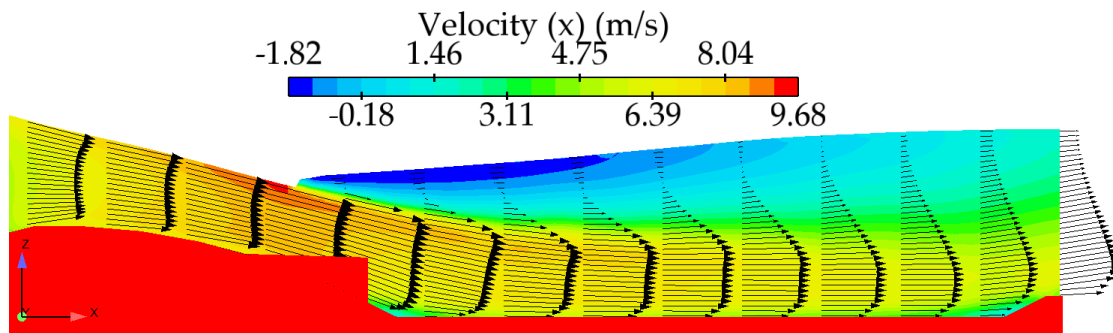
high velocity fluid was moving toward downstream and lesser amount of energy was dissipated in the basin. At the design discharge, the maximum velocity at the basin's end was reached 3.7 m/s. In comparison to the flood discharge, at designed discharge, the velocity values on the basin flood were higher and flow was found to be highly turbulent. However, at the basin end, the velocity values were found to be same as noted in flood discharge.

Fig. 4.26 (b) shows velocity field on Type (B) basin at design discharge. The pattern of velocity field was found similar to that was observed at the flood discharge. However, the results indicated higher velocity magnitude on the basin's floor in which larger boundary growth layers were noticed near the floor. In comparison to the flood discharge, at design discharge, the free surface profile of HJ was found to be different in which a strong re-circulation region was observed which continued to  $\frac{3}{4}$  of the basin's length. The overall free surface profile was found to be gradually increased towards the basin's end. In addition, after reaching to at basin's end, the end sill deflected the high velocity vector toward to upper fluid layer which slightly decreased the boundary growth layers in those regions as can be seen in Fig. 4.26 (b). At the design discharge, in Type (B) basin, the maximum velocity was observed on the downstream glacis which reached 8.60 m/s while at the end, the velocity magnitude reached 4 m/s.

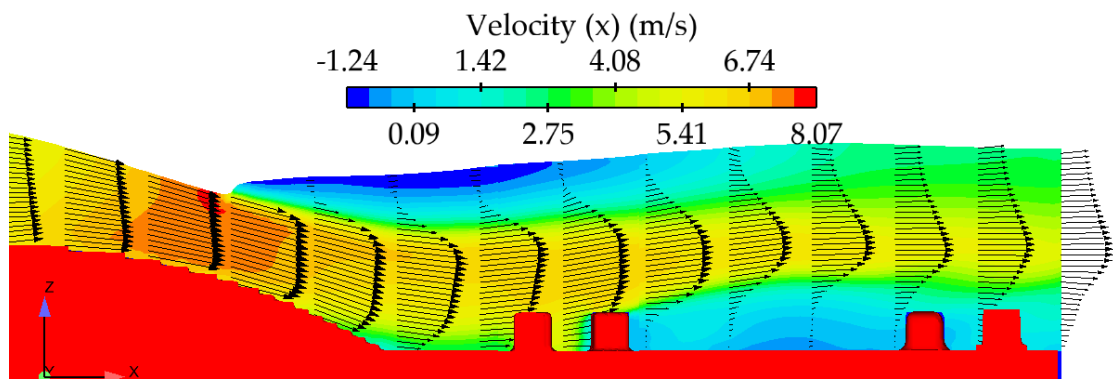
Fig. 4.26 (c) shows velocity pattern on Type (c) basin at the design discharge. Overall velocity pattern was found similar to that was observed at the flood discharge, however, at the design discharge, after impacting with the WSBB, the higher velocity vectors moved towards the upper fluid region and their distance from the basin floor was larger than that was observed at the flood discharge. In the HJ region, a strong re-circulation and negative velocity field was observed which converted into the forward velocity after the HJ. At the basin's end, due to the influence of friction blocks, the velocity near the basin was found to be reduced which indicated that at such higher discharge, the basin substantially decayed the velocity field. In Type (C) basin, the maximum velocity was found in the supercritical region as noticed in the other basins while at basin's end, the velocity value reached to 3.18 m/s.



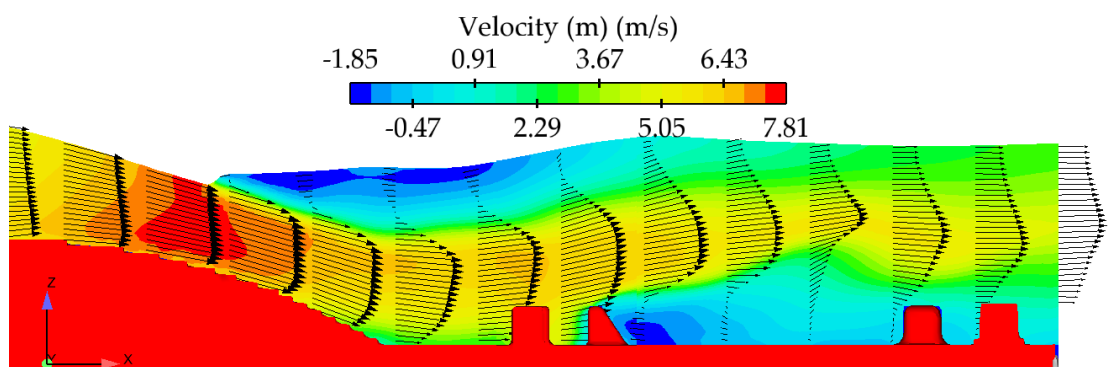
(a)



(b)



(c)



(d)

FIGURE 4.26: 2-D Illustration of velocity distribution downstream of different basins at design discharge of  $24.30 \text{ m}^3/\text{s}/\text{m}$ , (a) Type (A), (b) Type (B), (c) Type (C) and (d) Type (D)

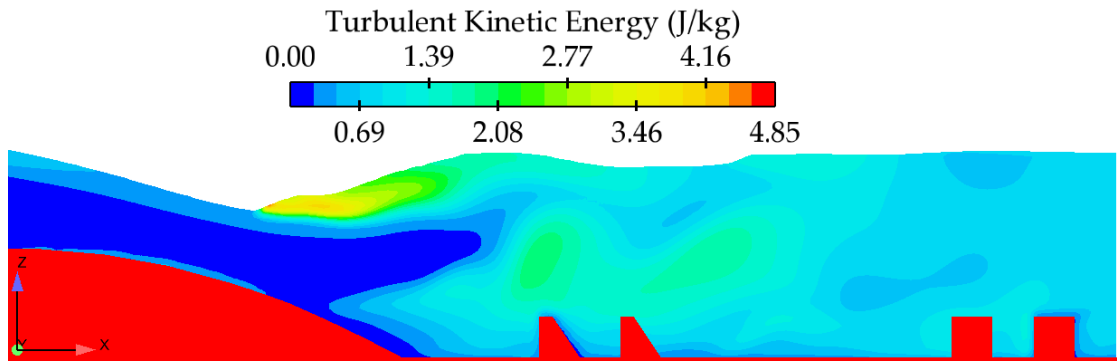
Fig. 4.26 (d) represents velocity field on Type (D) basin at design discharge. The pattern of velocity field was found to be different than that was noted in flood discharge. In addition, the velocity field also differed with Type (C) basin. After impacting with baffle blocks, the fluid was moved toward the upper fluid region and distance of this region from basin's end was higher as compared to flood discharge. In addition, after the baffle blocks, large wake region was noted, and its dimensions were found to be larger than that was noticed at flood discharge. Furthermore, at design discharge, a strong HJ was observed in Type (D) and its profile was different to that was noticed at flood discharge. In Type (D) basin, the maximum velocity at the basin reached 3 m/s which was found to be slightly lesser than Type (c) basin.

### 4.5.3 Turbulent Kinetic Energies

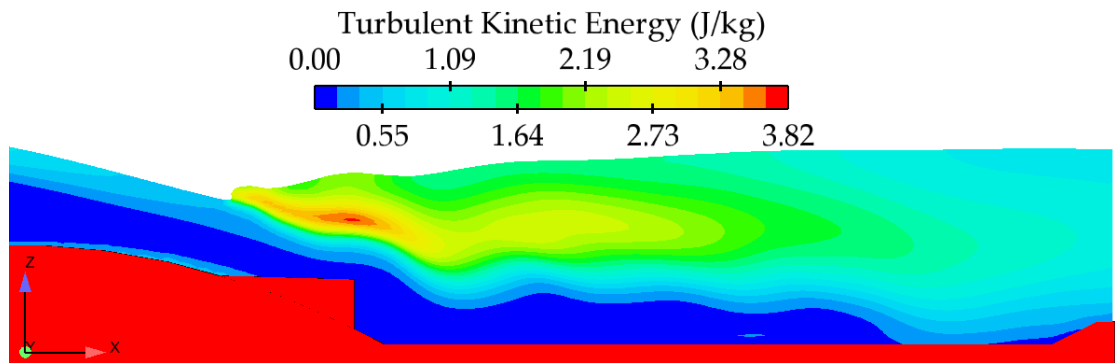
#### 4.5.3.1 Turbulent Kinetic Energies (TKEs) at Flood Discharge

Fig. 4.27 illustrates 2-D contours of turbulent kinetic energy (TKEs) in Type (A), (B), (C) and (D) basins at flood discharge of  $18 \text{ m}^3/\text{s}/\text{m}$ . The contours are drawn from the center-line ( $y/2$ ) of the models. Fig. 4.27 (a) shows TKEs in Type (A) basin at the flood discharge. Due to the highly turbulent flow, the maximum TKEs in Type (A) basin was reached to  $4.85 \text{ m}^2/\text{s}^2$  in the HJ region. The values of TKEs were found to be reduced as the flow moved towards the downside of basin. However, the results indicated a uniform distribution of TKEs soon after the downstream toe of glacis. However, over the baffle blocks region, the TKEs were ranged between  $2.08 \text{ m}^2/\text{s}^2$  to  $2.77 \text{ m}^2/\text{s}^2$ . At the flood discharge, the maximum value of TKEs at the basin's end were found between 0.69 to  $1.39 \text{ m}^2/\text{s}^2$ .

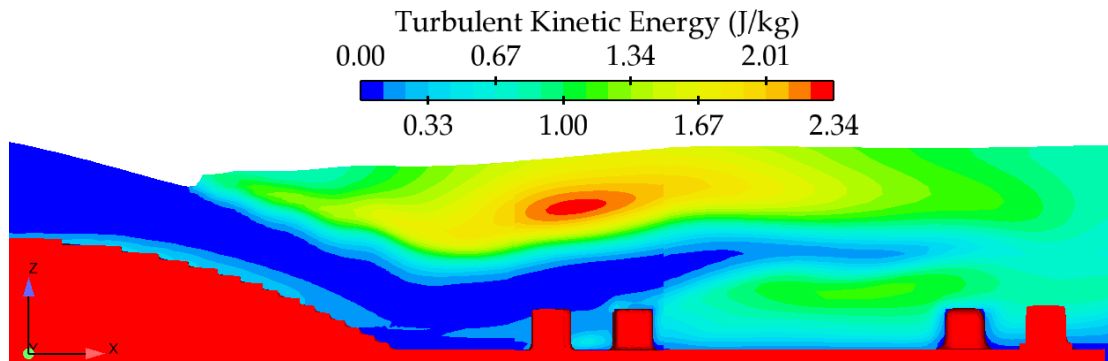
Fig. 4.27 (b) shows TKEs in Type (B) basin at  $18 \text{ m}^3/\text{s}/\text{m}$ . The maximum TKE values were observed in the HJ region and in the central fluid depths which gradually decreased as the distance from the jump was increased. Due to the absence of basin's appurtenances, the TKEs were found in the lower fluid depths



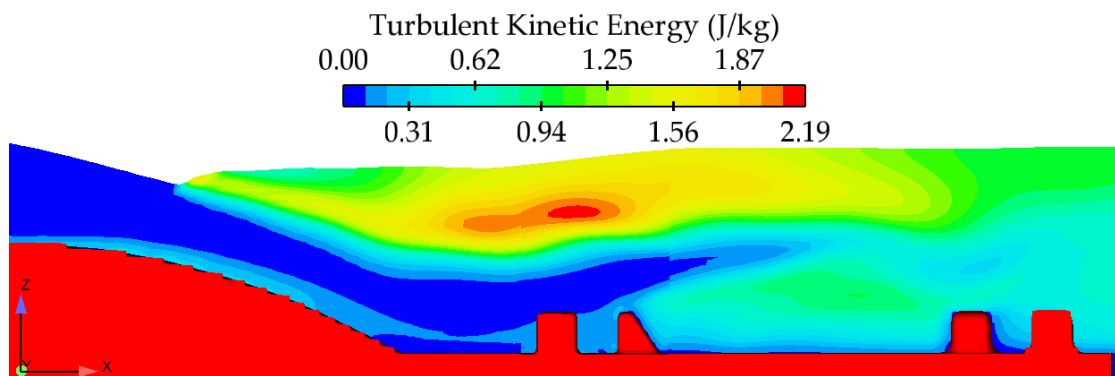
(a)



(b)



(c)



(d)

FIGURE 4.27: 2-D Illustration of turbulent kinetic energies in different basins at flood discharge of  $18 \text{ m}^3/\text{s}/\text{m}$ , (a) Type (A), (b) Type (B), (c) Type (C) and (d) Type (D)



and near the floor as can be seen in Fig. (b). In addition, as the fluid moved toward the downside of the basin, the TKEs were found on the end sill and floor which indicated that after the rigid bed, the TKEs will erode the loose riverbed. In Type (B) basin, the maximum TKEs reached to  $3.82 \text{ m}^2/\text{s}^2$  in HJ region while on near the end sill these values reached  $1.1 \text{ m}^2/\text{s}^2$ .

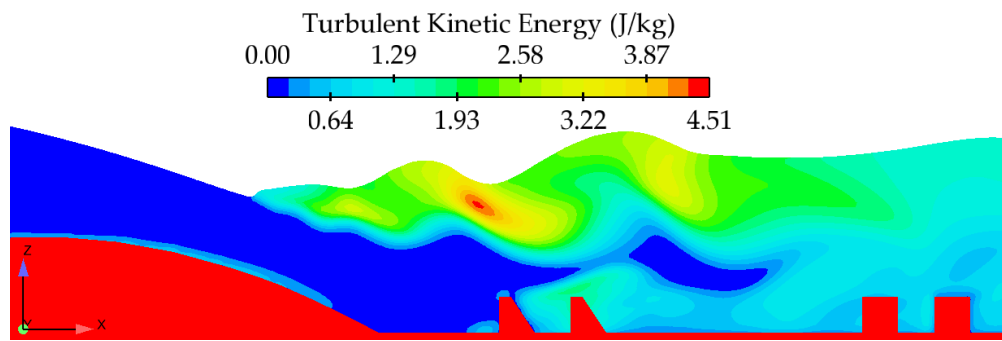
Fig. 4.27 (c) shows TKEs in Type (C) basin at flood discharge. The pattern of TKEs was found to different than Type (A) and (B) basins. The maximum TKEs values were observed in the HJ region which reached to  $2.34 \text{ m}^2/\text{s}^2$  while at the basin's end these values declined below  $1 \text{ m}^2/\text{s}^2$  as shown in Fig. 4.27 (c). The results further showed that due to the presence of baffle blocks, the higher TKEs from the HJ was deflected towards the free surface while smaller value of TKEs were observed near the floor and with the baffle and friction blocks regions. The maximum values of TKEs with the baffle and friction blocks regions were ranged between  $1 \text{ m}^2/\text{s}^2$  to  $0.33 \text{ m}^2/\text{s}^2$  as can be seen from Fig. 4.27 (c). In addition, the results also showed lower TKE values over the rigid surface of downstream glacis which diminished as the fluid contacted basin's floor.

Fig. 4.27 (d) shows TKEs in Type (D) basin at the flood discharge. The pattern of TKEs was similar to that was observed in Type (C) basin. The maximum values of TKEs were observed in the HJ region which reached to  $2.19 \text{ m}^2/\text{s}^2$ . The results showed that as the distance from the HJ was increased, the TKE magnitude was found to be decreased and near the floor, these values were ranged between  $0.94 \text{ m}^2/\text{s}^2$  to  $0.31 \text{ m}^2/\text{s}^2$ . However, above the central fluid region and at the free surface, the TKEs were found between  $0.94$  to  $1.25 \text{ m}^2/\text{s}^2$ . As compared to Type (B) and (C) basins, the overall TKE values were found to be less in Type (D) basin. From the TKEs analysis of flood discharge, the results revealed that out of the tested basins, the minimum amount TKEs were found in Type (C) and (D) basins. The results further indicated that wedge-shaped baffle blocks are improving the flow on the basins.

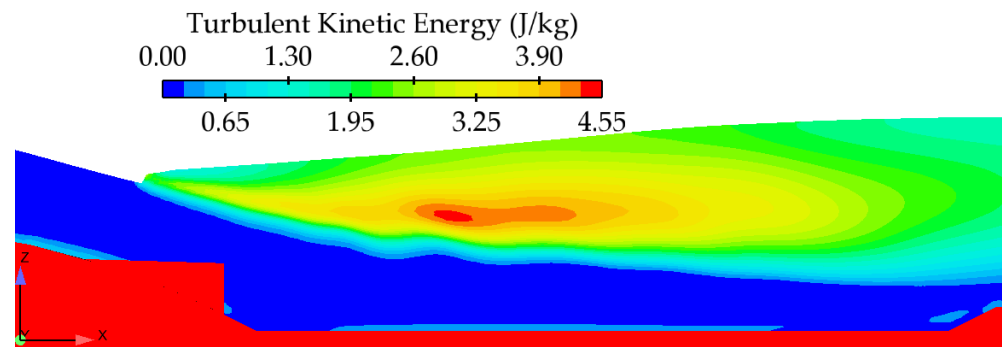
#### 4.5.3.2 Turbulent Kinetic Energies (TKEs) at Design Discharge

Fig. 4.28 (a) displays TKEs field in Type (A) basin at design discharge. The pattern of TKEs at the design discharge was found to be different than that was observed at the flood discharge. In Type (A) basin, two different TKEs regions were noted. The first region was noted at the free surface and its depths was extend up to the top surface of basin's appurtenance, i.e., baffle and friction blocks, while second region was noted near the floor which was found to be extended towards the bottom of first region. The maximum amount of TKEs was observed at the free surface in the first region and the maximum value of TKE reached to  $4.51 \text{ m}^2/\text{s}^2$ . Because of the highly turbulent flow, the first TKEs zone was found to be travelled as the flow headed towards the downside of the basin, however, the TKEs in this region were found to declined before the friction blocks. At design discharge, near the floor and at the basin's end, the TKE values were found to be between  $0.64$  to  $1.29 \text{ m}^2/\text{s}^2$ . In comparison to the flood discharge, at the design discharge, the TKEs values at the end of Type (A) basin was found to be less.

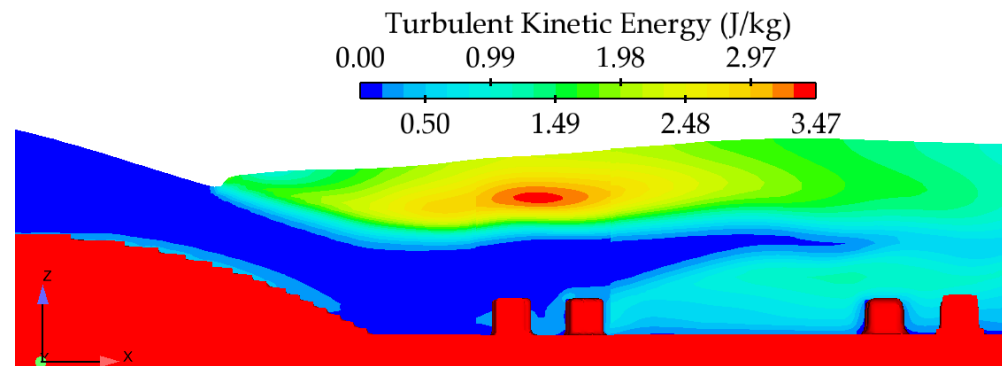
Fig. 4.28 (b) shows TKEs in Type (B) basin at design discharge. The patterns of TKEs were found to be dissimilar than that were noticed at the flood discharge. At the start of basin, the depth of TKEs was less which increased as the flow moved toward the downside. At the basin's end, the depth of TKEs reached to the top surface of end sill. The maximum amount of TKEs was observed within HJ region as noted in earlier at the flood discharge. However, at the design discharge, the distance of higher TKEs fluid layers was less from the basin's floor. In addition, at the design discharge, the overall depth of higher TKEs fluid layer also increased which indicated that more energy was travelled near the bed. Furthermore, the results also showed small TKEs near the basin's floor and their values found between  $0.65$  to  $1.30 \text{ m}^2/\text{s}^2$ . In Type (B) basin the maximum amount of TKE reached to  $4.55 \text{ m}^2/\text{s}^2$  and was found higher than that was noted at flood discharge. At the basin's end, the TKEs values were reached to  $1.30 \text{ m}^2/\text{s}^2$ . Conclusively, at the design discharge, the TKEs were found higher near the rigid floor which moved towards the downside of basin and caused scouring of riverbed.



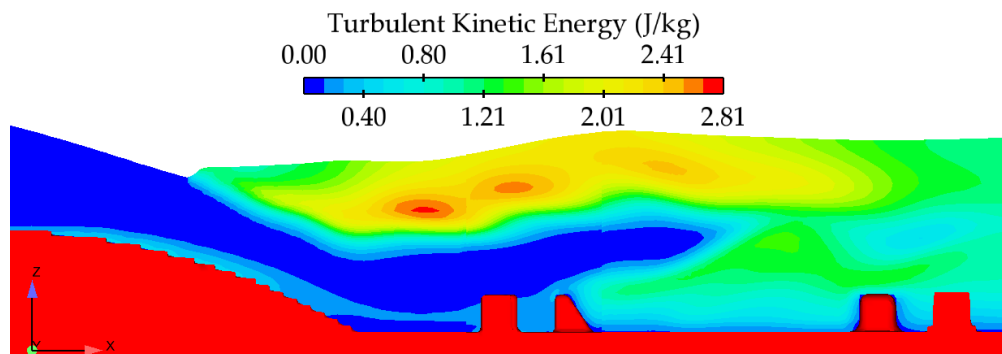
(a)



(b)



(c)



(d)

FIGURE 4.28: 2-D Illustration of turbulent kinetic energies in different basins at design discharge of  $24.30 \text{ m}^3/\text{s}/\text{m}$ , (a) Type (A), (b) Type (B), (c) Type (C) and (d) Type (D)

Fig. 4.28 (c) illustrates TKEs in Type (C) basin at design discharge of 24.30 m<sup>3</sup>/s/m. The results indicated a similar pattern of TKEs as noted at flood discharge. However, the TKEs values were found to be higher at design discharge. In addition, at the design discharge, the depth of higher TKE fluid layer was found less than that was noted at flood discharge, while near the floor depth of small TKEs fluid layer increased as can be seen in Fig. 4.28 (c). Furthermore, at the design discharge, in the baffle blocks region, the TKEs zone was found to be decreased while after the baffle blocks a relatively higher depth of TKEs region was noted as mentioned before. The overall magnitude of TKE in Type (C) basin was increased at the design discharge for which the maximum value reached to 3.47 m<sup>2</sup>/s<sup>2</sup> while at the basin's end and in the friction blocks region the TKE values were ranged between 0.50 to 0.99 m<sup>2</sup>/s<sup>2</sup> Fig. 4.28 (d) shows TKEs patterns on Type (D) basin at design discharge. The overall TKEs pattern was found dissimilar to that were observed at flood discharge. In addition, as compared to Type (B) and (C) basin, the results indicated different TKEs magnitude in Type (D) basin. The maximum TKEs value were noted in the HJ region at different locations as can be seen in Fig. 4.28 (d). Furthermore, at design discharge, the maximum TKEs in Type (D) was found to less than Type (B) and (C) basins which reached to 2.81 m<sup>2</sup>/s<sup>2</sup> in the HJ region. On the basin's end, the maximum TKEs values were ranged between 0.40 to 0.80 m<sup>2</sup>/s<sup>2</sup> which were less as compared to Type (B) and (C) basins. In conclusion, based on the TKEs patterns in studied basin, the results showed that Type (D) is producing less TKEs on the floor and at the basin's end.

## 4.6 Tail Water Rating Curves and Locations of Hydraulic Jumps (HJ<sub>s</sub>)

In the preceding sections 4.4 and 4.5, the results of hydraulic parameters for gated and free flow discharge are analysed and discussed. However, the focus of this section is to compare the predicted results with the prototype barrage data. In

addition, the results of HJ<sub>s</sub> locations for the studied discharges are also compared to drawn comparison among the studied basins, i.e., Type (A), (B), (C), and (D). It is important to mention that the present gated and free flow models are operated

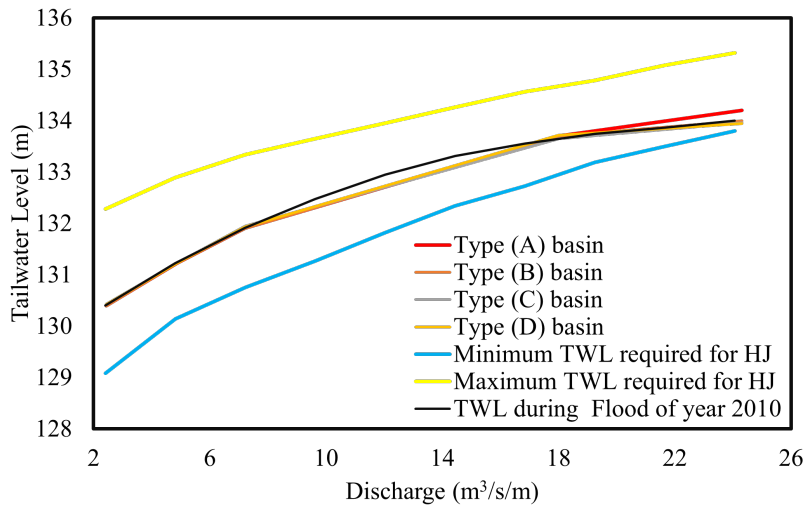


FIGURE 4.29: Tail water rating curves of the studied basins at gated and free flow discharges

on the hydraulic conditions of year 2010 flood. From Fig. 4.29, it can be seen that the tail water levels are found within the maximum and minimum limits of HJ requirements. However, the trends of trends followed the tail water levels of year 2010. In addition, from 7.22 m<sup>3</sup>/s/m to 18 m<sup>3</sup>/s/m discharges, the tail water levels of the present models are found to be deviated because at present, these discharges have not been investigated. Furthermore, at the investigated free flow discharges, the tail water levels predicted in Type (A) basin are found be above than that are observed in year 2010 and other models (presently studied). In conclusion, it can be said, under the operation conditions, i.e., tail water, pond level, geometries, gate openings, meshing and boundary conditions, all the basins have retained the tail water levels within the thresh hold limit of HJ conditions.

Fig.4.30 shows comparison of HJ location within studied basins at gated and free flow discharges. At the gated flows, the results indicated that Type (A) basin is holding the HJ well above the downstream toe of the glacis. However, the minimum distance of HJ from the glacis toe is found at in Type (D) basin which reached to 4.5 m at 2.44 m<sup>3</sup>/s/m discharge. On the other hand, at the designed and flood discharges, the locations of HJ in Type (c) and (D) basins are found to

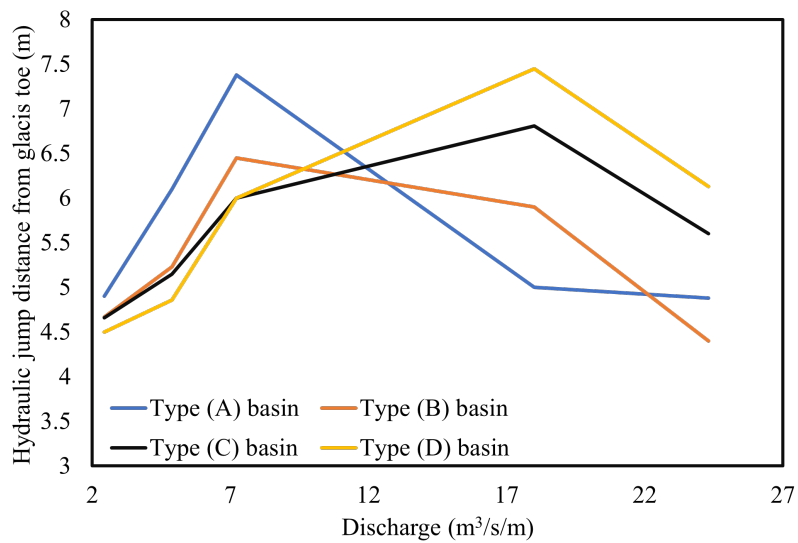


FIGURE 4.30: Comparison of hydraulic jump locations at gated and free flow discharges for the studied basins

be noted above on the glacia. The maximum distances of HJ in Type (c) and (D) basin is reached to 7.45 m and 6.81 m at 18 m<sup>3</sup>/s/m and 24.30 m<sup>3</sup>/s/m discharge, respectively. In contrast, at 18 m<sup>3</sup>/s/m discharge, the minimum distance of HJ from the glacia toe is found in Type (A) basin which reached to 5 m while at 24.30 m<sup>3</sup>/s/m discharge, the minimum distance of HJ from the glacia toe is found in Type (B) basin. From the present results of HJ locations, it is found that at gated flows, Type (A) and (B) basins are retaining the HJ well above than Type (C) and (D) basin while at the free flows, a reverse phenomena is noticed. Therefore, it can be said, the newly proposed Type (C) and (D) are keeping the HJ at the downstream glacia while when after remodeling (Type (b) basin), the location of HJs at the higher discharge are on the downside of downstream glacia.

The Table 4.10 shows the overall results of  $CHP_s$  at the gated discharge. The detailed discussions on these parameters have already be made in section 4.4. Similarly, Table 4.11 shows overall values of different hydraulic parameters at the flood and design discharges. It is important to mentioned here, some of parameters values, i.e., hydraulic jump length ( $L_j$ ), roller length of HJ ( $L_r$ ), and relative energy loss is not included in the Table, because at such higher discharges, these

TABLE 4.10: Summarized results of Critical Hydraulic parameters (CHPs) in Type (A), (B), (C) and (D) basins at gated flows

Stilling Basins	$q$ ( $\text{m}^3/\text{s}/\text{m}$ )	$V_1$ ( $\text{m}/\text{s}$ )	$V_2$ ( $\text{m}/\text{s}$ )	$y_1$ ( $\text{m}$ )	$y_2$ ( $\text{m}$ )	$y_2/y_1$	$Fr_1$	$Fr_2$	$L_j$ ( $\text{m}$ )	$L_r/d_1$	$E$ (%)
Type (A)	2.44	8.79	0.41	0.29	3.53	12.17	5.53	0.10	9.70	33.45	19
Type (B)		8.54	1.42	0.28	3.13	13.88	5.55	0.26	5	17.86	19
Type (C)		9.10	1.15	0.28	3.63	12.80	5.28	0.19	9.50	33.93	18
Type (D)		9.16	1.20	0.26	3.61	11.18	5.74	0.20	9.30	35.77	19
Type (A)	4.88	9.13	0.70	0.54	4.36	8.00	4.00	0.11	11.50	21.30	8
Type (B)		9.36	2.65	0.52	3.95	7.60	4.15	0.43	7	13.46	14
Type (C)		10.00	1.81	0.54	4.39	8.13	4.36	0.28	10.70	19.81	19
Type (D)		9.47	1.81	0.53	3.61	8.30	4.46	0.30	10.50	19.81	26
Type (A)	7.22	9.19	1.03	0.85	4.95	5.82	3.12	0.15	12.90	15.20	3
Type (B)		9.61	2.07	0.96	4.90	5.55	3.46	0.30	13	16.29	4
Type (C)		9.41	2.21	0.86	4.90	5.70	3.26	0.32	12	14.20	4
Type (D)		9.47	2.27	0.85	4.97	5.85	3.30	0.33	12.10	14.50	3

values are always found to be fluctuating and due to nature of highly turbulent flow, the output values can not be taken with high precision. Therefore, only velocities, flow depths, and Froude number values are simulated before the HJ and at the basins' end. However, the performance of the stilling basins at the studied flood and design discharges is assessed by the scour models as presented in Chapter 5.

TABLE 4.11: Summary of Hydraulic parameters in Type (A), (B), (C) and (D) basins at flood and design discharges

Stilling Basins	$q$ ( $m^3/s/m$ )	$V_1$ ( $m/s$ )	$V_2$ ( $m/s$ )	$y_1$ ( $m$ )	$y_2$ ( $m$ )	$y_2/y_1$	$Fr_1$	$Fr_2$
<b>Type (A)</b>	18	7.2	3.2	2.5	6.9	2.7	1.5	0.3
<b>Type (B)</b>		7.3	3.0	2.6	6.3	2.4	1.4	0.4
<b>Type (C)</b>		7.0	2.7	2.6	6.9	2.6	1.3	0.3
<b>Type (D)</b>		6.8	2.5	2.6	6.9	2.6	1.4	0.3
<b>Type (A)</b>	24.30	8.0	3.8	2.9	7.4	2.5	1.5	0.4
<b>Type (B)</b>		8.6	4.1	3.0	6.2	2.1	1.6	0.5
<b>Type (C)</b>		7.7	3.2	3.0	7.2	2.4	1.4	0.4
<b>Type (D)</b>		7.6	3.0	3.0	7.1	2.4	1.4	0.4



# Chapter 5

## Flow Field, Local Scour and Bed Retrogression

### 5.1 Background

After the hydraulic modelling of different parameters in the studied basins, it was found that in Type (A), (C) and (D) basins the results of hydraulic parameters were close, while dissimilar results were noted in Type (B) basin. Therefore, to further assess the performance of investigated basins, scour models were developed at designed and uncontrolled free conditions such as 24.30, and 18 m<sup>3</sup>/s/m unit discharges, respectively. This chapter begins with the validation of scour models of Type (B) basin with the probing data of year 2015. After validation, the chapter discusses and compares the flow field, scour/retrogression patterns, and longitudinal profiles of different stilling basins.

### 5.2 Validation on Scour Models

Type (A) basin was made functional in year 1958 and continued till 2003. During years 2005 to 2008, barrage's basin was remodelled (Type (B)) as described in

section. Even after the remodelling, probing data of years 2010 to 2014 revealed damages and large scour pits on the barrage downstream.

As the investigated Type (B) basin is full scaled model of existing prototype barrage, therefore, scour results downstream of Type (B) basin were focused for comparison with the field data. For validation, the probing data of year 2015 of bays 33, 34 and 55 were used. The data in hard form was digitized using Auto-CAD, and approximate values of bed profiles were obtained from center line of the bays. At present, different turbulent models were used to investigate the bed profiles and their results were compared with the profiles of bays 33, 34 and 55 of the prototype barrage. The present models were run for two different uncontrolled free flows i.e., 24.30 and 18 m<sup>3</sup>/s/m.

For 24.30 m<sup>3</sup>/s/m. discharge, Fig. 5.1 illustrates comparison of bed profile of bay 33 with LES, Standard K- $\epsilon$  (hereafter, Std) and RNG K- $\epsilon$  models. The results of modelled bed profiles were computed at  $T_s=500$  s. Up to X=6 m after the rigid floor, all the turbulence models showed a similar pattern of bed profiles which agreed well with the field observation. However, upon comparison with K- $\epsilon$  models, LES model overestimated bed profiles as the distance from end of rigid floor was increased. Upon use of LES model, after X= 9 m from the rigid floor, results showed that about 97 % of the sediment bed was eroded, while results of both K- $\epsilon$  models agreed well with the field data as shown in Fig 5.1. In both K- $\epsilon$  models, the sediment bed profiles showed identical trends, however, in comparison to RNG k- $\epsilon$  model, the Std K- $\epsilon$  model showed higher bed scour on upstream side while lesser values of scour were noticed on downstream side of the sediment bed. Additionally, upon comparison of maximum scour depths with bay 33, present models showed higher scour depths, for which the maximum errors reached 13.5%, 13.5% and 10 % in LES, RNG and Std K- $\epsilon$  models, respectively.

Fig 5.2 compares the bed profiles of bay 34 with the profiles downstream of Type (B) basin. For the initial 15 m length of scoured bed, as compared to field data of bay 34, the present models showed higher bed degradation. On the contrary, as

compared to K- $\epsilon$  models, results of LES model showed higher deviation from the observed field data.

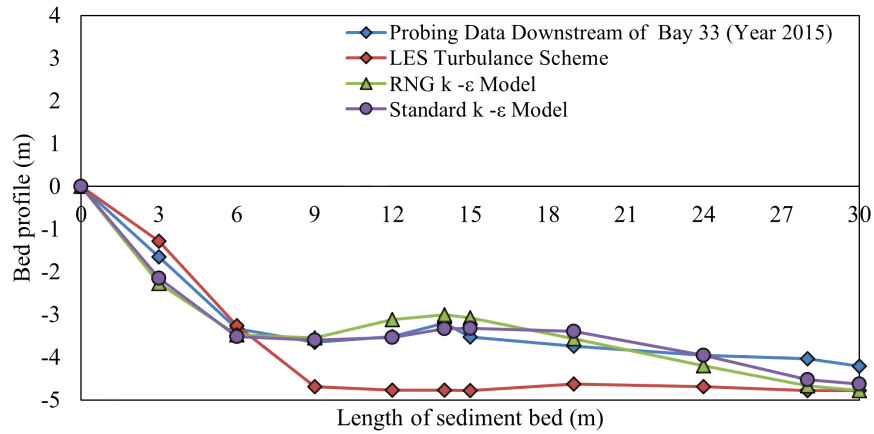


FIGURE 5.1: Comparison of modelled scour profiles using different turbulence schemes with bay 33 of Prototype

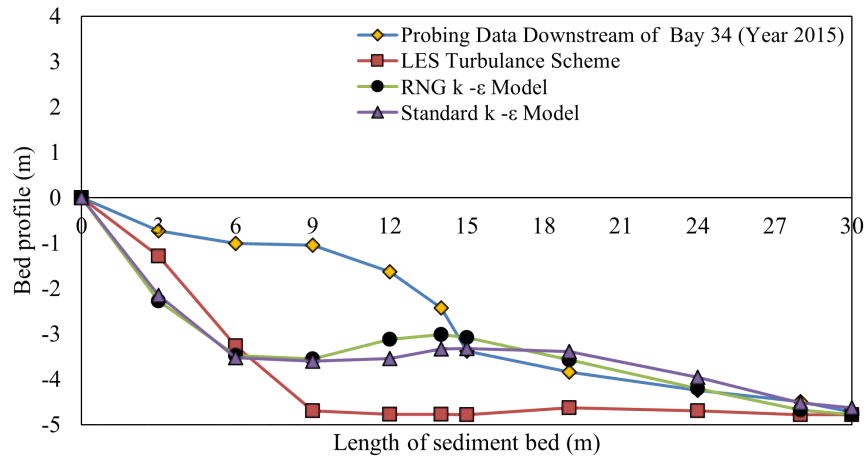


FIGURE 5.2: Comparison of modelled scour profiles using different turbulence schemes with bay 34 of Prototype

Upon comparison of maximum scour depths with bay 34, the results revealed higher scour in LES and RNG K- $\epsilon$  models, for which the maximum error reached to 1.3%. On the contrary, as compared to the field data, Std K- $\epsilon$  model underestimated the maximum scour depth which showed 2% error.

Fig 5.3 compares the bed profiles of present models with bay 55. Similar to bay 33, as compared to the observed data of bay 55, present models overestimated the bed profiles for the initial bed length up to X=15 m. However, after X=15 m, as

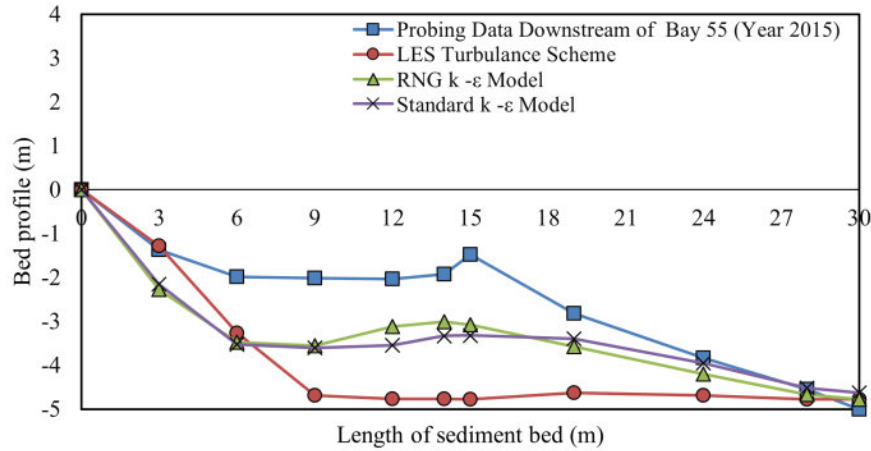


FIGURE 5.3: Comparison of modelled scour profiles using different turbulence schemes with bay 55 of Prototype

compared to LES model, RNG and Std K- $\epsilon$  models showed less deviations. On the downstream side of scoured bed from X= 24 m to 30 m, bed profiles using Std and RNG K- $\epsilon$  models were found to be matched with the results of bay 55.

The performance of present scour models is also assessed by Coefficient of determination ( $R^2$ ), and Nash-Sutcliffe Model Efficiency Coefficient (NSE). The model performance is said to be perfect when the value reaches 1 while it is said to be poor if the values reach to 0 and negative for  $R^2$  and NSE, respectively. The simulated scour profiles were compared with bays 33, 34 and 55 of the prototype barrage as shown in Figs. 5.4, 5.5, and 5.6, respectively. For bay 33, the models showed close agreement for which the values of  $R^2$  reached 0.908, 0.909 and 0.953 in LES, RNG K- $\epsilon$  and Std K- $\epsilon$  models, respectively as show in Figs. 5.4 (a), 5.4 (b), and 5.4 (c), respectively. On the other hand, for bay 33, the  $NSE_s$  reached to 0.423, 0.896, and 0.944 ES, RNG K- $\epsilon$  and Std K- $\epsilon$  models, respectively.

Upon comparison with bay 34, the predicted results of scour profiles were found to be deviated for which 0.501, 0.60 and 0.545 values of  $R^2$  were noted in LES, RNG K- $\epsilon$  and Std K- $\epsilon$  models, respectively, as shown in Figs. 5.5 (a), 5.5 (b), and 5.5 (c), respectively. In contrast, the  $NSE_s$  values for bay 34 reached to -0.273, 0.396, and 0.322 in LES, RNG K- $\epsilon$  and Std K- $\epsilon$  models, respectively,

It can be noted that out of the used models, RNG K- $\epsilon$  was found to be better than LES and Std K- $\epsilon$  models. However, as compared to bay 33, the models results

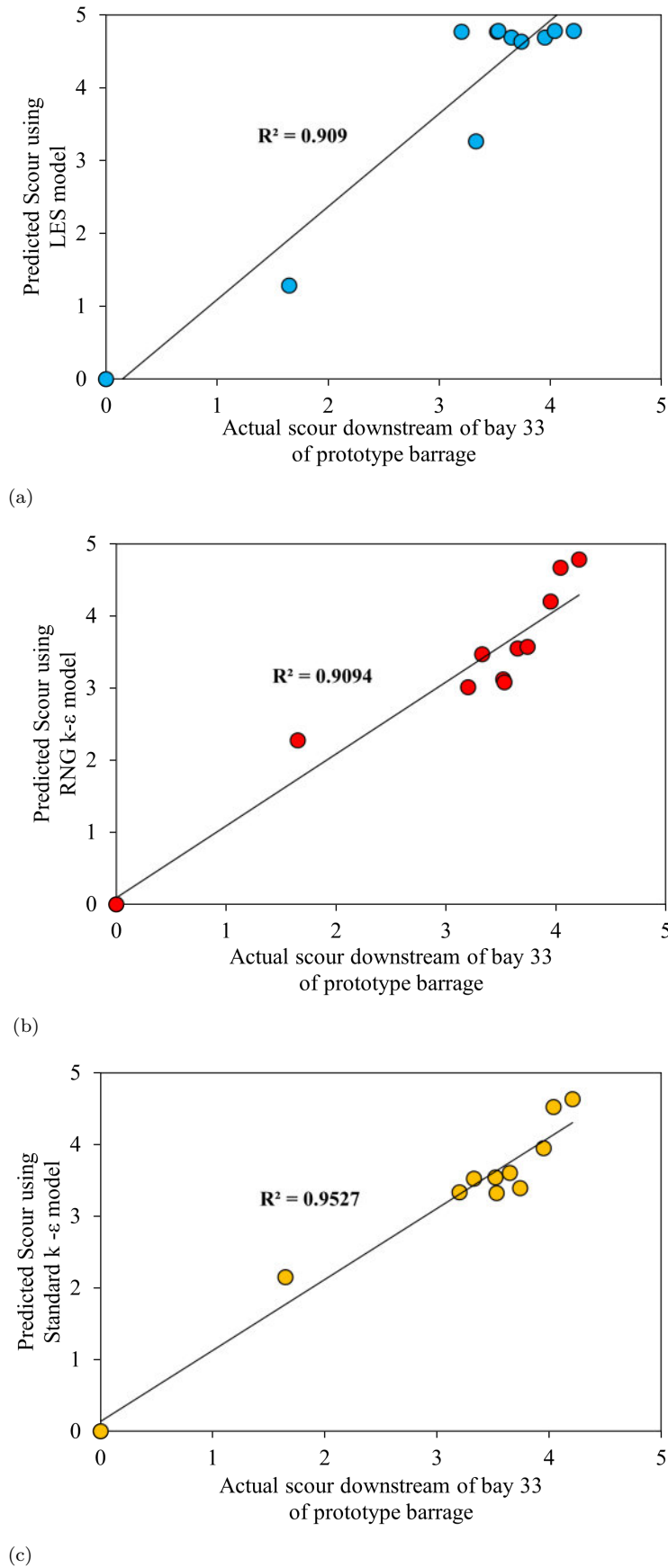
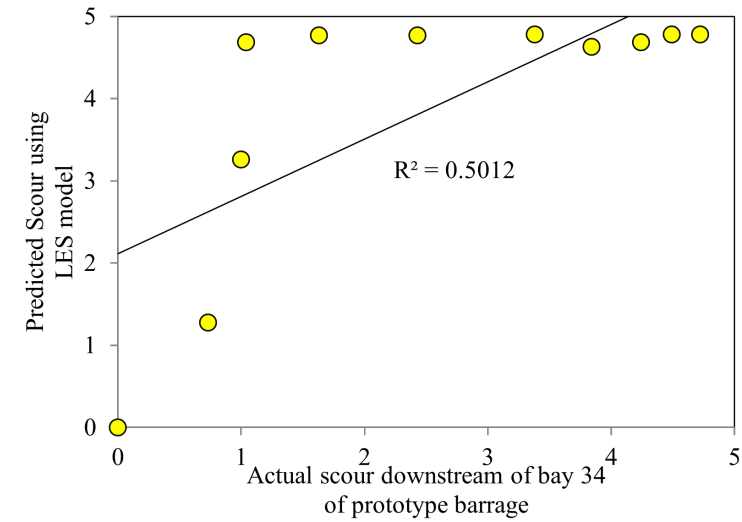
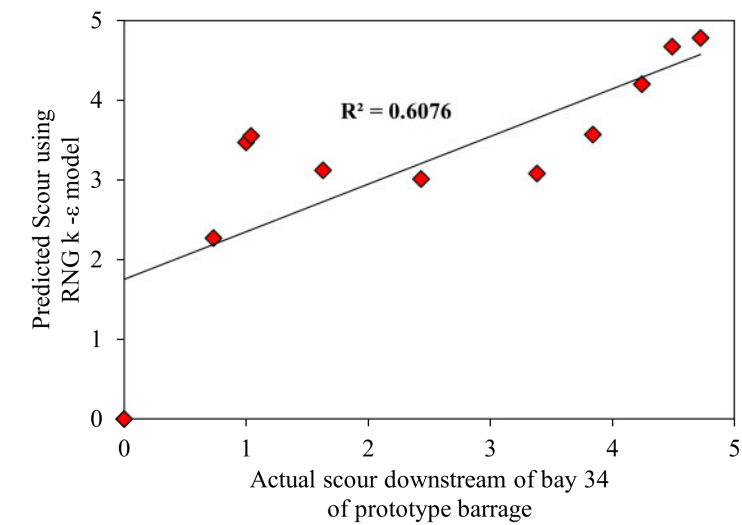


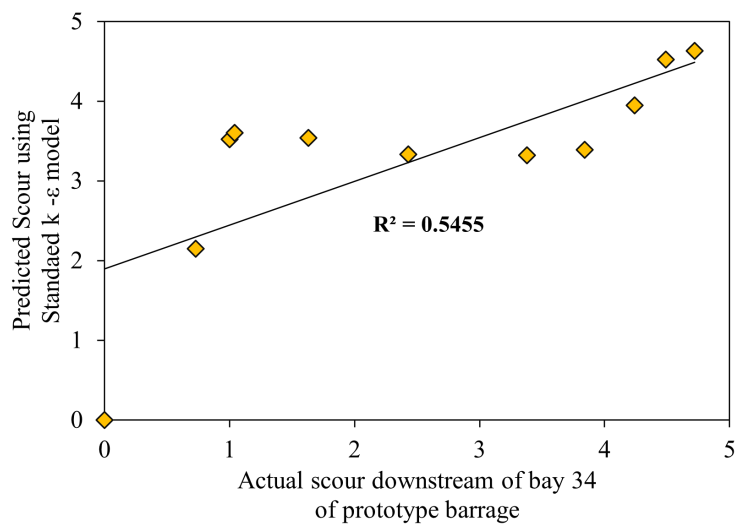
FIGURE 5.4: Comparison of scour profile of Bay 33 with the numerical models, (a) LES, (b) RNG k-ε, and (c) Std K-ε model



(a)



(b)



(c)

FIGURE 5.5: Comparison of scour profile of Bay 34 with the numerical models, (a) LES, (b) RNG k-ε and (c) Std K-ε model

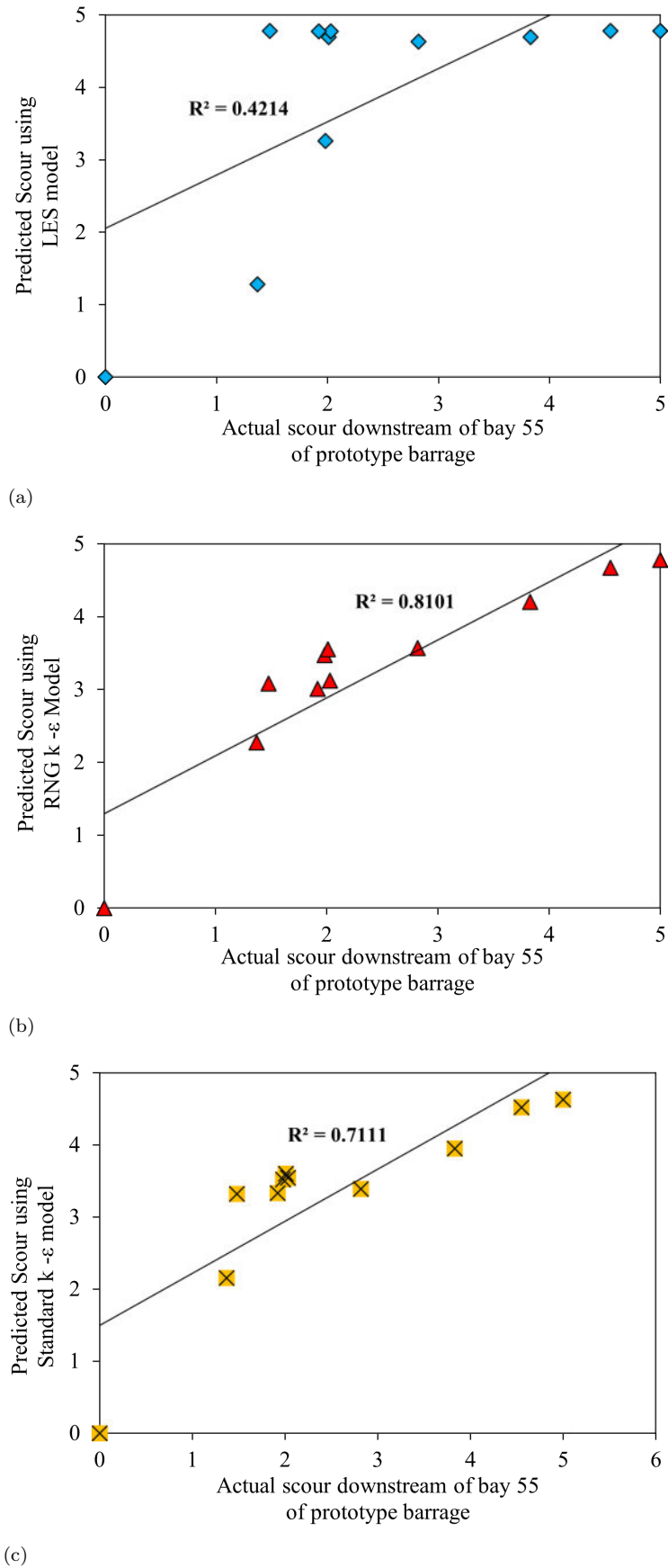


FIGURE 5.6: Comparison of scour profile of Bay 55 with the numerical models, (a) LES, (b) RNG k-ε and (c) Std K-ε model

(LES, RNG and Std K- $\epsilon$ ) deviated from the observed profiles of bay 34.

Upon comparison with bay 55 indicated the  $R^2$  values reached 0.42, 0.81 and 0.71 in LES, RNG K- $\epsilon$  and Std K- $\epsilon$  models, respectively, as shown in Figs. 5.6 (a), 5.6 (b), and 5.6 (c), respectively. For bay 55, as compared to LES and Std K- $\epsilon$  model, results of RNG K- $\epsilon$  model were found to be more accurate which agreed well with the field data. Similarly, after analysing the profiles with  $NSE_s$ , the models predicted -0.799, 0.494, and 0.378 in LES, RNG K- $\epsilon$  and Std K- $\epsilon$  models, respectively. The deviation of scour profile by LES can be due to: 1) the LES model is mesh dependent which requires finer cell size in the turbulent flow zones to capture the small scale fluctuations, i.e., turbulent eddies, and 2) within the scour hole, strong vortexes are generated for which the model employed sub grid turbulence model which captured small eddies in the scour hole and consequently increased the scour depth and overall retrogression on the downside of sediment bed. On the contrary, due to the limitation in computing the wake velocities in the shear region, RNG K- $\epsilon$  model predicted less scour in the scour hole and on the downward areas.

Conclusively, based on the results of scour profiles, it is believed that the present models showed reasonable accuracy of scour profiles, especially for bay 33. Based on the validation results, present models allowed to analysis the flow field, bed shear stress and scour profiles downstream of Type (B) and other studied basins.

## 5.3 Flow Field

### 5.3.1 Velocity Distribution at Designed Discharge

At present, the effects of stilling basin appurtenances are focused on local scour downstream of the barrage, therefore, flow field is described both for rigid and scour bed. To describe the flow fields on different beds, velocity distribution and bed shear stress are analyzed using LES, K- $\epsilon$  models. At  $T_s=500s$  (Finish time),



2D and 3D plots of velocity and bed shear stress are drawn from the center line of bay for  $24.3 \text{ m}^3/\text{s}/\text{m}$  and  $18 \text{ m}^3/\text{s}/\text{m}$  discharges.

Fig. 5.7 (a) shows velocity field in Type (A) basin using RNG K- $\epsilon$  model. Fig 5.7 (a), on fore side of HJ, flow is found to be highly turbulent. The flow pattern produced by the present models is found similar to prototype where at such discharge ( $24.3 \text{ m}^3/\text{s}/\text{m}$ ) high kinetic energies travel through the barrage. The maximum forward and backward velocities were noticed at downstream glacis and in HJ which reached to  $9 \text{ m/s}$  and  $-2.56 \text{ m/s}$ , respectively. Fig 5.7 (a) also shows that due to the contracted jet of upstream flow, high velocity flow travelled in lower fluid depths while large fluid re-circulations were observed at the free surface. After impacting with baffle block, high velocity fluid in lower fluid depths was deflected to the middle fluid region which travelled to the end of rigid floor as can be seen in Fig 5.7 (a). Between the two rows of baffle blocks, a considerable eddies and re-circulations were also developed which created discontinuities in the turbulent fluid layers near basin's floor. After baffle blocks, due to abrupt decrease in velocity magnitude, the flow velocities near basin's floor were declined. On downstream side of Type (A) basin, the approaching high velocity fluid in central region was deflected by friction blocks, while after the friction blocks, results also showed small number of eddies near the basin's floor which further reduced the velocities.

Using RNG K- $\epsilon$  model, the velocity field downstream of Type (A) basin is shown in Fig 5.7. After rigid floor, the velocity field on scour bed showed two different flow zones, i.e., slow moving zone near the scoured bed, high velocity zone from central fluid region to free surface. Downstream of Type (A) basin, result indicated forward velocity contours which eroded/retrogressed the sediment bed. At the start of sediment bed, depth of slow moving and wake zone was less which increased as flow moved towards downstream. It is important to mention that the slow moving fluid near sediment bed was triggering erosion/bed retrogression which further increased the bed retrogression as depth of wake and slow-moving zone increased, as shown in Fig 5.7 (a). Upon use of RNG K- $\epsilon$  model, no fluid re-circulations were observed on the scoured bed, therefore, only bed retrogression was observed downstream of Type (A) basin.

Using Std K- $\epsilon$  model, results showed different flow field downstream of Type (A) basin which indicated low velocity contours on the fore side and within HJ as shown in Fig 5.7 (b). However, as compared to RNG K- $\epsilon$  model, higher velocity magnitude was noted in the HJ region near basin's floor which was deflected by baffle blocks toward central fluid region. Furthermore, this higher velocity travelled towards downstream up to initial 15 m length of sediment bed. After comparing the results with RNG K- $\epsilon$  model, Std K- $\epsilon$  model revealed higher change in the initial 15 m length of sediment bed. However, from 15 m to the end of sediment bed, the net height change using Std K- $\epsilon$  model was found less than RNG k- $\epsilon$  model. Using Std k- $\epsilon$  model, a slow-moving fluid zone was also noted on the scoured bed which showed the similar flow pattern as was noticed in RNG K- $\epsilon$  model as shown in Fig 5.7 (b). Similar to RNG K- $\epsilon$  model, the results showed no scour hole on the scoured bed, however, due to the forward velocity profile, results showed only bed retrogression.

Upon use of LES model, results showed irregular distribution of velocity field on Type (A) basin, and the flow pattern was found to be dissimilar as compared to Std and RNG K- $\epsilon$  models as shown in Fig.5.7 (c). In HJ region, maximum velocity field was found from basin's floor to middle fluid region, while large eddies and re-circulations were noticed at the free surface. As compared to RNG and Std K- $\epsilon$  models, magnitude of reserve velocity vectors was found higher which reached to 3.05 m/s. Additionally, in LES model, size of eddies and fluid re-circulations were bigger than that were noticed in RNG K- $\epsilon$  and Std k- $\epsilon$  model. The larger size of eddies was due to the nature and formulation of LES model. In addition to the surface rollers, a small number of eddies and fluid circulations were also found in between the two rows of baffle blocks. After impacting baffle blocks, flow was deflected towards free surface which stopped rollers of the HJ. However, soon after the baffle blocks, high velocity fluid was found to be striking at the basin's floor which gradually moved toward upper fluid layer as shown in Fig.5.7 (c).

On the contrary, no such flow patterns were seen in RNG K- $\epsilon$  model while a similar phenomenon was also found in Std K- $\epsilon$  models. In comparison to K- $\epsilon$  models, in LES model, smaller number of eddies were found after the friction blocks. In the

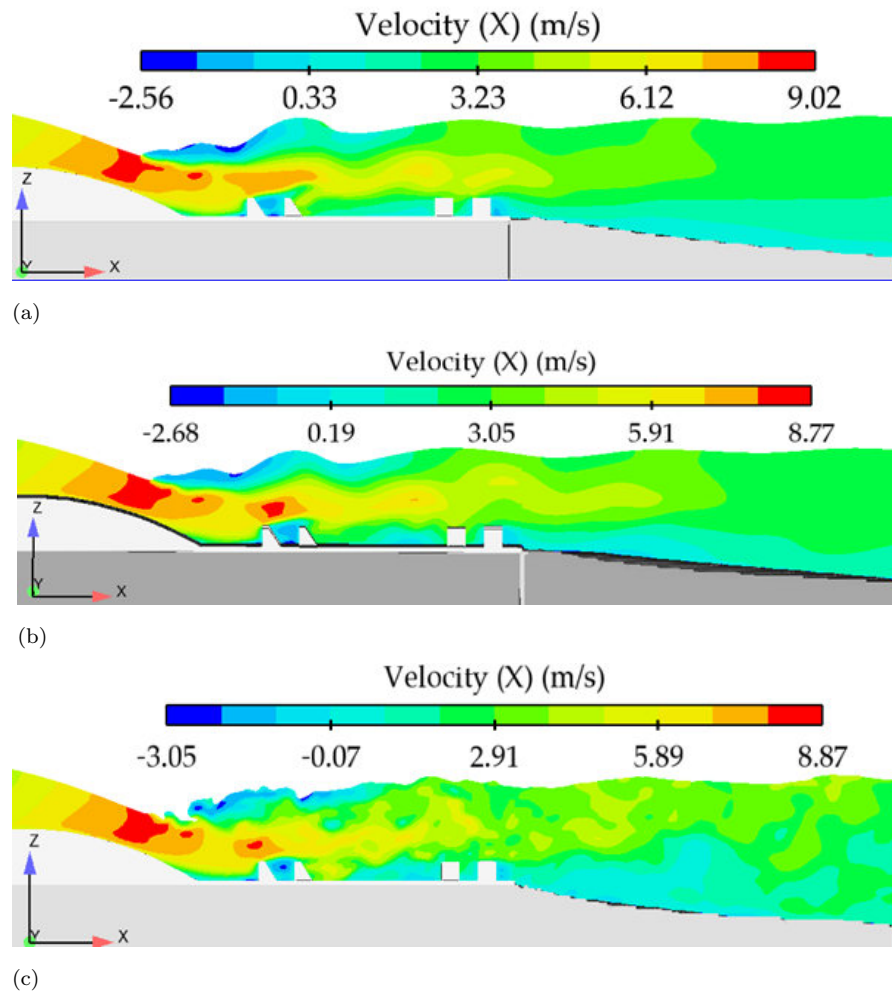


FIGURE 5.7: 2-D Illustration of velocity distribution downstream of Type (A) basin at  $24.30 \text{ m}^3/\text{s}/\text{m}$ , (a) RNG K- $\epsilon$ , (b) Std K- $\epsilon$  model, and (c) LES model

LES model, at the start of sediment bed, high velocity flow was found from middle fluid region to free surface, while at end of sediment bed, these high velocity flow moved towards scoured bed as shown in Fig.5.7 (c).

Overall, in LES model, depth of slow-moving flow near the scour bed was larger than that was found in RNG and Std K- $\epsilon$  models. Due to the larger depth of slow-moving fluid, the results showed higher retrogression in LES model. Conclusively, in comparison to K- $\epsilon$  models, LES model produced higher velocity magnitude and irregular flow pattern on rigid and scoured bed downstream of Type (A) basin.

Fig. 5.8 shows velocity field on Type (B) basin using RNG, Std K- $\epsilon$  and LES turbulence models. Using RNG K- $\epsilon$  model, the concentrated supercritical jet was found to be impinging on the floor as shown in Fig. 5.8 (a). Below the HJ, velocity

field was distributed into three different zones. The first zone was started from basin's floor to the central fluid depth which showed higher velocity magnitude that was ranged between 6 to 8 m/s, while second zone was initiated from central region to lower part of HJ for which the results indicated moderate velocity values those were ranged between 1 m/s to 3 m/s. However, third zone was the free surface of HJ which displayed rollers and re-circulations. As compared to Type (A) basin, due to absence of basin's appurtenances, results showed higher velocity on the entire length of Type (B) basin. However, in Type (B) basin, the free surface profile on rigid and scour bed was found to be stable. In addition to the above mentioned, at the end of Type (B) basin, the end sill deflected the higher velocity flow towards the middle fluid region.

In Type (B) basin, at the start of sediment bed, high velocity flow was found above the height of end sill. However, near the scoured bed, results showed wakes zones and slow-moving flow which caused bed erosion, and this gradual process developed a large scour hole just downstream of the end sill. Additionally, results also indicated that as the depth of slow-moving flow was increased, the scour hole and bed retrogression were also increased.

Fig. 5.8 (b) shows velocity distribution on Type (B) using Std K- $\epsilon$  model. Similar to RNG K- $\epsilon$  model, in Std K- $\epsilon$  model, the results showed three different flow zones. However, their patterns and intensity were found to be different in Std K- $\epsilon$  model. Furthermore, in Std K- $\epsilon$  model, the depth and length of HJ rollers was also found dissimilar than that were noticed in RNG K- $\epsilon$  model. Downstream of rigid floor, the high velocity zone was fluctuating in Std K- $\epsilon$  model which travelled to the end of scoured bed. Below the high velocity zone, a large wake zone and slow-moving flow was noticed, which developed scour hole below the end sill. Additionally, from the scour hole towards downstream, the depth of wake zone and slow-moving flow also increased which caused bed retrogression on the downstream end.

Fig. 5.8 (c) shows velocity distribution on Type (B) basin using LES model. In the LES model, velocity distribution and flow patterns were found to be different than that were noticed in K- $\epsilon$  models. The results showed that highly turbulent

flow was impinging on the basin's floor which continued to travel at the end of basin as shown in Fig. 5.8 (c). As compared to K- $\epsilon$  models, in the LES model, flow depth on the rigid bed was mainly comprised of two fluid zones, i.e, bottom zone, and upper zone. The bottom zone started from basin's floor to the bottom of surface rollers while the upper zone was found between rollers' bottom and surface rollers. The results also showed that the bottom zones were found to be highly turbulent in which the velocity values were approximately above 6 m/s, while in the upper zone velocity magnitude was below 1 m/s. In between these two zones, the results indicated a thin fluid layer which was separating the bottom and upper zones.

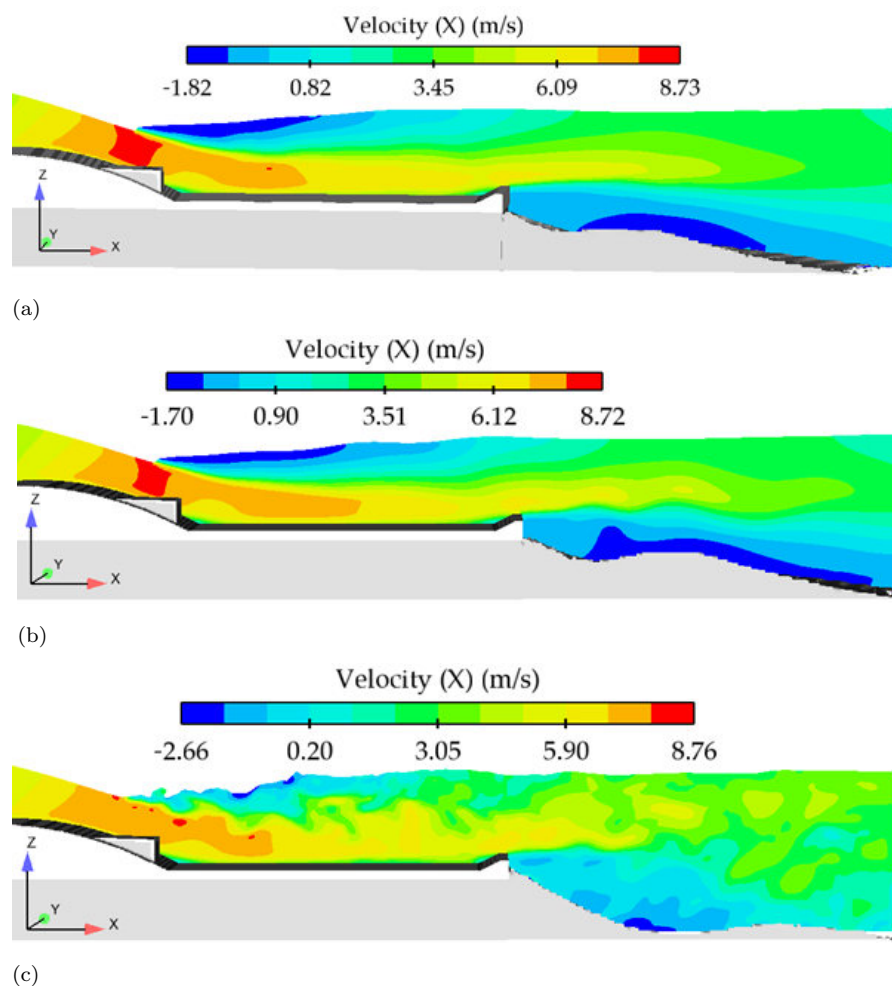


FIGURE 5.8: 2-D Illustration of velocity distribution downstream of Type (B) basin at  $24.30 \text{ m}^3/\text{s}/\text{m}$ , (a) RNG K- $\epsilon$ , (b) Std K- $\epsilon$  model, and (c) LES model

Fig. 5.8 (c), as the distance from HJ initial location was increased, the depths of above mentioned two zones were found to be decreased, while the depth of thin

fluid layer was gradually increased which traveled to the end of sediment bed. As compared to K- $\epsilon$  models, free surface rollers in LES model traveled to the entire basin's length which created undulations on the free surface. Using LES model, Fig. 5.8 (c) shows velocity distribution downstream of Type (B) basin. From Fig. 5.8 (c), it can be seen that similar to the rigid bed, velocity distribution of scoured bed was found scattered on the entire length of scoured bed. Moreover, on scoured bed, the velocity distribution was mainly separated into two different zones, i.e., high velocity zone from middle to free surface, and slow-moving zone near the bed. The depth of slow-moving zone was found high near the rigid bed which developed large scour hole and exposed the sediment bed when simulation reached to finish time ( $T_s=500$  s).

Additionally, at the location of scour hole, large re-circulation of flow was noticed. After leaving the scour hole, depths of slow-moving zone were found to be decreased while a considerable increase in the upper zone was noticed which later retrogressed the bed. Upon use of LES turbulence model, flow pattern and velocity distribution on the scour bed downstream of Type (B) basin was dissimilar than that was observed in K- $\epsilon$  models.

Using RNG K- $\epsilon$  model, Fig. 5.9 (a) shows velocity distribution in Type (C) basin. The maximum magnitude of velocity was observed in fore side of HJ which declined as the flow moved towards downstream. The pattern of velocity distribution in Type (C) basin was found to be different than that was observed in Type (A) and (B) basin. In Type (C) basin, results indicated a stable free surface profile on rigid bed which indicated that shortly the flow would achieve hydraulic stability, however, at  $T_s= 500$  s, no hydraulic stability was noticed in Type (C) basin. In Type (C) basin, results indicated high velocity flow in between rows of baffle blocks. However, after the baffle blocks, as compared to Type (A) basin, a large wake zone was observed. The length and depth of wake zone was found to be larger than that was noticed in Type (A) basin, and this zone traveled to end of the rigid floor. Additionally, velocity in wake zone near the rigid floor was less than 1 m/s while higher velocity flow was found above the wake zone up to free surface region. In Type (C) basin, a small wake region was also noticed after friction

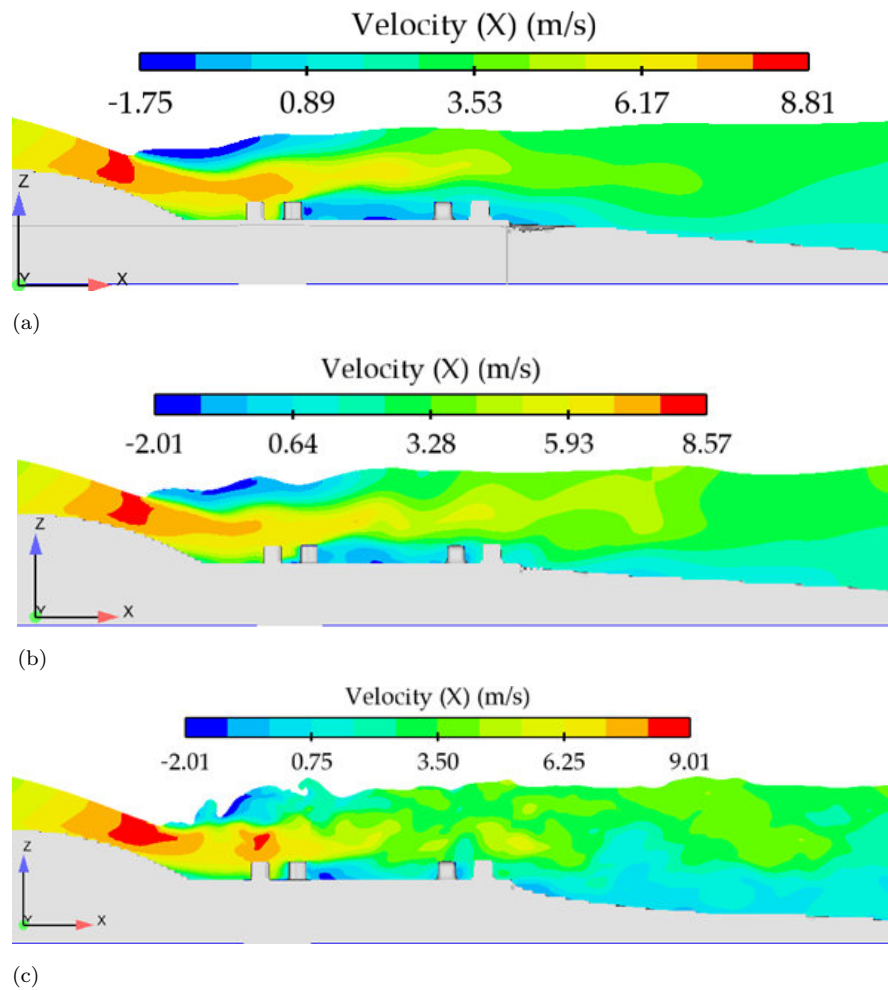


FIGURE 5.9: 2-D Illustration of velocity distribution downstream of Type (C) basin at  $24.30 \text{ m}^3/\text{s}/\text{m}$ , (a) RNG K- $\epsilon$ , (b) Std K- $\epsilon$  model, and (c) LES model

blocks. Like rigid bed, in comparison to Type (A) and (B) basins, a dissimilar flow pattern was observed on scoured bed downstream of Type (C) basin. On scoured bed, the lower region of high velocity flow was undulating while upper region was found to be stable as shown in Fig. 5.9 (a). In Type (C) basin, at start of the scoured bed, depth of wake zone was less which increased as the flow moved towards downstream. The maximum depth of wake zone was noticed at the end of scoured bed.

Fig. 5.9 (b) shows velocity distribution on Type (C) basin using Std K- $\epsilon$  model. In comparison to RNG K- $\epsilon$  model, using Std K- $\epsilon$ , a different pattern of velocity distribution was noted on Type (C) basin. In HJ region, the free surface was undulating and the results showed a turbulent velocity field downstream of the

rigid bed. After baffle blocks, the depth of wake zone was found to be less than that was observed in RNG K- $\epsilon$  model. As compared to RNG K- $\epsilon$  model, upon use of Std K- $\epsilon$  model, a different velocity distribution was observed on the scour bed downstream of Type (C) basin as can be seen in Fig. 5.9 (b). On the scoured bed, depths of high and slow-moving zones were also found different, therefore, as compared to RNG K- $\epsilon$ , scour depth and retrogression phenomena was also found to be different in Std K- $\epsilon$  models.

Fig. 5.9 (c) shows velocity distribution on Type (C) basin using LES turbulence model. In LES model, an irregular distribution of velocity was noticed in all fluid depths. The results showed highly turbulent flow in the central region while a large fluctuating roller were observed at the free surface. After the baffle blocks, wake zone was noticed near basin's floor while results showed an undulating high velocity zone which was ranged from upper layer of wake zone to the free surface. Fig. 5.9 (c) also shows velocity distribution on scoured bed downstream of Type (C) basin and results indicated two different zones i.e., slow-moving, and high velocity zones on the sediment bed. The depth and pattern of slow-moving zones was dissimilar to that was observed in K- $\epsilon$  models as shown in Fig. 5.9 (c).

Using RNG K- $\epsilon$  model, the velocity distribution in Type (D) basin is shown in Fig. 5.10 (a). As Compared to Type (C) basin, the velocity distribution in Type (D) was found to be dissimilar which showed large undulation on the free surface in HJ region while after baffle blocks depth and length of wake zone was smaller than that was observed in Type (C) basin. In Type (D) basin, the length of wake zone near the floor was gradually declined up to end of rigid bed and started to increase again on the scoured bed to end of sediment bed. After comparing with Type (C) basin, in Type (D) basin, the free surface profiles on rigid and scoured bed were wavy which created varying depths of high and slow velocity zones as shown in Fig. 5.10 (a). On the scoured bed, maximum depths of slow-moving zone were found at the end of sediment bed ( $X=30$  m, from rigid floor). Fig. 5.10 (b) shows velocity distribution on Type (D) basin using Std K- $\epsilon$  model. As compared to RNG K- $\epsilon$  model, in Type (D) basin, a strong turbulent and fluctuating free surface was noted in HJ region, while after the baffle blocks high velocity flow was



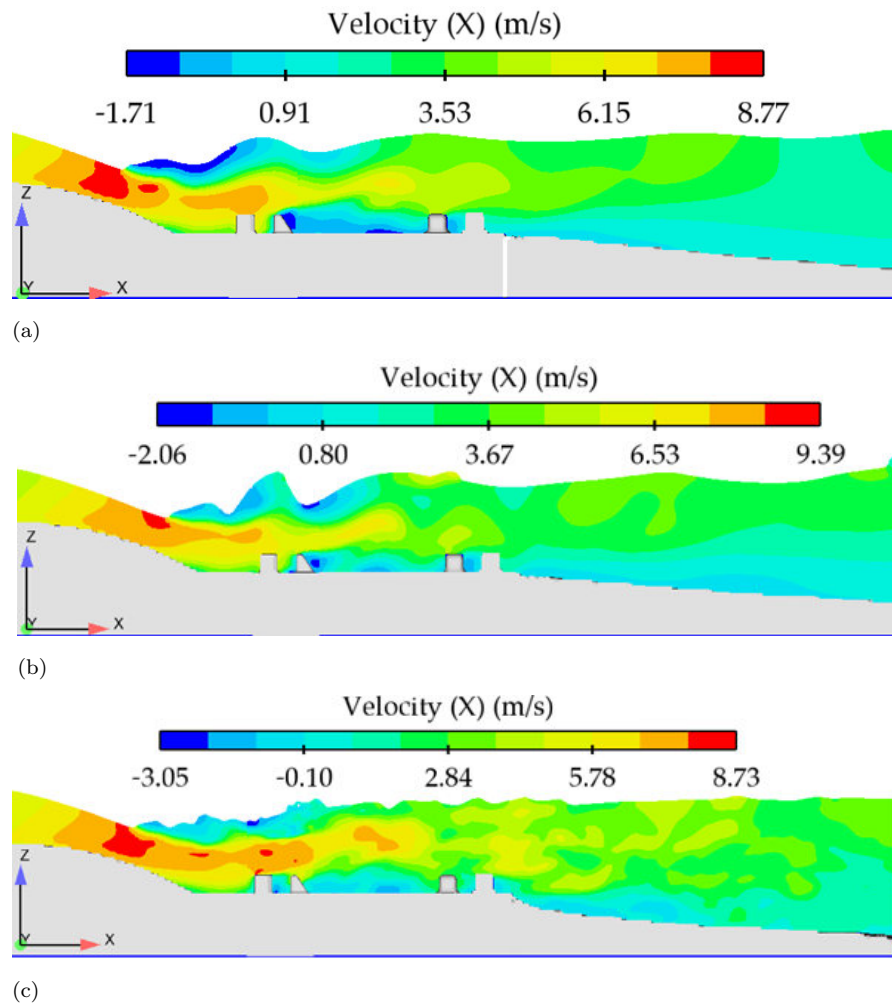


FIGURE 5.10: 2-D Illustration of velocity distribution downstream of Type (D) basin at  $24.30 \text{ m}^3/\text{s}/\text{m}$ , (a) RNG  $K-\epsilon$ , (b) Std  $K-\epsilon$  model, and (c) LES model

found to be deflected towards basin floor which decreased the depth of wake zone. As compared to RNG  $K-\epsilon$  model, Std  $K-\epsilon$  model showed that higher velocity flow was travelling toward downstream of Type (D) basin. Upon use of Std  $K-\epsilon$  model, the free surface profile on scoured bed downstream of Type (D) basin was also undulating which showed high velocity flow from middle zone to the free surface. However, near the scoured bed, depth of wake zone and velocity distribution were different than that were observed in Type (A), and (C) basins.

Fig. 5.10 (c) shows velocity distribution on Type (D) basin using LES turbulence model. The results indicated a fluctuating free surface profiles within and after the HJ region. After the HJ, the WSBB deflected the upcoming high velocity flow towards free surface which travelled to the end of sediment. However, as the

distance from baffle blocks increased the depths of high velocity zone was found to become larger as can be seen in Fig. 5.10 (c). Upon use of LES model, as compared to Type (C) basin, the free surface profiles in Type (D) basin were found to be stable which showed large re-circulation in the HJ region, and depth of wake zone after the baffle blocks was also found larger than that was observed in Type (C) basin. In Type (D), using LES model, the results further indicated irregular pattern of velocity distribution in all fluid depths. After the rigid bed, the depths of wake zone on scoured bed showed different pattern which differed from Type (C) basin.

### 5.3.2 Velocity Field at High Flood Discharge

Fig. 5.11 (a) shows horizontal velocity field in Type (A) basin at  $18 \text{ m}^3/\text{s}/\text{m}$  discharge using RNG K- $\epsilon$  model. The maximum velocity values were observed at downstream glaxis in the supercritical region as was noticed at  $24.30 \text{ m}^3/\text{s}/\text{m}$ . However, at  $18 \text{ m}^3/\text{s}/\text{m}$  discharge, large fluid re-circulation was observed in HJ region at the free surface. In addition, as compared to  $24.30 \text{ m}^3/\text{s}/\text{m}$  discharge, a stable free surface was noticed at  $18 \text{ m}^3/\text{s}/\text{m}$  discharge, and the central fluid layers were also found to be unchanging. After the first row of baffle blocks, as compared to designed discharge, at  $18 \text{ m}^3/\text{s}/\text{m}$  flow, large wake region was observed which indicated more turbulence. Downstream of Type (A) basin, at  $18 \text{ m}^3/\text{s}/\text{m}$  flow, depth of high velocity field reduced which decayed before the end of sediment bed. On the retrogressed bed, the depth of slow-moving fluid was also less than that was observed at designed discharge, therefore, results showed less bed retrogression at  $18 \text{ m}^3/\text{s}/\text{m}$  discharge.

Fig. 5.11 (c) shows velocity contour downstream of Type (A) basin using LES model. The velocity fields on rigid and scoured bed showed an irregular pattern. The velocity patterns were found different than that were observed at the designed discharge ( $24.30 \text{ m}^3/\text{s}/\text{m}$ ). The depth of supercritical fluid at the impingement point in the HJ region was also found higher than that was observed in designed discharge. However, as compared to designed discharge, the free surface on rigid

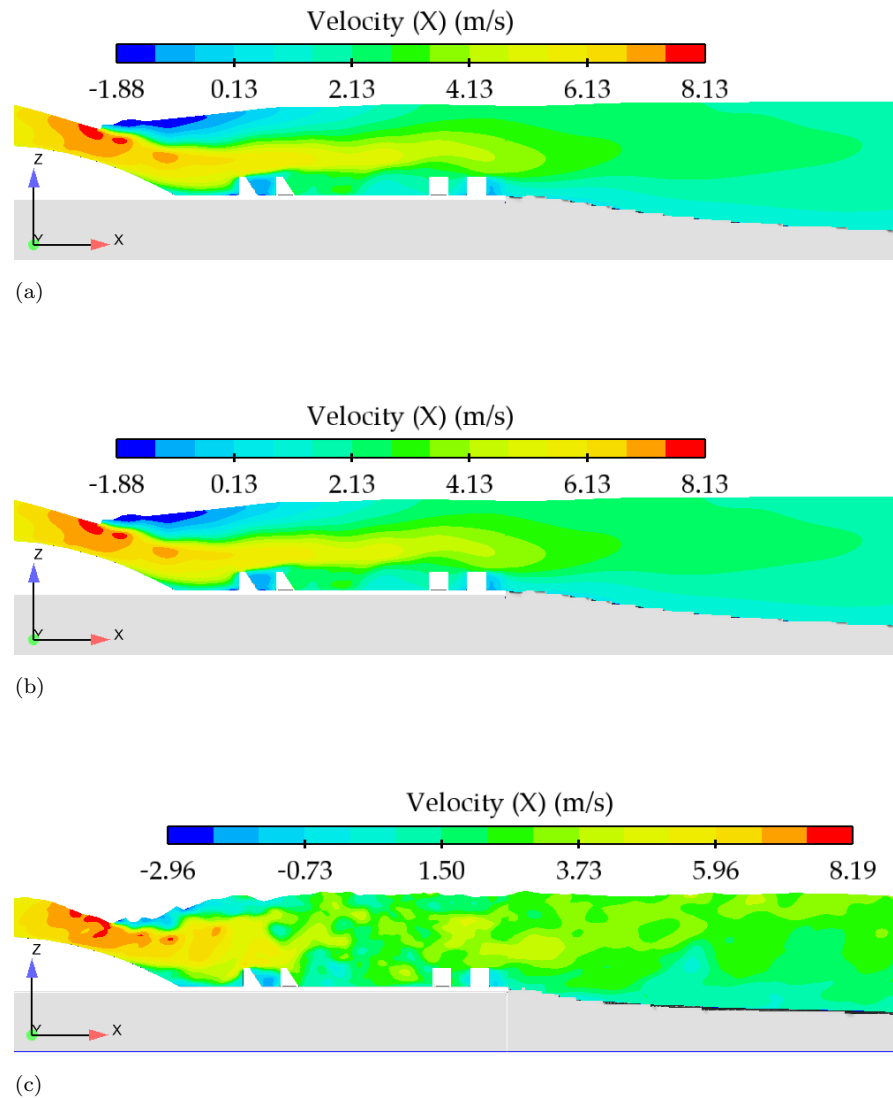


FIGURE 5.11: 2-D Illustration of velocity distribution downstream of Type (A) basin at  $18 \text{ m}^3/\text{s}/\text{m}$ , (a) RNG K- $\epsilon$ , (b) Std K- $\epsilon$  model, and (c) LES model

and scoured bed was found to be stable, due to which the lower fluid depth was also found un-fluctuating. Additionally, at  $18 \text{ m}^3/\text{s}/\text{m}$  discharge, the depth of wake zones and slow-moving fluid on the retrogressed bed was also less, due to which less change in bed retrogression was witnessed.

Fig. 5.12 (a) illustrates velocity field downstream of Type (B) basin using RNG K- $\epsilon$  model at  $18 \text{ m}^3/\text{s}/\text{m}$  discharge. As compared to designed discharge, the results showed different pattern of velocity at  $18 \text{ m}^3/\text{s}/\text{m}$  discharge, which indicated smaller region of fluid re-circulation on the free surface of HJ. After downstream glaxis, the supercritical flow was found to be impinging on the basin's floor which

reached to the end of rigid bed and deflected by end sill towards the central fluid. At the rigid bed, the flow depths showed three different velocity zones, i.e., higher velocity zones from floor to central fluid depth, intermittent velocity zones, and lower velocity zone near the free surface. Out of the three zones, the depth of higher velocity zone was found equivalent to the rest of two zones. The velocity contours further showed that as the flow moved towards the downstream end, the depths of high velocity and intermittent zones were found to be increased. Conversely, the depth of upper fluid zones with lower velocity contours was found to be decreased. The maximum velocity on the basin floor was reached 6.5 m/s. Additionally, at the end of basin's, end sill deflected the higher and intermittent velocity regions towards upper fluid region which were found to be decayed after 12 m from the end sill. On the scoured bed, just downstream of end rigid, a large fluid re-circulation and wake zones were observed which developed scour hole, however, the net length and depth of wake zone was less than that was noticed at designed discharge. After the scour hole, depth of slow-moving zone on the retrogressed bed was also found less as compared to designed discharge, due to that less retrogression of bed was noticed at 18 m<sup>3</sup>/s/m discharge.

Fig. 5.12 (b) show velocity contour in Type (B) basin using Std K- $\epsilon$  model. The overall pattern of velocity profile on rigid and scoured bed was found similar to RNG K- $\epsilon$  model. However, in Std K- $\epsilon$  model, length of roller in HJ region was found less as compared to RNG K- $\epsilon$  model. Similarly, after the rigid bed, the higher and intermittent velocity zones travelled longer distance on the scoured bed, and due to that length of scour hole and maximum scour depth in Std K- $\epsilon$  model was found higher than RNG K- $\epsilon$  model.

Fig. 5.12 (c) shows velocity field in Type (B) basin using LES model at 18 m<sup>3</sup>/s/m discharge. The overall pattern of velocity field was found similar to that was observed at designed discharge. However, the velocity field at the free surface were found different at 18 m<sup>3</sup>/s/m discharge and compared to 24.30 m<sup>3</sup>/s/m discharge, large fluid re-circulation was observed in HJ region at 18 m<sup>3</sup>/s/m discharge. As compared to 24.30 m<sup>3</sup>/s/m discharge, depth of high velocity zone at the floor was also found higher at 18 m<sup>3</sup>/s/m discharge. Additionally, at 18 m<sup>3</sup>/s/m discharge,

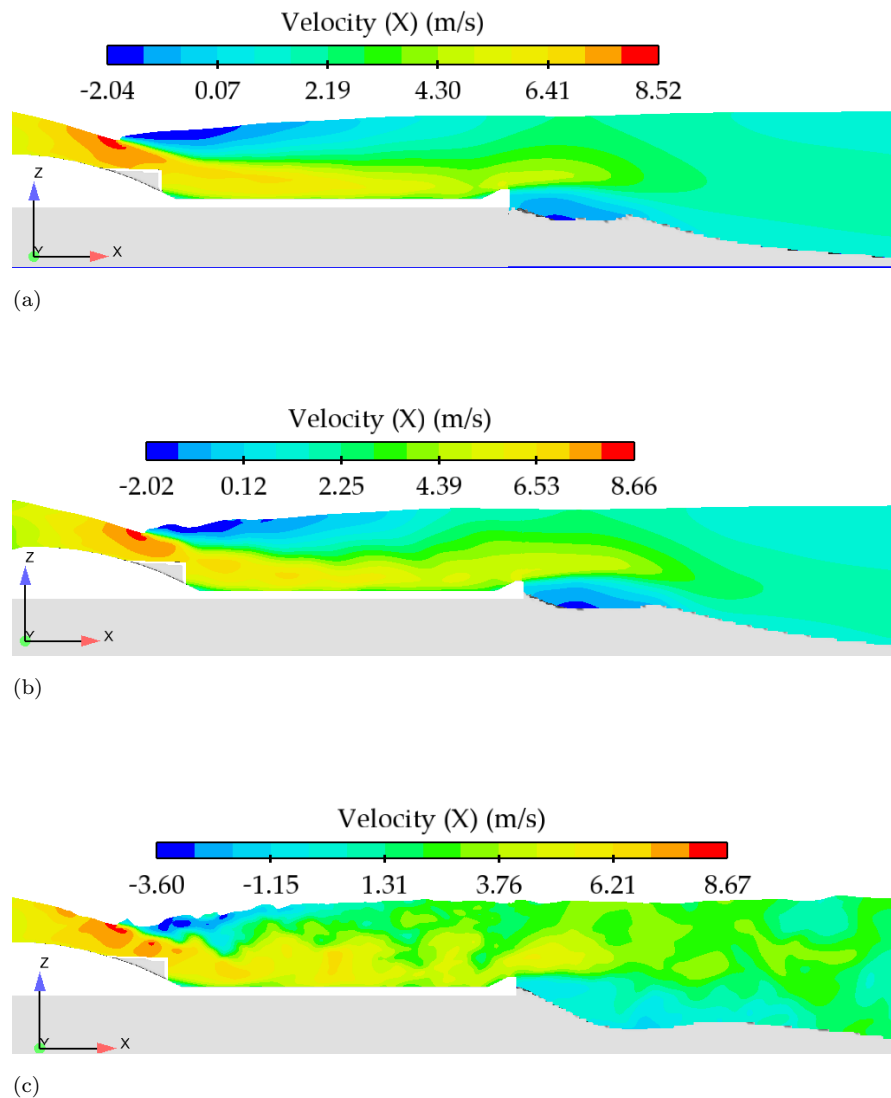


FIGURE 5.12: 2-D Illustration of velocity distribution downstream of Type (B) basin at  $18 \text{ m}^3/\text{s}/\text{m}$ , (a) RNG K- $\epsilon$ , (b) Std K- $\epsilon$  model, and (c) LES model

the intensity of fluid re-circulation and depth of wake zone on the scoured bed were found less that were noticed at the designed discharge. Due to the less depth of wake zone of the scour depth, the overall length and depth of scour hole was also reduced. Furthermore, after the scour hole, a forward velocity profile was noticed downstream of Type (B) basin, as can be seen in Fig. 5.12 (c).

Fig.5.13 (a) shows velocity field in Type (C) basin using RNG K- $\epsilon$  model at  $18 \text{ m}^3/\text{s}/\text{m}$  discharge. The velocity pattern in Type (C) basin was found dissimilar to that were observed in Type (A) and (B) basins. The results showed higher fluid re-circulation in the roller region of HJ which indicated a stable HJ in Type (C) basin.

The results further indicated that after impacting with WSBB, the supercritical flow was directed towards free surface. In Type (C) basin, the results also showed a free stable surface on rigid and scour bed. Additionally, depth of high velocity zone in Type (C) basin was less than that was observed in Type (A) basin, and its distance from the basin floor was found larger. After the WSBB, a large wake zone region was noticed which further reduced the magnitude of velocities near the basin's floor. However, in Type (A) basin, strong current near the basin's floor were observed. Downstream of Type (C) basin, the velocity contours further indicated a larger depth of slow-moving zone near the retrogressed, however, the overall retrogression was found less than that was noticed in Type (A) basin. Furthermore, as compared to designed discharge, the pattern of velocity in Type (C) basin was found dissimilar at  $18 \text{ m}^3/\text{s}/\text{m}$  discharge.

Fig. 5.13 (b) shows velocity field in Type (C) basin using Std K- $\epsilon$  model at  $18 \text{ m}^3/\text{s}/\text{m}$  discharge. The patterns of velocity field on rigid and scour bed were found similar to RNG K- $\epsilon$  model. However, the depths of slow-moving zone in the scour bed were found less than that was observed in RNG K- $\epsilon$  model. Additionally, using Std K- $\epsilon$  model, as compared to Type (A) basin, velocity after the WSBB was found dissimilar which showed large wake region and decayed the velocity earlier on rigid bed. Additionally, as compared to designed discharge, the middle fluid depths were found to be stable at  $18 \text{ m}^3/\text{s}/\text{m}$  discharge as can be seen in Fig.5.13 (b). Overall, due to a smaller depth of slow-moving zone, the retrogression of sediment bed downstream of Type (C) basin was found less than that was observed in RNG K- $\epsilon$  model.

Fig. 5.13 (c) shows velocity field in Type (C) basin using LES model at  $18 \text{ m}^3/\text{s}/\text{m}$  discharge. As compared to RNG and Std K- $\epsilon$  model, in LES model the velocity distribution was found irregular on the retrogressed bed, while as compared to the designed discharge a quite regular velocity field was noticed on rigid floor of Type (C) basin. After the WSBB, similar to RNG and Std K- $\epsilon$  models, large wake zone was developed which declined the velocity magnitude.

On the contrary, using LES model at the designed discharge, the depth of wake zone after the baffle region was found be less. Similarly, at  $18 \text{ m}^3/\text{s}/\text{m}$  discharge, downstream of Type (C) basin, the slow-moving flow on retrogressed bed was dissimilar to that was noticed at designed discharge. Hence, using LES model, at  $18 \text{ m}^3/\text{s}/\text{m}$  discharge, the net change in the sediment downstream of Type (C) basin was less than that was noticed at designed discharge. However, as compared to Std K- $\epsilon$  model, upon use of LES model, the results showed higher net change in the sediment bed. Furthermore, as compared to Type (A) basin, the velocity field on rigid and retrogressed was found to be regular which indicated higher velocity at the free surface.

Fig. 5.14 (a) shows velocity field at  $18 \text{ m}^3/\text{s}/\text{m}$  discharge downstream of Type (D) basin using RNG K- $\epsilon$  model. On the rigid bed, the overall velocity field at floor and free surface was similar to that was noticed in Type (C) basin. However, in the HJ region, strong rollers were noticed. After the baffle blocks, large wake and fluid re-circulation were noticed which ended at the start of friction blocks. As compared to Type (C) basin, the depth of wake zone after the baffle was found less in Type (D) basin. For the central fluid depths, the results showed identical velocity profiles as was noticed in Type (C) basin. Downstream of Type (D) basin, the depths of wake and slow-moving fluid was found to be increased as the flow moved towards the end of sediment bed. Therefore, higher bed retrogression was noticed downstream of Type (D) basin, however, in comparison to Type (A) basin, the net change in the bed was found less.

Fig. 5.14 (b) shows velocity field in Type (D) basin at  $18 \text{ m}^3/\text{s}/\text{m}$  discharge using Std K- $\epsilon$  model. The pattern of velocity field on rigid and retrogressed bed was found identical to that was observed in RNG K- $\epsilon$  mode. However, overall velocity values in the different zones, i.e., near the flow, at free surface and after the baffle blokes were different than RNG K- $\epsilon$  model. Therefore, as compared to RNG K- $\epsilon$  model, upon use of Std K- $\epsilon$  model, net change in the sediment bed downstream of Type (D) basin was found to be less. On the contrary, as compared to Type (C) basin, upon use of Std K- $\epsilon$  model, the net change in sediment was higher in Type (D) basin.

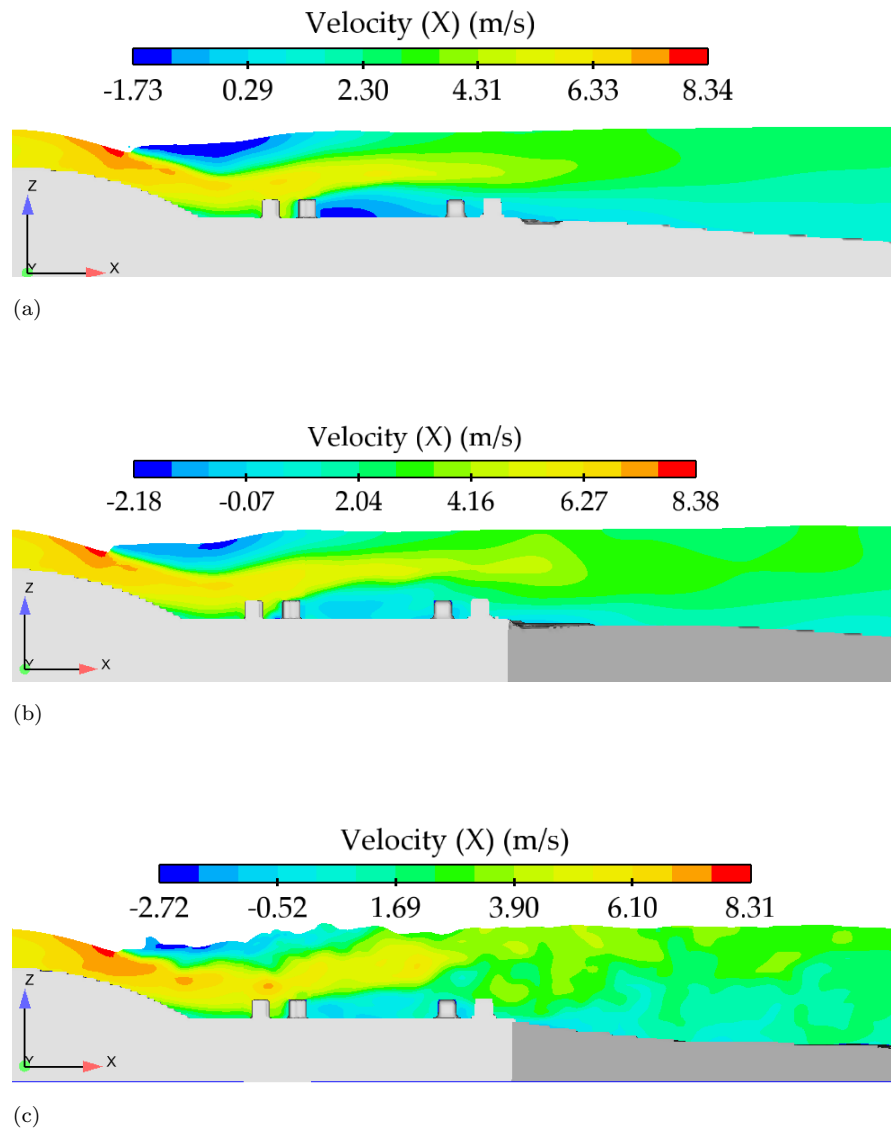


FIGURE 5.13: 2-D Illustration of velocity distribution downstream of Type (C) basin at  $18 \text{ m}^3/\text{s}/\text{m}$ , (a) RNG K- $\epsilon$ , (b) Std K- $\epsilon$  model, and (c) LES model

Fig. 5.14 (c) displays velocity field at  $18 \text{ m}^3/\text{s}/\text{m}$  discharge in Type (D) basin using LES model. In comparison to Type (C) basin, length of roller region in the HJ was found be less in Type (D) basin, and overall depth of high velocity zone after the baffle block region was also found less than that was observed in Type (C) basin. However, upon use of LES model, after the baffle block region, the depth of wake zone near floor was found high in Type (D) basin as can be seen in Fig. 5.14 (c).

On the other hand, on the retrogressed bed, the pattern of slow-moving flow was found dissimilar while net depth of slow-moving flow on retrogressed bed was high.



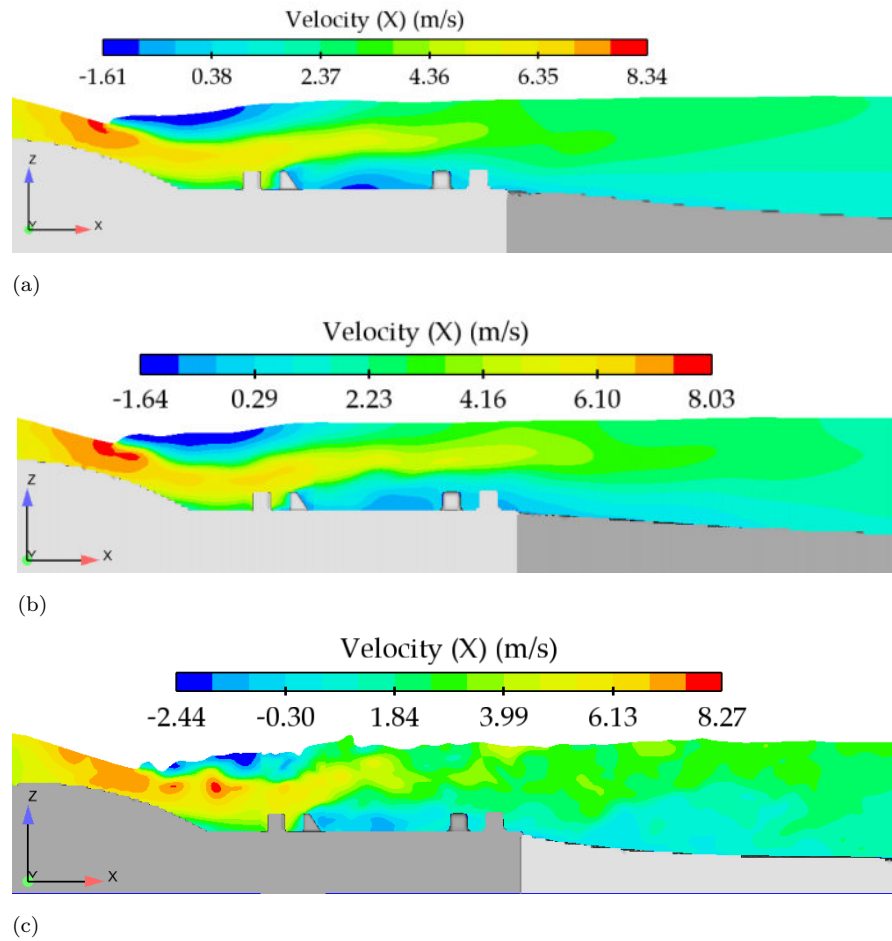


FIGURE 5.14: 2-D Illustration of velocity distribution downstream of Type (D) basin at  $18 \text{ m}^3/\text{s}/\text{m}$ , (a) RNG K- $\epsilon$ , (b) Std K- $\epsilon$  model, and (c) LES model

However, the magnitude of velocity in the slow-moving zone was less than that was observed in Type (C) basin. As compared to designed discharge, downstream of Type (D) basin, the velocity magnitude on rigid and retrogressed bed was found to less at  $18 \text{ m}^3/\text{s}/\text{m}$  discharge. Therefore, at  $18 \text{ m}^3/\text{s}/\text{m}$  discharge, using LES model, the overall net change in the sediment downstream Type (D) basin as found less than designed discharge.

### 5.3.3 Bed Shear Stress on Sediment Beds at Designed Discharge

Another parameter that influences local scour is the shear stress on sediment bed which is calculated by wall function for three dimensional turbulent flow.

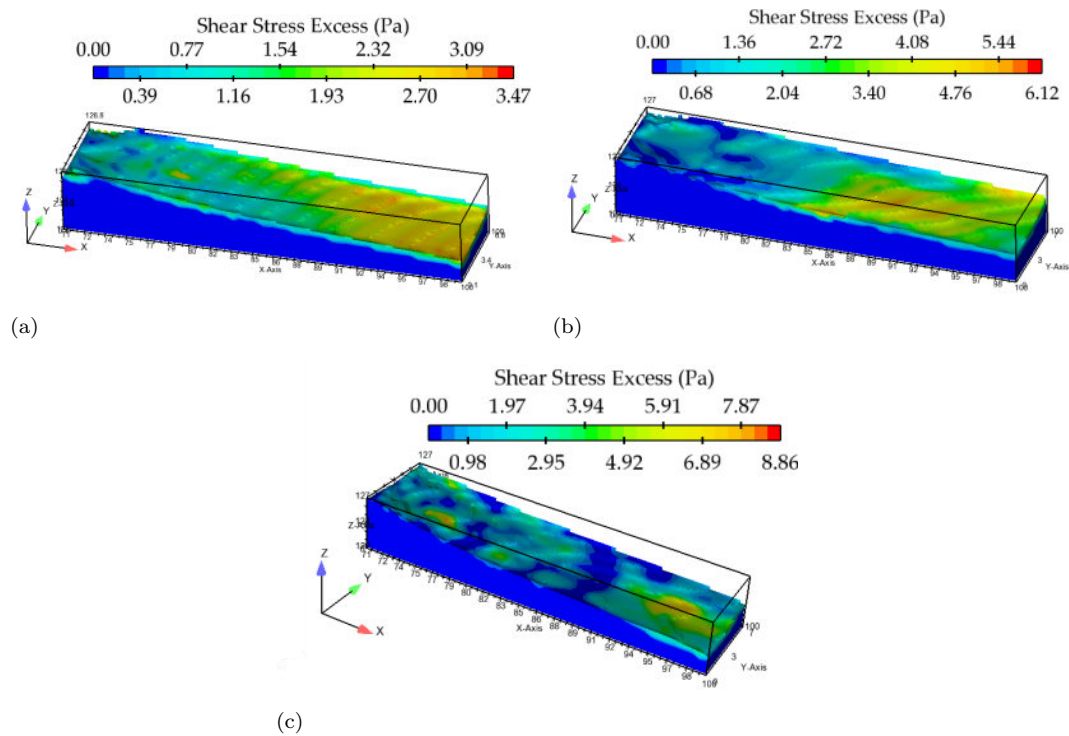


FIGURE 5.15: Shear stress distribution downstream of Type (A) basin at designed discharge, (a) RNG K- $\epsilon$ , (b) Std K- $\epsilon$  model, and (c) LES model

Therefore, the contours of bed shear stress on sediment bed downstream of the investigated basins are drawn for designed ( $24.30 \text{ m}^3/\text{s}/\text{m}$ ) and flood discharges ( $18 \text{ m}^3/\text{s}/\text{m}$ ) to illustrate shear stress on different locations of scoured and retrogressed beds.

Fig. 5.15 shows the shear stress contours downstream of Type (A) basin using RNG K- $\epsilon$ , Std K- $\epsilon$ , and LES turbulence models. From Fig. 5.15 (a), using RNG K- $\epsilon$  model, the maximum magnitude of shear stress downstream of Type (A) basin was found on left side of the sediment bed which indicated maximum scour depth in that region, while in Std K- $\epsilon$  model, the maximum shear stress contours were noticed on the right as shown in Fig. 5.15 (b). On the contrary, upon use of LES turbulence model, the maximum shear stress was found in the central region of sediment bed as shown in Fig. 5.15 (c).

Fig. 5.16 shows bed shear stress downstream of Type (B) basin using different turbulence models. Figs. 5.16 (a) and (b), the maximum magnitude of bed shear stress was noticed on the downside of scoured hole and within the scoured hole

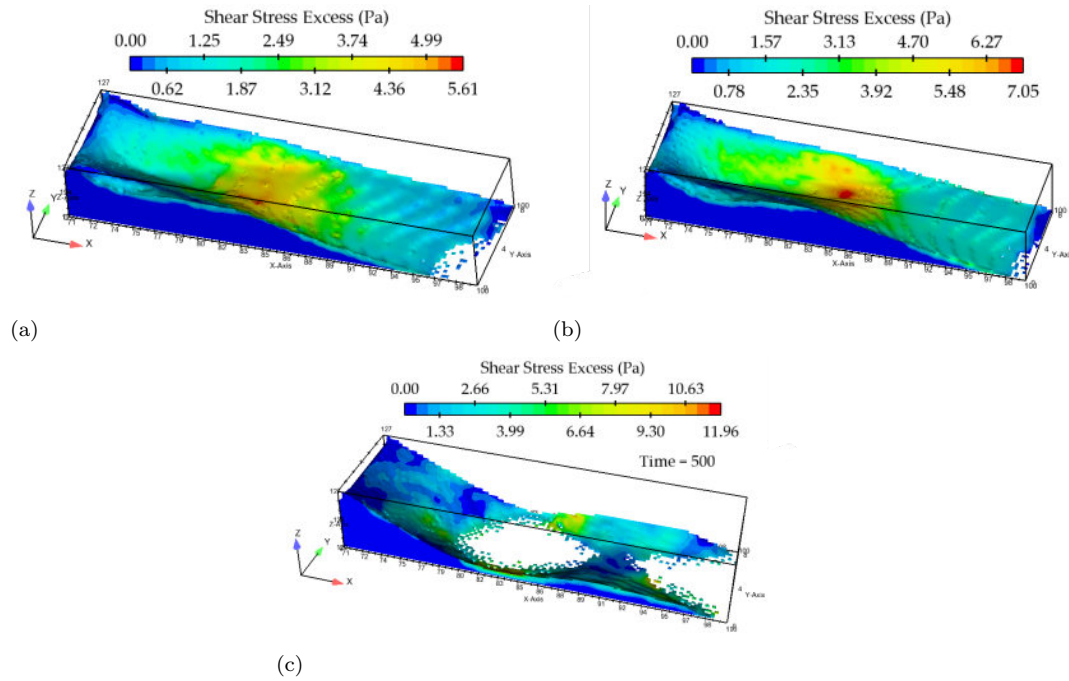


FIGURE 5.16: Shear stress distribution downstream of Type (B) basin at designed discharge, (a) RNG K- $\epsilon$ , (b) Std K- $\epsilon$  model, and (c) LES model

using RNG and Std K- $\epsilon$  models, respectively. However, upon use of LES model, at  $T_s=500$  s, it can be said that the maximum bed shear stress was on the exposed regions of sediment bed such as downstream of rigid bed and the end of sediment bed as shown in Fig. 5.16 (c)

Fig. 5.17 shows shear stress contours downstream of Type (C) basins. Fig. 5.17 (a), upon use of RNG K- $\epsilon$  model, results indicated maximum magnitude of shear stress on right side of sediment while using Std K- $\epsilon$  model, the maximum shear stress was noticed on the left side of sediment bed as shown in Fig. 5.17 (b). The results further indicated that the shear stress pattern downstream on Type (C) basin was entirely different than that was seen in Type (A) and (B) basins.

It is important to mention that the overall regions under high shear stress on right and left sides of sediment bed downstream of Type (C) basin were found to be less than that were observed in Type (A), and (B) basins as shown in Figs. 5.17 (a) and (b). On the other hand, using LES model, the maximum shear stress downstream of Type (C) basin was noticed on right side of sediment bed from  $X=10$  to  $18$  m from the end of rigid bed, while at the end of sediment bed, as

compared to Type (A) basin, less shear stress was noticed downstream of Type (C) basin as shown in Fig. 5.17 (c).

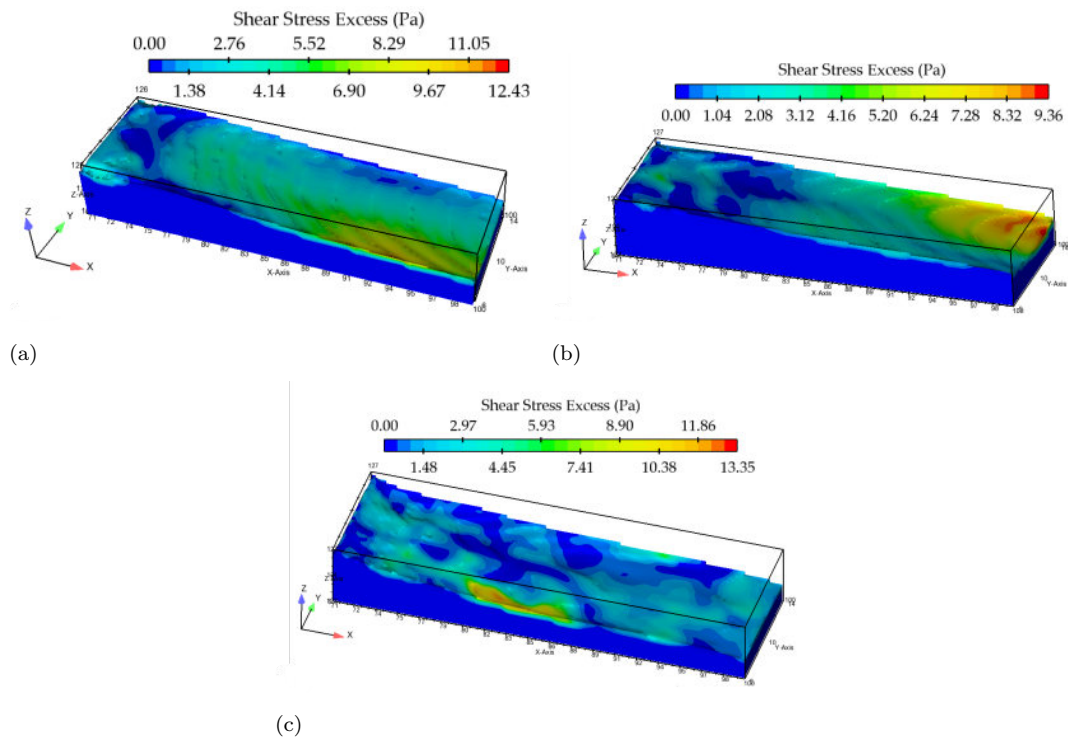


FIGURE 5.17: Shear stress distribution downstream of Type-C basin at designed discharge, (a) RNG K- $\epsilon$ , (b) Std K- $\epsilon$  model, and (c) LES model

Fig. 5.18 shows shear stress contours downstream of Type (D) basin. From Figs. 5.18 (a) and (b), the pattern of shear stress contours on scoured bed downstream of Type (D) basin was found similar to Type (A) basin using RNG and Std K- $\epsilon$  models, respectively. However, the area under shear stress was found to be less than that was noticed in Type (A) basin.

On the contrary, using LES model, a scattered distribution of shear stress was observed on scoured bed downstream of Type (D) basin which showed deviation from the shear stress pattern of Type (A) basin. However, using LES model, the shear stress pattern downstream of Type (D) basin was found similar to that was observed on Type (C) basin as shown in Fig. 5.17 (c).

Conclusively, the distribution of shear stress downstream of studied stilling basins were found dissimilar. In Type (A), (B), (C), and (D) basins, the minimum and maximum magnitude of bed shear stress was noticed in RNG K- $\epsilon$  and LES model,

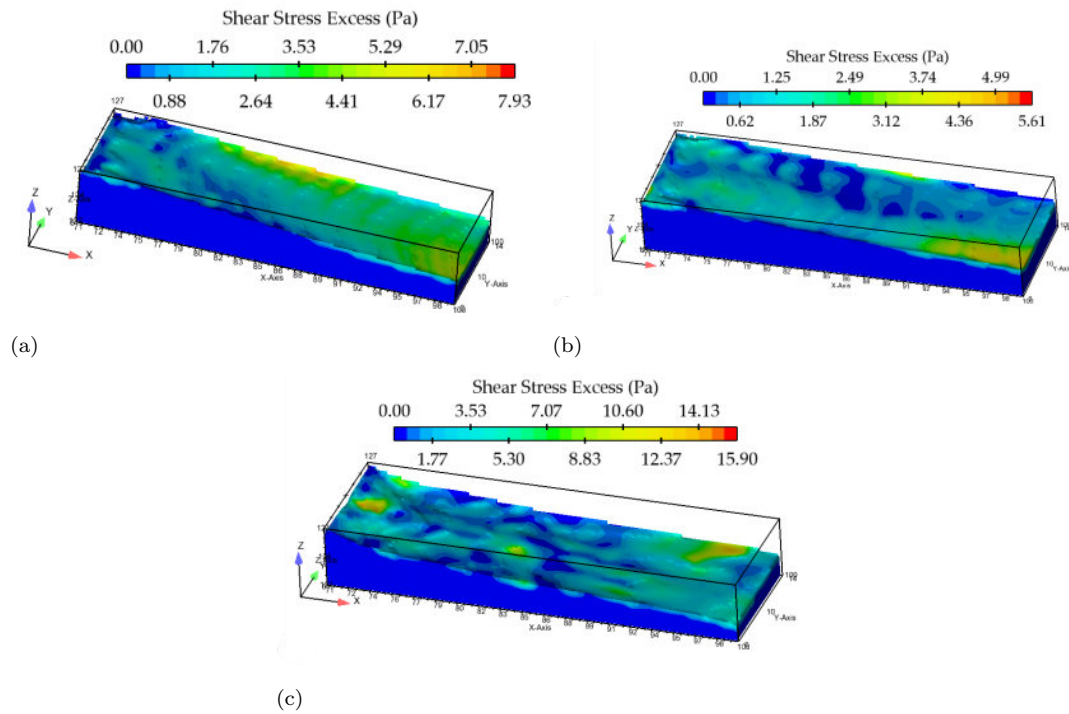


FIGURE 5.18: Shear stress distribution downstream of Type-D basin at designed discharge, (a) RNG K- $\epsilon$ , (b) Std K- $\epsilon$  model, and (c) LES model

respectively. The stilling basin with wedge-shaped baffle blocks i.e., Type (C) and (D) showed different shear stress patterns using RNG and Std K- $\epsilon$  models, while identical trends were noticed in LES model. At the simulation end ( $T_s=500$  s), as compared to Type (A) basin, the total area under shear stress was found less in Type (C) and (D) basins.

### 5.3.4 Bed Shear Stress on Sediment Beds at High Flood Discharge

Fig. 5.19 (a) shows bed shear stress at  $18 \text{ m}^3/\text{s}/\text{m}$  discharge downstream of Type (A) basin using RNG K- $\epsilon$  model. As compared to designed discharge, at  $18 \text{ m}^3/\text{s}/\text{m}$  discharge, different pattern of bed shear stress was noticed which indicated a uniform distribution of shear stress from  $X=10$  to  $30$  m. However, at the end of sediment (from  $X=25$  to  $28$  m), bed shear stress on right side of bed was found to be higher than rest of the locations, as can be seen in Fig. 5.19 (a). On the contrary, using Std K- $\epsilon$  model, different patterns of shear stress were

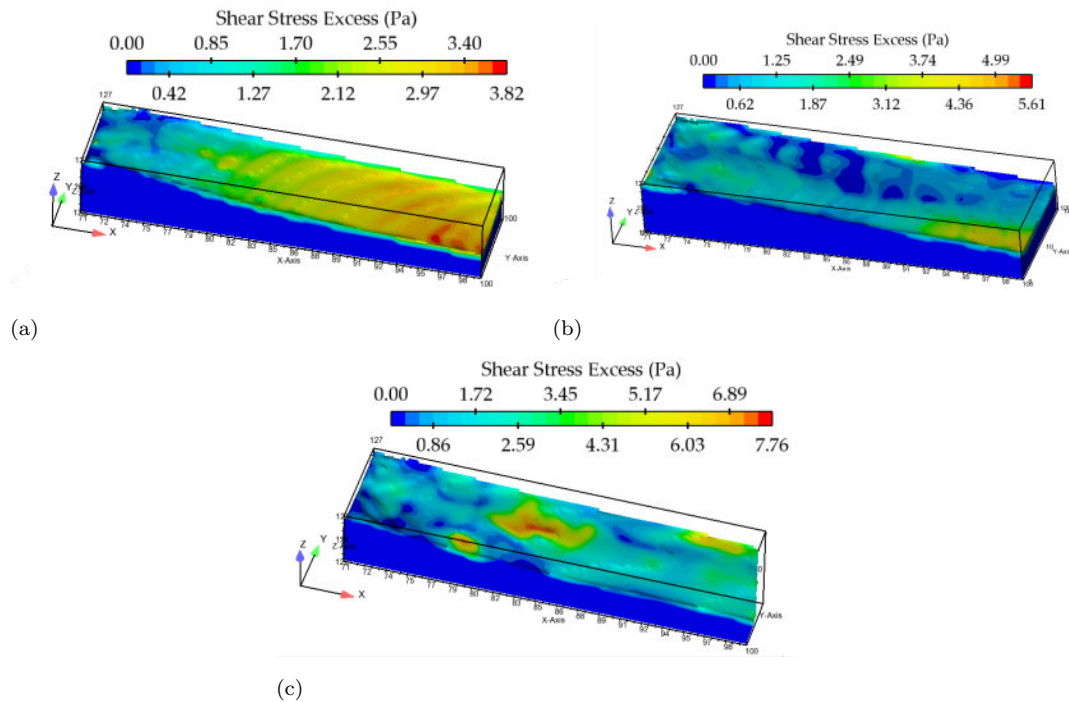


FIGURE 5.19: Shear stress distribution downstream of Type (A) basin at Flood discharge, (a) RNG  $k-\epsilon$ , (b) Std  $K-\epsilon$  model, and (c) LES model

noticed which indicated maximum shear zone on right side of the retrogressed bed as shown in Fig. 5.19 (b). Fig. 5.19 (c) indicated bed shear stress downstream of Type (A) basin using LES model. As compared to RNG and Std  $K-\epsilon$  models, non-uniform distribution of bed shear stress was noticed on the retrogressed bed. However, maximum bed shear stress was noticed from  $X=10$  to  $18$  m, from the rigid bed as can be seen from Fig. 5.19 (c).

Fig. 5.20 (a) shows bed shear stress on the scoured bed downstream of Type (B) basin using RNG  $K-\epsilon$  model at  $18 \text{ m}^3/\text{s}/\text{m}$  discharge. It can be seen from Fig. 5.20 (a) that the maximum bed shear stress was occurred in scour hole and at end of the sediment bed. After the scour hole, from  $X=20$  to  $30$  m, the distribution of bed shear stress was found to uniform. As compared to designed discharge, upon use of RNG  $K-\epsilon$  model, the bed shear stress downstream of Type (B) basin was found dissimilar. At the designed discharge, the maximum bed shear stress was found at the downstream end of scour hole.

Fig. 5.20 (b) shows bed shear stress profile downstream of Type (B) basin using Std  $K-\epsilon$  model. The pattern of shear stress distribution in the scour hole and at

end of the sediment was found dissimilar to that was observed in RNG K- $\epsilon$  model. In the scour hole, the maximum shear stress was observed at the upstream end of scour hole, while a non-uniform distribution of shear stress was found on the downstream end. On the other hand, after the scour hole, the maximum shear stress was noticed on the left side of sediment bed (from X= 22 to 30 m), as can be seen in Fig. 5.20 (b).

Fig. 5.20 (c) shows shear stress distribution downstream of Type (B) basin using LES model. As compared to RNG and Std K- $\epsilon$  models, a non-uniform shear stress distribution was found on the scoured bed, in which the maximum net change in the bed was noticed at the end of sediment bed, as can be seen in Fig. 5.20 (c). In addition, the results revealed high bed shear stress on the left side of scour hole. On the contrary, at the designed discharge, maximum bed shear stress was noticed in scour hole and at the end of sediment bed (from, X=25 to 30 m) and as a result complete bed was exposed, while no such results were found at 18 m<sup>3</sup>/s/m discharge.

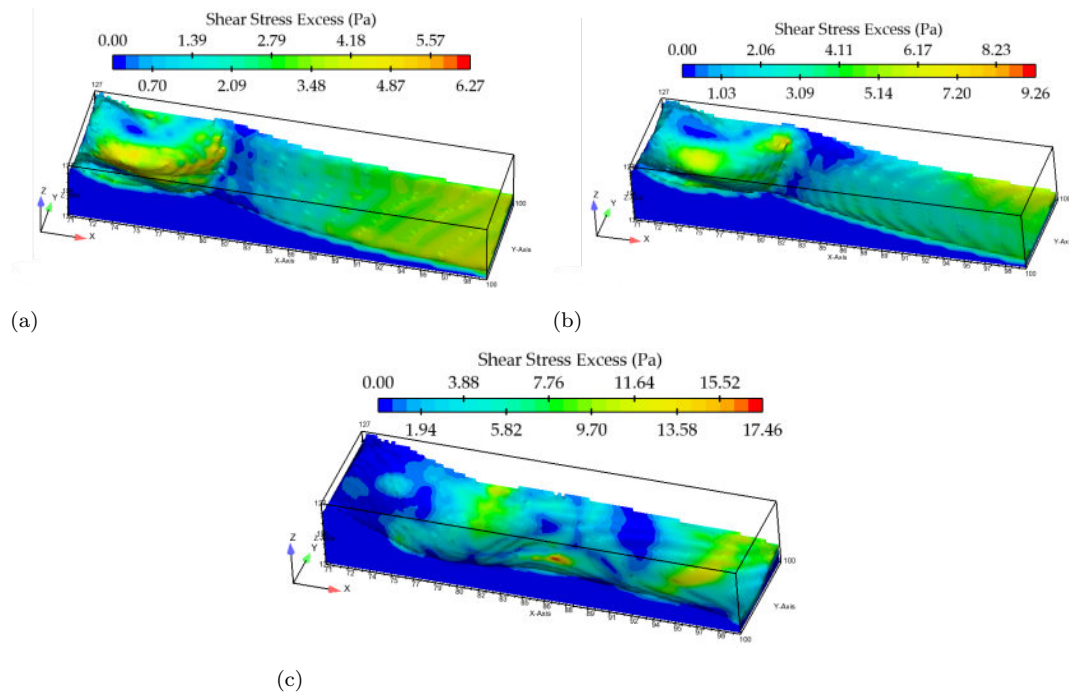


FIGURE 5.20: Shear stress distribution downstream of Type (B) basin at Flood discharge, (a) RNG k- $\epsilon$ , (b) Std K- $\epsilon$  model, and (c) LES model

Fig. 5.21 shows distribution of bed shear stress downstream of Type (C) basin using RNG K- $\epsilon$ , Std K- $\epsilon$  and LES models at 18 m<sup>3</sup>/s/m discharge. Fig. 5.21 (a) shows that upon use of RNG k- $\epsilon$  model, a uniform distribution of shear stress was developed on the retrogressed bed. The maximum shear stress was found from X=18 m to 30 m. As compared to designed discharge, the pattern of shear stress was found be regular at 18 m<sup>3</sup>/s/m discharge. However, compared to Type (A) basin, at 18 m<sup>3</sup>/s/m discharge, less area of bed was affected by high shear stress.

Fig. 5.21 (b) shows bed shear stress on retrogressed bed of Type (C) basin using Std K- $\epsilon$  model. In Std K- $\epsilon$  model, less area of sediment bed was found under high shear stress, due to that reason net change/retrogression in the bed was found less. The maximum shear stress was noticed from X=9 m to 18 m in the center-line of bay. At 18 m<sup>3</sup>/s/m discharge, the pattern of shear stress using Std K- $\epsilon$  model was also different than that was noticed at the designed discharge.

Fig. 5.21 (c) indicated bed shear stress downstream of Type (C) basin using LES model. As compared to RNG and Std K- $\epsilon$  models, irregular distribution of shear stress was noticed in the retrogressed of Type (C) basin. Upon of LES model, the shear stress pattern was also differed to that was observed in Type (A) basin. As compared to designed flow, at 18 m<sup>3</sup>/s/m discharge, the net shear stress was found less on the retrogressed bed of Type (C) basin, thereby, less net change in the sediment was occurred.

Fig. 5.22 shows bed shear stress downstream of Type (D) basin using RNG K- $\epsilon$ , Std K- $\epsilon$ , and LES models at 18 m<sup>3</sup>/s/m discharge. Fig. 5.22 (a), upon use of RNG K- $\epsilon$  models, the results indicated different pattern of shear stress on retrogressed of Type (D) basin. As compared to Type (C) basin, more shear stress was noticed on eroded bed downstream of Type (D) basin. Additionally, downstream of Type (D) basin, net area under high shear stress was also found larger than that was noticed in Type (C) basin. Therefore, higher change in the sediment was observed downstream of Type (D) basin. However, upon use RNG K- $\epsilon$  model, the magnitude of shear stress at 18 m<sup>3</sup>/s/m discharge was found to be less than that was seen at designed discharge. On the other hand, as compared



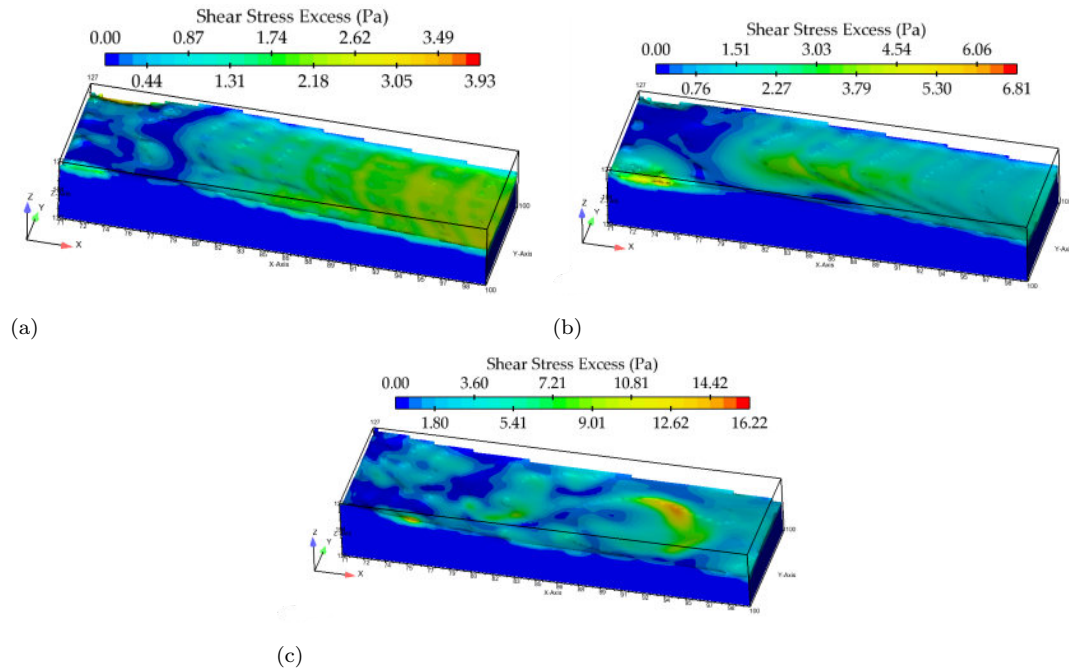


FIGURE 5.21: Shear stress distribution downstream of Type (C) basin at Flood discharge, (a) RNG  $k-\epsilon$ , (b) Std  $K-\epsilon$  model, and (c) LES model

to Type (A) basin, less shear stress was noticed on retrogressed of Type (D) basin which indicated less net change in sediment bed.

Similar to RNG  $K-\epsilon$  model, the overall bed shear stress downstream of Type (D) basin was found be higher than Type (C) basin, as can be seen in Fig. 5.22 (b). However, the shear pattern was found different which indicated maximum shear stress on the left side of sediment bed from  $X=20$  m to 30 m.

Fig. 5.22 (c) indicates shear stress downstream of Type (D) basin using LES model at  $18 \text{ }^3/\text{s}/\text{m}$  discharge. The distribution of shear stress was non-uniform which resembled with the results of Type (C) basin. Upon use of LES model, the pattern of shear stress downstream of Type (D) was found dissimilar to Type (A) and (C) basin, however, the maximum shear stress magnitude was found equivalent to that was noticed in Type (C) basin.

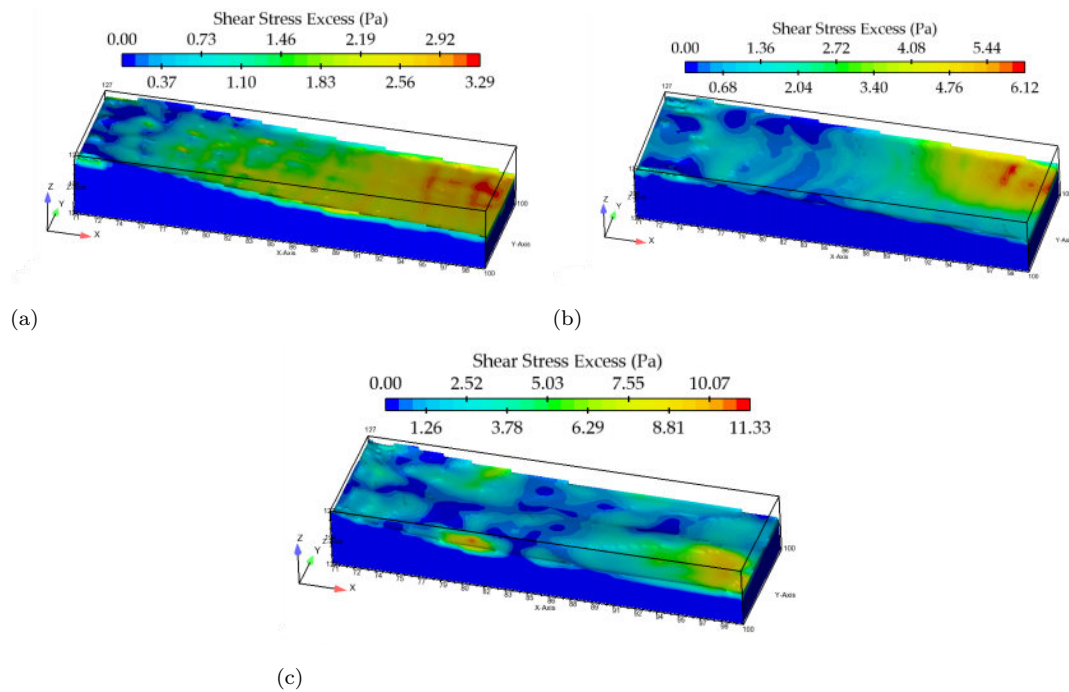


FIGURE 5.22: Shear stress distribution downstream of Type (D) basin at Flood discharge, (a) RNG  $k-\epsilon$ , (b) Std  $K-\epsilon$  model, and (c) LES model

## 5.4 Local Scour and Bed Retrogression

### 5.4.1 Scour and Retrogression Pattern at Designed Discharge

Fig. 5.23 shows three dimensional (3-D) illustration of scoured bed downstream of Type (A) basin using different turbulence models. The 3-D plots are drawn at finish time of  $T_s=500$  s. Fig. 5.23 (a) indicates scoured bed downstream of Type (A) basin using RNG  $K-\epsilon$  model. The results showed that maximum bed was retrogressed at the end of sediment for which maximum scour depth reached 2.44 m. Near rigid bed, bed retrogression was found to be less, however, as the distance from the rigid bed was increased the bed retrogression was increased and the results showed that about 51 % bed was retrogressed at  $X=30$  m (from the rigid bed). From the plot, it can be seen that no scour hole developed on downstream of the Type (A) basin, however, the results showed only bed retrogression.

Similar to RNG K- $\epsilon$  model, upon use of Std K- $\epsilon$  model, the result showed only bed retrogression downstream of Type (A) basin as shown in Fig. 5.23 (b) However, as compared to RNG K- $\epsilon$  model, the pattern of bed retrogression was found to be different in Std K- $\epsilon$  model. In Std k- $\epsilon$  model, the maximum scour depth downstream of Type (A) basin was found at the end of sediment bed which reached to 2.71 m.

Fig. 5.23 (c) illustrates scour and bed retrogression downstream of Type (A) basin using LES model. In LES model, bed retrogression pattern was found different than RNG K- $\epsilon$  and Std K- $\epsilon$  models. However, the overall net height change in LES model was found higher which reached 3.11 m (65%) at the end of sediment bed.

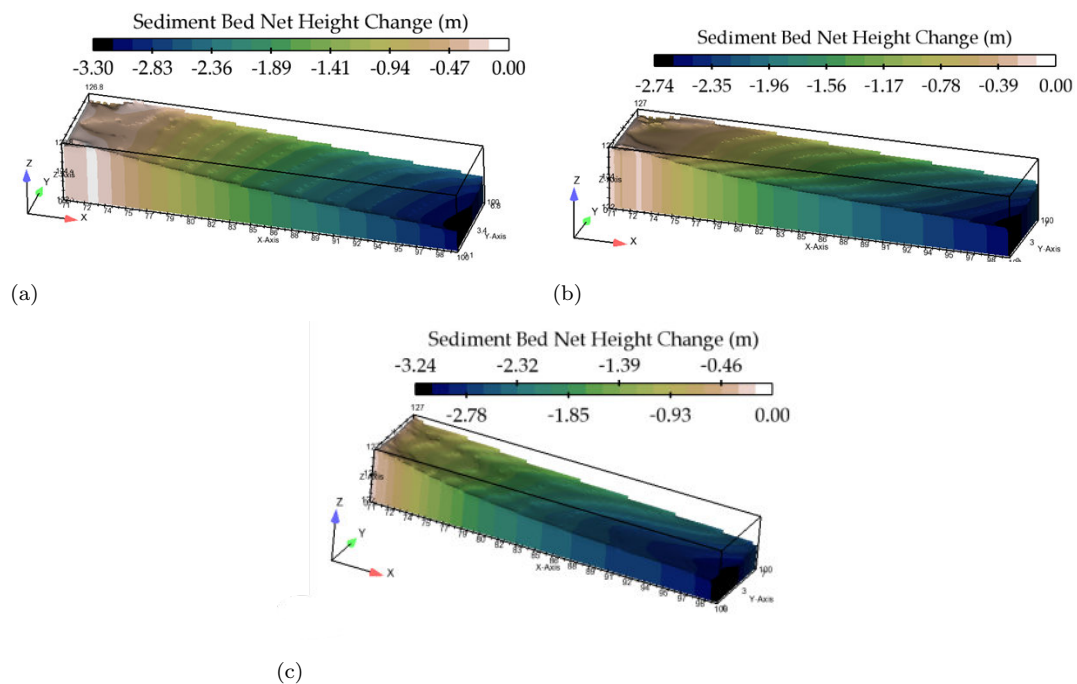


FIGURE 5.23: 3-D representation of scoured bed below Type (A) basin at designed discharge, (a) RNG k- $\epsilon$ , (b) Std K- $\epsilon$  model, and (c) LES model

Fig. 5.24 shows 3-D illustration of scoured bed downstream of Type (B) basin using different turbulence models. Upon use of RNG K- $\epsilon$  model, results showed a large scour hole after the rigid bed as shown in Fig. 5.24 (a). The length of scour hole was 14 m and its maximum depth reached to 3.57 m. After the scour hole, the sediment bed continued to retrogress and was completely exposed at the end

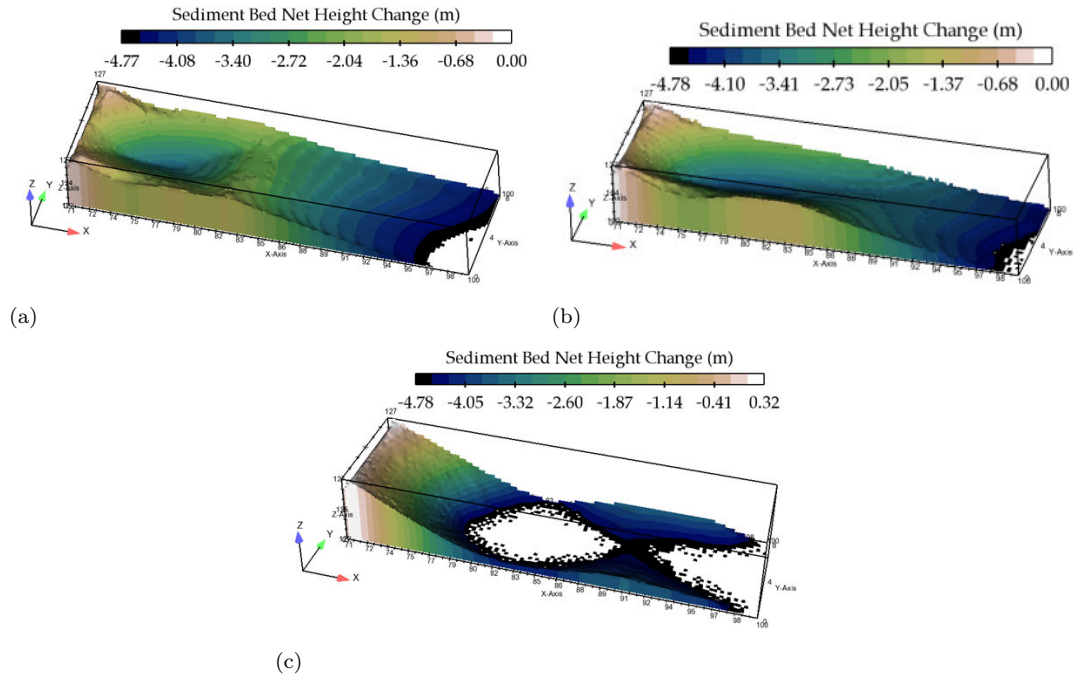


FIGURE 5.24: 3-D representation of scoured bed below Type (B) basin at designed discharge, (a) RNG  $k-\epsilon$ , (b) Std  $K-\epsilon$  model, and (c) LES model

sediment packed as shown in Fig. 5.24 (a). The total net height change in scour hole and end of the sediment bed was reached to 75% and 100%, respectively.

Fig.5.24 (b) shows scour and retrogression pattern downstream of Type (B) basin using Std  $K-\epsilon$  model. In Std  $K-\epsilon$  model, the pattern of scour and retrogression was found to be different than that was seen in RNG  $K-\epsilon$  model. The overall length of depth of scour hole was also found to be larger than RNG  $K-\epsilon$  model. Upon use of Std  $K-\epsilon$  model, the maximum net height change in scour hole and at the sediment end was reached to 76% and 100%, respectively. In Std  $K-\epsilon$  model, after the scour hole, the bed was retrogress at higher rate of net height change than RNG  $K-\epsilon$  model. The shape of scour hole and pattern of bed retrogression using Std  $K-\epsilon$  model was also found to be different than RNG  $K-\epsilon$  model.

Fig. 5.24 (c) illustrates 3-D pattern of scour and bed retrogression downstream of Type (B) basin using LES model. In LES model, at  $T_s=500$  s, the 65% of the sediment length was exposed. At  $T_s=380$  s, a large scour hole of 15 m was formed downstream of rigid bed which continued to eroded as the simulation proceeded to the end time. At  $T_s=500$  s, the sediment bed from scour hole was found to be

fully exposed as shown in Fig. 5.24 (c), and the similar pattern was also observed after the scour hole. Fig. 5.25 shows the scour and retrogression pattern in Type (C) basin using different turbulence models. The results showed bed retrogression in all the turbulence models, however, the retrogression patterns were found to be different in various models. The maximum bed was retrogressed in RNG K- $\epsilon$  model, in which the maximum net change in bed was reached to 67% as shown in Fig. 5.25 (a). However, in LES and Std K- $\epsilon$  models, the maximum net change was noticed 58% and 66% respectively, as can be seen in Fig. 5.25 (b), and (c), respectively. The results further showed the pattern of scoured bed in LES model was found to be different than RNG and Std K- $\epsilon$  models. Additionally, in Type (C) basin no scour hole was noticed on the entire length of sediment bed.

Fig. 5.26 shows the scoured bed downstream of Type (D) basin using different turbulence models. The pattern of scour in Type (D) basin was found similar to that was noticed in Type (C) basin. At finished time, the sediment bed downstream of Type (D) basin showed bed ripple which continued to the end of basin, and the pattern was found similar to that was noticed in Type (C) basin. Out of the tested turbulence models, the maximum change in sediment bed was noticed in LES model which reached to 68%. However, maximum net change in height of sediment in RNG K- $\epsilon$  and Std K- $\epsilon$  models were reached to 65% and 55%, respectively, as can be seen in Fig. 5.26 (a), and (b), respectively.

In conclusion, at the designed discharge, the results of scour and bed retrogression indicated that the maximum bed retrogression downstream of Type (A) basin was reached to 65% in LES model and the similar results were noticed in Type (B) basin. However, downstream of Type (B) basin, the bed was found to be completely exposed just near the rigid floor and at the end of sediment bed. On the other hand, in Type (C) and (D) basins, the maximum net change of sediment bed at the designed discharge was reached 67% and 68% in RNG K- $\epsilon$  and LES model, respectively.

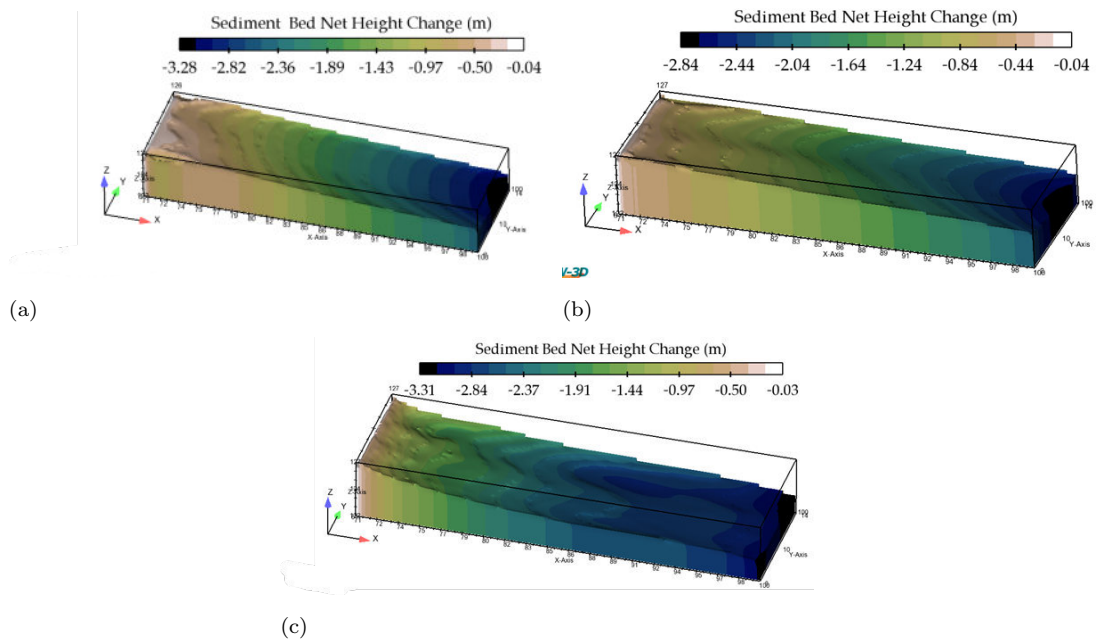


FIGURE 5.25: 3-D representation of scoured bed below Type (C) basin at designed discharge, (a) RNG  $k-\epsilon$ , (b) Std  $K-\epsilon$  model, and (c) LES model

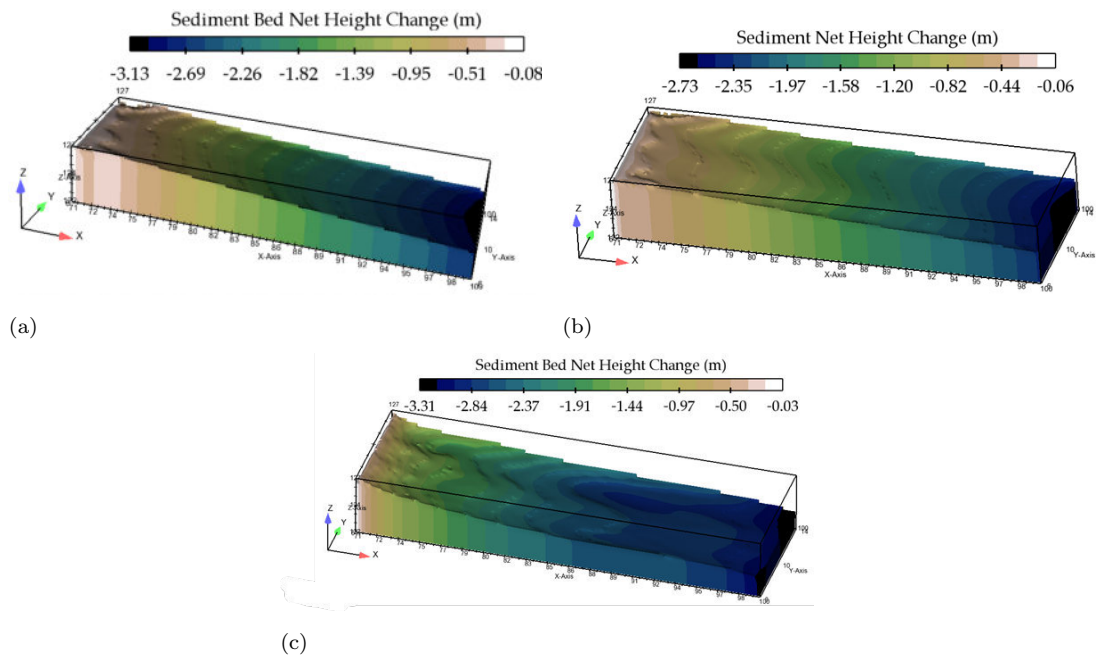


FIGURE 5.26: 3-D representation of scoured bed below Type (D) basin at designed discharge (a) RNG  $k-\epsilon$ , (b) Std  $K-\epsilon$  model, and (c) LES model

### 5.4.2 Scour and Retrogression Pattern at High Flood Discharge

Fig. 5.27 shows bed retrogression downstream of Type (A) basin at  $18 \text{ m}^3/\text{s}/\text{m}$  discharge. Using RNG K- $\epsilon$  model, the maximum bed was retrogressed at the end of sediment bed for which the maximum scour depth reached 2.87 m as can be seen in Fig. 5.27 (a). As compared to the designed discharge, 14 % higher maximum depth was observed at  $18 \text{ m}^3/\text{s}/\text{m}$  discharge. However, the pattern of bed retrogression was found to be identical as witnessed at the designed discharge. At  $18 \text{ m}^3/\text{s}/\text{m}$  discharge, using RNG K- $\epsilon$  model, the net change in bed downstream of Type (A) basin was reached 58%. On the contrary, at  $18 \text{ m}^3/\text{s}/\text{m}$  discharge, using Std K- $\epsilon$  model, different pattern was noticed downstream of Type (A) basin. The maximum net change of bed was noticed at the centre-line of bay which reached to 47% as shown in Fig. 5.27 (b). Fig. 5.27 (c) shows bed retrogression downstream of Type (A) basin using LES. As compared to K- $\epsilon$  models, the retrogression in LES model was found to be dissimilar. After comparing with designed discharge, at  $18 \text{ m}^3/\text{s}/\text{m}$ , the maximum change in the bed reached 40% which was 25% less than the designed discharge. However, at both the investigated discharges, upon use of LES model, the patterns of bed retrogression were found to be identical.

Fig. 5.28 displays scour pattern downstream of Type (B) basin at  $18 \text{ m}^3/\text{s}/\text{m}$  discharge. Fig. 5.28 (a) Upon use of RNG K- $\epsilon$  model, a large scour hole was developed downstream of rigid in which the maximum scour depth reached 2.93 m which was about 6% less than was noticed at the designed discharge. After the scour hole, the bed was found to be retrogressed up to the end of sediment bed. The net change in the sediment downstream of Type (B) basin was 84%. On the other hand, at the designed discharge, the complete bed was found to be exposed.

Fig. 5.28 (b) shows scoured bed downstream of Type (B) basin using Std K- $\epsilon$  model at  $18 \text{ m}^3/\text{s}/\text{m}$  discharge. The overall patterns of scour hole and bed retrogression were found different than that was observed at designed discharge. At designed discharge, the downstream end of scour hole was collapsed while at  $18 \text{ m}^3/\text{s}/\text{m}$  discharge, the scour hole remained visible. After the scour hole, the

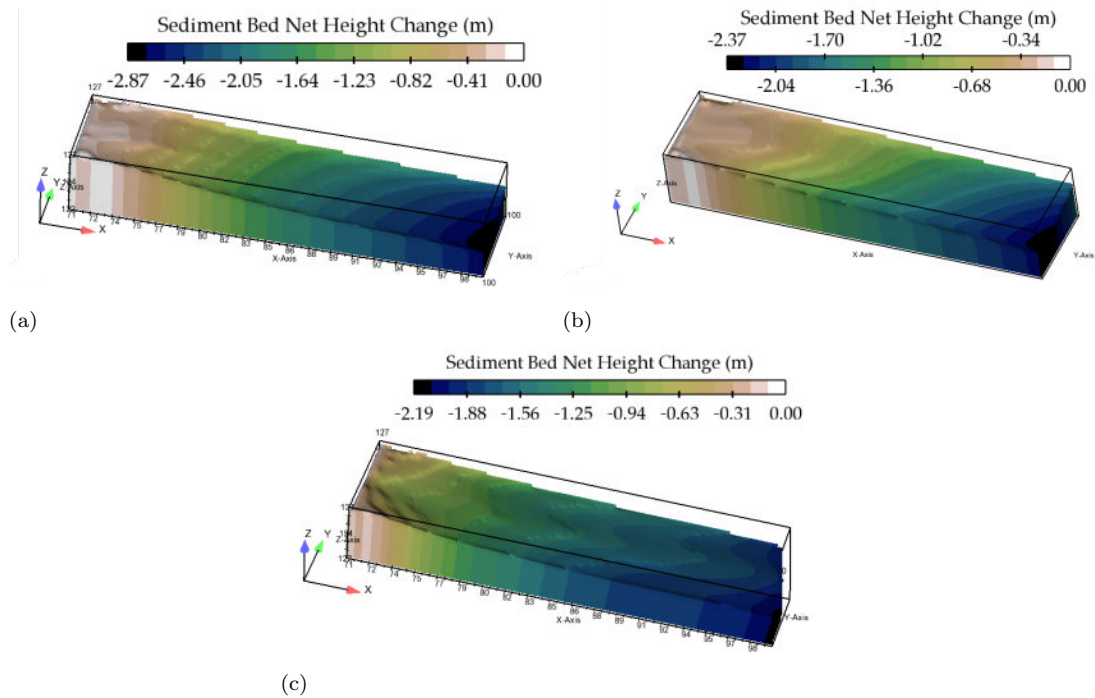


FIGURE 5.27: 3-D representation of scoured bed below Type (A) basin at  $18 \text{ m}^3/\text{s}/\text{m}$ , (a) RNG  $k-\epsilon$ , (b) Std  $K-\epsilon$  model, and (c) LES model

sediment continued to be eroded. At  $18 \text{ m}^3/\text{s}/\text{m}$  discharge, the maximum scour depth in scour hole and at the end of sediment was reached to 2.87 m and 4.25 m, respectively, which indicated that 89% of the bed was scoured. As compared to RNG and the Std  $K-\epsilon$  model showed higher net change in the sediment bed downstream of Type (B) basin.

Using LES model, the pattern of scour hole and bed retrogression on downstream of Type (B) basin was found to be different than that was observed in RNG and Std  $K-\epsilon$  models, as shown in Fig. 5.27 (c). The results further showed that downstream end of scour hole was also eroded and the maximum scour depth in scour hole was reached 3.57 m. The scour depth in LES model was about 22% and 24% higher as compared to RNG and Std  $K-\epsilon$  models, respectively. However, in LES model, the net change of sediment bed downstream of Type (B) basin was found equivalent to the prediction of Std  $K-\epsilon$  model.

Fig. 5.29 shows scour and bed retrogression downstream of Type (C) basin using different turbulence models. Using RNG  $K-\epsilon$  model, the pattern of bed retrogression downstream of Type (C) basin was found to be changed than that were



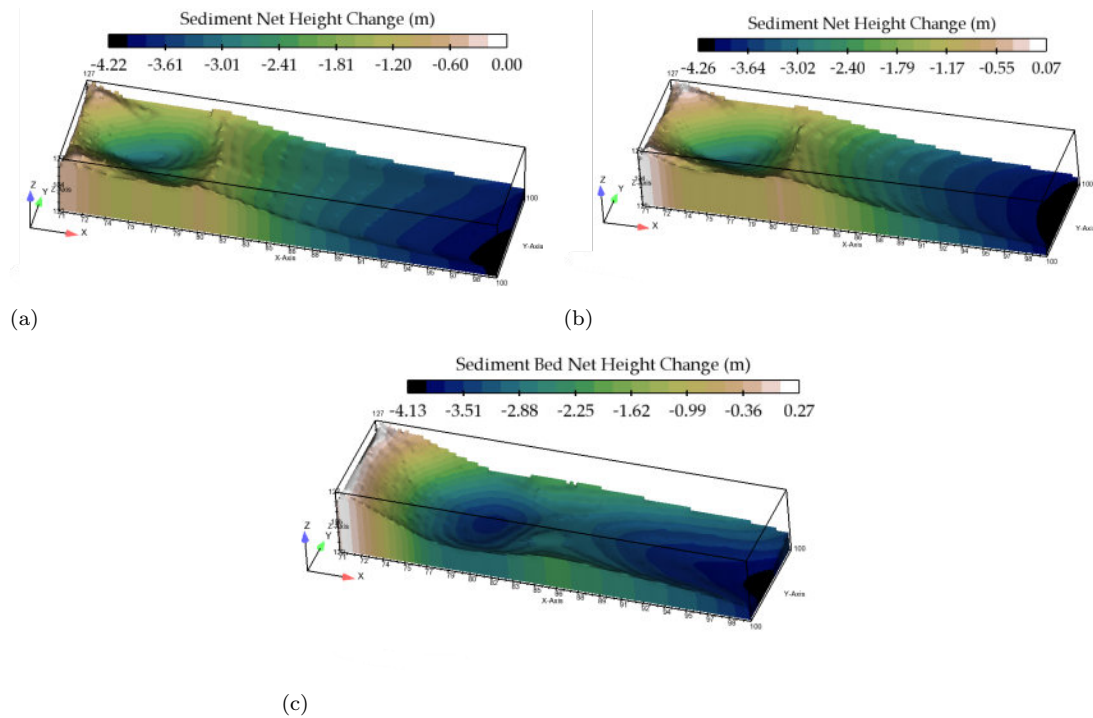


FIGURE 5.28: 3-D representation of scoured bed below Type (B) basin at 18  $\text{m}^3/\text{s}/\text{m}$ , (a) RNG  $k-\epsilon$ , (b) Std  $K-\epsilon$  model, and (c) LES model

noticed in Type (A) and (B) basins as shown in Fig. 5.29 (a). The results showed ripple and wavy bed surface which continued to the end of sediment bed. The net change in the sediment end downstream of Type (C) basin was reached 2.30 m which was about 20% less than Type (A) basin. Similarly, upon use of Std  $K-\epsilon$  model, overall net change in the sediment downstream of Type (C) basin was 11% than Type (A) basin. However, the retrogressed pattern was dissimilar to that was witnessed downstream Type (A) basin as shown in Fig. 5.29 (b). However, upon use of LES model, the maximum net change downstream Type (C) basin reached 2 m which was 5% higher than Type (A) basin. After using LES, the pattern of retrogressed bed downstream of Type (C) basin was different than RNG and Std  $K-\epsilon$  models as shown in Fig. 5.29 (c).

Fig. 5.30 shows bed retrogression downstream of Type (D) basin with different turbulence models at discharge. From Fig. 5.30 (a), using RNG  $K-\epsilon$  model, the bed retrogression was found to be different than observed in Type (A) and (C) basins. In RNG  $K-\epsilon$  model, the net change in the sediment bed was found to 52% which was 3% less than the designed discharge. At 18  $\text{m}^3/\text{s}/\text{m}$  discharge, the

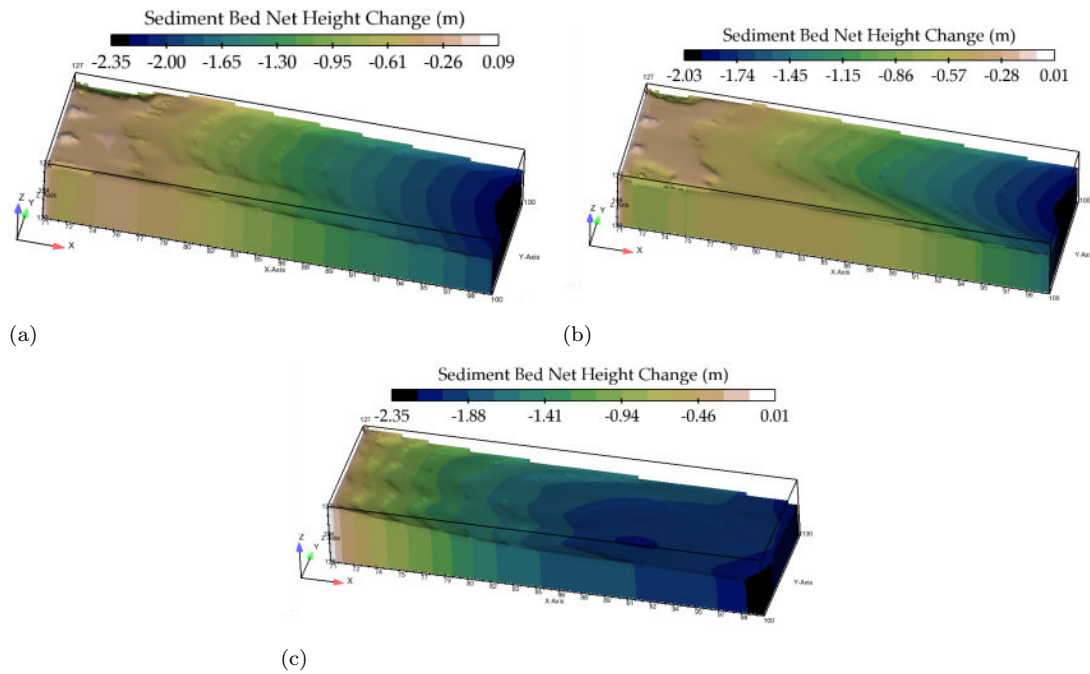


FIGURE 5.29: 3-D representation of scoured bed below Type (C) basin at  $18 \text{ m}^3/\text{s}/\text{m}$ , (a) RNG  $k-\epsilon$ , (b) Std  $K-\epsilon$  model, and (c) LES model

pattern of bed retrogression was found to be uniform as the flow moved towards the downstream end of sediment bed.

Fig. 5.30 (b) shows bed retrogression using Std  $K-\epsilon$  model, and the maximum change in the sediment bed reached 2.12 m which was 8% less as compared to RNG  $K-\epsilon$  model. As compared to RNG  $K-\epsilon$  model, in Std  $K-\epsilon$  mode, the retrogression pattern on the upstream of sediment was found to be dissimilar, however, on downstream side, a similar pattern was noticed as can be seen in Fig. 5.30 (b). Additionally, the pattern of bed retrogression at  $18 \text{ m}^3/\text{s}/\text{m}$  discharge was also found different than that was observed at the designed discharge.

Upon use of LES model, the maximum change in the sediment bed downstream of Type (D) basin was reached 2 m, which was 11% and 1% less than  $K-\epsilon$  models. In LES model, the pattern of bed retrogression on downstream of the sediment bed was found identical to Type (C) basin, however, at the upstream, a different pattern of bed retrogression was noticed, as shown in Fig. 5.30 (c). Additionally, using LES model, at  $18 \text{ m}^3/\text{s}/\text{m}$  discharge, the pattern of retrogressed bed downstream of Type (D) was found similar to that was noticed at designed discharge.

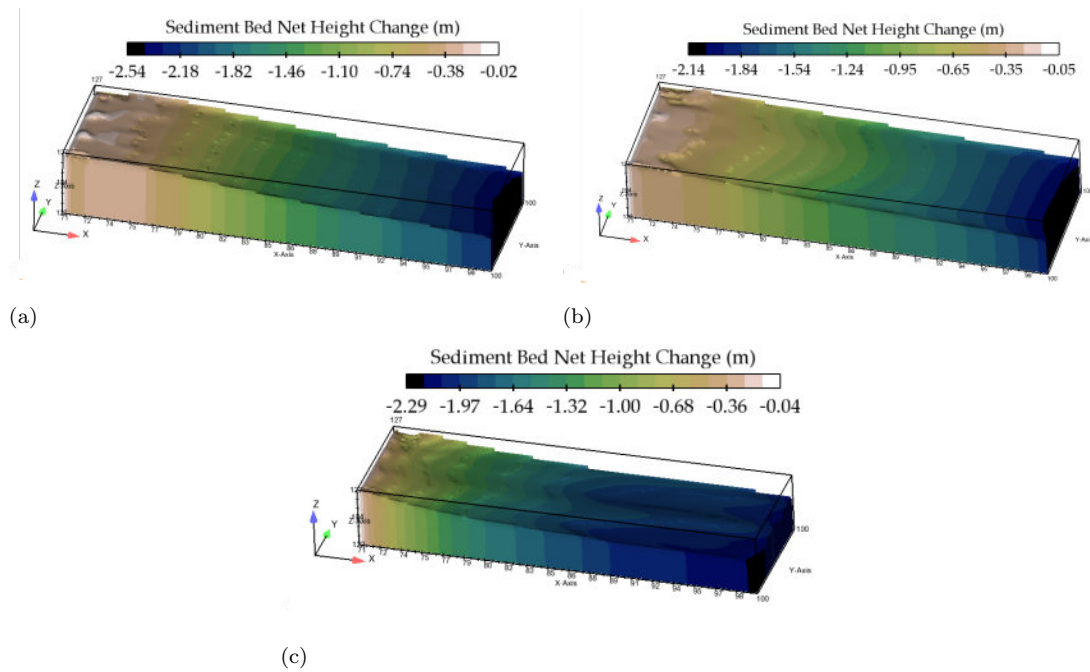


FIGURE 5.30: 3-D representation of scoured bed below Type (D) basin at  $18 \text{ m}^3/\text{s}/\text{m}$ , (a) RNG  $k-\epsilon$ , (b) Std  $K-\epsilon$  model, and (c) LES model

Conclusively, at  $18 \text{ m}^3/\text{s}/\text{m}$  discharge, the scour and bed retrogression downstream of studied stilling basins were found less than the designed discharge. The maximum change in sediment bed was found downstream of Type (B) basin which reached 89% in Std  $K-\epsilon$  model, while the minimum net change was noticed downstream of Type (C) basin which was ranged between 42% to 48% using different turbulence models. Therefore, based on the results, it can be said, the stilling basin with WSBB produced less bed retrogression at the investigated flood discharge.

### 5.4.3 Longitudinal Bed Profiles at Designed Discharge

Using different turbulence models, at  $24.30 \text{ m}^3/\text{s}/\text{m}$  discharge, Figs. 5.31, 5.32, and 5.33 show the longitudinal profiles of scoured bed downstream of Type (A), (B), (C), and (D) basins, respectively. At the finish time of  $T=500 \text{ s}$ , the profiles were drawn from the center-line of the models.

Using RNG  $K-\epsilon$  model, Fig. 5.31 shows longitudinal bed profiles downstream of Type (A), (B), (C), and (D) basin. In Type (A), (C), and (D) basins, the sediment

was found to be retrogressed, which continued until the end of simulations.

At the end of sediment bed, the net change in the beds was reached to 51%, 67% and 63% in Type (A), (C), and (D) basins, respectively as shown in Fig. 5.31. On the contrary, in Type (B) basin, a large scour hole was noticed just downstream of end sill which continued to be extended up to  $T=500$  s. At the finished time, maximum depth of scour hole was reached 3.57 m (75%). After the scour hole, the bed continued to retrogress, and the at  $T= 500$ s, the entire sediment bed was found to bed eroded as shown in Fig. 5.31.

Fig. 5.32 shows longitudinal bed profiles in Type (A), (B), (C), and (D) basins using Std K- $\epsilon$  model. As compared to RNG K- $\epsilon$  model, the overall net height change of beds in Std K- $\epsilon$  model was found to be less in all the tested stilling basin. However, out of the investigated basins, Type (A) basin showed less bed scour and retrogression. At the end of simulation, the total change in bed downstream of Type (A), (C), and (D) basins was reached to 54 %, 58 %, and 55 %, respectively.

On the other hand, in Type (B) basin, the pattern on scour hole and bed retrogression was found different to that was observed in RNG K- $\epsilon$  model. From the rigid bed to  $X=8$  m, the overall, 76 % of sediment bed was eroded while a the end of the sediment bed, the sediment bed was completely exposed as can be seen in Fig. 5.32

Fig. 5.33 indicates longitudinal scour profiles downstream of different stilling basins using LES model. In Type (A), (C), and (D) basins, the sediment bed was found to be retrogressed which increased as the simulation time approached to  $T= 500$  s. However, at the start of sediment bed up to  $X=20$  m, the bed retrogression in Type (A) basin was found to less than Type (C), and (D) basins. However, after  $X=20$  m, the retrogression Type (C) basin was found less than Type (A), and (D) basins. The maximum net height change in the sediment was noticed at the end of sediment beds ( $X=30$  m, from the rigid floor).

At the end of simulations, the total change in bed downstream of Type (A), (C), and (D) basins was reached to 65 %, 65 %, and 68 %, respectively. On the contrary,

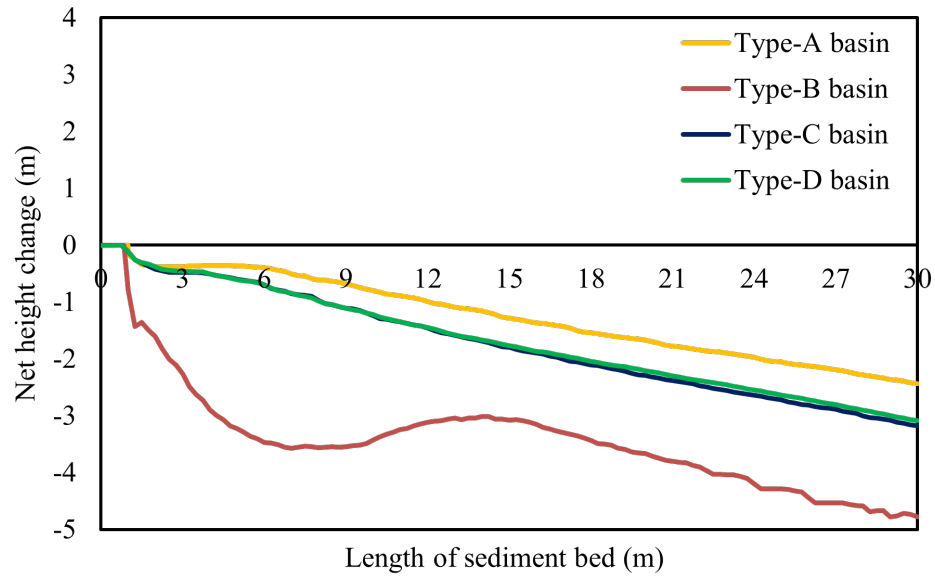


FIGURE 5.31: Longitudinal scour profiles at  $24.30 \text{ m}^3/\text{s}/\text{m}$  discharge using RNG K- $\epsilon$  model

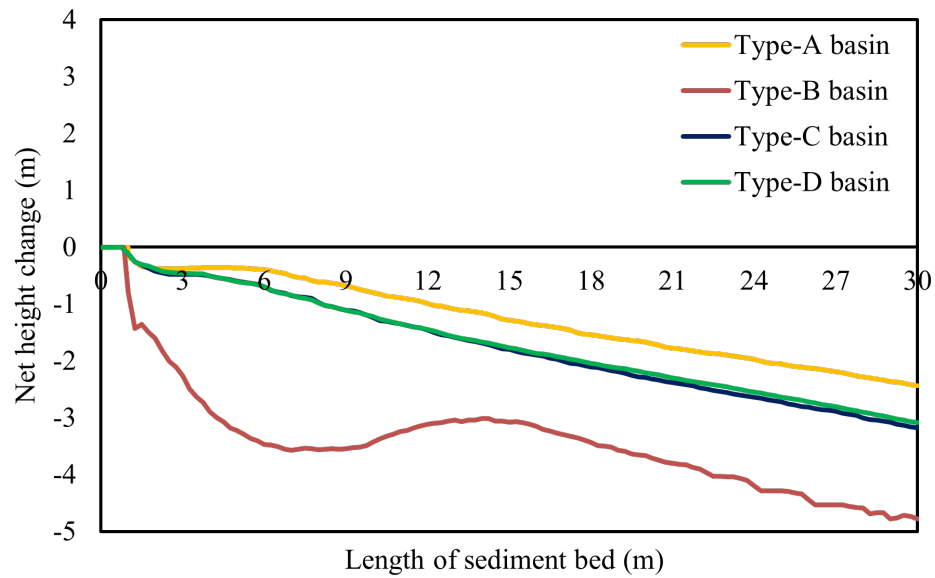


FIGURE 5.32: Longitudinal scour profiles at  $24.30 \text{ m}^3/\text{s}/\text{m}$  discharge using Std K- $\epsilon$  model

in Type (B) basin, at the start of simulation, a large scour hole was noticed below the rigid bed, and after the scour hole, the bed continued to retrogress which was completely eroded when the simulation reached to finish time ( $T_s = 500 \text{ s}$ ) as shown in Fig. 5.33.

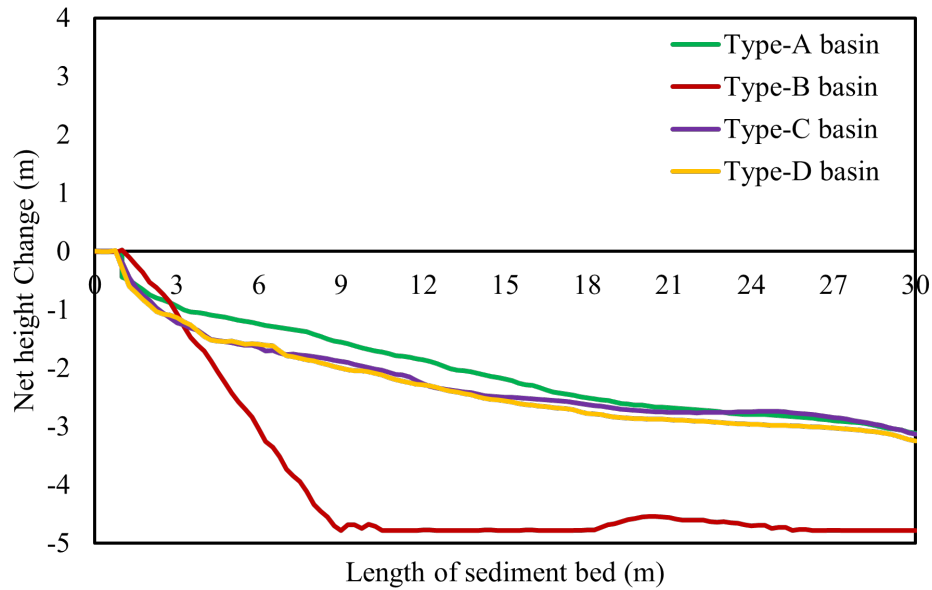


FIGURE 5.33: Longitudinal scour profiles at  $24.30 \text{ m}^3/\text{s}/\text{m}$  discharge using LES model

#### 5.4.4 Longitudinal Bed Profiles at High Flood Discharge

Figs. 5.34, 5.35, and 5.36 show longitudinal bed profiles at  $18 \text{ m}^3/\text{s}/\text{m}$  discharge downstream of Type (A), (B), (C) and (D) basins. Out of the studied basins, the maximum scour was noticed in Type (B) basin, in which the maximum scour depths were reached 2.92 m and 4.04 m in the scour hole and at the sediment end, respectively, as can be seen in Fig. 5.34. However, as compared to the designed discharge, the bed was found to be less scoured in Type (B) basin. Out of the investigated basins, Upon use of RNG K- $\epsilon$  model, the minimum change in the sediment bed was observed downstream of Type (C) basin. The maximum scour depth downstream of Type (C) basin was reached 2.29 m at end of sediment bed as shown in Fig. 5.34.

Fig. 5.35 indicates scour and bed retrogression downstream of different stilling basins using Std K- $\epsilon$  model. Similar to RNG K- $\epsilon$  model, the maximum scour depth was observed downstream of Type (B) basin which reached to 4.25 m at the end of sediment bed (At, X=30 m). However, in the scour hole, the scour depth was reached 2.87 m. Similarly, at  $18 \text{ m}^3/\text{s}/\text{m}$  discharge, the minimum change in the sediment bed was noticed downstream of Type (C) basin which reached 1.99 m.

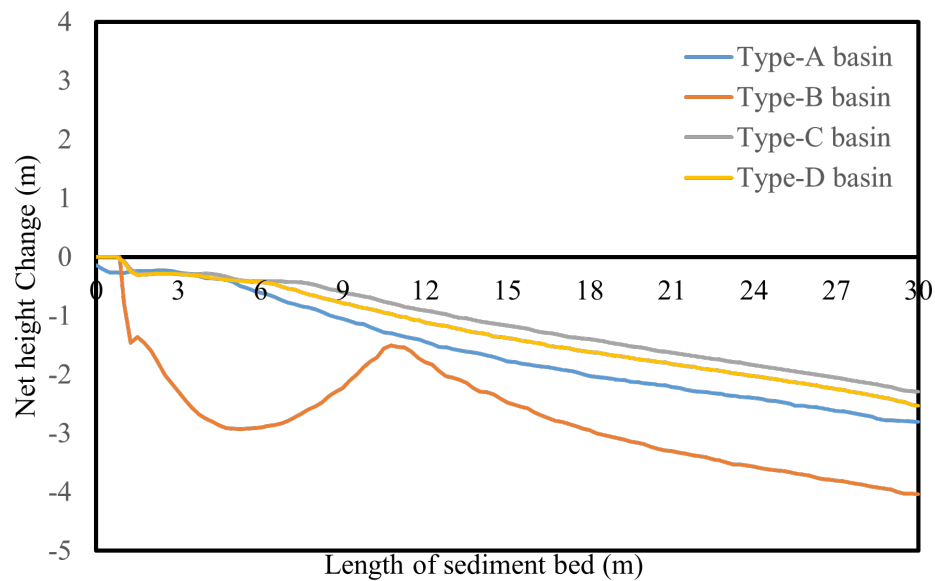


FIGURE 5.34: Longitudinal scour profiles at  $18 \text{ m}^3/\text{s}/\text{m}$  discharge using RNG  $k\text{-}\epsilon$  model

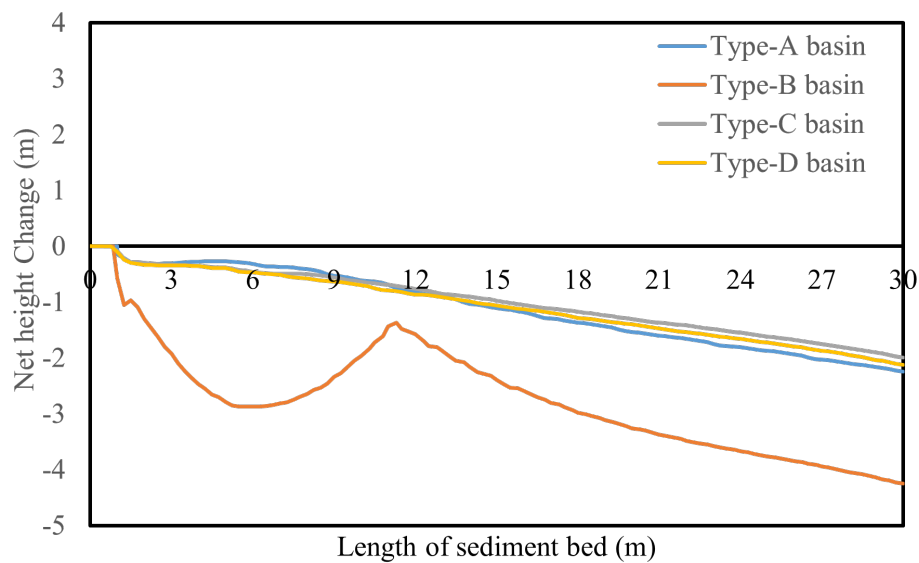


FIGURE 5.35: Longitudinal scour profiles at  $18 \text{ m}^3/\text{s}/\text{m}$  discharge using Std  $k\text{-}\epsilon$  model

As compared to RNG  $K\text{-}\epsilon$  model, using Std  $K\text{-}\epsilon$  mode, the sediment downstream of Type (C) basin was found to be less retrogressed as shown in Fig. 5.35. However, on the other hand, upon use of Std  $K\text{-}\epsilon$  model, the scour depth downstream of Type (B) basin was increased than that was observed in RNG  $K\text{-}\epsilon$  model.

Fig. 5.36 shows longitudinal bed profiles downstream of studied basins at  $18 \text{ m}^3/\text{s}/\text{m}$  discharge using LES model. As compared to  $K\text{-}\epsilon$  models, the patterns of

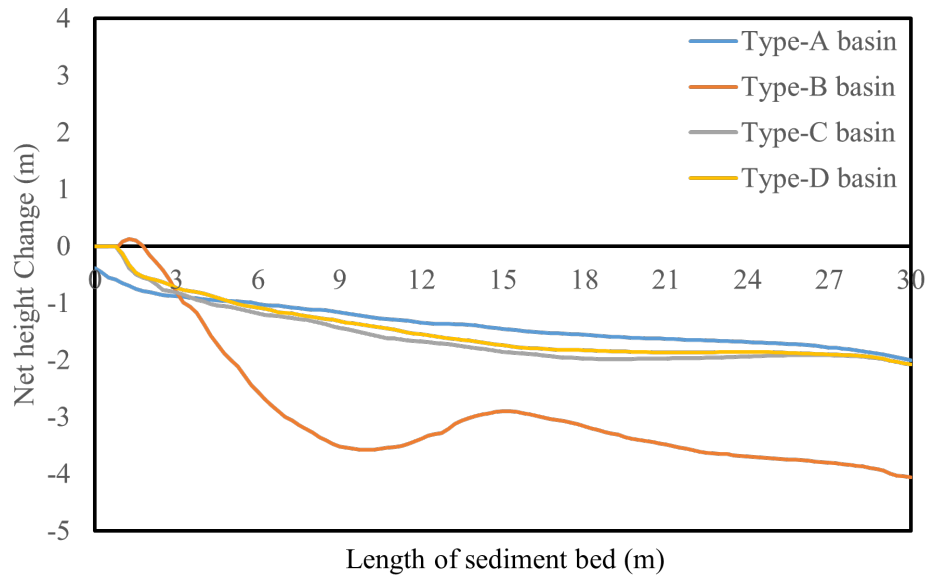


FIGURE 5.36: Longitudinal scour profiles at 18 m<sup>3</sup>/s/m discharge using LES model

scour and bed retrogression downstream of investigated basins were found to be different in LES model. As noticed in RNG K- $\epsilon$  and Std K- $\epsilon$  model, the results showed that the maximum bed was retrogressed downstream of Type (B) basin which reached 4 m at end of sediment bed while in the scour hole the maximum scour depth reached 3.57 m. However, upon use of LES model, the overall change on the bed downstream of Type (A) was found to be same as noticed in Type (C) and (D) basin.

TABLE 5.1: Maximum scour depths at different Y-sections downstream of studied basins at designed discharge

Stilling Basins	RNG K- $\epsilon$ model			Std K- $\epsilon$ model			LES model		
	$\frac{y}{4}$	$\frac{y}{2}$	$\frac{3y}{4}$	$\frac{y}{4}$	$\frac{y}{2}$	$\frac{3y}{4}$	$\frac{y}{4}$	$\frac{y}{2}$	$\frac{3y}{4}$
	<b>Type (A)</b>	69%	51%	64%	57%	54%	49%	69%	65%
<b>Type (B)</b>	100%	100%	97%	100%	97%	95%	100%	100%	100%
<b>Type (C)</b>	60%	67%	69%	53%	58%	58%	65%	65%	68%
<b>Type (D)</b>	63%	65%	64%	53%	55%	56%	70%	68%	66%



TABLE 5.2: Maximum scour depths at different Y-sections downstream of studied basins at flood discharge

Stilling Basins	RNG K- $\epsilon$			Std K- $\epsilon$			LES		
	model			model			model		
	$\frac{y}{4}$	$\frac{y}{2}$	$\frac{3y}{4}$	$\frac{y}{4}$	$\frac{y}{2}$	$\frac{3y}{4}$	$\frac{y}{4}$	$\frac{y}{2}$	$\frac{3y}{4}$
<b>Type (A)</b>	60%	58%	54%	49%	47%	42%	43%	40%	42%
<b>Type (B)</b>	87%	85%	82%	87%	89%	87%	84%	85%	76%
<b>Type (C)</b>	46%	48%	48%	37%	42%	41%	46%	44%	45%
<b>Type (D)</b>	51%	53%	52%	44%	44%	43%	44%	43%	45%

Above Tables 5.1, and 5.2 show the overall net change in the sediment beds downstream of the investigated basins. It can be seen from Table 5.1 that at the designed discharge, the maximum scour and bed retrogression occurred downstream of Type (B) basin, whereas, the results of scour and bed profiles in Type (A), (C) and (D) basins were found to be close. On the other hands, similar to designed discharge at the flood discharge, the maximum net change in the sediment bed was found downstream of Type (B) basin, whereas, the minimum change in the sediment was noticed downstream of Type (C) basin as can be seen in Table 5.2.

In Conclusion, it can be said that at the flood discharge, Type (C) and (D) basin showed less bed retrogression. On the contrary, at the flood discharge, Type (B) basin showed higher scour and bed retrogression.

## 5.5 Economic Analysis

For the investigated stilling basin, i.e., Type (A), (B), (C) and (D) a tentative economic analysis is performed based on current market schedule rates. The analysis is carried out for the baffle blocks region where new energy dissipators (as shown in Fig.3.9) are installed to check their hydraulic efficiency and effects on the riverbed for different gated and free flow discharges.

After the hydraulic and scour analysis, the results showed that Type (B) basin is producing higher velocity and turbulent kinetic energies at the basin's end. In addition, at the design flow, the employed sediment packed bed is found to be explored while a flood discharge about 84 % of the sediment eroded. Thereby, in view of the scour analysis downstream of Type (B), this basin is excluded from the cost analysis, and at present, the comparison is performed among Type (A), (C) and (D) basins.

To perform the economic analysis, the cost of unit baffle block is computed for which a lump-sum rate of 4000 psi concrete under water is utilized. The overall external sizes of the baffle blocks are same while due to the change in the internal geometry, the overall volume of the studied baffle blocks are found to be dissimilar. This increase in the volume resulted in the material cost being used for the construction of WSBB. The comparison of cost has depicted that the cost of baffle blocks in Type (C) and (D) basin increase up to 10.20 %, 19 %, respectively. Therefore, it is important to mention that this minimal increase in cost does not bear much impact in overall cost of the barrage construction as the cost of these appurtenances is much less. In addition from the analysis of cost, it is concluded that for hydraulic structures, i.e., barrages, spillways and dams, hydraulic stability and stilling basin performance are the dominating parameters than the cost.

# Chapter 6

## Conclusions & Recommendations

### 6.1 General

This study developed FLOW-3D hydraulic and scour models to investigate different stilling basins of river diversion barrage. Before the development of numerical models, the most critical parameters for the hydraulic investigations were identified using statistical methods i.e., frequency analysis, relative importance index and relative percentage score. For the hydraulic models, free surface profiles, sequent depths, roller lengths, hydraulic jump efficiency, velocity profiles, and turbulent kinetic energy were the main investigated parameters. The results from the 4<sup>th</sup> chapter confirmed by suitability of WSBB downstream of river diversion barrage. The result further revealed that the stilling basin with chute blocks and end sill (Type (B)) was dissipating less energy. On the contrary, to understand the scour and retrogression behaviours downstream of studied stilling basins, velocity field, shear stress and 3-D scour contours, and longitudinal bed profiles were assessed. From chapter 5, the results of scour and bed retrogression showed that downstream of remodeled basin (Type (B)), the sediment bed was exposed up to 100% and 89% at designed and flood discharge, respectively. Furthermore, the results of bed retrogression profiles downstream of wedge-shaped baffle block basins (Type (C) & (D)) revealed that up to 18 m<sup>3</sup>/s/m discharge, these basins performed better

than rest of the investigated basins (Type (A) & (B)). This chapter presents the conclusions drawn from the results of hydraulic and scour modelling. The chapter also provides significance and implications of the present study, and lay out future recommendations.

## 6.2 Conclusions

1. Frequency analysis, relative importance index (RII) and relative percentage score revealed that velocity, initial Froude number, free surface profile, shape of stilling basin, turbulent kinetic energy and tail water were the most critical parameters which were focused on the previous hydraulic studies. Hence, the above-mentioned hydraulic parameters are also studied for the present hydraulic models.
2. FLOW-3D numerical models produced acceptable results of designed, flood and gated discharges. The numerical models showed a little overestimation of modelled discharges for which the maximum and minimum errors reached 14% and -3%, respectively. Hence, it is believed that FLOW-3D is an effective and efficient 3-D numerical code for the measurement of discharge downstream of river diversion barrages. It is also believed that RNG K- $\epsilon$  turbulence model has shown better performance in measuring the volume flow rates on the studied stilling basins.
3. The free surface profiles revealed that at the investigated flows, the initial locations of the hydraulic jumps were established on the downstream glacis which further indicated no sweeping of hydraulic jump on the basin's floor. However, in comparison to Type (B), (C) and (D) basins, in Type (A) basin, the initial locations of hydraulic jumps occurred up on the downstream glacis.
4. As compared to Type (A) and (B) basins, at the studied gated flows, wedge-shaped baffle block basins ((Type (C) and (D))) produced lesser lengths of hydraulic jumps. Therefore, it is concluded that the proposed new basins

i.e., Type (C) and (D), for river diversion barrages are efficiently containing the hydraulic jumps between downstream glacis and baffle blocks' regions.

5. At the studied gated flows, i.e.,  $2.44 \text{ m}^3/\text{s}/\text{m}$ ,  $4.88 \text{ m}^3/\text{s}/\text{m}$ , and  $7.22 \text{ m}^3/\text{s}/\text{m}$ , the results of free surface profiles, roller lengths, sequent depth agreed well with the previous relevant studied. Thereby, it can be concluded that the developed numerical models using volume of fluid (VOF) technique are promising to study the hydraulics of different stilling basins.
6. At the lower discharge, i.e.,  $2.44 \text{ m}^3/\text{s}/\text{m}$ , the relative energy loss within the hydraulic jumps was identical in the studied basins, whereas, upon increase of flow, in comparison to Type (A) and (B) basins, wedge-shaped baffle blocks basins (Type (C) and (D)) revealed higher energy loss within the hydraulic jumps.
7. The vertical velocity profiles revealed that due to absence of baffle blocks, the maximum magnitude of velocity was striking at the floor of remodelled basin (Type (B)), and it was further increased as the flow increased, whereas, upon increase of flow, the velocity near the floor of wedge-shaped baffle block basins (Type (C) and (D)) was observed to be decreased. Additionally, up to  $4.88 \text{ m}^3/\text{s}/\text{m}$  discharge, the minimum velocity values at basins' end was noticed in wedge-shaped baffle blocks basins (Type (C) and (D)), whereas, at  $7.22 \text{ m}^3/\text{s}/\text{m}$  discharge, in comparison to Type (A) basin, 10% increase of velocity magnitude was observed Type (C) and (D) basins. On comparison, the results revealed that the maximum velocities at the basin's floor and at the basin's end were developed in Type (B) basin. Based on the results of velocity profiles, it can be concluded the use of chute blocks and sills (Type (B)) downstream of the river diversion barrage are generating higher velocity in the basin and thereby dissipating less energy.
8. The study also revealed that as the WSBB produced larger wake zones and controlled fluid reattachment, thereby, as compared to Type (A) and (B) basins, minimum turbulent kinetic energy and turbulent intensity were noticed at the floors of Type (C) and (D) basins. Therefore, it is believed that at

the studied discharges, the newly proposed energy dissipating arrangements such as Type (C) and (D) have improved the hydraulic behavior downstream of the studied barrage than the traditional (Type (A)) and existing basins (Type (B)).

9. The validation results of scour profiles downstream of Type (B) have indicated that the present FLOW-3D scour models are well agreeing with the field data for which the values of  $R^2$  reached 0.908, 0.909 and 0.953 in LES, RNG K- $\epsilon$  and Standard K- $\epsilon$  models, respectively. On comparison of scour profiles with three sets of field data, it is concluded that the scour models with RNG K- $\epsilon$  turbulence model are more promising than LES and Standard K- $\epsilon$  model.
10. At the designed discharge, the flow fields have revealed a forward velocity profile on the scoured and retrogressed beds of Type (A), Type (C) and Type (D) basins, whereas large fluid re-circulation are noticed near the rigid of Type (B) basin which develops large scour hole, and later the complete bed is exposed. Therefore, it is believed that due to the absence of baffle and friction blocks, the Type (B) basin is generating higher scour and bed retrogression on its downstream. At the designed discharge, the maximum net change in the sediment beds downstream of Type (A), Type (C) and (D) basins reaches 65%, 68% and 67%, respectively. Furthermore, as the scour phenomena is found to be very complex in nature and results are diverse as the turbulence models are changed, therefore, it is concluded that for the barrages up to the designed discharge of  $24.30 \text{ m}^3/\text{s}/\text{m}$ , the new proposed wedge-shaped baffle blocks basins i.e., Type (C) and (D) are capable to save the basin against scouring.
11. At the flood discharge of  $18 \text{ m}^3/\text{s}/\text{m}$ , as compared to the designed discharge, the results showed different patterns of scour and bed retrogression downstream of the studied basins. The maximum net change in the bed was noticed downstream of Type (B) basin which indicated 89% loss of sediment bed, whereas the minimum net change in the sediment bed was noticed

downstream of Type (C) and (D) basins which reached 37% and 44%, respectively. Therefore, based on the results of scour profiles, it is confirmed that the proposed Type (C) and (D) basins are suitable for barrages up to the  $18 \text{ m}^3/\text{s}/\text{m}$  discharge, and they are found more efficient than the Type (A) and Type (B) basins.

In conclusion, it is believed that the existing remodelled basin (Type (B)) of the studied barrage is generating higher velocity and turbulent kinetic energies on the rigid and erodible beds. On the contrary, the newly proposed basin with combination of WSBB and impact USBR baffle improved the hydraulic jump and flow characteristics on the rigid and erodible beds. It is further concluded that FLOW-3D is an effective tool to predict the hydraulic and scour behavior downstream of river diversion barrages as the validation results agree with field observations.

### 6.3 Research Significance and Implications

Since the last thirty years, all around the world, the use of numerical modelling in hydraulic and scour investigations of spillways, sluice gates and low head hydraulic structures has become prevalent. However, the use of such modelling tools is found very limited in Pakistan and for the development of irrigation and power projects, traditional physical modelling is employed.

Since the last decade, based on the limited hydraulic and scour investigations, many of the barrages in the plain area of Pakistan are remodelled and rehabilitated. Almost the old stilling basins of the barrage in Pakistan are the modified form of USBR Type-III basin (Type (A)) and since the results of FLOW-3D models with different turbulence schemes have shown that the impact baffle blocks used in USBR basins are causing flow reattachment and produce less wake region while the use of WSBB increases the wake region and energy dissipation, therefore, the results of wedge-shape baffle block basin's (Type (C) and (D)) ensured their

suitability downstream of lower head hydraulic structures, i.e., sluice gate, barrage, and canal head regulators. The results of present FLOW-3D numerical models also revealed that Type (B) is less efficient for the dissipation of flow energy which produce higher local scour.

The present results of numerical models also provide confidence to the hydraulic engineer that a little change in the input of FLOW-3D models, i.e., discharge, geometry, gate opening, turbulence models, sediment transport rate equations, and hydraulic parameters can offer necessary outputs in a very limited time frame, which is found to be very expensive and time consuming in physical modelling. Therefore, for the future intervention in the hydraulic structures, the results of present models will help Civil and Hydraulic engineers to assess different energy dissipation arrangements within the stilling basins and will provide suitable alternative solutions.

## 6.4 Recommendations

1. Based on the results of scour and bed retrogression, the study recommends that before the remodelling of any hydraulic structure, the hydraulic engineers and practitioner may investigate the critical hydraulic parameters i.e., velocity, initial Froude number, free surface profile, shape of stilling basin and its appurtenances, turbulent kinetic energy and tail water. Additionally, it is further recommended that geometric design of the stilling basins' must be tested after employing the erodible bed downstream of the investigated basins.
2. The study recommends investigating hydraulic jump and flow behavior with discharges higher than  $7.22 \text{ m}^3/\text{s}/\text{m}$  using other turbulence models.
3. Presently, the geometry of investigated WSBB is fixed, therefore, the study recommends examining the WSBB downstream of river diversion barrages with other vertex and cutback angles.



4. Presently, a single bay of studied barrage is modelled to investigate the effects of different stilling basins on flow characteristic and local scour. However, it is suggested to employing two bays, and their effects may be tested for hydraulic and local scour.
5. For scour modelling, the study recommends employing other transport rate equation i.e., Nielsen Equation, and Meyer, Peter, and Müller Equation.
6. It is also recommended that for a particular discharge, the effects of barrages' stilling basins may be investigated by employing multiple gates, and there hydraulic and local scour effects may also be assessed.

# Bibliography

- [1] S.-H. Chen and S.-H. Chen, “Irrigation and drainage works,” *Hydraulic Structures*, pp. 897–928, 2015.
- [2] A. Baylar, M. Unsal, and F. Ozkan, “Hydraulic structures in water aeration processes,” *Water, Air, & Soil Pollution*, vol. 210, pp. 87–100, 2010.
- [3] Y. I. Hafez, “Scour due to turbulent wall jets downstream of low-/high-head hydraulic structures,” *Cogent Engineering*, vol. 3, no. 1, p. 1200836, 2016.
- [4] J. A. Vasquez and J. J. Roncal, “Testing river2d and flow-3d for sudden dam-break flow simulations,” 2009.
- [5] B. James, A. F. Roger, E. Christopher, and A. Reza, “Physical and numerical modelling of the severn barrage,” *Science China Technological Sciences*, vol. 57, pp. 1471–1481, 2014.
- [6] S. Bray, R. Ahmadian, and R. A. Falconer, “Impact of representation of hydraulic structures in modelling a severn barrage,” *Computers & geosciences*, vol. 89, pp. 96–106, 2016.
- [7] V. Vuik, “Numerical modeling of sediment transport over hydraulic structures,” 2010.
- [8] M. Khanpour, A. R. Zarrati, M. Kolahdoozan, A. Shakibaeinia, and S. Jafarinik, “Numerical modeling of free surface flow in hydraulic structures using smoothed particle hydrodynamics,” *Applied Mathematical Modelling*, vol. 40, no. 23-24, pp. 9821–9834, 2016.

- [9] H. Teraguchi, H. Nakagawa, K. Kawaike, B. Yasuyuki, and H. Zhang, “Effects of hydraulic structures on river morphological processes,” *International Journal of Sediment Research*, vol. 26, no. 3, pp. 283–303, 2011.
- [10] P. Grivalszki, G. Fleit, S. Baranya, and J. Józsa, “Assessment of cfd model performance for flows around a hydraulic structure of complex geometry,” *Periodica Polytechnica Civil Engineering*, vol. 65, no. 1, pp. 109–119, 2021.
- [11] J. Zeng, M. Ansar, Z. Rakib, M. Wilsnack, and Z. Chen, “Applications of computational fluid dynamics to flow rating development at complex prototype hydraulic structures: Case study,” *Journal of Irrigation and Drainage Engineering*, vol. 145, no. 12, p. 05019009, 2019.
- [12] M. Rahmanshahi, J. Jafari-Asl, M. Shafai Bejestan, and S. Mirjalili, “A hybrid model for predicting the energy dissipation on the block ramp hydraulic structures,” *Water Resources Management*, vol. 37, no. 8, pp. 3187–3209, 2023.
- [13] U. K. Singh and P. Roy, “Energy dissipation in hydraulic jumps using triple screen layers,” *Applied Water Science*, vol. 13, no. 1, p. 17, 2023.
- [14] M. Fathi Moghadam and E. Parsi, “Experimental investigation of the effect of hydraulic jump location on flow velocity in type ii stilling basin,” *Irrigation Sciences and Engineering*, vol. 36, no. 2, pp. 13–21, 2014.
- [15] W. Widiarti, R. Wiyono, N. Laksono, and S. Wahyuni, “The hydraulics analysis of the usbr stilling basin type of a dam under multiple flow discharge scenarios (a case study of temef dam, east nusa tenggara, indonesia),” in *IOP Conference Series: Earth and Environmental Science*, vol. 724, p. 012043, IOP Publishing, 2021.
- [16] S. N. Mousavi, D. Farsadizadeh, F. Salmasi, and A. Hosseinzadeh Dalir, “Evaluation of pressure fluctuations coefficient along the usbr type ii stilling basin using experimental results and ai models,” *ISH Journal of Hydraulic Engineering*, vol. 28, no. sup1, pp. 207–214, 2022.

- [17] A. N. Hilo, N. S. Ayoob, and Y. H. Daek, “Numerical simulation to evaluate the effect of the stepped chute on abrasion erosion of a stilling basin type iii,” in *IOP Conference Series: Materials Science and Engineering*, vol. 1090, p. 012116, IOP Publishing, 2021.
- [18] I. Stojnic, M. Pfister, J. Matos, and A. J. Schleiss, “Air–water flow in a plain stilling basin below smooth and stepped chutes,” *Journal of Hydraulic Research*, vol. 61, no. 1, pp. 51–66, 2023.
- [19] E. Fatimah, A. Azmeri, M. Fauzi, M. Rizalihadi, *et al.*, “Analysis of the hydraulic jump characteristics in a stilling basin to avoid dam failure,” *International Journal of Disaster Management*, vol. 6, no. 1, pp. 75–88, 2023.
- [20] F. Bahmanpouri, C. Gualtieri, and H. Chanson, “Flow patterns and free-surface dynamics in hydraulic jump on pebbled rough bed,” in *Proceedings of the Institution of Civil Engineers-Water Management*, vol. 176, pp. 32–49, Thomas Telford Ltd, 2023.
- [21] H. Wang, R. Tang, Z. Bai, S. Liu, W. Sang, and R. Bai, “Prototype air–water flow measurements in d-type hydraulic jumps,” *Journal of Hydraulic Research*, vol. 61, no. 1, pp. 145–161, 2023.
- [22] D. De Padova, M. Mossa, and S. Sibilla, “Sph modelling of hydraulic jump at high froude numbers at an abrupt drop: vorticity and turbulent pressure fluctuations,” *Environmental Fluid Mechanics*, pp. 1–21, 2023.
- [23] A. Agresta, C. Biscarini, F. Caraffini, and V. Santucci, “An intelligent optimised estimation of the hydraulic jump roller length,” in *International Conference on the Applications of Evolutionary Computation (Part of EvoStar)*, pp. 475–490, Springer, 2023.
- [24] J. Bradley and A. Peterka, “Hydraulic design of stilling basins: Hydraulic jumps on a horizontal apron (basin i),” *Journal of the Hydraulics Division*, vol. 83, no. 5, pp. 1401–1, 1957.

- [25] A. Peterka, *Hydraulic design of stilling basins and energy dissipators*. No. 25, US Department of the Interior, Bureau of Reclamation, 1964.
- [26] W. H. Hager and D. Li, “Sill-controlled energy dissipator,” *Journal of Hydraulic Research*, vol. 30, no. 2, pp. 165–181, 1992.
- [27] S. Erpicum, O. Machiels, B. Dewals, M. Pirotton, and P. Archambeau, “Numerical and physical hydraulic modelling of piano key weirs,” in *Asia 2012-4th Int. Conf. on Water Resources and Renewable Energy Development in Asia*, 2012.
- [28] K. Xu, Z. Han, H. Xu, and L. Bin, “Rapid prediction model for urban floods based on a light gradient boosting machine approach and hydrological–hydraulic model,” *International Journal of Disaster Risk Science*, vol. 14, no. 1, pp. 79–97, 2023.
- [29] A. Zanfei, A. Menapace, B. M. Brentan, R. Sitzenfriei, and M. Herrera, “Shall we always use hydraulic models? a graph neural network metamodel for water system calibration and uncertainty assessment,” *Water Research*, p. 120264, 2023.
- [30] V. Heller, “Scale effects in physical hydraulic engineering models,” *Journal of Hydraulic Research*, vol. 49, no. 3, pp. 293–306, 2011.
- [31] D. Yamazaki, S. Kanae, H. Kim, and T. Oki, “A physically based description of floodplain inundation dynamics in a global river routing model,” *Water Resources Research*, vol. 47, no. 4, 2011.
- [32] A. Hamedi and M. Ketabdar, “Energy loss estimation and flow simulation in the skimming flow regime of stepped spillways with inclined steps and end sill: A numerical model,” *International Journal of Science and Engineering Applications*, vol. 5, no. 7, pp. 399–407, 2016.
- [33] V. Jothiprakash, V. Bhosekar, and P. Deolalikar, “Flow characteristics of orifice spillway aerator: numerical model studies,” *ISH Journal of Hydraulic Engineering*, vol. 21, no. 2, pp. 216–230, 2015.

- [34] P. D. Bates, M. S. Horritt, and T. J. Fewtrell, "A simple inertial formulation of the shallow water equations for efficient two-dimensional flood inundation modelling," *Journal of hydrology*, vol. 387, no. 1-2, pp. 33–45, 2010.
- [35] E. Frank, G. Sofia, and S. Fattorelli, "Effects of topographic data resolution and spatial model resolution on hydraulic and hydro-morphological models for flood risk assessment," in *Flood risk assessment and management*, WIT Press Southhampton, 2012.
- [36] E. Afaridegan, N. Amanian, A. Haghiabi, A. Parsaie, and A. Goodarzi-Mohammadi, "Numerical investigation of modified semi-cylindrical weirs," *Water Resources Management*, pp. 1–14, 2023.
- [37] F. A. Dehrashid, M. Heidari, H. Rahimi, A. Khoshkonesh, S. Yuan, X. Tang, C. Lu, and X. Wang, "Cfd modeling the flow dynamics in an open channel with double-layered vegetation," *Modeling Earth Systems and Environment*, vol. 9, no. 1, pp. 543–555, 2023.
- [38] R. A. Jasim, W. Q. Hussen, M. F. Abdullah, and R. Zulkifli, "Numerical simulation of characterization of hydraulic jump over an obstacle in an open channel flow," *Journal of Advanced Research in Fluid Mechanics and Thermal Sciences*, vol. 106, no. 1, pp. 1–15, 2023.
- [39] N. K. Al-Bedyry, M. A. Kadim, S. H. Hussein, Z. S. Al-Khafaji, and F. N. Al-Husseinawi, "Experimental establishing of moving hydraulic jump in a trapezoidal channel," *Civil Engineering Journal*, vol. 9, no. 4, pp. 873–881, 2023.
- [40] A. Guven, "A multi-output descriptive neural network for estimation of scour geometry downstream from hydraulic structures," *Advances in Engineering Software*, vol. 42, no. 3, pp. 85–93, 2011.
- [41] A. Güven, M. Günal, and A. Çevik, "Prediction of pressure fluctuations on sloping stilling basins," *Canadian Journal of Civil Engineering*, vol. 33, no. 11, pp. 1379–1388, 2006.

- [42] K. R. Abed, M. H. Hobi, and A. J. Jihad, "Numerical modeling of sediment transport upstream of al-ghammas barrage," *International Journal of Scientific & Engineering Research*, vol. 5, no. 11, pp. 469–477, 2014.
- [43] S. Zaidi, M. Amin, and M. Ahmadani, "Performance evaluation of taunsa barrage emergency rehabilitation and modernization project. pakistan engineering congress," *71st Annual Session Proceedings, Paper*, no. 705, pp. 650–682, 2011.
- [44] Z. Chaudhry *et al.*, "Hydraulic/structural deficiencies at the taunsa barrage.," *Pakistan Journal of Science*, vol. 61, no. 3, pp. 135–140, 2009.
- [45] Z. A. Chaudhry, "Performance assessment of taunsa barrage subsidiary weir for long term rehabilitation planning," *Pakistan Journal of Engineering and Applied Sciences*, 2010.
- [46] K. O. Ahmed, N. Nariman, D. M. Hawez, O. Kisi, and A. Amini, "Predicting and optimizing the influenced parameters for culvert outlet scouring utilizing coupled flow 3d-surrogate modeling," *Iranian Journal of Science and Technology, Transactions of Civil Engineering*, pp. 1–14, 2023.
- [47] S. Mostafazadeh-Fard and Z. Samani, "Dissipating culvert end design for erosion control using cfd platform flow-3d numerical simulation modeling," *Journal of pipeline systems engineering and practice*, vol. 14, no. 1, p. 04022064, 2023.
- [48] A. M. A. Amin, "Physical model study for mitigating local scour downstream of clear over-fall weirs," *Ain Shams Engineering Journal*, vol. 6, no. 4, pp. 1143–1150, 2015.
- [49] C. Zulfiqar and M. Sarwar, "Launching/disappearance of stone apron, block floor downstream of the taunsa barrage and unprecedented drift of the river towards kot addu town," *Science, Technology and Development*, vol. 34, pp. 60–65, 01 2015.
- [50] H. Chanson, *Energy dissipation in hydraulic structures*. CRC Press, 2015.

- [51] A. Hamed and H. R. Fuentes, “New relationship between a vertical gate opening and downstream flow stability: experimental development,” in *World Environmental and Water Resources Congress 2016*, pp. 47–57, 2016.
- [52] S. Soori, H. Babaali, and N. Soori, “An optimal design of the inlet and outlet obstacles at usbr ii stilling basin,” *International Journal of Science and Engineering Applications*, vol. 6, no. 05, 2017.
- [53] T. Mohammed, M. Noor, B. Huat, A. Ghazali, and T. Yunis, “Effect of curvature and end sill angle on local scouring at downstream of a spillway,” *International Journal of Engineering and Technology*, vol. 1, no. 1, pp. 96–101, 2004.
- [54] H. N. Hashmi, Q. T. M. Siddiqui, A. R. Ghumman, M. A. Kamal, H. Mughal, *et al.*, “A critical analysis of 2010 floods in pakistan,” *African Journal of Agricultural Research*, vol. 7, no. 7, pp. 1054–1067, 2012.
- [55] A. Ghaderi, M. Dasineh, R. Daneshfaraz, and J. Abraham, “Reply to the discussion on paper: 3-d numerical simulation of water flow over a broad-crested weir with openings by daneshfaraz et al., 2019, in ish journal of hydraulic engineering, doi: 10.1080/09715010.2019. 1581098,” *ISH Journal of Hydraulic Engineering*, vol. 28, no. sup1, pp. 564–566, 2022.
- [56] K. Attia and H. El-Sersawy, “River regulation downstream new esna barrage using mathematical model,” in *Ninth International Water Technology Conference, IWTC9*, pp. 329–344, 2005.
- [57] H. Mirzaei and H. Tootoonchi, “Experimental and numerical modeling of the simultaneous effect of sluice gate and bump on hydraulic jump,” *Modeling Earth Systems and Environment*, vol. 6, pp. 1991–2002, 2020.
- [58] J. Chatila and M. Tabbara, “Computational modeling of flow over an ogee spillway,” *Computers & structures*, vol. 82, no. 22, pp. 1805–1812, 2004.



- [59] O. Herrera-Granados and S. W. Kostecki, “Numerical and physical modeling of water flow over the ogee weir of the new niedów barrage,” *Journal of Hydrology and Hydromechanics*, vol. 64, no. 1, p. 67, 2016.
- [60] D. R. Archer, N. Forsythe, H. J. Fowler, and S. M. Shah, “Sustainability of water resources management in the indus basin under changing climatic and socio economic conditions,” *Hydrology and Earth System Sciences*, vol. 14, no. 8, pp. 1669–1680, 2010.
- [61] P. C. Nettleton and J. A. McCorquodale, “Radial flow stilling basins with baffle blocks,” *Canadian Journal of Civil Engineering*, vol. 16, no. 4, pp. 489–497, 1989.
- [62] H. Tiwari, A. Pawar, B. Gehlot, and J. Singh, “Study of shape of intermediate sill on the design of stilling basin model,” *International Journal of Research in Egg and Technology (IJRET)*, vol. 3, no. 4, pp. 133–138, 2014.
- [63] H. Tiwari, A. Goel, S. Suresh, and S. Tiwari, “Effect of inverted t-shape splitter blocks on the performance of stilling basin models,” *Aquatic Procedia*, vol. 4, pp. 1561–1568, 2015.
- [64] A. Habibzadeh, M. Loewen, and N. Rajaratnam, “Performance of baffle blocks in submerged hydraulic jumps,” *Journal of Hydraulic Engineering*, vol. 138, no. 10, pp. 902–908, 2012.
- [65] J. D. Bricker and A. Nakayama, “Contribution of trapped air, deck super-elevation, and nearby structures to bridge deck failure during a tsunami,” *Journal of Hydraulic Engineering*, vol. 140, no. 5, p. 05014002, 2014.
- [66] A. Goel, “Design of stilling basin for circular pipe outlets,” *Canadian Journal of Civil Engineering*, vol. 35, no. 12, pp. 1365–1374, 2008.
- [67] A. Habibzadeh, S. Wu, F. Ade, N. Rajaratnam, and M. Loewen, “Exploratory study of submerged hydraulic jumps with blocks,” *Journal of Hydraulic Engineering*, vol. 137, no. 6, pp. 706–710, 2011.

- [68] A. Abbas, H. Alwash, and A. Mahmood, "Effect of baffle block configurations on characteristics of hydraulic jump in adverse stilling basins," in *MATEC Web of Conferences*, vol. 162, p. 03005, EDP Sciences, 2018.
- [69] A. Marion, M. A. Lenzi, and F. Comiti, "Effect of sill spacing and sediment size grading on scouring at grade-control structures," *Earth Surface Processes and Landforms: The Journal of the British Geomorphological Research Group*, vol. 29, no. 8, pp. 983–993, 2004.
- [70] N. N. Pillai, A. Goel, and A. K. Dubey, "Hydraulic jump type stilling basin for low froude numbers," *Journal of Hydraulic Engineering*, vol. 115, no. 7, pp. 989–994, 1989.
- [71] S. R. Mohammed, B. K. Nile, and W. H. Hassan, "Modelling stilling basins for sewage networks," in *IOP Conference Series: Materials Science and Engineering*, vol. 671, p. 012111, IOP Publishing, 2020.
- [72] A. Goel, "Experimental study on stilling basins for square outlets," in *3rd WSEAS International Conference on Applied and Theoretical Mechanics, Spain*, pp. 157–162, 2007.
- [73] J. Briscoe and U. Qamar, "Pakistan's water economy: Running dry," 2008.
- [74] A. Albinia, *Empires of the Indus: The story of a river*. WW Norton & Company, 2010.
- [75] M. A. Khan, "Planning and design of taunsa barrage rehabilitation project." 2004.
- [76] Z. Chaudary and M. K. Sarwar, "Rehabilitated taunsa barrage: prospects and concerns," *Science, Technology and Development*, vol. 33, no. 3, pp. 127–131, 2014.
- [77] Z. Chaudhry, "Surface flow hydraulics of taunsa barrage: Before and after rehabilitation," *Pakistan Journal of Science*, vol. 62, no. 2, 2010.

- [78] J. F. Macián-Pérez, R. García-Bartual, B. Huber, A. Bayón, and F. J. Vallés-Morán, “Approach to the void fraction distribution within a hydraulic jump in a typified usbr ii stilling basin,” in *Proceedings of the 38th IAHR World Congress, Panama City, Panama*, pp. 1–6, 2019.
- [79] H. Tiwari, V. Gehlot, and S. Tiwari, “Effect of height of triangular sill on the performance of stilling basin model,”
- [80] R. Gaudio and A. Marion, “Time evolution of scouring downstream of bed sills,” *Journal of hydraulic research*, vol. 41, no. 3, pp. 271–284, 2003.
- [81] B. Mansour, N. Nashed, and S. Mansour, “Model study to optimize the hydraulic performance of the new naga hammadi barrage stilling basin,” in *Bridging the Gap: Meeting the World’s Water and Environmental Resources Challenges*, pp. 1–9, 2001.
- [82] A. Alikhani, R. Behrozi-Rad, and M. Fathi-Moghadam, “Hydraulic jump in stilling basin with vertical end sill,” *International journal of physical sciences*, vol. 5, no. 1, pp. 25–29, 2010.
- [83] C. Grimaldi, R. Gaudio, F. Calomino, and A. H. Cardoso, “Control of scour at bridge piers by a downstream bed sill,” *Journal of Hydraulic Engineering*, vol. 135, no. 1, pp. 13–21, 2009.
- [84] A. Eloubaidy, J. Al-Baidhani, and A. Ghazali, “Dissipation of hydraulic energy by curved baffle blocks,” *Pertanika Journal Science Technology*, vol. 7, no. 1, pp. 69–77, 1999.
- [85] M. Omid, M. Esmaeeli Varaki, and R. Narayanan, “Gradually expanding hydraulic jump in a trapezoidal channel,” *Journal of Hydraulic Research*, vol. 45, no. 4, pp. 512–518, 2007.
- [86] H. Babaali, A. Shamsai, and H. Vosoughifar, “Computational modeling of the hydraulic jump in the stilling basin with convergence walls using cfd codes,” *Arabian Journal for Science and Engineering*, vol. 40, pp. 381–395, 2015.

- [87] G. H. Elsaheed, A. M. Ali, N. B. Abdelmageed, and A. M. Ibrahim, "Effect of end step shape in the performance of stilling basins downstream radial gates," *Journal of Scientific Research & Reports*, vol. 9, no. 1, pp. 1–9, 2016.
- [88] V. Armenio, P. Toscano, and V. Fiorotto, "On the effects of a negative step in pressure fluctuations at the bottom of a hydraulic jump," *Journal of Hydraulic Research*, vol. 38, no. 5, pp. 359–368, 2000.
- [89] D. Verma, A. Goel, and V. Rai, "New stilling basins designs for deep rectangular outlets," 2004.
- [90] D. Verma and A. Goel, "Stilling basins for pipe outlets using wedge-shaped splitter block," *Journal of Irrigation and Drainage Engineering*, vol. 126, no. 3, pp. 179–184, 2000.
- [91] D. Verma and A. Goel, "Development of efficient stilling basins for pipe outlets," *Journal of irrigation and drainage engineering*, vol. 129, no. 3, pp. 194–200, 2003.
- [92] T. Liu and J. Yang, "Three-dimensional computations of water–air flow in a bottom spillway during gate opening," *Engineering Applications of Computational Fluid Mechanics*, vol. 8, no. 1, pp. 104–115, 2014.
- [93] C. Biscarini, S. Di Francesco, and P. Manciola, "Cfd modelling approach for dam break flow studies," *Hydrology and Earth System Sciences*, vol. 14, no. 4, pp. 705–718, 2010.
- [94] C. Biscarini, S. Di Francesco, F. Nardi, and P. Manciola, "Detailed simulation of complex hydraulic problems with macroscopic and mesoscopic mathematical methods," *Mathematical Problems in Engineering*, vol. 2013, 2013.
- [95] D. G. Kim and J. H. Park, "Analysis of flow structure over ogee-spillway in consideration of scale and roughness effects by using cfd model," *KSCE Journal of Civil Engineering*, vol. 9, pp. 161–169, 2005.

- [96] M. Younus and M. Hanif Chaudhry, “A depth-averaged turbulence model for the computation of free-surface flow,” *Journal of Hydraulic Research*, vol. 32, no. 3, pp. 415–444, 1994.
- [97] A. Witt, J. Gulliver, and L. Shen, “Simulating air entrainment and vortex dynamics in a hydraulic jump,” *International Journal of Multiphase Flow*, vol. 72, pp. 165–180, 2015.
- [98] A. Ghaderi, R. Daneshfaraz, M. Dasineh, and S. Di Francesco, “Energy dissipation and hydraulics of flow over trapezoidal–triangular labyrinth weirs,” *Water*, vol. 12, no. 7, p. 1992, 2020.
- [99] A. Bayon-Barrachina and P. A. Lopez-Jimenez, “Numerical analysis of hydraulic jumps using openfoam,” *Journal of Hydroinformatics*, vol. 17, no. 4, pp. 662–678, 2015.
- [100] R. Carvalho, C. Lemos, and C. Ramos, “Numerical computation of the flow in hydraulic jump stilling basins,” *Journal of Hydraulic Research*, vol. 46, no. 6, pp. 739–752, 2008.
- [101] A. Ghaderi, M. Dasineh, F. Aristodemo, and C. Aricò, “Numerical simulations of the flow field of a submerged hydraulic jump over triangular macroroughnesses,” *Water*, vol. 13, no. 5, p. 674, 2021.
- [102] M. K. Sarwar, I. Ahmad, Z. A. Chaudary, and H.-U.-R. Mughal, “Experimental and numerical studies on orifice spillway aerator of bunji dam,” *Journal of the Chinese Institute of Engineers*, vol. 43, no. 1, pp. 27–36, 2020.
- [103] A. Bayon, D. Valero, R. García-Bartual, P. A. López-Jiménez, *et al.*, “Performance assessment of openfoam and flow-3d in the numerical modeling of a low reynolds number hydraulic jump,” *Environmental modelling & software*, vol. 80, pp. 322–335, 2016.

- [104] B. M. Savage and M. C. Johnson, “Flow over ogee spillway: Physical and numerical model case study,” *Journal of hydraulic engineering*, vol. 127, no. 8, pp. 640–649, 2001.
- [105] M. C. Johnson and B. M. Savage, “Physical and numerical comparison of flow over ogee spillway in the presence of tailwater,” *Journal of hydraulic engineering*, vol. 132, no. 12, pp. 1353–1357, 2006.
- [106] P. Lopes, J. Leandro, R. F. Carvalho, and D. B. Bung, “Alternating skimming flow over a stepped spillway,” *Environmental Fluid Mechanics*, vol. 17, no. 2, pp. 303–322, 2017.
- [107] V. Nguyen, F. Nestmann, and H. Scheuerlein, “Three-dimensional computation of turbulent flow in meandering channels and rivers,” *Journal of Hydraulic Research*, vol. 45, no. 5, pp. 595–609, 2007.
- [108] K. W. Frizell and C. D. Svoboda, *Performance of Type III Stilling Basins-Stepped Spillway Studies: Do Stepped Spillways Affect Traditional Design Parameters?* US Department of the Interior, Bureau of Reclamation, 2012.
- [109] J. F. Macián-Pérez, A. Bayón, R. García-Bartual, P. Amparo López-Jiménez, and F. J. Vallés-Morán, “Characterization of structural properties in high reynolds hydraulic jump based on cfd and physical modeling approaches,” *Journal of Hydraulic Engineering*, vol. 146, no. 12, p. 04020079, 2020.
- [110] A. Goel and M. Pal, “Application of support vector machines in scour prediction on grade-control structures,” *Engineering Applications of Artificial Intelligence*, vol. 22, no. 2, pp. 216–223, 2009.
- [111] S. Y. Kumcu, “Investigation of flow over spillway modeling and comparison between experimental data and cfd analysis,” *KSCE Journal of Civil Engineering*, vol. 21, pp. 994–1003, 2017.

- [112] A. M. Ali and Y. A. Mohamed, “Effect of stilling basin shape on the hydraulic characteristics of the flow downstream radial gates,” *Alexandria Engineering Journal*, vol. 49, no. 4, pp. 393–400, 2010.
- [113] H. Chanson, “Current knowledge in hydraulic jumps and related phenomena. a survey of experimental results,” *European Journal of Mechanics-B/Fluids*, vol. 28, no. 2, pp. 191–210, 2009.
- [114] R. Li, K. D. Splinter, and S. Felder, “Lidar scanning as an advanced technology in physical hydraulic modelling: The stilling basin example,” *Remote Sensing*, vol. 13, no. 18, p. 3599, 2021.
- [115] H. Wang and H. Chanson, “Experimental study of turbulent fluctuations in hydraulic jumps,” *Journal of Hydraulic Engineering*, vol. 141, no. 7, p. 04015010, 2015.
- [116] H. Wang, S. Felder, and H. Chanson, “An experimental study of turbulent two-phase flow in hydraulic jumps and application of a triple decomposition technique,” *Experiments in fluids*, vol. 55, pp. 1–18, 2014.
- [117] S. Ead and N. Rajaratnam, “Hydraulic jumps on corrugated beds,” *Journal of Hydraulic Engineering*, vol. 128, no. 7, pp. 656–663, 2002.
- [118] I. Ohtsu, Y. Yasuda, and Y. Yamanaka, “Drag on vertical sill of forced jump,” *Journal of Hydraulic Research*, vol. 29, no. 1, pp. 29–47, 1991.
- [119] M. Liu, N. Rajaratnam, and D. Z. Zhu, “Turbulence structure of hydraulic jumps of low froude numbers,” *Journal of Hydraulic Engineering*, vol. 130, no. 6, pp. 511–520, 2004.
- [120] S. Misra, J. Kirby, M. Brocchini, F. Veron, M. Thomas, and C. Kambhamettu, “The mean and turbulent flow structure of a weak hydraulic jump,” *Physics of Fluids*, vol. 20, no. 3, p. 035106, 2008.

- [121] N. Anjum, U. Ghani, G. A. Pasha, M. U. Rashid, A. Latif, and M. Z. Y. Rana, "Reynolds stress modeling of flow characteristics in a vegetated rectangular open channel," *Arabian Journal for Science and Engineering*, vol. 43, pp. 5551–5558, 2018.
- [122] A. Abbaspour, A. H. Dalir, D. Farsadizadeh, and A. Sadraddini, "Effect of sinusoidal corrugated bed on hydraulic jump characteristics," *Journal of Hydro-environment Research*, vol. 3, no. 2, pp. 109–117, 2009.
- [123] S. Pagliara, I. Lotti, and M. Palermo, "Hydraulic jump on rough bed of stream rehabilitation structures," *Journal of Hydro-environment research*, vol. 2, no. 1, pp. 29–38, 2008.
- [124] A. H. Zobeyer, N. Jahan, Z. Islam, G. Singh, and N. Rajaratnam, "Turbulence characteristics of the transition region from hydraulic jump to open channel flow," *Journal of Hydraulic Research*, vol. 48, no. 3, pp. 395–399, 2010.
- [125] E. Mignot and R. Cienfuegos, "Energy dissipation and turbulent production in weak hydraulic jumps," *Journal of Hydraulic Engineering*, vol. 136, no. 2, pp. 116–121, 2010.
- [126] I. Stojnic, M. Pfister, J. Matos, and A. J. SCHLEISS, "Hydraulic jump downstream of a stepped chute: an experimental study," in *Proc. 38th IAHR World Congress*, pp. 2056–2065, Panama City, Panama, 2019.
- [127] R. Padulano, O. Fecarotta, G. Del Giudice, and A. Carravetta, "Hydraulic design of a usbr type ii stilling basin," *Journal of Irrigation and Drainage Engineering*, vol. 143, no. 5, p. 04017001, 2017.
- [128] G. R. Fiala and M. L. Albertson, "Manifold stilling basin," *Transactions of the American Society of Civil Engineers*, vol. 128, no. 1, pp. 428–454, 1963.
- [129] G. H. Flammer, G. V. Skogerboe, C.-Y. Wei, and H. Rasheed, "Closed conduit to open channel stilling basin," *Journal of the Irrigation and Drainage Division*, vol. 96, no. 1, pp. 1–10, 1970.



- [130] J. Farhoudi, S. Sadat-Helbar, and N. I. Aziz, "Pressure fluctuation around chute blocks of saf stilling basins," 2010.
- [131] F. Wang, X. Chen, J. Chen, and Y. You, "Experimental study on a debris-flow drainage channel with different types of energy dissipation baffles," *Engineering Geology*, vol. 220, pp. 43–51, 2017.
- [132] A. Bestawy, H. Hazar, U. Ozturk, and T. Roy, "New shapes of baffle piers used in stilling basins as energy dissipators," *Asian Trans. Eng. (ATE)*, vol. 3, no. 1, pp. 1–7, 2013.
- [133] N. J. H. Al-Mansori, T. J. M. Alfatlawi, K. S. Hashim, and L. S. Al-Zubaidi, "The effects of different shaped baffle blocks on the energy dissipation," *Civil Engineering Journal*, vol. 6, no. 5, pp. 961–973, 2020.
- [134] W. Liu, B. Wang, Y. Guo, J. Zhang, and Y. Chen, "Experimental investigation on the effects of bed slope and tailwater on dam-break flows," *Journal of Hydrology*, vol. 590, p. 125256, 2020.
- [135] C. W. Tsai and B. C. Yen, "Shallow water wave propagation in convectively accelerating open-channel flow induced by the tailwater effect," *Journal of engineering mechanics*, vol. 130, no. 3, pp. 320–336, 2004.
- [136] L. Shearin-Feimster, "Impacts of tailwater on the design of several stilling basins in the usa," 2016.
- [137] S. Ead and N. Rajaratnam, "Plane turbulent surface jets in shallow tailwater," *J. Fluids Eng.*, vol. 123, no. 1, pp. 121–127, 2001.
- [138] S. Ead and N. Rajaratnam, "Plane turbulent wall jets on rough boundaries with limited tailwater," *Journal of Engineering Mechanics*, vol. 130, no. 10, pp. 1245–1250, 2004.
- [139] J. S. Maatooq, A. S. A. Adili, and S. S. Sameen, "Relevant problems of a hydraulic jump at diyala weir and the proposed remedy," *Eng. and Tech. Journal, University of Technology*, vol. 31, no. A, pp. 2504–2512, 2013.

- [140] S. M. Kaleem, “Research article launching/disappearance of stone apron, block floor downstream of the taunsa barrage and unprecedented drift of the river towards kot addu town chaudary zulfiqar ali department of civil engineering, university of engineering and technology, gt road, lahore, 54890, pakistan,” *Science*, vol. 34, no. 1, 2015.
- [141] M. Mossa, A. Petrillo, and H. Chanson, “Tailwater level effects on flow conditions at an abrupt drop,” *Journal of Hydraulic Research*, vol. 41, no. 1, pp. 39–51, 2003.
- [142] F. Bhuiyan, A. Habibzadeh, N. Rajaratnam, and D. Z. Zhu, “Reattached turbulent submerged offset jets on rough beds with shallow tailwater,” *Journal of Hydraulic Engineering*, vol. 137, no. 12, pp. 1636–1648, 2011.
- [143] P. Espa and S. Sibilla, “Experimental study of the scour regimes downstream of an apron for intermediate tailwater depth conditions,” *Journal of Applied Fluid Mechanics*, vol. 7, no. 4, pp. 611–624, 2014.
- [144] G. Mahtabi and H. Arvanaghi, “Experimental and numerical analysis of flow over a rectangular full-width sharp-crested weir,” *Water Science and Engineering*, vol. 11, no. 1, pp. 75–80, 2018.
- [145] S. Yoo, K. Hong, and M. Hwang, “A 3-dimensional numerical study of flow patterns around a multipurpose dam,” in *Proceedings of the 5th International Conference on Hydroinformatics, Cardiff, UK*, pp. 353–357, 2002.
- [146] J.-g. Chen, J.-m. Zhang, W.-l. Xu, and Y.-r. Wang, “Numerical simulation of the energy dissipation characteristics in stilling basin of multi-horizontal submerged jets,” *Journal of Hydrodynamics*, vol. 22, no. 5, pp. 732–741, 2010.
- [147] R. Daneshfaraz and A. Ghaderi, “Numerical investigation of inverse curvature ogee spillway,” *Civ Eng J*, vol. 3, no. 11, pp. 1146–1156, 2017.

- [148] S. Ebrahimiyan, H. Hajikandi, M. Shafai Bejestan, S. Jamali, and E. Asadi, “Numerical study on the effect of sediment concentration on jump characteristics in trapezoidal channels,” *Iranian Journal of Science and Technology, Transactions of Civil Engineering*, vol. 45, pp. 1059–1075, 2021.
- [149] N. u. Saqib, M. Akbar, P. Huali, and O. Guoqiang, “Numerical investigation of pressure profiles and energy dissipation across the stepped spillway having curved treads using flow 3d,” *Arabian Journal of Geosciences*, vol. 15, no. 15, p. 1363, 2022.
- [150] S. A. M. Al-Hashimi, K. A. Saeed, and T. N. Nahi, “Experimental and cfd modeling of hydraulic jumps forming at submerged weir,” *Journal of The Institution of Engineers (India): Series A*, vol. 100, pp. 487–493, 2019.
- [151] R. Stringer, J. Zang, and A. Hillis, “Unsteady rans computations of flow around a circular cylinder for a wide range of reynolds numbers,” *Ocean Engineering*, vol. 87, pp. 1–9, 2014.
- [152] A. Kamath, G. Fleit, and H. Bihs, “Investigation of free surface turbulence damping in rans simulations for complex free surface flows,” *Water*, vol. 11, no. 3, p. 456, 2019.
- [153] S. Jalil, J. M. Qasim, and S. Jalil, “Numerical modelling of flow over single-step broad-crested weir using flow-3d and hec-ras,” *Polytechnic General Sciences Journal/Erbil Polytechnic University*, vol. 6, pp. 435–448, 2016.
- [154] D. R. Parsons, I. J. Walker, and G. F. Wiggs, “Numerical modelling of flow structures over idealized transverse aeolian dunes of varying geometry,” *Geomorphology*, vol. 59, no. 1-4, pp. 149–164, 2004.
- [155] P. K. Tran, E. Fernandez, and J. S. Kapat, “Investigation of unsteady flow structures in a rectangular channel with pin fin array,” in *AIAA Propulsion and Energy 2019 Forum*, p. 4179, 2019.

- [156] K. Mishra, “3d numerical modelling of energy dissipation in flexible apron of barrages,” *Journal of The Institution of Engineers (India): Series A*, vol. 96, no. 1, pp. 47–56, 2015.
- [157] L. Cassan and G. Belaud, “Experimental and numerical investigation of flow under sluice gates,” *Journal of Hydraulic Engineering*, vol. 138, no. 4, pp. 367–373, 2012.
- [158] X. Liu and M. H. García, “Three-dimensional numerical model with free water surface and mesh deformation for local sediment scour,” *Journal of waterway, port, coastal, and ocean engineering*, vol. 134, no. 4, pp. 203–217, 2008.
- [159] K. Sergeenko, V. Malakhanov, A. Belousov, I. Vishnyakov, N. Karpov, and A. Nemolochnov, “Mathematical modeling of water flow through a broad-crested spillway using the cfd code star-ccm+,” *Power Technology and Engineering*, vol. 52, pp. 534–540, 2019.
- [160] Z. Zhou and J. Wang, “Numerical modeling of 3d flow field among a compound stilling basin,” *Mathematical Problems in Engineering*, vol. 2019, 2019.
- [161] S. Nikmehr and Y. Aminpour, “Numerical simulation of hydraulic jump over rough beds,” *Periodica Polytechnica Civil Engineering*, vol. 64, no. 2, pp. 396–407, 2020.
- [162] Y. Chen, Z. Fu, Q. Chen, and Z. Cui, “Discharge coefficient of rectangular short-crested weir with varying slope coefficients,” *Water*, vol. 10, no. 2, p. 204, 2018.
- [163] D. Valero, D. Bung, B. M. Crookston, and J. Matos, “Numerical investigation of usbr type iii stilling basin performance downstream of smooth and stepped spillways,” 2016.
- [164] J. F. Macián-Pérez, R. García-Bartual, B. Huber, A. Bayon, and F. J. Vallés-Morán, “Analysis of the flow in a typified usbr ii stilling basin through a

- numerical and physical modeling approach,” *Water*, vol. 12, no. 1, p. 227, 2020.
- [165] N. Viti, D. Valero, and C. Gualtieri, “Numerical simulation of hydraulic jumps. part 2: Recent results and future outlook,” *Water*, vol. 11, no. 1, p. 28, 2018.
- [166] D. Valero, R. García-Bartual, and J. Marco, “Optimisation of stilling basin chute blocks using a calibrated multiphase rans model,” in *Proc., 5th Int. Junior Researcher and Engineer Workshop on Hydraulic Structures*, 2015.
- [167] M. Tajnesaie, E. Jafari Nodoushan, R. Barati, and M. Azhdary Moghadam, “Performance comparison of four turbulence models for modeling of secondary flow cells in simple trapezoidal channels,” *ISH Journal of Hydraulic Engineering*, vol. 26, no. 2, pp. 187–197, 2020.
- [168] J. F. Rodriguez, F. A. Bombardelli, M. H. García, K. M. Frothingham, B. L. Rhoads, and J. D. Abad, “High-resolution numerical simulation of flow through a highly sinuous river reach,” *Water Resources Management*, vol. 18, pp. 177–199, 2004.
- [169] M. Heyrani, A. Mohammadian, I. Nistor, and O. F. Dursun, “Numerical modeling of venturi flume,” *Hydrology*, vol. 8, no. 1, p. 27, 2021.
- [170] J. Ma, A. A. Oberai, R. T. Lahey, and D. A. Drew, “Modeling air entrainment and transport in a hydraulic jump using two-fluid rans and des turbulence models,” *Heat and mass transfer*, vol. 47, pp. 911–919, 2011.
- [171] Y. Shekari, M. Javan, and A. Eghbalzadeh, “Effect of turbulence models on the submerged hydraulic jump simulation,” *Journal of Applied Mechanics and Technical Physics*, vol. 56, pp. 454–463, 2015.
- [172] V. Jesudhas, R. Balachandar, and T. Bolisetti, “Numerical study of a symmetric submerged spatial hydraulic jump,” *Journal of Hydraulic Research*, vol. 58, no. 2, pp. 335–349, 2020.

- [173] M. H. Azeez and R. Z. Azzubaidi, “Flow over the spillway of aladhiam dam under gated condition,” *Journal of Engineering*, vol. 28, no. 11, pp. 107–123, 2022.
- [174] E. Behnamtalab, V. Maskani, and H. Sarkardeh, “Numerical study of turbulent flow in usbr vi stilling basin,” *Applied Water Science*, vol. 13, no. 7, p. 146, 2023.
- [175] M. Moroni, M. Castellino, and P. De Girolamo, “Numerical and physical modeling of ponte liscione (guardialfiera, molise) dam spillways and stilling basin,” *Hydrology*, vol. 9, no. 12, p. 214, 2022.
- [176] J. F. Macián-Pérez, R. García-Bartual, P. A. López-Jiménez, and F. J. Vallés-Morán, “Numerical modeling of hydraulic jumps at negative steps to improve energy dissipation in stilling basins,” *Applied Water Science*, vol. 13, no. 10, p. 203, 2023.
- [177] D. J. E. Bryant and K. Ng, “Numerical modelling of hydraulic jump using mesh-based cfd method and its comparison with lagrangian moving-grid approach,” *Journal of Advanced Research in Micro and Nano Engineering*, vol. 10, no. 1, pp. 1–6, 2022.
- [178] P. K. W. Welahettige, B. Lie, and K. Vaagsaether, “Computational fluid dynamics study of flow depth in an open venturi channel for newtonian fluid,” 2017.
- [179] L. G. Castillo, J. M. Carrillo, and Á. Sordo-Ward, “Simulation of overflow nappe impingement jets,” *Journal of Hydroinformatics*, vol. 16, no. 4, pp. 922–940, 2014.
- [180] H. Pourshahbaz, S. Abbasi, M. Pandey, J. H. Pu, P. Taghvaei, and N. To-fangdar, “Morphology and hydrodynamics numerical simulation around groynes,” *ISH Journal of Hydraulic Engineering*, vol. 28, no. 1, pp. 53–61, 2022.

- [181] P. A. Le Quéré, I. Nistor, and A. Mohammadian, “Numerical modeling of tsunami-induced scouring around a square column: Performance assessment of flow-3d and delft3d,” *Journal of Coastal Research*, vol. 36, no. 6, pp. 1278–1291, 2020.
- [182] T. J. Rovesht, M. Manafpour, and M. Lotfi, “Effects of flow condition and chute geometry on the shockwaves formed on chute spillway,” *AQUA—Water Infrastructure, Ecosystems and Society*, vol. 71, no. 2, pp. 312–329, 2022.
- [183] P. G. Chanel and J. C. Doering, “Assessment of spillway modeling using computational fluid dynamics,” *Canadian Journal of Civil Engineering*, vol. 35, no. 12, pp. 1481–1485, 2008.
- [184] T. Mukha, S. K. Almeland, and R. E. Bensow, “Large-eddy simulation of a classical hydraulic jump: Influence of modelling parameters on the predictive accuracy,” *Fluids*, vol. 7, no. 3, p. 101, 2022.
- [185] O. Şimşek, N. G. Soydan, V. Gümüş, M. S. Aköz, and M. S. KIRKGÖZ, “Numerical modeling of b-type hydraulic jump at an abrupt drop,” *Teknik Dergi*, vol. 26, no. 4, pp. 7215–7240, 2015.
- [186] J. Vargas, L. Rivera, A. Salazar, V. Robledo, P. Chang, and A. Temgoua, “Comparative study of the hec-ras, iber and flow 3d softwares in studying flow characteristics across a dynamic meander in colombia,” in *CSCE Annual Conference Growing with youth. Laval*, p. 10, 2019.
- [187] M. Shademan, R. Barron, and R. Balachandar, “Evaluation of openfoam in academic research and industrial applications,” in *21st Conference of the CFD Society of Canada*, p. 7, 2013.
- [188] A. I. Rajaa and A. H. Kamela, “Performance study of fluent-2d and flow-3d platforms in the cfd modeling of a flow pattern over ogee spillway,” *Anbar Journal for Engineering Sciences*, vol. 8, no. 4, pp. 317–328, 2020.

- [189] S. Dey and A. Sarkar, “Response of velocity and turbulence in submerged wall jets to abrupt changes from smooth to rough beds and its application to scour downstream of an apron,” *Journal of Fluid Mechanics*, vol. 556, pp. 387–419, 2006.
- [190] T. Nagel, J. Chauchat, C. Bonamy, X. Liu, Z. Cheng, and T.-J. Hsu, “Three-dimensional scour simulations with a two-phase flow model,” *Advances in Water Resources*, vol. 138, p. 103544, 2020.
- [191] M. Zhao, “A review on recent development of numerical modelling of local scour around hydraulic and marine structures,” *Journal of Marine Science and Engineering*, vol. 10, no. 8, p. 1139, 2022.
- [192] D. Liang, L. Cheng, and F. Li, “Numerical modeling of flow and scour below a pipeline in currents: Part ii. scour simulation,” *Coastal engineering*, vol. 52, no. 1, pp. 43–62, 2005.
- [193] G. Dodaro, A. Tafarojnoruz, G. Sciortino, C. Adduce, F. Calomino, and R. Gaudio, “Modified einstein sediment transport method to simulate the local scour evolution downstream of a rigid bed,” *Journal of Hydraulic Engineering*, vol. 142, no. 11, p. 04016041, 2016.
- [194] G. Wei, J. Brethour, M. Grünzner, and J. Burnham, “The sedimentation scour model in flow-3d<sup>®</sup>,” *Flow Sci Rep*, vol. 3, pp. 1–29, 2014.
- [195] I. H. Obead and A. R. Sahib, “Mathematical models for simulating the hydraulic behavior of flow deflectors: laboratory and cfd-based study,” *Innovative Infrastructure Solutions*, vol. 8, no. 8, p. 213, 2023.
- [196] R. Balachandar, J. Kells, and R. Thiessen, “The effect of tailwater depth on the dynamics of local scour,” *Canadian Journal of Civil Engineering*, vol. 27, no. 1, pp. 138–150, 2000.



- [197] D. Wüthrich, S. Chamoun, G. De Cesare, P. Manso, and A. J. Schleiss, “Behaviour of a scour protection overlay with randomly distributed concrete prisms in plunge pools downstream of mobile barrages for exceptional operation conditions,” 2018.
- [198] H. Elsayed, E. Helal, M. El-Enany, and M. Sobeih, “Impacts of multi-gate regulator operation schemes on local scour downstream,” *ISH Journal of Hydraulic Engineering*, vol. 27, no. 1, pp. 51–64, 2021.
- [199] H. T. Le, C. V. Nguyen, and D.-H. Le, “Numerical study of sediment scour at meander flume outlet of boxed culvert diversion work,” *Plos one*, vol. 17, no. 9, p. e0275347, 2022.
- [200] J.-H. Tang and A. D. Puspasari, “Numerical simulation of local scour around three cylindrical piles in a tandem arrangement,” *Water*, vol. 13, no. 24, p. 3623, 2021.
- [201] R. Daneshfaraz, A. Ghaderi, M. Sattariyan, B. Alinejad, M. M. Asl, and S. Di Francesco, “Investigation of local scouring around hydrodynamic and circular pile groups under the influence of river material harvesting pits,” *Water*, vol. 13, no. 16, p. 2192, 2021.
- [202] N. Taha, M. M. El-Feky, A. A. El-Saiad, and I. Fathy, “Numerical investigation of scour characteristics downstream of blocked culverts,” *Alexandria Engineering Journal*, vol. 59, no. 5, pp. 3503–3513, 2020.
- [203] B. Shamohamadi and A. Mehboudi, “Analyzing parameters influencing scour bed in confluence channels using flow3d numerical model,” *Civil Engineering Journal*, vol. 2, no. 10, pp. 529–537, 2016.
- [204] D. Aloini, R. Dulmin, V. Mininno, and S. Ponticelli, “Supply chain management: a review of implementation risks in the construction industry,” *Business process management journal*, 2012.

- [205] F. Ullah, B. Ayub, S. Q. Siddiqui, and M. J. Thaheem, "A review of public-private partnership: Critical factors of concession period," *Journal of Financial Management of Property and Construction*, vol. 21, no. 3, pp. 269–300, 2016.
- [206] B. Ayub, M. J. Thaheem, and Z. ud Din, "Dynamic management of cost contingency: Impact of kpis and risk perception," *Procedia Engineering*, vol. 145, pp. 82–87, 2016.
- [207] S. Mazumder, "Hydraulic jump control using stilling basin with adverse slope and positive step," *ISH Journal of Hydraulic Engineering*, vol. 28, no. 1, pp. 18–20, 2022.
- [208] O. Karim and K. Ali, "Prediction of flow patterns in local scour holes caused by turbulent water jets," *Journal of Hydraulic Research*, vol. 38, no. 4, pp. 279–287, 2000.
- [209] V. D'Agostino and V. Ferro, "Scour on alluvial bed downstream of grade-control structures," *Journal of Hydraulic Engineering*, vol. 130, no. 1, pp. 24–37, 2004.
- [210] P. Jeffcoate, P. K. Stansby, and D. Apsley, "Near-field flow downstream of a barrage: experiments, 3-d, cfd and depth-averaged modelling," in *International Conference on Offshore Mechanics and Arctic Engineering*, vol. 44373, pp. 909–918, 2011.
- [211] P. Lin and W. Xu, "Newflume: a numerical water flume for two-dimensional turbulent free surface flows," *Journal of Hydraulic Research*, vol. 44, no. 1, pp. 79–93, 2006.
- [212] C. Adduce and G. Sciortino, "Scour due to a horizontal turbulent jet: Numerical and experimental investigation," *Journal of hydraulic research*, vol. 44, no. 5, pp. 663–673, 2006.
- [213] S. Maleki and V. Fiorotto, "Hydraulic jump stilling basin design over rough beds," *Journal of Hydraulic Engineering*, vol. 147, no. 1, p. 04020087, 2021.

- [214] D. Guan, B. W. Melville, and H. Friedrich, “Flow patterns and turbulence structures in a scour hole downstream of a submerged weir,” *Journal of Hydraulic Engineering*, vol. 140, no. 1, pp. 68–76, 2014.
- [215] M. Neisi and M. Shafai Bajestan, “Experimental investigation of discharge and flow energy dissipation of elliptical lopac gate in free flow condition,” *Irrigation Sciences and Engineering*, 2020.
- [216] Q. Chen, G. Dai, and H. Liu, “Volume of fluid model for turbulence numerical simulation of stepped spillway overflow,” *Journal of Hydraulic Engineering*, vol. 128, no. 7, pp. 683–688, 2002.
- [217] S. Dey and A. Sarkar, “Characteristics of turbulent flow in submerged jumps on rough beds,” *Journal of engineering mechanics*, vol. 134, no. 1, pp. 49–59, 2008.
- [218] A. Kabiri-Samani, A. Ansari, and S. M. Borghei, “Hydraulic behaviour of flow over an oblique weir,” *Journal of Hydraulic Research*, vol. 48, no. 5, pp. 669–673, 2010.
- [219] M. Sarker and D. Rhodes, “Calculation of free-surface profile over a rectangular broad-crested weir,” *Flow measurement and Instrumentation*, vol. 15, no. 4, pp. 215–219, 2004.
- [220] B. Dargahi, “Experimental study and 3d numerical simulations for a free-overflow spillway,” *Journal of Hydraulic Engineering*, vol. 132, no. 9, pp. 899–907, 2006.
- [221] N. D. Bennett, B. F. Croke, G. Guariso, J. H. Guillaume, S. H. Hamilton, A. J. Jakeman, S. Marsili-Libelli, L. T. Newham, J. P. Norton, C. Perrin, *et al.*, “Characterising performance of environmental models,” *Environmental modelling & software*, vol. 40, pp. 1–20, 2013.
- [222] Y. Chachereau and H. Chanson, “Free-surface fluctuations and turbulence in hydraulic jumps,” *Experimental Thermal and Fluid Science*, vol. 35, no. 6, pp. 896–909, 2011.

- [223] G. Muneeswaran, P. Manoharan, P. Awoyera, and A. Adesina, “A statistical approach to assess the schedule delays and risks in indian construction industry,” *International Journal of Construction Management*, vol. 20, no. 5, pp. 450–461, 2020.
- [224] M. Gündüz, Y. Nielsen, and M. Özdemir, “Quantification of delay factors using the relative importance index method for construction projects in turkey,” *Journal of management in engineering*, vol. 29, no. 2, pp. 133–139, 2013.
- [225] Z. Ahmad, M. J. Thaheem, and A. Maqsoom, “Building information modeling as a risk transformer: An evolutionary insight into the project uncertainty,” *Automation in Construction*, vol. 92, pp. 103–119, 2018.
- [226] S. Q. Siddiqui, F. Ullah, M. J. Thaheem, and H. F. Gabriel, “Six sigma in construction: a review of critical success factors,” *International Journal of Lean Six Sigma*, vol. 7, no. 2, pp. 171–186, 2016.
- [227] D. C. Wilcox *et al.*, *Turbulence modeling for CFD*, vol. 2. DCW industries La Canada, CA, 1998.
- [228] F. Salazar, R. Morán, R. Rossi, and E. Oñate, “Analysis of the discharge capacity of radial-gated spillways using cfd and ann–oliana dam case study,” *Journal of Hydraulic Research*, vol. 51, no. 3, pp. 244–252, 2013.
- [229] L. Lu, Y.-C. Li, B. Teng, and B. Chen, “Numerical simulation of turbulent free surface flow over obstruction,” *Journal of Hydrodynamics*, vol. 20, no. 4, pp. 414–423, 2008.
- [230] T. Stoesser, “Large-eddy simulation in hydraulics: Quo vadis?,” *Journal of Hydraulic Research*, vol. 52, no. 4, pp. 441–452, 2014.
- [231] S. Ghosal and P. Moin, “The basic equations for the large eddy simulation of turbulent flows in complex geometry,” *Journal of Computational Physics*, vol. 118, no. 1, pp. 24–37, 1995.

- [232] H. K. Versteeg and W. Malalasekera, *An introduction to computational fluid dynamics: the finite volume method*. Pearson education, 2007.
- [233] V. Yakhot, S. Orszag, S. Thangam, T. Gatski, and C. Speziale, “Development of turbulence models for shear flows by a double expansion technique,” *Physics of Fluids A: Fluid Dynamics*, vol. 4, no. 7, pp. 1510–1520, 1992.
- [234] P. Bradshaw, “Understanding and prediction of turbulent flow—1996,” *International journal of heat and fluid flow*, vol. 18, no. 1, pp. 45–54, 1997.
- [235] P. Bradshaw, B. E. Launder, and J. L. Lumley, “Collaborative testing of turbulence models,” 1996.
- [236] F. Science, “Flow-3d user manual v11. 2.,” 2018.
- [237] R. Tadayon and A. S. Ramamurthy, “Turbulence modeling of flows over circular spillways,” *Journal of Irrigation and Drainage Engineering*, vol. 135, no. 4, pp. 493–498, 2009.
- [238] R. Eymard, T. Gallouët, and R. Herbin, “Finite volume methods,” *Handbook of numerical analysis*, vol. 7, pp. 713–1018, 2000.
- [239] H. Le Dret, B. Lucquin, H. Le Dret, and B. Lucquin, “The finite volume method,” *Partial Differential Equations: Modeling, Analysis and Numerical Approximation*, pp. 345–382, 2016.
- [240] T. Siuta, “The impact of deepening the stilling basin on the characteristics of hydraulic jump,” *Technical Transactions*, vol. 115, no. 3, pp. 173–186, 2018.
- [241] C. Hirt and B. Nichols, “A computational method for free surface hydrodynamics,” 1981.
- [242] M. Javan and A. Eghbalzadeh, “2d numerical simulation of submerged hydraulic jumps,” *Applied Mathematical Modelling*, vol. 37, no. 10-11, pp. 6661–6669, 2013.

- [243] H. Afshin, B. Firoozabadi, and M. Mahdinia, “Performance of different turbulence models in modeling two-dimensional density current with hydraulic jumps,”
- [244] M.-P. REGION, “Folsom dam joint federal project existing spillway modeling,” 2008.
- [245] W. F. Noh and P. Woodward, “Slic (simple line interface calculation),” in *Proceedings of the fifth international conference on numerical methods in fluid dynamics June 28–July 2, 1976 Twente University, Enschede*, pp. 330–340, Springer, 2005.
- [246] H. Saghi and M. Ketabdari, “A modification to slic and plic volume of fluid models using new advection method,” *Arabian Journal for Science and Engineering*, vol. 39, pp. 669–684, 2014.
- [247] M. Lehmann and S. Gekle, “Analytic solution to the piecewise linear interface construction problem and its application in curvature calculation for volume-of-fluid simulation codes,” *Computation*, vol. 10, no. 2, p. 21, 2022.
- [248] M. Huang, L. Wu, and B. Chen, “A piecewise linear interface-capturing volume-of-fluid method based on unstructured grids,” *Numerical Heat Transfer, Part B: Fundamentals*, vol. 61, no. 5, pp. 412–437, 2012.
- [249] K. S. Bhole and B. Kale, “Techniques to minimise stair-stepping effect in micro-stereolithography process: a review,” *Advances in Materials and Processing Technologies*, vol. 8, no. 4, pp. 3615–3634, 2022.
- [250] K. E. FADAEI and G. Barani, “Numerical simulation of flow over spillway based on the cfd method,” 2014.
- [251] Z. Dong, J. Wang, D. F. Vetsch, R. M. Boes, and G. Tan, “Numerical simulation of air–water two-phase flow on stepped spillways behind x-shaped flaring gate piers under very high unit discharge,” *Water*, vol. 11, no. 10, p. 1956, 2019.

- [252] B. Savage, K. Frizell, and J. Crowder, “Brains versus brawn: the changing world of hydraulic model studies,” in *Proc. of the ASDSO Annual Conference*, 2004.
- [253] D. Ho and K. Riddette, “Application of computational fluid dynamics to evaluate hydraulic performance of spillways in australia,” *Australian Journal of Civil Engineering*, vol. 6, no. 1, pp. 81–104, 2010.
- [254] P. Lopes, *Free-surface flow interface and air-entrainment modelling using OpenFOAM*. PhD thesis, 2013.
- [255] H. K. Jalal and W. H. Hassan, “Three-dimensional numerical simulation of local scour around circular bridge pier using flow-3d software,” in *IOP Conference Series: Materials Science and Engineering*, vol. 745, p. 012150, IOP Publishing, 2020.
- [256] T. O’Donoghue, J. Doucette, J. J. van der Werf, and J. S. Ribberink, “The dimensions of sand ripples in full-scale oscillatory flows,” *Coastal Engineering*, vol. 53, no. 12, pp. 997–1012, 2006.
- [257] L. K. Gupta, M. Pandey, and P. Anand Raj, “Numerical simulation of local scour around the pier with and without airfoil collar (afc) using flow-3d,” *Environmental Fluid Mechanics*, pp. 1–19, 2023.
- [258] H. Pourshahbaz, S. Abbasi, *et al.*, “Numerical scour modeling around parallel spur dikes in flow-3d,” *Drinking Water Engineering and Science Discussions*, pp. 1–16, 2017.
- [259] B. A. Bakhmeteff and A. E. Matzke, “The hydraulic jump in terms of dynamic similarity,” *Transactions of the American Society of Civil Engineers*, vol. 101, no. 1, pp. 630–647, 1936.
- [260] F. G. Carollo, V. Ferro, and V. Pampalone, “Hydraulic jumps on rough beds,” *Journal of Hydraulic Engineering*, vol. 133, no. 9, pp. 989–999, 2007.
- [261] S. Kucukali and H. Chanson, “Turbulence in hydraulic jumps: experimental measurements,” 2007.

- 
- [262] F. Murzyn and H. Chanson, “Experimental investigation of bubbly flow and turbulence in hydraulic jumps.,” *Environmental Fluid Mechanics*, vol. 9, no. 2, 2009.



# Annex-3A

TABLE 1: Strongly desired features of three dimensional (3-D) numerical codes and their comparison

TABLE 1: Strongly desired features of three dimensional (3-D) numerical codes and their comparison

FEATURE	FLOW3D [86][164]	FLUENT [157] [156]	PHOENICS [154]	Open FOAM [99][106]
Solution technique	FVM, co-located grid	FVM, Co-located grid	FVM, staggered grid	FVM, staggered grid
Dimensions	2D, 3D	2D, 3D	2D, 3D	2D, 3D
Mesh type	Structured, multi-block	Structured	Structured	Structured
Cell limit	Hardware limited	150,000 (Hardware limit reached first)	Hardware limited	Hardware limited
Geometry and mesh generation	GUI, command language	Menu driven. (keyboard)	GUI, PHOENICS Input Language	Open FOAM toolbox
Flexibility of boundary conditions	Very	Very	Very	Very
Reynolds number (Re)	(Low and high Re)	(Low and high Re)	Laminar and turbulent	(Low and high Re)
Turbulence models	K- $\epsilon$ , ASM, RSM, DSM, Reynolds flux model	K- $\epsilon$ , RSM, RNG	K- $\epsilon$ , K-1, constant eddy viscosity, RSM (Not available with BFCs)	K- $\epsilon$ , ASM, RSM, DSM, Reynolds flux model
Particle tracking	Transport model, multi-phase, scalar	Lagrangian	Separate module GENTRA	Lagrangian
Multi-phase	Yes	No	Yes	Yes
Multi-species	Yes	Yes	Yes	Yes
Multi-zone regions	multi-block	'Blocking off' cells	'Blocking off' cells	Split meshing
Solution monitoring	Yes (Graphical and numerical)	Yes (Graphical and numerical)	Yes (Graphical and numerical)	Yes (Graphical and numerical)
Post-processing	All features	All features	All features	All features
User friendliness	Excellent	Unfriendly, but manuals are good	Excellent good to get started	Excellent good to get started

## Annex-3B

FIGURE 1: Time rate change of discharge at  $2.44 \text{ m}^3/\text{s}/\text{m}$ , **(a)** Type (A), **(b)** Type (B), **(c)** Type (C), and **(d)** Type (D) basins

FIGURE 2: Time rate change of discharge at  $4.88 \text{ m}^3/\text{s}/\text{m}$ , **(a)** Type (A), **(b)** Type (B), **(c)** Type (C), and **(d)** Type (D) basins

FIGURE 3: Time rate change of discharge at  $7.22 \text{ m}^3/\text{s}/\text{m}$ , **(a)** Type (A), **(b)** Type (B), **(c)** Type (C), and **(d)** Type (D) basins

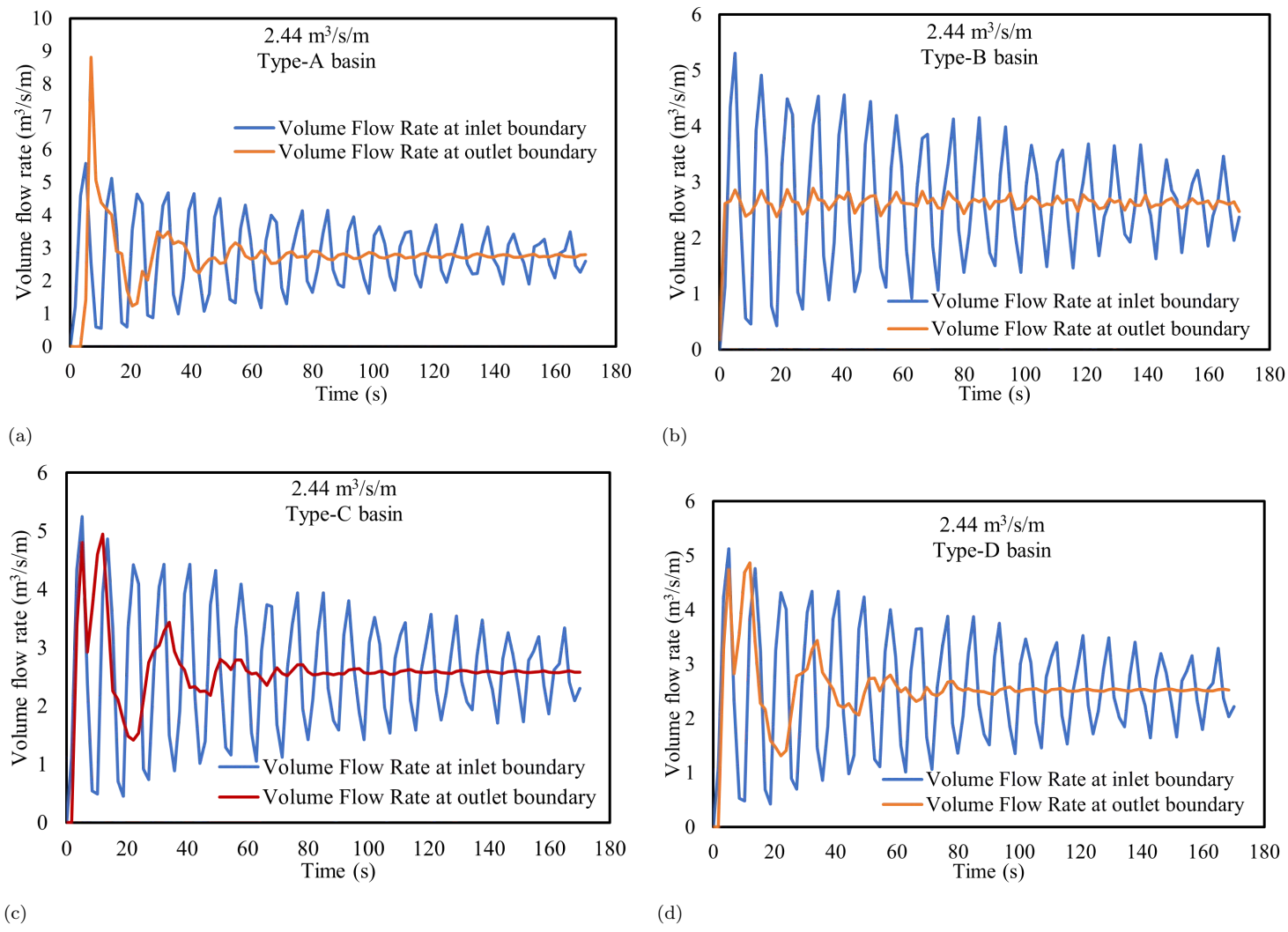


FIGURE 1: Time rate change of discharge at 2.44 m<sup>3</sup>/s/m, (a) Type (A), (b) Type (B), (c) Type (C), and (d) Type (D) basins

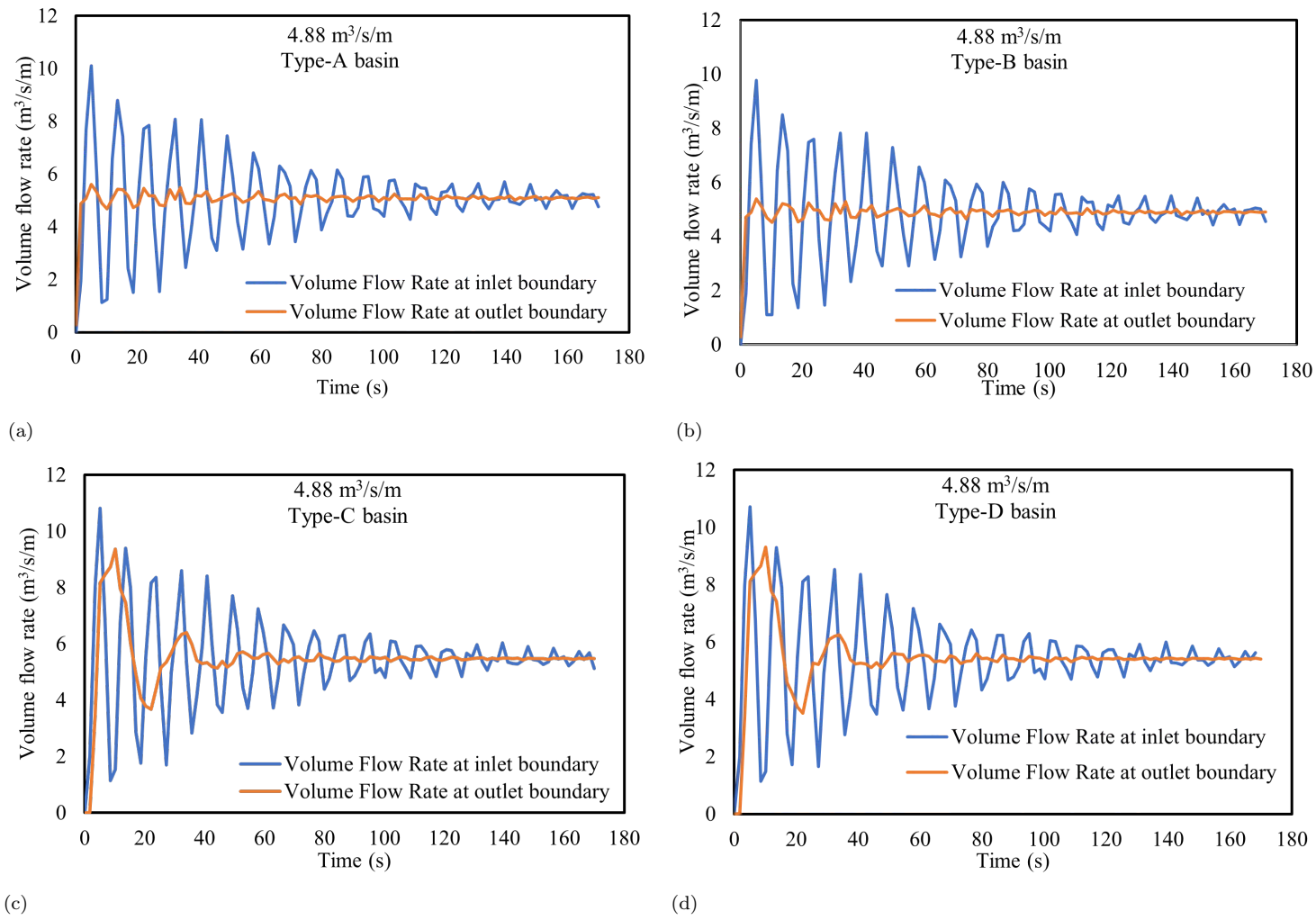


FIGURE 2: Time rate change of discharge at  $4.88 \text{ m}^3/\text{s}/\text{m}$ , (a) Type (A), (b) Type (B), (c) Type (C), and (d) Type (D) basins

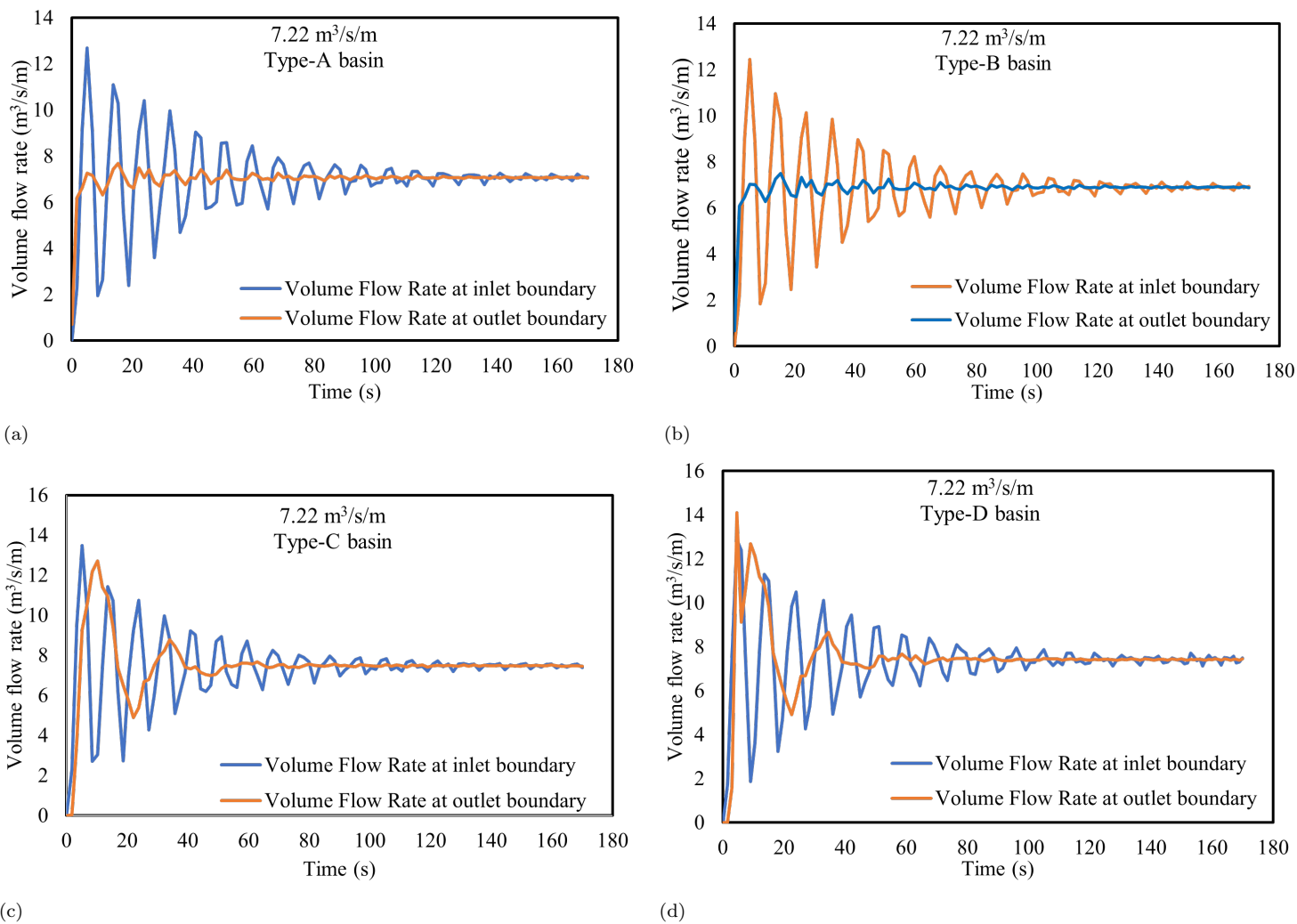


FIGURE 3: Time rate change of discharge at  $7.22 \text{ m}^3/\text{s}/\text{m}$ , (a) Type (A), (b) Type (B), (c) Type (C), and (d) Type (D) basins